universität wien

DISSERTATION / DOCTORAL THESIS

Titel der Dissertation /Title of the Doctoral Thesis

Assessment of the global distribution of coarse-mode aerosol and clouds with large-scale in situ aircraft observations

verfasst von / submitted by

Maximilian Dollner, MSc

angestrebter akademischer Grad / in partial fulfilment of the requirements for the degree of

Doktor der Naturwissenschaften (Dr. rer. nat.)

Wien, 2022 / Vienna 2022

Studienkennzahl lt. Studienblatt / degree programme code as it appears on the student record sheet:	A 796 605 411
Dissertationsgebiet lt. Studienblatt / field of study as it appears on the student record sheet:	Physik
Betreut von / Supervisor:	Univ.-Prof. Dr. Bernadett Weinzierl

ABSTRACT

Atmospheric aerosols and clouds interact with solar and terrestrial radiation, influencing the Earth's climate in many complex ways. However, many of these complex interactions are not fully understood leading to the largest uncertainties in future climate predictions. In particular cloud feedback and aerosol-cloud interaction pose the largest contribution to these uncertainties. Especially the investigation of aerosol-cloud interactions remains challenging since cloud particles measurements in the relevant size range of sub 100 µm continue to be difficult. Coarse-mode aerosol (> 1 µm) influences cloud formation and cloud properties with its ability to act as Cloud Condensation Nuclei (CCN) and Ice Nuclei (IN) and impacts the atmosphere through radiative interactions. Even though atmospheric coarse-mode aerosol has large implications on weather and climate, it tends to be neglected in atmospheric observations and climate models.

The focus of this research dissertation is on the assessment of the global distribution of coarse-mode aerosol and clouds, which involves laboratory experiments, airborne observations, theoretical simulations, and major algorithm developments. In this dissertation, (1) measurement capabilities for airborne coarse-mode aerosol and cloud observations were enhanced, (2) a novel algorithm for automatic detection and classification of periods inside clouds was developed, (3) the significance of coarse-mode aerosol to properly characterize the properties of global atmospheric aerosol was shown, and (4) the formation of dust-impacted ice clouds in the Mediterranean was investigated. The data sets for the analysis of this research were collected during three international airborne field campaigns: Atmospheric Tomography (ATom; 2016-2018), Absorbing aerosol layers in a changing climate: aging, lifetime, and dynamics (A-LIFE; 2017), and Fire Influence on Regional to Global Environments Experiment - Air Quality (FIREX-AQ; 2019)

(1) Next-generation measurements of coarse-mode aerosol and cloud particles

The second-generation Cloud, Aerosol, and Precipitation Spectrometer (CAPS; Droplet Measurement Technologies Inc, Longmont, USA), a wing-mounted optical spectrometer and optical array probe, is the central instrument of this dissertation. Methodological developments include the characterization of mounting-location induced flow distortions on airborne in situ measurements of aerosols and clouds. Using a combination of airborne in situ data with numerical simulations the particle size-dependent effects of flow-induced errors on particle number concentration and droplet measurements were quantified. Also, in the framework of this dissertation, an improved calibration process and a novel size distribution retrieval for optical spectrometer data from CAPS were developed. The novel calibration setup and procedure enables the calibration of the entire size range between 0.5 and 50 µm not only in the lab but also in the field and results in a refractive index independent calibration output. This refractive index independent calibration builds the foundation for the novel size distribution retrieval, which considers instrumental uncertainties and reports particle sizes in geometric diameters considering non-sphericity and refractive indices of the measured aerosol. These novel characterizations and techniques now allow a more reliable and precise measurement and quantification of atmospheric coarse-mode aerosol and cloud particles.

(2) A novel algorithm for automatic detection and classification of clouds

The *Cloud Indicator* algorithm was developed based on observations from the ATom, A-LIFE, and FIREX-AQ field campaigns. It utilizes size distribution, temperature, and relative humidity measurements to detect and classify periods into cloud-free sequences, Aerosol-Cloud Transition Regime (ACTR), liquid, Mixed-Phase Temperature Regime (MPTR), or cirrus clouds. The algorithm contains a cloud-aerosol volume factor, designed in the course of this dissertation to ensure

robust and precise discrimination of clouds from aerosol layers with enhanced coarse-mode aerosol concentrations (e.g. mineral dust, sea salt, or biomass burning) and, hence, reduces the number of misclassifications of aerosol layers as clouds. This novel algorithm now opens the door to greatly expanded analyses of the scientific drivers of cloud processes like aerosol-cloud interactions.

(3) Significance of coarse-mode aerosol

The importance and atmospheric abundance of coarse-mode aerosol was revealed with observations from ATom and A-LIFE. CAPS measurements were processed with the novel size distribution retrieval and combined with aircraft in-cabin measured size distributions, together covering the size range from the nucleation mode to the coarse mode. The combined size distributions were used to calculate intensive and extensive aerosol properties, revealing the importance of precise coarse-mode aerosol measurements to correctly represent atmospheric aerosol properties. Particularly the Northern hemisphere's lower and free troposphere contained substantially more coarse-mode aerosol from continental origins than the Southern hemisphere. Furthermore, dust and biomass burning contributed significantly to the Aerosol Optical Depth (AOD) not only above the Atlantic downwind of the major sources in Africa but also in the free troposphere above the Northern Pacific.

(4) The formation of dust-impacted ice clouds

For the analysis of global-scale tropospheric clouds, the novel *Cloud Indicator* algorithm was applied to the measurements from ATom, A-LIFE, and FIREX-AQ, which resulted in a unique global-scale data set of clouds. For this dissertation, particular investigations were focused on unique observations of clouds embedded in a mineral dust layer measured during A-LIFE. This unprecedented case shows atmospheric in situ measurements of the activation and growth of mineral dust aerosol to cloud particles for the first time. Chemical analysis of samples taken from the particles in the dust layer revealed the composition of the mineral dust and enabled the comparison of the ice nucleation temperature and relative humidity with values from laboratory studies. Furthermore, the fractions of aerosol particles nucleating to cloud particles were compared to laboratory measurements and provided a unique opportunity to validate ice nucleation particle (INP) parameterizations which are commonly used to predict atmospheric INP concentrations.

ZUSAMMENFASSUNG

Atmosphärische Aerosole und Wolken wechselwirken mit solarer und terrestrischer Strahlung. Sie beeinflussen das Klima der Erde durch vielen komplexe Prozesse. Viele dieser Prozesse sind jedoch nicht vollständig verstanden, was zu den größten Unsicherheiten im Zusammenhang mit Klimavorhersagen führt. Insbesondere Wolkenrückkopplungseffekte und Aerosol-Wolken-Wechselwirkung leisten den größten Beitrag zu diesen Unsicherheiten. Trotz intensiver Forschung bleibt die Untersuchung der Aerosol-Wolken-Wechselwirkung eine Herausforderung, da verlässliche Messungen von Wolkenpartikeln im relevanten Größenbereich von unter 100 µm weiterhin schwierig sind. Coarse-Mode Aerosolpartikel (> 1 µm) können als Wolkenkondensations- (CCN) und Eiskeime (IN) die Wolkenbildung und die Wolkeneigenschaften beeinflussen und wirken sich durch Strahlungswechselwirkungen auf die Atmosphäre aus. Obwohl atmosphärisches Coarse-Mode Aerosol einen großen Einfluss auf Wetter und Klima hat, wird es bei atmosphärischen Messungen und in Klimamodellen oft vernachlässigt.

Der Schwerpunkt dieser Dissertation liegt auf der Untersuchung der globalen Verteilung von Coarse-Mode Aerosol und Wolken. Dies erfolgt durch Laborexperimente, flugzeuggetragene Messungen, theoretische Simulationen und die Entwicklung von Algorithmen. In dieser Arbeit wurden (1) die Messmöglichkeiten für flugzeuggestützte Messungen von Coarse-Mode Aerosol und Wolken verbessert, (2) ein neuartiger Algorithmus zur automatischen Erkennung und Klassifizierung von Messzeiten innerhalb von Wolken entwickelt, (3) die Bedeutung von Coarse-Mode Aerosol für die korrekte Charakterisierung der Eigenschaften des globalen atmosphärischen Aerosols aufgezeigt und (4) die Bildung von staubbeeinflussten Eiswolken im Mittelmeerraum untersucht. Die Datensätze für die Analysen in dieser Arbeit wurden während dreier internationaler Flugzeugmesskampagnen erhoben: Atmospheric Tomography (ATom; 2016-2018), Absorbing aerosol layers in a changing climate: aging, lifetime and dynamics (A-LIFE; 2017) und Fire Influence on Regional to Global Environments Experiment - Air Quality (FIREX-AQ; 2019)

(1) Verbesserte Messungen von Coarse-Mode Aerosol- und Wolkenpartikeln

Das CAPS Messgerät (CAPS: Cloud, Aerosol, and Precipitation Spectrometer; Droplet Measurement Technologies Inc, Longmont, USA) ist ein am Flugzeugflügel montiertes Instrument, welches mit einem optischen Spektrometer und durch Aufzeichnung von Schattenbildern Messungen von Aerosol- und Wolkenpartikeln ermöglicht. Das CAPS Messgerät ist das zentrale Instrument dieser Arbeit. Im Rahmen dieser Dissertation wurde der Einfluss der durch die Montageposition bedingten Strömungsverzerrungen bei Flugzeugmessungen von Aerosolen und Wolken charakterisiert. Dazu wurden Daten aus solchen flugzeuggetragenen Messungen mit numerischen Simulationen kombiniert. Dies ermöglichte die Quantifizierung des partikelgrößenabhängigen Effekts auf die gemessene Partikelanzahlkonzentration und Partikelbilder. Darüber hinaus wurde für das optische Spektrometer vom CAPS Messgerät der Kalibrierungsprozess verbessert und ein neuartiges Verfahren für die Berechnung der Partikelgrößenverteilung entwickelt. Diese ermöglichen die Kalibrierung des gesamten Größenbereichs zwischen 0.5 und 50 µm nicht nur im Labor, sondern auch auf Messkampagnen und liefert ein brechungsindexunabhängiges Ergebnis der Kalibrierung. Dieses Kalibrierergebnis bildet die Grundlage für die neuartige Berechnung der Partikelgrößenverteilung, welche instrumentelle Unsicherheiten berücksichtigt und die Partikelgrößen in geometrischen Durchmessern angibt. Hierbei werden auch Effekte von nicht-runden Partikeln und die Brechungsindizes des gemessenen Aerosols berücksichtigt. Durch diese methodischen Arbeiten steht nun eine zuverlässigere und präzisere Messung und Quantifizierung von atmosphärischen Coarse-Mode Aerosol- und Wolkenpartikeln zur Verfügung.

(2) Ein neuer Algorithmus zur automatischen Erkennung und Klassifizierung von Wolken

Der „Cloud Indicator“ Algorithmus wurde basierend auf Flugzeugmessungen aus den ATom, A-LIFE und FIREX-AQ Messkampagnen entwickelt. Er verwendet Partikelgrößenverteilungen, Temperatur und relativen Luftfeuchtigkeit, um wolkenfreie Regionen, Regionen im Aerosol-Wolken-Übergangsregime (ACTR: Aerosol-Cloud Transition Regime), flüssig Wasser Wolken, Wolken im Mischphasen-Temperaturregime (MPTR: Mixed-Phase Temperature Regime) oder Zirruswolken zu erkennen und zu klassifizieren. Der Algorithmus nutzt einen neuartigen, im Rahmen dieser Dissertation entwickelten Wolken-Aerosol-Volumenfaktor um eine robuste und präzise Unterscheidung zwischen Wolken und Aerosolschichten mit erhöhter Coarse-Mode Aerosolkonzentration
(z. B. Mineralstaub, Meersalz oder Waldbrandaerosol) zu gewährleisten und somit die Zahl der Fehlklassifikationen von Aerosolschichten als Wolken zu verringern. Dieser neuartige Algorithmus ermöglicht nun verbesserte Analysen von Wolkenprozessen wie Aerosol-Wolken-Wechselwirkungen.

(3) Bedeutung des Coarse-Mode Aerosols

Die Bedeutung von Coarse-Mode Aerosol in der Atmosphäre wurde anhand der ATom und A-LIFE Messungen aufgezeigt. Dazu wurden die CAPS-Daten mit dem neuartigen Größenverteilungsverfahren ausgewertet und mit den in der Flugzeugkabine gemessenen Größenverteilungen kombiniert. Zusammen decken die Messungen den Größenbereich von der Nukleation-Mode bis zur Coarse-Mode ab. Anhand dieser kombinierten Größenverteilungen wurden intensive und extensive Aerosoleigenschaften berechnet, was die Bedeutung präziser Coarse-Mode Aerosolmessungen für die korrekte Darstellung atmosphärischer Aerosoleigenschaften aufzeigte. Die Analysen zeigen, dass insbesondere die untere und freie Troposphäre der nördlichen Hemisphäre wesentlich mehr Coarse-Mode Aerosol kontinentalen Ursprungs als die südliche Hemisphäre enthielt. Darüber hinaus trugen Mineralstaub- und Waldbrandaerosol nicht nur über dem Atlantik nahe der Hauptquellen in Afrika, sondern auch in der freien Troposphäre über dem nördlichen Pazifik erheblich zur aerosoloptischen Dicke bei.

(4) Mineralstaubeinfluss bei der Bildung von Eiswolken

Um die troposphärischen Wolken zu analysieren wurde der neuartige „Cloud Indicator“ Algorithmus auf die Messungen von ATom, A-LIFE und FIREX-AQ angewendet und ein einzigartiger Wolkendatensatz mit globaler Abdeckung erstellt. Mit besonderem Fokus wurden einzigartige Beobachtungen von in Mineralstaubschicht eingebettete Wolken, welche während A-LIFE gemessen wurde, analysiert. Diese Daten zeigen -unseres Wissens- zum ersten Mal die Aktivierung und das Wachstum von Mineralstaub-Aerosol zu Wolkenpartikeln in der Atmosphäre. Die chemische Analyse von Partikelproben der Staubschicht lieferten Informationen über die Zusammensetzung des Mineralstaubs. Diese chemischen Zusammensetzungen in Kombination mit gemessener Temperatur und relativen Feuchte bei der Wolkenbildung wurden mit Laborstudien zu Aktivierungstemperatur und -feuchte von Mineralstaub verglichen. Die Messungen ermöglichten außerdem die Bestimmung des Anteils der Aerosolpartikel, die zu Wolkenpartikeln anwuchsen. Des Weiteren erlaubten die Messungen eine Validierung gängiger Parametrisierungen für eiskeimbildende Partikel (INP: Ice-Nucleating Particle), die üblicherweise zur Vorhersage atmosphärischer INP-Konzentrationen verwendet werden.

LIST OF PUBLICATIONS

This section lists all publications connected to this dissertation. The first four papers include the main results of the dissertation, whereas the remaining 17 publications include contributions emerging from the work of this doctoral dissertation.

Paper I (published)

Flow-induced errors in airborne in situ measurements of aerosols and clouds

Spanu, A., **Dollner, M.**, Gasteiger, J., Bui, T.P., Weinzierl, B.

(2020), *Atmospheric Measurement Techniques* 13, 1963–1987, 3

DOI: https://doi.org/10.5194/amt-13-1963-2020

Paper II (manuscript in preparation)

The *Cloud Indicator*: A novel algorithm for automatic detection and classification of clouds using airborne in situ observations

Dollner, M., Gasteiger, G., Schöberl, M., Gattringer, A., Beres, N. D., Bui, T. P., Diskin, G. and Weinzierl, B.

(2022) Manuscript in preparation for *Atmospheric Research*

Paper III (published)

Ambient aerosol properties in the remote atmosphere from global-scale in situ measurements

Brock, C. A., Froyd, K. D., **Dollner, M.**, Williamson, C. J., Schill, G., Murphy, D. M., Wagner, N. J., Kupc, A., Jimenez, J. L., Campuzano-Jost, P., Nault, B. A., Schroder, J. C., Day, D. A., Price, D. J., Weinzierl, B., Schwarz, J. P., Katich, J. M., Wang, S., Zeng, L., Weber, R., Dibb, J., Scheuer, E., Diskin, G. S., DiGangi, J. P., Bui, T., Dean-Day, J. M., Thompson, C. R., Peischl, J., Ryerson, T. B., Bourgeois, I., Daube, B. C., Commane, R., and Wofsy, S. C.

(2021), *Atmospheric Chemistry and Physics*, 21, 15023–15063

DOI: https://doi.org/10.5194/acp-21-15023-2021

Paper IV (manuscript in preparation)

Aerosol-cloud interactions of Saharan mineral dust over the Eastern Mediterranean

Dollner, M., Gasteiger, J., Kandler, K., Schöberl, M., Sudharaj, A., Witaschs, B. and Weinzierl, B.

(2022) Manuscript in preparation

Other Publications which include contributions emerging from the work of this doctoral dissertation:

5) The NASA Atmospheric Tomography (ATom) Mission: Imaging the Chemistry of the Global Atmosphere

Thompson, C.R., Wofsy, S.C., Prather, M.J., Newman, P.A., Hanisco, T.F., Ryerson, T.B., Fahey, D.W., Apel, E.C., Brock, C.A., Brune, W.H., Froyd, K., Katich, J.M., Nicely, J.M., Peischl, J., Ray, E., Veres, P.R., Wang, S., Allen, H.M., Asher, E., Bian, H., Blake, D., Bourgeois, I., Budney, J., Bui, T.P., Butler, A., Campuzano-Jost, P., Chang, C., Chin, M., Commane, R., Correa, G., Crounse, J.D., Daube, B., Dibb, J.E., DiGangi, J.P., Diskin, G.S., **Dollner, M.**, Elkins, J.W., Fiore, A.M., Flynn, C.M., Guo, H., Hall, S.R., Hannun, R.A., Hills, A., Hintsa, E.J., Hodzic, A., Hornbrook, R.S., Huey, L.G., Jimenez, J.L., Keeling, R.F., Kim, M.J., Kupc, A., Lacey, F., Lait, L.R., Lamarque, J.-F., Liu, J., McKain, K., Meinardi, S., Miller, D.O., Montzka, S.A., Moore, F.L., Morgan, E.J., Murphy, D.M., Murray, L.T., Nault, B.A., Neuman, J.A., Nguyen, L., Gonzalez, Y., Rollins, A., Rosenlof, K., Sargent, M., Schill, G., Schwarz, J.P., Clair, J.M.St., Steenrod, S.D., Stephens, B.B., Strahan, S.E., Strode, S.A., Sweeney, C., Thames, A.B., Ullmann, K., Wagner, N., Weber, R., Weinzierl, B., Wennberg, P.O., Williamson, C.J., Wolfe, G.M., Zeng, L.,
(2022), Bulletin of the American Meteorological Society 103, E761–E790.
DOI: https://doi.org/10.1175/BAMS-D-20-0315.1

6) A large source of cloud condensation nuclei from new particle formation in the tropics

Williamson, C.J., Kupc, A., Axisa, D., Bilsback, K.R., Bui, T., Campuzano-Jost, P., **Dollner, M.**, Froyd, K.D., Hodshire, A.L., Jimenez, J.L., Kodros, J.K., Luo, G., Murphy, D.M., Nault, B.A., Ray, E.A., Weinzierl, B., Wilson, J.C., Yu, F., Yu, P., Pierce, J.R., Brock, C.A.
(2019) Nature 574, 399–403.
DOI: https://doi.org/10.1038/s41586-019-1638-9

7) Global airborne sampling reveals a previously unobserved dimethyl sulfide oxidation mechanism in the marine atmosphere

Veres, P.R., Neuman, J.A., Bertram, T.H., Assaf, E., Wolfe, G.M., Williamson, C.J., Weinzierl, B., Tilmes, S., Thompson, C.R., Thames, A.B., Schroder, J.C., Saiz-Lopez, A., Rollins, A.W., Roberts, J.M., Price, D., Peischl, J., Nault, B.A., Møller, K.H., Miller, D.O., Meinardi, S., Li, Q., Lamarque, J.-F., Kupc, A., Kjaergaard, H.G., Kinnison, D., Jimenez, J.L., Jernigan, C.M., Hornbrook, R.S., Hills, A., **Dollner, M.**, Day, D.A., Cuevas, C.A., Campuzano-Jost, P., Burkholder, J., Bui, T.P., Brune, W.H., Brown, S.S., Brock, C.A., Bourgeois, I., Blake, D.R., Apel, E.C., Ryerson, T.B.
(2020), Proc Natl Acad Sci USA 201919344.
DOI: https://doi.org/10.1073/pnas.1919344117

8) Rapid cloud removal of dimethyl sulfide oxidation products limits SO_2 and cloud condensation nuclei production in the marine atmosphere

Novak, G.A., Fite, C.H., Holmes, C.D., Veres, P.R., Neuman, J.A., Faloona, I., Thornton, J.A., Wolfe, G.M., Vermeuel, M.P., Jernigan, C.M., Peischl, J., Ryerson, T.B., Thompson, C.R., Bourgeois, I., Warneke, C., Gkatzelis, G.I., Coggon, M.M., Sekimoto, K., Bui, T.P., Dean-Day, J., Diskin, G.S., DiGangi, J.P., Nowak, J.B., Moore, R.H., Wiggins, E.B., Winstead, E.L., Robinson, C., Thornhill, K.L., Sanchez, K.J., Hall, S.R., Ullmann, K., **Dollner, M.**, Weinzierl, B., Blake, D.R., Bertram, T.H.
(2021), Proc Natl Acad Sci USA 118, e2110472118.
DOI: https://doi.org/10.1073/pnas.2110472118

9) Sea spray aerosol concentration modulated by sea surface temperature

Liu, S., Liu, C.-C., Froyd, K.D., Schill, G.P., Murphy, D.M., Bui, T.P., Dean-Day, J.M., Weinzierl, B., **Dollner, M.**, Diskin, G.S., Chen, G., Gao, R.-S.
(2021), Proc Natl Acad Sci 118.
DOI: https://doi.org/10.1073/pnas.2020583118

10) Measurements from inside a Thunderstorm Driven by Wildfire: The 2019 FIREX-AQ Field Experiment

Peterson, D.A., Thapa, L.H., Saide, P.E., Soja, A.J., Gargulinski, E.M., Hyer, E.J., Weinzierl, B., **Dollner, M.**, Schöberl, M., Papin, P.P., Kondragunta, S., Camacho, C.P., Ichoku, C., Moore, R.H., Hair, J.W., Crawford, J.H., Dennison, P.E., Kalashnikova, O.V., Bennese, C.E., Bui, T.P., DiGangi, J.P., Diskin, G.S., Fenn, M.A., Halliday, H.S., Jimenez, J., Nowak, J.B., Robinson, C., Sanchez, K., Shingler, T.J., Thornhill, L., Wiggins, E.B., Winstead, E., Xu, C.
(2022), Bulletin of the American Meteorological Society 1.
DOI: https://doi.org/10.1175/BAMS-D-21-0049.1

11) Global-scale constraints on light-absorbing anthropogenic iron oxide aerosols

Lamb, K.D., Matsui, H., Katich, J.M., Perring, A.E., Spackman, J.R., Weinzierl, B., **Dollner, M.**, Schwarz, J.P.
(2021), npj Climate and Atmospheric Science 4, 1–12.
DOI: https://doi.org/10.1038/s41612-021-00171-0

12) Aerosol size distributions during the Atmospheric Tomography Mission (ATom): methods, uncertainties, and data products

Brock, C.A., Williamson, C., Kupc, A., Froyd, K.D., Erdesz, F., Wagner, N., Richardson, M., Schwarz, J.P., Gao, R.-S., Katich, J.M., Campuzano-Jost, P., Nault, B.A., Schroder, J.C., Jimenez, J.L., Weinzierl, B., **Dollner, M.,** Bui, T., Murphy, D.M.
(2019), Atmos. Meas. Tech. 12, 3081–3099
DOI: https://doi.org/10.5194/amt-12-3081-2019

13) Large hemispheric difference in nucleation mode aerosol concentrations in the lowermost stratosphere at mid- and high latitudes

Williamson, C.J., Kupc, A., Rollins, A., Kazil, J., Froyd, K.D., Ray, E.A., Murphy, D.M., Schill, G.P., Peischl, J., Thompson, C., Bourgeois, I., Ryerson, T.B., Diskin, G.S., DiGangi, J.P., Blake, D.R., Bui, T.P.V., **Dollner, M.**, Weinzierl, B., Brock, C.A.
(2021), Atmospheric Chemistry and Physics 21, 9065–9088.
DOI: https://doi.org/10.5194/acp-21-9065-2021

14) Observationally constrained analysis of sea salt aerosol in the marine atmosphere

Bian, H., Froyd, K., Murphy, D.M., Dibb, J., Darmenov, A., Chin, M., Colarco, P.R., Silva, A. da, Kucsera, T.L., Schill, G., Yu, H., Bui, P., **Dollner, M.**, Weinzierl, B., Smirnov, A.
(2019), Atmospheric Chemistry and Physics 19, 10773–10785
DOI: https://doi.org/10.5194/acp-19-10773-2019

15) **The importance of size ranges in aerosol instrument intercomparisons: a case study for the Atmospheric Tomography Mission**

Guo, H., Campuzano-Jost, P., Nault, B.A., Day, D.A., Schroder, J.C., Kim, D., Dibb, J.E., **Dollner, M.**, Weinzierl, B., Jimenez, J.L.
(2021), Atmospheric Measurement Techniques 14, 3631–3655
DOI: https://doi.org/10.5194/amt-14-3631-2021

16) **Strong Contrast in Remote Black Carbon Aerosol Loadings Between the Atlantic and Pacific Basins**

Katich, J.M., Samset, B.H., Bui, T.P., **Dollner, M.**, Froyd, K.D., Campuzano-Jost, P., Nault, B.A., Schroder, J.C., Weinzierl, B., Schwarz, J.P.
(2018), J. Geophys. Res. Atmos. 123
DOI: https://doi.org/10.1029/2018JD029206

17) **The potential role of organics in new particle formation and initial growth in the remote tropical upper troposphere**

Kupc, A., Williamson, C.J., Hodshire, A.L., Kazil, J., Ray, E., Bui, T.P., **Dollner, M.**, Froyd, K.D., McKain, K., Rollins, A., Schill, G.P., Thames, A., Weinzierl, B.B., Pierce, J.R., Brock, C.A.
(2020), Atmospheric Chemistry and Physics 20, 15037–15060.
DOI: https://doi.org/10.5194/acp-20-15037-2020

18) **The distribution of sea-salt aerosol in the global troposphere**

Murphy, D.M., Froyd, K.D., Bian, H., Brock, C.A., Dibb, J.E., DiGangi, J.P., Diskin, G., **Dollner, M.**, Kupc, A., Scheuer, E.M., Schill, G.P., Weinzierl, B., Williamson, C.J., Yu, P.
(2019), Atmospheric Chemistry and Physics 19, 4093–4104.
DOI: https://doi.org/10.5194/acp-19-4093-2019

19) **Atmospheric Acetaldehyde: Importance of Air-Sea Exchange and a Missing Source in the Remote Troposphere**

Wang, S., Hornbrook, R.S., Hills, A., Emmons, L.K., Tilmes, S., Lamarque, J., Jimenez, J.L., Campuzano-Jost, P., Nault, B.A., Crounse, J.D., Wennberg, P.O., Kim, M., Allen, H., Ryerson, T.B., Thompson, C.R., Peischl, J., Moore, F., Nance, D., Hall, B., Elkins, J., Tanner, D., Huey, L.G., Hall, S.R., Ullmann, K., Orlando, J.J., Tyndall, G.S., Flocke, F.M., Ray, E., Hanisco, T.F., Wolfe, G.M., St. Clair, J., Commane, R., Daube, B., Barletta, B., Blake, D.R., Weinzierl, B., **Dollner, M.**, Conley, A., Vitt, F., Wofsy, S.C., Riemer, D.D., Apel, E.C.
(2019), Geophys. Res. Lett. 46, 5601–5613.
DOI: https://doi.org/10.1029/2019GL082034

20) **Emission factors and evolution of SO_2 measured from biomass burning in wild and agricultural fires**

Rickly, P., Guo, H., Campuzano-Jost, P., Jimenez, J.L., Wolfe, G.M., Bennett, R., Bourgeois, I., Crounse, J.D., Dibb, J.E., DiGangi, J.P., Diskin, G.S., **Dollner, M.**, Gargulinski, E.M., Hall, S.R., Halliday, H.S., Hanisco, T.F., Hannun, R.A., Liao, J., Moore, R., Nault, B.A., Nowak, J.B., Robinson, C.E., Ryerson, T., Sanchez, K.J., Schöberl, M., Soja, A.J., St. Clair, J.M., Thornhill, K.L., Ullmann, K., Wennberg, P.O., Weinzierl, B., Wiggins, E.B., Winstead, E.L., Rollins, A.W.
(2022), Atmospheric Chemistry and Physics Discussions 1–29.
DOI: https://doi.org/10.5194/acp-2022-309

21) Measurement report: Balloon-borne in situ profiling of Saharan dust over Cyprus with the UCASS optical particle counter

Kezoudi, M., Tesche, M., Smith, H., Tsekeri, A., Baars, H., **Dollner, M.**, Estellés, V., Bühl, J., Weinzierl, B., Ulanowski, Z., Müller, D., Amiridis, V.
(2021), Atmospheric Chemistry and Physics 21, 6781–6797.
DOI: https://doi.org/10.5194/acp-21-6781-2021

ACKNOWLEDGMENTS

This work was supported by the European Research Council under the European Community's Horizon 2020 research and innovation framework program/ERC (grant no. 640458 A-LIFE and 875036 ACACIA), the National Aeronautics and Space Administration's Earth Venture program (grant no. NNX15AJ23G ATom) and the University of Vienna. I acknowledge the use of imagery from the NASA Worldview application (https://worldview.earthdata.nasa.gov/), part of the NASA Earth Observing System Data and Information System (EOSDIS).

At this point, I would like to thank all those who supported me throughout the time as a PhD student and contributed to the success of this dissertation.

First, I would like to thank Bernadett Weinzierl for supervising my dissertation, for introducing me into the world of atmospheric science and the scientific community, for her knowledgeable and wise guidance, for the continuous and outstanding support, and for the friendship we developed. I would also like to thank Wladyslaw Szymanski for mentoring my PhD dissertation with his wise advice and supportive assistance. I would like to thank the Faculty of Physics, the Vienna Doctoral School in Physics, the entire Aerosol Group of the University of Vienna, and in particular, my colleagues, former colleagues and friends Nicholas Beres, Nikolaus Fölker, Josef Gasteiger, Andreas Gattringer, Judith Hahofer, Katharina Heimerl, Manuel Schöberl, Harald Schuh, Antonio Spanu, Agnieszka Straus, Marilena Teri, and Adrian Walser, who made the PhD work not only productive but also fun. A special thank goes to Josef Gasteiger, Manuel Schöberl, and, in particular, Nicholas Beres for proofreading my dissertation.

I would like to thank all the friends, colleagues, and participants from the ATom, A-LIFE, and FIREX-AQ field campaigns. In particular, I would like to thank David Fahey, Joshua Schwarz, and Charles Brock for supportive advice over the past years.

A special thank goes to Darrel Baumgardner and Jyrki Mäkelä for reviewing my dissertation, for their thoughtful comments, and for constructive feedback.

In particular, I would like to thank my Family. My mother Angelika Dollner and my brother Marius Dollner for the enormous support. You are the best mother and brother I can imagine. I would like to thank my father Manfred Dollner, who may be reading this in some other dimension of our universe. You taught me the fundamentals and the way of thinking, which set the foundation of my mindset for this entire dissertation. Finally, I would like to thank my partner and children, Vanessa Rieger, and Viktoria and Julian Dollner. I would like to thank Vanessa for coming with me to Vienna, for the continuous and enormous support, for the patience, particularly in the period close to the completion of this dissertation, and most of all, for the love and for being the best partner I can imagine. I would like to thank my beloved children Viktoria and Julian for being unbelievably patient during the past weeks but most important for their love which makes all the stress disappear within one second.

CONTENTS

Chapter 1

I. Introduction

1. Motivation and Background

Climate change has become one of the most significant challenges for humanity, starting to affect every region across the globe with, for example, increased weather and climate extremes. Within the past four decades, every decade was the warmest since 1850, leading to a 1.09°C (0.95 - 1.20°C) warmer surface temperature in the period 2011-2020 compared to the preindustrial reference time 1850-1900 (IPCC, 2021). Over the last decades, significant progress in understanding and modeling the Earth's energy budget has been made. Climate models are used to simulate the future Earth's energy budget and climate. However, predictions are still associated with significant uncertainties (IPCC, 2021). In particular, processes and parameterizations of aerosols and clouds pose the largest contributions to these uncertainties (Boucher, 2013; Sherwood et al., 2014). A complex system of processes and interactions of aerosols and clouds affects the Earth's atmosphere in a variety of ways. Incomplete understanding and the impossibility of reflecting these processes and interactions in global-scale climate models are reasons for these significant uncertainties.

Aerosol basics

An aerosol is the suspension of particles of liquid or solid matter in air from natural and anthropogenic sources. The size of aerosol particles covers the range between a few nanometers (nm) up to several micrometers (µm). Typical concentrations of particles below 1 µm are between ten to several thousands per cm^3, whereas particles larger than 1 µm appear only about 1 per cm^3 (Seinfeld and Pandis, 2006). Figure I 1-1 shows an exemplary particle number size distribution of atmospheric aerosol with the black line. The particle size distribution can be represented as a combination of four log-normal distributions, which are indicated with the different colors in Figure I 1-1: blue for the nucleation mode (D < 0.02 µm), green for the accumulation mode (D = 0.02 – 0.1 µm), orange for Aitken mode (D = 0.1 – 1 µm) and brown for the coarse-mode (D > 1µm) (Schumann, 2012). The sources of particles for each mode are connected to specific processes. For example, homogeneous particle formation via gas-to-particle conversion defines the source of particles in the nucleation mode.

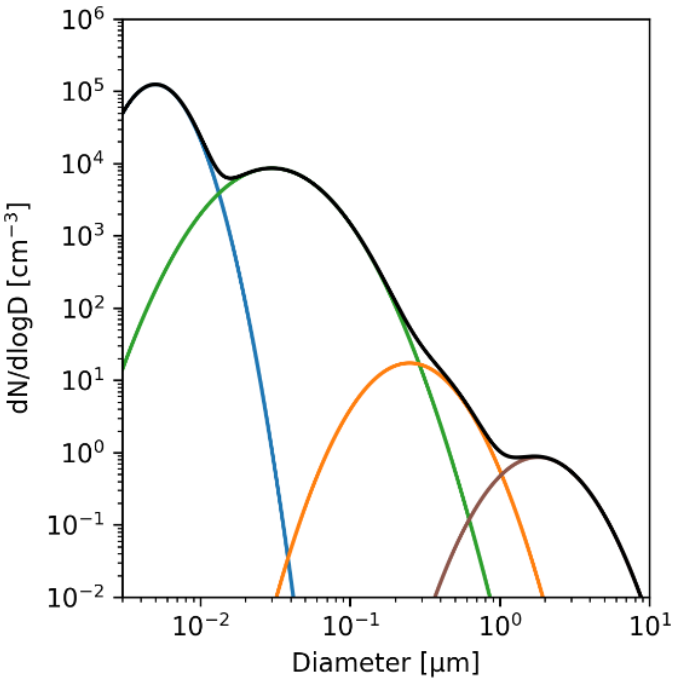

Figure I 1-1. Exemplary lognormal number size distribution in black. Colored curves represent the different modes: nucleation mode (blue), accumulation mode (green), Aitken mode (orange) and coarse-mode (brown).

Particles in the Aitken and accumulation modes are either emitted directly in the atmosphere or consist of initially smaller particles grown by coagulation or condensed vapor. Coarse-mode particles are generated and emitted mechanically, e.g. by wind and erosion (Seinfeld and Pandis, 2006). Atmospheric coarse-mode aerosol particles, which primarily consist of mineral dust and sea salt (Brock et al., 2021), have a particularly pronounced impact on the radiation budget of the Earth's climate (Balkanski et al., 2007; Kok et al., 2017; Ma et al., 2008; Sokolik et al., 2001; Tegen, 2003). This effect is commonly known as the *aerosol-radiation interaction*.

Aerosol-cloud interactions

Furthermore, aerosol particles can act as cloud condensation nuclei (CCN) and ice nucleating particles (INPs) (Froyd et al., 2022, 2013; Hoose and Möhler, 2012; Seinfeld and Pandis, 2006). Aerosol particles acting as CCNs activate and grow to liquid cloud droplets if the water vapor of the environment is sufficiently supersaturated (Seinfeld and Pandis, 2006). An aerosol particle's CCN ability depends on its size and chemical composition as described by the Köhler theory (Köhler, 1936). The κ-Köhler theory is a commonly used parametrization of this CCN ability and represents the relative humidity-dependent growth of aerosol particles for different materials and particle sizes with the parameter κ (Petters and Kreidenweis, 2007). For a completely insoluble aerosol particle, κ equals zero. κ increases with an increasing solubility of the aerosol particle with ranges between 0.003 - 0.023 for mineral dust (Tang et al., 2016), 0.1 - 0.2 for organic aerosols, 0.6 for ammonium sulfate, 1.0-1.16 for sea salt (Zieger et al., 2017), and 1.2 for sodium chloride (Lohmann et al., 2016). However, the chemical composition has a less pronounced effect on the CCN activity compared to the size of the aerosol particles (Dusek et al., 2006). For ice crystals, INPs are the fundamental component of heterogeneous ice nucleation, which is the mechanism of primary ice formation at temperatures > -38°C. Heterogeneous ice nucleation has several different modes, with definitions being a matter of change within the past (Kanji et al., 2017). A commonly used definition was formulated by Vali et al. (2015) and has a separation of the nucleation in deposition and freezing: deposition nucleation is the growth via direct deposition of supersaturated vapor on an INP, whereas freezing nucleation includes a liquid state. Freezing nucleation can be separated into immersion freezing, contact freezing, and condensation freezing. For immersion and contact freezing, the ice nucleation is initiated by the INP, whereas for immersion freezing, the INP is immersed within the liquid droplet. Condensation freezing is defined as the concurrent initiation of the liquid droplet formation process and the freezing process, where the droplet formation happens at conditions below the melting point of ice. Properties, formation, and abundance of clouds are tightly connected to the concentration of atmospheric CCN and INP. Hence, a change in the atmospheric concentration of these CCNs and INPs is directly connected to an immediate modification of cloud albedo (Twomey effect - Twomey, 1974), cloud lifetime, and cloud thermodynamics. The Twomey effect and its subsequent modifications of cloud lifetime and cloud thermodynamics make up what's called *aerosol-cloud interaction*.

Clouds in the climate system

Clouds cover about 70% of the globe, especially the tropics with deep convective clouds and the mid-latitudes with oceanic storm tracks (Stubenrauch et al., 2013). In contrast, continental desert regions and the central subtropical oceans are largely cloud-free (Boucher, 2013). Clouds directly affect the Earth's energy budget in two ways. First, they reflect the sun's shortwave radiation, cooling the Earth's atmosphere by about -50 Wm^{-2} (Boucher, 2013). However, clouds, i.e., ice clouds, also contribute to the greenhouse effect, where the capture of the terrestrial longwave radiative increases the energy budget by about 30 Wm^{-2} (Loeb et al., 2009). The combined net global mean radiative effect of clouds is approximately -20 Wm^{-2}, which indicates a cooling effect on the climate. These cooling and warming effects of clouds are prone to climate change-driven modifications of the atmosphere's temperature, dynamics, and aerosol loads,

impacting the formation, lifetime, and radiative properties of clouds. However, future climate predictions are associated with large uncertainties of these modifications, with significant contributions from aerosol-cloud interactions and cloud feedbacks (Meehl et al., 2020).

A reason for the large uncertainties is the wide range of scales covering the relevant processes controlling cloud formation, lifetime, and radiative properties: from sub-micrometer-sized CCN and INP to large cloud systems several thousand kilometers in size. A horizontal resolution of 100 to 200 km and a minimum vertical resolution of 100 m near the ground used in current climate models are far too coarse to reproduce the relevant atmospheric variability of nucleation, condensation, evaporation, precipitation, and cloud-radiation(Barker et al., 2003; Boucher, 2013; Pincus and Klein, 2000; Wu et al., 2017). Parameterizations are used to reflect these sub-grid processes in climate models (Barker et al., 2016; Elsaesser et al., 2017). However, newer prognostic aerosol schemes are suspected to be the reason for increased uncertainties of cloud feedbacks and cloud-aerosol interactions compared to previous predictions (Meehl et al., 2020; Wang et al., 2021). These large uncertainties demonstrate the importance of investigations that fill the knowledge gap connected to the processes behind cloud feedbacks and cloud-aerosol interactions. Continued improvements in the model representation and enhanced, high-quality remote sensing and in situ observations of aerosols, clouds, and their interaction are required to reduce these large uncertainties (Cesana and Del Genio, 2021; Chang et al., 2021; Meehl et al., 2020; Seinfeld et al., 2016).

The way forward with airborne in situ observations

Within the past decades, airborne in situ investigations of aerosols and clouds were carried out, and recent observations with state-of-the-art instrumentation were conducted at various locations around the globe (e.g., Antarctic: Lachlan-Cope et al. (2016), Grosvenor et al. (2012); mid-latitudes: Luebke et al. (2016); tropics & mid-latitudes & Arctic: Patnaude and Diao (2020), Krämer et al. (2020)). Furthermore, interhemispheric aircraft observations were conducted to increase knowledge of clouds and their properties (e.g., Ström et al. (2003)) and to validate model simulations (e.g., Wu et al. (2017)). Global-scale airborne in situ observations of dust aerosol in the upper troposphere were combined with detailed cirrus-formation simulations. The study determined that dust aerosol dominates the cirrus formation process in the northern hemispherical extra-tropics in all seasons (Froyd et al., 2022). This finding supports the results from another set of airborne in situ observations, which analyzed residual particles from melted cirrus ice crystals and revealed mineral dust and metallic particles as the dominant INP of the measured ice crystals (Cziczo et al., 2013). The significance of mineral dust as INP was also investigated by numerous laboratory studies (Hoose and Möhler, 2012; Kanji et al., 2017) and model-tuning studies (Villanueva et al., 2021). Even though these numerous airborne-, laboratory-, and model-based studies contributed significantly to increasing the knowledge about atmospheric processes, there are still significant gaps remaining in understanding aerosol-cloud interactions. One challenge to improving the understanding of aerosol-cloud interactions and cloud feedbacks is the limited capabilities of state-of-the-art instrumentation and data processing procedures. Continuous advancements are pushing these limits by providing techniques for more reliable and precise measurement.

This dissertation assesses the global distribution of coarse-mode aerosol and clouds based on airborne in situ measurements from three international aircraft field campaigns: The Atmospheric Tomography Mission (ATom, 2016 - 2018), the Absorbing aerosol layers in a changing climate: aging, lifetime, and dynamics (A-LIFE, 2017), and the Fire Influence on Regional to Global Environments Experiment and Air Quality (FIREX-AQ, 2019). All three field missions deployed the University of Vienna second-generation Cloud, Aerosol, and Precipitation Spectrometer (UNIVIE-CAPS), which is the central instrument of this dissertation. The general scientific questions of this dissertation are the following:

- How well can we measure the aerosol and cloud particle properties with UNIVIE-CAPS?
- What is the global distribution of coarse-mode aerosol and clouds?
- How do the aerosol type and concentration influence the appearance and microphysical properties of clouds?

To address these research questions novel calibration and data processing techniques are developed for the UNIVIE-CAPS instrument allowing more reliable and precise measurements and quantifications of atmospheric coarse-mode aerosol and cloud particles. Furthermore, a novel cloud detection and classification algorithm is introduced, greatly expanding the capability to analyze the scientific drivers of cloud processes like aerosol-cloud interactions. The global-scale measurements from the ATom and A-LIFE field campaigns are used to provide evidence of coarse-mode aerosol's significance and atmospheric abundance. Furthermore, mineral dust particles are investigated with respect to their impact on clouds embedded in a mineral dust layer. This cumulative dissertation is organized as follows: Chapter I.2 introduces the UNIVIE-CAPS instrument, presents the newly developed procedures, retrievals, and algorithms, and describes the field campaigns relevant for this dissertation. Chapter II presents the publications included in this dissertation: Paper I investigates the flow-induced errors in airborne in situ measurements of aerosols and clouds, Paper II presents the novel *Cloud Indicator* algorithm, Paper III observes the ambient aerosol properties in the remote atmosphere with global-scale in situ measurements, and Paper IV investigates clouds embedded in a dense mineral dust layer in the Mediterranean. Chapter III summarizes the overarching results of this dissertation.

2. Methods

The following section describes the methods used throughout this dissertation. First, the second-generation Cloud, Aerosol, and Precipitation Spectrometer (CAPS, Droplet Measurement Technologies Inc., Longmont, USA), its measurement principle, and the novel calibration procedure are introduced. Furthermore, a novel retrieval for size distributions from optical spectrometers, like the CAPS, is presented. The second part of this chapter describes the three campaigns that provide this dissertation's data. The third section introduces the *Cloud Indicator* algorithm, which was also developed in the framework of this dissertation.

2.1. Second-generation Cloud, Aerosol, and Precipitation Spectrometer

The second-generation Cloud, Aerosol, and Precipitation Spectrometer (CAPS, Droplet Measurement Technologies Inc., Longmont, CO, USA) is a wing-mounted instrument for aerosol and cloud particle measurements in the nominal size range between 0.5 and 930 µm. Figure I 2-1 shows an image of the CAPS from the University of Vienna (UNIVIE-CAPS) mounted at the wing of the NASA DC-8 aircraft. In the following chapter, the general measurement principle and primary data products are described (2.1.1), followed by the introduction of a novel calibration procedure (2.1.2), size

Figure I 2-1. The second-generation Cloud, Aerosol, and Precipitation Spectrometer (CAPS) instrument of University of Vienna mounted under the wing of the NASA DC-8 aircraft.

distribution retrieval (2.1.3), and machine learning method for the hotwire calibration for liquid water content (LWC) measurement (2.1.4).

2.1.1. Measurement principle

The second-generation Cloud, Aerosol, and Precipitation Spectrometer (CAPS) is a wing-mounted airborne in situ instrument for aerosol and cloud particle measurements. It combines two main components: The Cloud and Aerosol Spectrometer (CAS) and the Cloud Image Probe (CIP) (Baumgardner et al., 2001). Additional sensors provide information about the true air speed (TAS), relative humidity, temperature, and liquid water content (LWC).

CAS is an optical spectrometer that reports particle size distributions in the nominal range between 0.5 and 50 µm. The CIP component is an Optical Array Probe (OAP), which records grey-scale shadow images of aerosol and cloud particles in the nominal size range between 15 and 930 µm. Combining the measurements of CAS and CIP, CAPS reports size distributions of particles in the nominal size range between 0.5 and 930 µm. A more detailed description of the measurement principle and the primary data products can be found in Section II.2.2.1.1 (page 14) and II.2.2.1.3 (page 18) (Dollner et al., 2022a, in prep.).

2.1.2. Novel calibration procedure

Within this dissertation, a novel calibration procedure comprising a novel analysis algorithm and a newly developed calibration setup was developed. Paper II (Dollner et al., 2022a, in prep.) includes a detailed presentation of the analysis algorithm and the calibration setup (see section II.2.2.1.2; page 15). The following serves as a brief description of the new procedure.

The basic principle of an optical spectrometer is the measurement of light scattered by single aerosol or cloud particles when intersecting the beam of a light source, e.g. a laser (Kulkarni et al., 2011). Optical spectrometers are equipped with photodetectors measuring the intensity of the scattered light and a signal processing unit, which converts the signal from the photodetector to a scattering signal amplitude. The calibration of an optical spectrometer retrieves the instrument-specific relationship between the measured scattering signal amplitude and the corresponding theoretically calculated scattering cross-section (Szymanski et al., 2009; Walser et al., 2017). The novel calibration procedure for the CAS provides an algorithm reporting this relationship, independent from the refractive index of the calibration material, and includes uncertainties of the calibration coefficients. The mobilization of particles in the CAS size range (0.5 – 50 µm) is challenging, particularly outside the laboratory during field campaigns. Within this dissertation, a new calibration setup was developed, which utilizes a closed-loop design with high flow rates to enable the CAS calibration with particles covering the entire size range between 0.5 and 50 µm.

The newly developed calibration setup and calibration analysis algorithm ensure precise calibrations of the CAS instrument, including information about the uncertainty of the retrieved calibration coefficients. This output is a crucial input for the newly developed size distribution retrieval, introduced in the following chapter.

2.1.3. Novel size distribution retrieval

Within the scope of this dissertation, a novel size distribution retrieval for the CAS was developed and is described in detail in Paper IV (Dollner et al., 2022b, in prep.) (see section II.4.2.2.3, page 39). However, for consistency, the following will introduce the retrieval and provide a brief description.

A common way to present particle size distributions is the equivalent diameter method. With this method, scattering amplitude signals are converted to particle sizes using the scattering cross-section function of an equivalent material (e.g., spherical ammonium sulfate), neglecting effects of the aerosol composition, particle non-sphericity, and in most cases, instrumental uncertainties. The newly developed CAS size distribution retrieval utilizes Monte Carlo simulations and

information about the aerosol composition to calculate ensembles of possible particle size distributions considering non-sphericity and refractive index variations of the measured aerosol composition. Furthermore, uncertainties in the calibration coefficients and other input parameters (e.g., true airspeed) are considered. Following the approach of Brock et al. (2016), the size distribution ensembles are also converted from ambient relative humidity conditions to dry relative humidity conditions using hygroscopic growth values representative of the measured aerosol composition. The final output of the novel retrieval is a set of particle size distribution ensembles that reflect instrumental uncertainties, refractive index variations, and non-sphericity. The reported size distributions represent the aerosol and cloud particles with geometric diameters at ambient and, for aerosol particles, dry relative humidity conditions.

This novel size distribution retrieval enables a more reliable and precise characterization of atmospheric aerosol and cloud particles.

2.1.4. Novel machine learning method for hotwire calibration

The CAPS is equipped with a hotwire LWC sensor (Baumgardner et al., 2001; King et al., 1978). The sensor consists of a cylindrical wire kept at a constant temperature above the water boiling temperature. LWC is measured via the additional energy consumption required to keep the wire at a constant temperature when a droplet evaporates at the wire. Energy is constantly lost due to convection and radiation. The radiation term is comparably small and neglected for the calculations. However, the air density- and airspeed-dependent convective loss needs to be considered and subtracted from the measured total power consumption of the hotwire. In general, the scientific community applies two ways of estimating convection. The first way is by averaging the measured power consumption before and after a targeted cloud, assuming that the conditions before and after a cloud passage are comparable to those inside the cloud. Another approach uses the optimum parameterization method (OPM) presented in McFarquhar et al. (2017), which iteratively varies the input parameters for calculating the convective loss until the calculated and measured power outside of clouds agree.

The newly developed machine learning (ML) method is comparable to the OPM approach since measurements outside clouds are also used to constrain the convective loss. However, instead of iteratively trying to find parameters for the convective loss calculations, a neural network is supplied with measurements of temperature, pressure, and airspeed to train a model that can predict the convective loss. This trained model is then used to predict convective loss during measurements inside clouds. Paper IV (Dollner et al., 2022b, in prep.) provides a more detailed description of the novel ML method and presents the application to measurements done during the A-LIFE campaign (see II.4.2.2.4, page 43)

2.2. Field experiments and resulting data sets

Participation in three major international aircraft field campaigns provided the data sets for this dissertation's algorithm development and analysis. Figure I 2-2 depicts the flight tracks of the campaigns: four ATom deployments (ATom-1, ATom-2, ATom-3, and ATom-4), A-LIFE, and FIREX-AX. The following introduces the campaigns with contents primarily taken from Paper II (see II.2.2.2, page 19 f.) (Dollner et al., 2022a, in prep.).

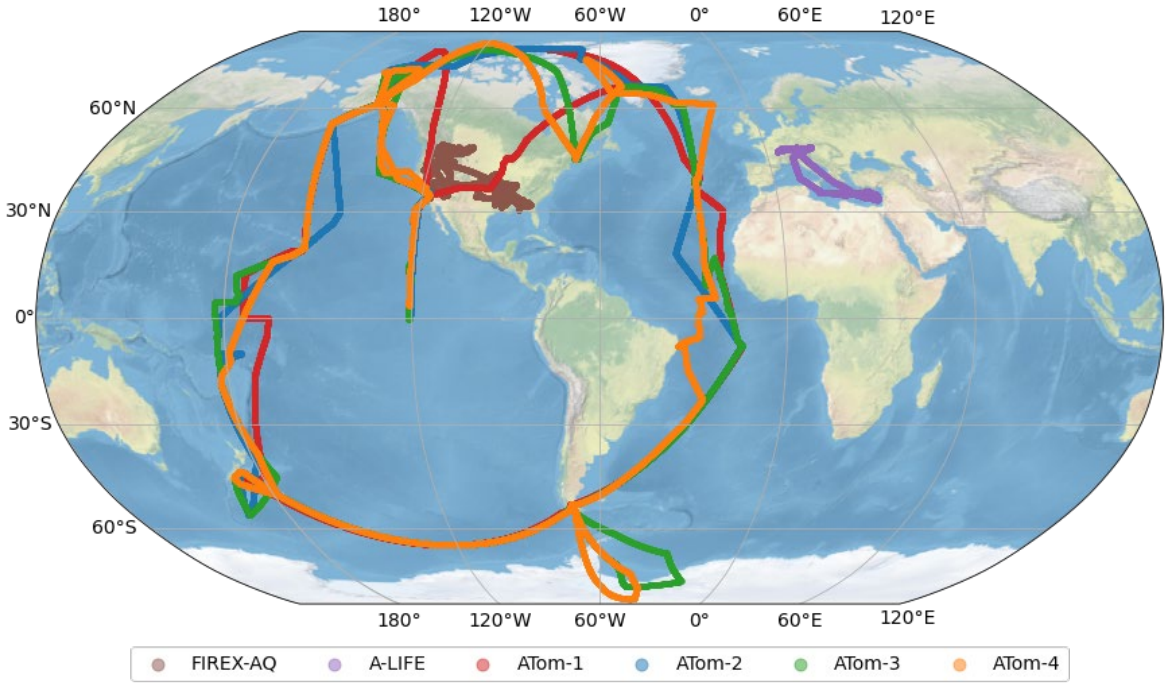

Figure I 2-2. Map with flight tracks of the FIREX-AQ (brown), A-LIFE (purple), and the four ATom (red, blue, green, orange) deployments. The figure is taken from Paper II (Dollner et al., 2022a, in prep.)

2.2.1. ATom

The NASA-funded Atmospheric Tomography Mission (ATom) aimed to investigate the distribution of aerosols and trace gases in the remote global atmosphere between 2016 and 2018 (Thompson et al., 2022; Wofsy et al., 2021). The NASA DC-8 aircraft was equipped with an extensive gas and aerosol payload, providing approximately 700 different meteorological, trace gas, aerosol, and cloud parameters. The profiling flights took place in latitudes between nearly 90°N and 90°S up to 13 km altitude above the Pacific and Atlantic Oceans and were conducted in each of the four seasons. About 301000 km and 645 vertical profiles were flown, providing 53h of measurements inside clouds.

From the extensive ATom instrumentation, data from the UNIVIE-CAPS instrument, a Diode Laser Hygrometer (DLH), and the Meteorological Measurement System (MMS) are relevant for the *Cloud Indicator*, a new algorithm that was developed to determine airborne measurement sequences inside clouds and classify the general cloud type and is the core achievement of Paper II. DLH measures water vapor by detecting individual rotation-vibration lines of H_2O using wavelength modulated differential absorption spectroscopy (Diskin et al., 2002). Measurements of GPS position, true airspeed, pressure, temperature, and three-dimensional wind were performed with the Meteorological Measurement System (MMS, Scott et al., 1990; Chan et al., 1998). MMS uses high-precision sensors for air motion sensing and a separate internal navigation system for accurate wind calculations. Temperature measurements from MMS are also used for the *Cloud Indicator* algorithm. Additionally, the true airspeed data is used to calculate the CAS and CIP number size distributions.

For the analysis in Paper III (Brock et al., 2021), measurements from additional instrumentations were used. The combined size distributions consist of individual size distributions from the CAS part of the UNIVIE-CAPS and the aerosol microphysical property (AMP) system, which is a combination of several instruments: the nucleation-mode aerosol size spectrometer (NMASS), an ultrahigh-sensitivity aerosol spectrometer (UHSAS, Droplet Measurement Technologies, Longmont, CO, USA) and a laser aerosol spectrometer (LAS, TSI Inc., St. Paul, MN, USA). The

aerosol composition was retrieved with a combination of several instruments: an instrument for particle analysis by laser mass spectrometry (PALMS), a high-resolution time-of-flight aerosol mass spectrometer (HR-ToF-AMS), a single-particle soot photometer (SP2), and brown carbon from offline analysis of aerosols from collected filters. The Instruments are described in more detail and with references in Brock et al. (2021) (see Appendix A).

2.2.2. A-LIFE

The European Research Council (ERC)-funded "Absorbing aerosol layers in a changing climate: aging, lifetime and dynamics (A-LIFE)" project aimed to study the properties of mixtures of absorbing aerosols in the Eastern Mediterranean (Weinzierl and Coauthors, in prep.). During the 74h of airborne sampling, multiple dust outbreaks from the Saharan and Arabian deserts, pollution layers, mixtures of polluted dust layers, and clouds were measured by in situ and remote sensing techniques. A-LIFE deployed the German Aerospace Center (DLR) Falcon 20 E-5 aircraft to the Eastern Mediterranean Sea with the UNIVIE-CAPS as part of an extensive aerosol and cloud payload between 3 and 30 April 2017. Additional measurements of GPS position and meteorological parameters (i.e., temperature, true airspeed, and pressure) were collected with the meteorological measurement system of the DLR Flacon (CMET). The in situ instrumentation was extended with a Doppler Wind Lidar (DWL) installed in the Falcon.

2.2.3. FIREX-AQ

The Fire Influence on Regional to Global Environments Experiment and Air Quality (FIREX-AQ) mission was an extensive, joint NASA and NOAA venture investigating the impact of agricultural fires and wildfires in the US on air quality, weather, and climate using airborne in situ and remote sensing as well as ground-based observations (Warneke and Coauthors, in prep.). Smoke plumes of agricultural fires and wildfires were sampled and characterized in situ and close to the point of emission with the NASA DC-8 equipped with an extensive payload for measurements of aerosols, trace gases, and clouds. In total, 151h of airborne measurements were conducted, including emissions from approx. 90 agricultural fires, 11 wildfires, and a pyrocumulonimbus event (Peterson et al., 2022). During FIREX-AQ, the DC-8 also carried the UNIVIE-CAPS instrument and the same DLH and MMS instruments used during Atom (see Section 2.2.1). The CAPS, DLH, and MMS measurements during FIREX-AQ provided a large data set of in-cloud and cloud-free measurements, which contributed to the development of the *Cloud Indicator* algorithm.

2.3. The *Cloud Indicator* algorithm

The *Cloud Indicator* algorithm is one significant achievement of this dissertation and the core topic of Paper II (see chapter II.2, page 11 ff.). The following brief description originates from Paper IV Chapter II.4.2.2.2 (Dollner et al., 2022b, in prep.). However, the paragraph is repeated in this chapter to provide a coherent description of the methods used in this dissertation.

The *Cloud Indicator* is an algorithm that automatically detects and classifies measurement periods inside clouds (Dollner et al., 2022a, in prep.). The algorithm distinguishes periods in cloud-free, Aerosol-Cloud Transition Regime (ACTR), liquid clouds, clouds in the Mixed-Phase Temperature Regime (MPTR), and cirrus clouds. Furthermore, it utilizes size distribution, relative humidity, and temperature measurements to automatically detect and classify the cloud type of flight periods in clouds. An additional cloud-aerosol volume factor (f_{ca}) is used to ensure a robust distinction of aerosol layers with enhanced coarse-mode concentration (e.g., a mineral dust layer) from clouds and, hence, reduce misclassification of the two. In general, the size distribution data is not restricted to any specific instrument; however, the size distribution input to the *Cloud Indicator* algorithm should cover the range between approx. 0.5 µm and at least 50 µm. For this study, size distribution measurements were taken from the UNIVIE-CAPS.

Chapter 2

II. Results

The results of this dissertation consist of four publications. The abstract, author contribution, and relevance for the dissertation of the four publications are presented in this chapter. Manuscripts in preparation are presented directly in this chapter. For the published papers, the abstracts are a copy of the published version. The full reprints of the published papers are presented in Appendix A.

1. Paper I: Spanu et al. (2020) - Flow-induced errors in airborne in situ measurements of aerosols and clouds

Spanu, A., **Dollner, M.**, Gasteiger, J., Bui, T.P., Weinzierl, B.

Published 2020 in *Atmospheric Measurement Techniques* 13, 1963–1987, 3

DOI: https://doi.org/10.5194/amt-13-1963-2020

Abstract

Aerosols and clouds affect atmospheric radiative processes and climate in many complex ways and still pose the largest uncertainty in current estimates of the Earth's changing energy budget.

Airborne in situ sensors such as the Cloud, Aerosol, and Precipitation Spectrometer (CAPS) or other optical spectrometers and optical array probes provide detailed information about the horizontal and vertical distribution of aerosol and cloud properties. However, flow distortions occurring at the location where these instruments are mounted on the outside of an aircraft may directly produce artifacts in detected particle number concentration and also cause droplet deformation and/or breakup during the measurement process.

Several studies have investigated flow-induced errors assuming that air is incompressible. However, for fast-flying aircraft, the impact of air compressibility is no longer negligible. In this study, we combine airborne data with numerical simulations to investigate the flow around wing-mounted instruments and the induced errors for different realistic flight conditions. A correction scheme for deriving particle number concentrations from in situ aerosol and cloud probes is proposed, and a new formula is provided for deriving the droplet volume from images taken by optical array probes. Shape distortions of liquid droplets can either be caused by errors in the speed with which the images are recorded or by aerodynamic forces acting at the droplet surface caused by changes of the airflow when it approaches the instrument. These forces can lead to the dynamic breakup of droplets causing artifacts in particle number concentration and size. An estimation of the critical breakup diameter as a function of flight conditions is provided.

Experimental data show that the flow speed at the instrument location is smaller than the ambient flow speed. Our simulations confirm the observed difference and reveal a size-dependent impact on particle speed and concentration. This leads, on average, to a 25 % overestimation of the number concentration of particles with diameters larger than 10 µm diameter and causes distorted images of droplets and ice crystals if the flow values recorded at the instrument are used. With the proposed corrections, errors of particle number concentration and droplet volume, as well as image distortions, are significantly reduced by up to 1 order of magnitude.

Although the presented correction scheme is derived for the DLR Falcon research aircraft (Saharan Aerosol Longrange Transport and Aerosol-Cloud-Interaction Experiment (SALTRACE) campaign) and validated for the DLR Falcon (Absorbing aerosol layers in a changing climate: aging,

lifetime and dynamics mission conducted in 2017 (A-LIFE) campaign) and the NASA DC-8 (Atmospheric Tomography Mission (ATom) campaigns), the general conclusions hold for any fast-flying research aircraft.

Author contributions

This publication uses CAPS measurements from the ATom and A-LIFE field campaigns. I played a major role in the preparation of CAPS for the aircraft field experiments and performed the CAPS measurements during a large number of ATom- and A-LIFE flights. I performed the quality assurance, processing, and selection of all CAPS data presented in the paper. During the analysis phase, I was heavily involved in the discussion of preliminary results with the first author, Antonio Spanu. Furthermore, I contributed to the discussion of the final results during the preparation of the manuscript.

Relevance for the dissertation

The results from this paper explain the effect of flow-induced errors on measurements with the CAPS instrument. The provided correction scheme was used to tune the airspeed measurements at the mounting location of the CAPS in order to record undistorted images of droplets and ice crystals. The proposed corrections for particle number concentration are input for the size distribution retrieval, which was developed within this dissertation. The results from this publication contribute significantly to the achievements of this dissertation and lead to more reliable and precise observations of coarse-mode aerosol and cloud particles.

2. Paper II: Dollner et al. (2022a, in prep.) - The *Cloud Indicator*: A novel algorithm for automatic detection and classification of clouds using airborne in situ observations

Dollner, M., Gasteiger, J., Schöberl, M., Gattringer, A., Beres, N. D., Bui, T. P., Diskin, G. and Weinzierl, B.

In preparation 2022, planned for *Atmospheric Research*

Abstract

Airborne in situ observations of aerosols and clouds provide relevant data sets crucial to improving the understanding of cloud microphysical processes and reducing uncertainties connected to future climate predictions. However, the selection and classification of cloud sequences in such data sets can be very time-consuming if done manually, and criteria used by the community are numerous and prone to misclassification, especially when coarse aerosol particles (> 1 µm diameter) are present.

In this study, we present the *Cloud Indicator*, a novel algorithm that automatically detects and classifies measurement periods inside clouds. The *Cloud Indicator* was developed using data from three international airborne field campaigns, including ATom (Atmospheric Tomography; 2016-2018), A-LIFE (Absorbing aerosol layers in a changing climate: aging, lifetime and dynamics; 2017), and FIREX-AQ (Fire Influence on Regional to Global Environments Experiment and Air Quality; 2019). The algorithm utilizes size distribution measurements, combined with measurements of relative humidity and temperature, to automatically detect flight sequences in clouds and classify the cloud type. As an additional criterion for the *Cloud Indicator*, we established the cloud-aerosol volume factor f_{CA} to ensure a precise and robust distinction between clouds and aerosol layers such as mineral dust or biomass burning thereby reducing misclassifications. The *Cloud Indicator* algorithm was developed with data from a second-generation Cloud, Aerosol, and Precipitation Spectrometer (CAPS) which was calibrated with a novel calibration procedure – introduced in this study - that results in a refractive index independent calibration and works also in the field. However, the *Cloud Indicator* algorithm is not restricted specifically to the CAPS and thus allows its application to a variety of in situ instruments that measure coarse aerosol and cloud particle size.

Case studies from ATom and A-LIFE demonstrate the ability of the *Cloud Indicator* to precisely screen (airborne) in situ data sets for clouds. The algorithm separates the data set into cloud-free periods, Aerosol-Cloud Transition Regime (ACTR), liquid clouds, clouds in the Mixed-Phase Temperature Regime (MPTR), and cirrus clouds. The unique ability of the *Cloud Indicator* to successfully differentiate between layers of enhanced coarse-mode aerosol concentrations and clouds is demonstrated by measurements in a complex mixture of clouds embedded into a mineral dust layer during the A-LIFE. The empirically derived parameter thresholds of the *Cloud Indicator* are in good agreement with values in the literature.

Author contributions

This publication was designed and written by myself, with contributions and comments from coauthors. All figures incorporated in this paper are prepared by myself. I played a major role in the preparation of CAPS for the aircraft field experiments and performed the CAPS measurements during a large number of ATom-, A-LIFE, and FIREX research flights. I developed the novel CAS calibration procedure, consisting of a newly developed calibration setup and a novel algorithm for

calibration analysis. The new calibration process improved the existing way of calibrating the CAS. The *Cloud Indicator* algorithm was developed and improved by myself. Discussion with coauthors triggered improvements during the development phase.

Relevance for the dissertation

The novel *Cloud Indicator* algorithm and CAS calibration procedure established the foundation for the analysis in this dissertation. The novel calibration procedure provides the calibration coefficients with uncertainties relevant to calculating the newly developed size distribution retrieval. The *Cloud Indicator* was applied to the ATom and A-LIFE measurements for two use cases. First, only non-cloud periods detected with the *Cloud Indicator* were considered to analyze the significance and abundance of coarse-mode aerosol. For the cloud analysis, detections and classifications of the *Cloud Indicator* provided the foundation for the in-depth analyses of the clouds. The *Cloud Indicator* is one major achievement of this dissertation.

2.1. Introduction

Clouds, aerosols, and their interaction pose the largest uncertainty in current climate models simulating and predicting the Earth's climate (Boucher, 2013; Sherwood et al., 2014). Aerosol particles can impact Earth's climate directly by scattering and absorbing solar and terrestrial radiation. In particular, coarse-mode aerosol particles (> 1 µm diameter), which largely consist of mineral dust and sea salt (Brock et al., 2021), influence the radiation budget of the Earth's climate (Balkanski et al., 2007; Kok et al., 2017; Ma et al., 2008; Sokolik et al., 2001; Tegen, 2003). Furthermore, aerosols influence the formation of clouds by acting as cloud condensation nuclei (CCN) and ice nucleating particle (INP) (Froyd et al., 2022, 2013; Hoose and Möhler, 2012). Changes to the concentration of CCN and INP result in an immediate modification of cloud albedo (Twomey, 1974b), cloud lifetime, and cloud thermodynamics. Clouds affect the Earth's climate via reflection of solar shortwave radiation and, thus, enhance the planetary albedo and cool the Earth's climate by about -50 Wm^{-2} (Boucher, 2013). This large cooling effect is opposed by the cloud's contribution to the natural greenhouse effect, warming the atmosphere by about 30 Wm^{-2} by absorbing terrestrial longwave radiation (Loeb et al., 2009). A changing climate modifies these cooling and warming effects of clouds with variations in the atmosphere's temperature, dynamics, and aerosol loads, impacting the formation, lifetime, and radiative properties of clouds. However, the magnitude of these changes for future climate scenarios is connected to large uncertainties, with major contributions to these uncertainties from aerosol-cloud interactions and cloud feedbacks (Meehl et al., 2020).

One reason for the large uncertainties is the impossibility of current global climate models to explicitly represent all processes related to clouds (Boucher, 2013; Seinfeld et al., 2016). Processes responsible for cloud formation, lifetime, and radiative properties occur on a wide range of scales – from sub-micrometer-sized CCN and INP to cloud systems several thousand kilometers in size. Current climate models use a horizontal resolution of 100 to 200 km and a vertical resolution of 100 m near the ground, changing to 1000 m in the free atmosphere (Boucher, 2013). Such a grid box resolution is far too coarse to represent the variability of processes like nucleation, condensation, evaporation, precipitation, and cloud-radiation (Barker et al., 2003; Pincus and Klein, 2000; Wu et al., 2017) and, therefore, parameterizations are used to reflect these sub-grid processes in global climate models (Barker et al., 2016; Elsaesser et al., 2017).

The Coupled Model Intercomparison Project (CMIP) compares the performance and results of state-of-the-art global coupled climate models to better understand past, present, and future climate changes and became a fundamental input for assessment reports, the most prominent being those from the Intergovernmental Panel on Climate Change (IPCC) (Meehl et al., 2000;

Touzé-Peiffer et al., 2020). Cloud feedbacks and cloud-aerosol interactions resulting from newer prognostic aerosol schemes in the models of the latest CMIP phase (CMIP 6) are likely the reason for the largest range and absolute values of possible future climate predictions since the start of CMIP (Meehl et al., 2020; Wang et al., 2021). These large uncertainties in the CMIP6 global climate models demonstrate the need to continue investigations of the processes behind cloud feedbacks and cloud-aerosol interactions not only by improving the representation in models but also with enhanced, high-quality remote sensing and in situ observations (Cesana and Del Genio, 2021; Chang et al., 2021; Meehl et al., 2020; Seinfeld et al., 2016).

Airborne in situ investigations of aerosols and clouds have been carried out over several decades, and recent observations with state-of-the-art instrumentation were conducted at various locations around the globe (e.g., Antarctic: Lachlan-Cope et al. (2016), Grosvenor et al. (2012); mid-latitudes: Luebke et al. (2016); tropics & mid-latitudes & Arctic: Patnaude and Diao (2020), Krämer et al. (2020)). However, there is a variety of different measurement techniques and methods to detect and measure cloud particles. For the airborne in situ observation of cloud particles, mainly three measurement principles are used: impaction and replication (e.g., video microscopy of impacted ice crystals), single-particle optical methods for size and morphology (e.g., optical spectrometer and optical array probes), and methods retrieving integral properties of an ensemble of particles (e.g., thermal techniques like hot-wire or inlet-based evaporation) (Wendisch and Brenguier, 2013). Each of the three measurement principles can be used to determine measurement periods inside clouds. Amongst recent publications, the most common technique to determine periods inside clouds is based solely on single-particle optical spectrometers and/or optical array probes which observe size-resolved cloud particle number concentration and particle shape (e.g., Boutle et al., 2014; D'Alessandro et al., 2019, 2017; Diao et al., 2017, 2015, 2014; Jourdan et al., 2003; Liu et al., 2022; Patnaude and Diao, 2020; Woods et al., 2018). Thermal techniques detecting liquid, ice, or total water content (LWC, IWC, or TWC, respectively) via evaporation measurements of droplets or ice crystals (e.g., Nevzorov LWC/TWC, SEA WC-2000) are also used for the determination of in-cloud periods - either applied as a standalone method (e.g. Huang et al., 2021; Korolev et al., 2003) or in combination with single-particle optical methods (Ahn et al., 2017; Grosvenor et al., 2012; Guan et al., 2001; Wood and Field, 2011). A more advanced determination of in-cloud periods is presented in Krämer et al. (2020), where single-particle optical methods are combined with hygrometer measurements of evaporated ice crystals behind a heated inlet.

Common criteria for cloud detection with single-particle optical methods include thresholds of measured particle number concentrations above a certain diameter and LWC, IWC, or TWC above a certain value derived from integrating the measured particle size distributions. Previous studies show good agreement for IWC derived from particle size distributions and hygrometer measurements of evaporated ice crystals behind a heated inlet (Afchine et al., 2018) and for LWC retrieved from particle size distributions and thermal methods like bulk hot-wire measurements (Boutle et al., 2014; Wendisch and Brenguier, 2013). However, these commonly used criteria are prone to misclassifications of aerosol layers as clouds since large aerosol particles (e.g., super-micron mineral dust, biomass burning aerosol (Chakrabarty et al., 2014; Miller et al., 2021) or sea salt) overlap with the size range of cloud particles.

The presented study introduces a novel algorithm called *Cloud Indicator*, which automatically detects and classifies clouds using measurements from single-particle optical spectrometers and optical array probes combined with observations of relative humidity and temperature. Furthermore, the novel algorithm minimizes the likelihood of misclassifications during cloud-free periods with coarse-mode aerosol particles present. The algorithm was developed in the framework of three major aircraft field campaigns: The Atmospheric Tomography Mission (ATom, 2016 - 2018), the Absorbing aerosol layers in a changing climate: aging, lifetime, and dynamics (A-

LIFE, 2017), and the Fire Influence on Regional to Global Environments and Air Quality (FIREX-AQ, 2019). All three field missions deployed a second-generation Cloud, Aerosol, and Precipitation Spectrometer (CAPS), which served as the basis for the development of the *Cloud Indicator* algorithm. This algorithm is presented based on two case studies from ATom and A-LIFE. Cloud periods and phases are derived with the new algorithm, and images of cloud particles taken with the CAPS instrument serve as independent validation of the algorithm. Additionally, by comparing the *Cloud Indicator* parameter thresholds to published values obtained from previous cloud investigations, our novel algorithm is further validated. Since the CAPS was central to the development of the *Cloud Indicator* algorithm, a detailed description of the instrument is presented, including a novel calibration and data analysis procedure. Even though the *Cloud Indicator* algorithm was developed with the CAPS instrument, its application is not limited to CAPS instruments and can be applied to any instrument which detects the relevant size range from approx. 0.5 and to at least 50 µm.

2.2. Methodology

The *Cloud Indicator* algorithm utilizes in situ measurements of particle size distributions, relative humidity, and temperature to detect and classify clouds and is designed to minimize misclassifications of periods with enhanced coarse-mode aerosol concentrations (e.g., mineral dust layers or biomass burning smoke plumes) as clouds. For the algorithm development, the University of Vienna second-generation Cloud, Aerosol, and Precipitation Spectrometer (UNIVIE-CAPS) was used for the particle size distribution measurements between nominally 0.5 and 930 µm. The middle photograph on the right side of Figure II 2-3 shows the UNIVIE-CAPS used during all three field campaigns. The UNIVIE-CAPS measurement principle, calibration procedure, and data products are summarized in Section 2.1, the field campaigns are introduced in Section 2.2., and the *Cloud Indicator* algorithm is described in Section 2.3.

2.2.1. Second-generation CAPS instrument

The following describes how the UNIVIE-CAPS is specifically implemented for a more robust evaluation of the measurements using well-defined theory to yield a more confident set of data products.

2.2.1.1. Measurement principle

The second-generation Cloud, Aerosol, and Precipitation Spectrometer (CAPS, Droplet Measurement Technologies, Longmont, CO, USA) consists of two main instruments: the Cloud and Aerosol Spectrometer (CAS) and the Cloud Image Probe (CIP) (Baumgardner et al., 2001). The CAPS is equipped with additional sensors for true airspeed, pressure, relative humidity, temperature, and liquid water content (LWC).

The CAS is an optical spectrometer capable of detecting particles in the size range between approximately 0.5 and 50 µm. The underlying measurement principle is scattering of laser light (wavelength 658 nm) by single aerosol or cloud particles. The forward-scattered light is collected in the angular range between 4.2° to 13.2° with a photosensitive detector. An additional detector equipped with an optical mask is used to restrict the detection of CAS to particles that are in the depth of field of the instrument (Glen and Brooks, 2013). The measured signals from particles outside the instrument's depth of field are rejected. Furthermore, the CAS collects backscattered light in an angular range between 168° and 176° using two backward detectors. The first measures total backscattered light intensity, which can be used to obtain information about the particle's shape (Glen and Brooks, 2013). A second detector acts as an additional source to determine the particle size and measures the polarized fraction of the backscattered light (Baumgardner et al., 2001). The combination of both backward detectors can be used to obtain information about the

polarization ratio; however, this polarization ratio is not comparable to the depolarization ratio achieved with lidar measurements (Glen and Brooks, 2013).

The size range from the CAS is extended by measurements of the Cloud Image Probe (CIP). The CIP covers the nominal size range between 15 and 930 µm and uses the technique of an optical array probe (OAP) (Knollenberg, 1970). Shadow images of aerosol and cloud particles passing a 658 nm collimated laser beam are obtained with a linear array of 64 photodiodes. Each photodiode has a resolution of 15 µm and, in the case of the UNIVE CAPS, records greyscale intensities of the shadow with pre-set shadow level thresholds of 30, 50, and 70%. The recordings of the 64 photodiodes are called "slices" and are taken with a frequency proportional to the true airspeed (Baumgardner and Korolev, 1997; Korolev et al., 1998a; Spanu et al., 2020). During data processing, the "slices" are reconstructed into a complete image and used to obtain information about the size and shape of the detected particles.

2.2.1.2. Calibration

The general goal of an optical spectrometer calibration is to retrieve the instrument-specific relationship between the measured scattering signal amplitude (i.e., the digital value for the light intensity collected with the detector) and the corresponding theoretically calculated scattering cross-section (Szymanski et al., 2009; Walser et al., 2017). The following paragraphs mainly focus on the calibration of CAS, for which the novel calibration method was developed. This new method allows the calibration of the entire size range of the instrument, not only in the lab but also in the field, and leads to a calibration output independent from the calibration material's refractive index.

Figure II 2-1 visualizes the new calibration setup for CAS. A centrifugal fan is used to drive the circulation of the air, followed by a combination of a dryer and a HEPA filter. Calibration particles are mobilized and introduced into the airflow of the calibration setup as close to the measurement volume as possible to the CAS sampling tube to reduce sedimentation losses (see Figure II 2-1).

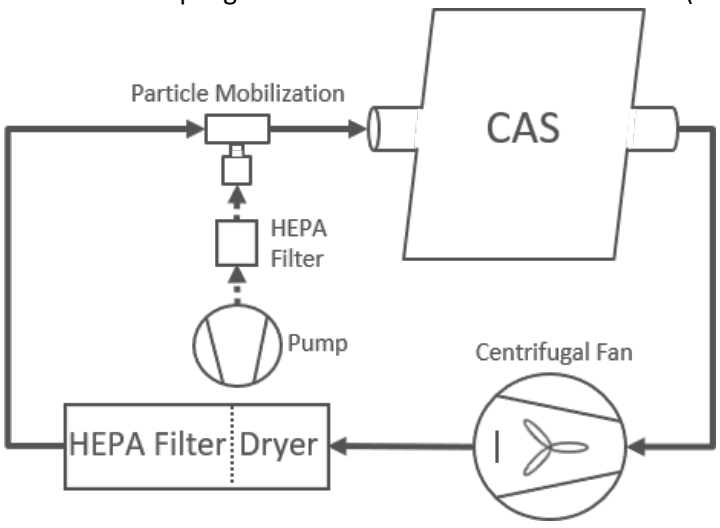

Figure II 2-1. Calibration setup for laboratory and in-field calibration of the Cloud and Aerosol Spectrometer (CAS) with standardized calibration particles, e.g., polystyrene latex (PSL) and glass spheres. A centrifugal fan provides a high flow and is used to circulate the air of the closed-loop flow system. Calibration particles are mobilized and introduced into the dried and filtered sample air in front of the CAS sample tube inlet. The centrifugal fan is connected to the outlet of the CAS sample tube, closing the loop of the flow system.

Figure II 2-2 summarizes the entire calibration process, including an experimental part and a theoretical part. Usually, particle standards with well-defined size and refractive index are used for calibrations of optical spectrometers. For the CAS size range from 0.5 to 50 µm, polystyrene latex (PSL) and glass (soda-lime or borosilicate) spheres are available with size and refractive index

certified by the United States National Institute of Standards and Technology (NIST). Size distributions of these particle standards are Gaussian distributed and with known means and standard deviations. The measurement of a single calibration standard results in a distribution of measured scattering signal amplitudes, which are the digital values of the light intensity recorded by the detector. In addition to the initial particle size distribution of the calibration standard, instrumental effects like spectral broadening (Walser et al., 2017) and contaminated sample air can lead to a widening of the signal amplitude histogram.

Panels a) and b) of Figure II 2-2 show two scattering signal amplitude histograms for 0.5 µm PSL and 42 µm glass spheres, respectively. Figure II 2-2 c) represents the result of the experimental part and shows a size-resolved combination of scattering signal amplitude histograms of all used calibration standards. The left side of Figure II 2-2 visualizes the theoretical calculations necessary for a CAS calibration. For the experimental calibration, only spherical particles are used. Therefore, Mie–Lorenz theory (Mie, 1908) can be used to calculate the scattering cross-section functions for calibration particles (Figure II 2-2 d). For Mie-Lorenz theory, the size-dependent scattering cross-section depends on intrinsic particle properties like particle size, complex refractive index, and the geometry of the optical setup of the instrument. The scattering cross-section functions are used to simulate scattering cross-section histograms for the used calibration particle standards. For this simulation, Gaussian size distributions of the particle standards are calculated with the known mean and standard deviation. Using the scattering cross-section functions of the corresponding material, this theoretical size distribution can be converted to a theoretical distribution of scattering cross-sections, as presented in Figure II 2-2 e) and f) for 0.5 µm PSL and 42 µm glass particles, respectively. The visualization of size-resolved scattering cross-section distributions for all used calibration standards represents the result of the theoretical part and is depicted in Figure II 2-2 g). Using the results of the experimental and theoretical parts of the calibration, combined distributions of scattering cross-sections and scattering signal amplitudes are generated for all particle sizes used during the calibration (Figure II 2-2 h). This combination provides the instrument-specific relationship between measured scattering signal amplitude and the theoretical scattering cross-section. For CAS, this relationship has a linear dependency. Figure II 2-2 h) visualizes the linear fit function with a black line. The fit coefficients of the linear relationship are the final result of the calibration, enabling the conversion of any measured scattering signal amplitude to a scattering cross-section. Note that this calibration procedure leads to a calibration output independent of the calibration material's refractive index. Furthermore, it allows the calculation of the size of any measured particle by applying a scattering-cross section function for either the particles' corresponding refractive index (leading to geometric diameters) or for a fixed refractive index (leading to equivalent diameters). Mobilization and sedimentation losses resulting from gravity pose a challenge for calibrating the upper size range of CAS. The novel setup shown in Figure II 2-1 improves the mobilization and reduces the sedimentation losses, enabling calibration of the CAS instrument with particles up to 50 µm diameter. However, sampling statistics for these large particles are poor. For the CAS calibration, a Monte Carlo method (Metropolis and Ulam, 1949) was used to obtain more robust results by increasing the samples of the experimental scattering signal amplitudes and the theoretical scattering cross-sections via random resampling. The measured scattering signal amplitudes and the calculated scattering cross-sections were resampled 100000 times for each calibration standard, and a least-squares optimization algorithm was used to retrieve the optimal fit parameters and the covariance for the linear relationship. With the covariance, Monte Carlo methods can be applied to propagate uncertainties of the calibration to retrievals of the particle diameters.

While the calibration of the CAS requires several newly-developed steps, the calibration of the CIP – which follows the manufacturer-recommended method – is rather a validation of the alignment of its optical components. The CIP optics and the laser alignment are adjusted to

represent the shadow of a particle on the diode array. The inspection of the setup ensures the proper alignment of the optical components. For calibration of the CIP, a transparent disk with imprinted representations of spheres of known diameters is spun through the object plane of the collimated laser beam of the CIP. If the measured sizes differ from the known diameter of the spheres on the disk, a realignment of the optics and laser is required.

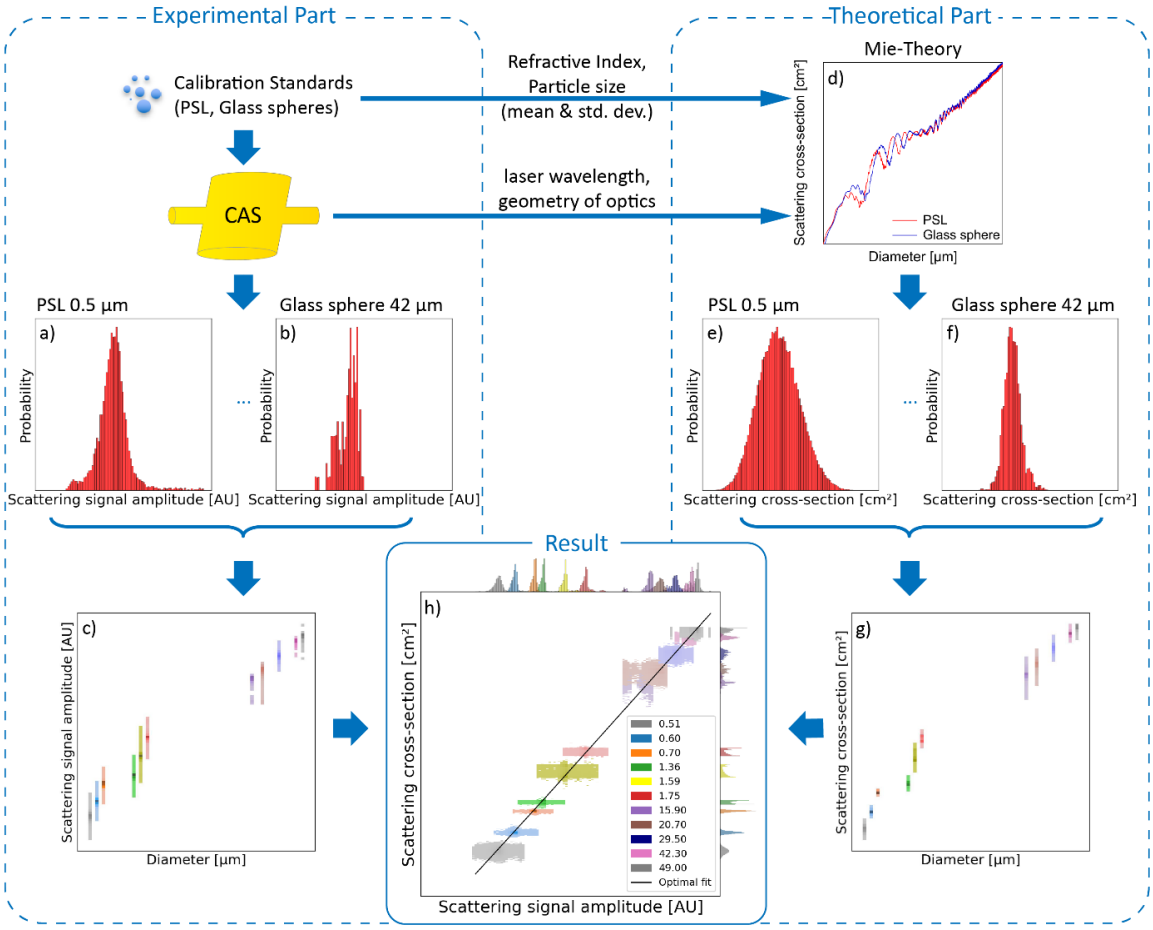

Figure II 2-2. Schematic of novel CAS calibration procedure. The calibration procedure includes experimental (left side) and theoretical work (right side). For the experimental work, a calibration setup, as shown in Figure II 2-1, is used to mobilize standardized calibration particles (e.g., PSL and glass spheres). Graphs a) and b) visualize example distributions of the measured scattering signal amplitudes for 0.5 µm PSL and 42 µm glass spheres, respectively. Graph c) shows the scattering signal amplitude distributions of all calibration sizes and represents the result of the experimental part. The theoretical work applies Mie-Lorenz theory to calculate scattering cross-section functions dependent on a specific refractive index and CAS-specific laser wavelength and optics geometry. Scattering cross-section functions for PSL and glass spheres are depicted in plot d). Using the corresponding scattering cross-section functions from plot d) and the size distribution information from the calibration standards, scattering cross-section distributions are simulated, exemplarily visualized in plot e) and f) for 0.5 µm PSL and 42 µm glass spheres, respectively. Plot g) combines the scattering cross-section distributions of particle standards used for the calibration and represents the result of the theoretical section. Plot h) presents the size-dependent combination of the scattering signal amplitudes from the experimental part and the scattering cross-section distributions from the theoretical part as a 2d histogram. At the top and right side of plot h) the histograms of the scattering signal amplitudes and scattering cross-sections are shown, respectively. The colors of plots c), g) and h) represent the different particle diameters. The final result of the calibration is the linear dependency between scattering signal amplitudes and scattering cross-sections, visualized with the optimal fit as a black line.

2.2.1.3. Data products

The CAPS instrument provides two types of data outputs. The first type is a standard time-series product available for the CAS, CIP, and LWC measurements, commonly reported with a 1s resolution. The second output type is single-particle data for measurements from the CAS and CIP.

The standard time-series for the CAS provides relevant housekeeping data (e.g., laser reference voltage and laser temperature), pre-calculated quantities like volume and number concentrations, and binned size distribution data (i.e., counts of measured particles sorted into pre-set size channels). The lower and upper limits of the size channels (for which the factory settings correspond to optical equivalent diameters of water with a refractive index of m=1.33+0.00i) are defined in a configuration file. The structure of the CIP standard time-series product is mostly similar to that of the CAS product. It also contains relevant housekeeping data (e.g., laser reference voltage, laser temperature, and dark current of the diodes), pre-calculated quantities like volume and number concentrations, and binned size distribution data. In contrast to the binned data from CAS where the size channels are defined in a configuration file, the CIP size bins are fixed and determined by the resolution and number of diodes on the diode array. The 64 diodes of the CIP of the UNIVIE-CAPS have a resolution of 15 µm, but because measurements of particles triggering the lower and upper edge diodes are rejected, a total of 62 bins are utilized, covering the size range between 15 and 930 µm.

The single-particle data for the CAS (particle-by-particle, or "PbP"), which reports a selection of unprocessed, single-particle information, extend the flexibility to calculate the size of a measured particle. Most important for this study, PbP data includes the forward scattering signal amplitude values. These values can be converted to scattering cross-sections using the result of the calibration procedure described in Section 2.2.1.2 and enable the derivation of the geometric particle size for a particular aerosol type, i.e., using the theoretical scattering cross-section functions for a specific refractive index and particle shape. Since Mie–Lorenz theory only applies to spherical particles, other methods like the T-matrix method (Waterman, 1965) or the discrete dipole approximation (Purcell and Pennypacker, 1973) must be used to calculate scattering cross-section functions for more complex particle shapes (Gasteiger and Wiegner, 2018). Resulting from data transmission rate limitations, the PbP data of the CAS from the UNIVIE-CAPS are available for 1474 particles per second. In sequences with concentrations exceeding this threshold, the PbP counts are saturated and do not represent the "true" ambient concentrations. Therefore, the PbP counts need to be upscaled based on the counts given in the binned data of the CAS standard time-series product. This scaling assumes that particles from all sizes are evenly distributed and the PbP data are representative of the size distribution in a particular time interval.

The single-particle measurements of the CIP consist of greyscale images of single aerosol and cloud particles. The greyscale images are stored in a binary format, which is decompressed during data processing. Subsequent processing of the single aerosol and cloud particle images enables one to retrieve detailed information about a particle's size, shape, and type (e.g., ice crystal, droplet, or biomass burning aerosol).

For the development of the *Cloud Indicator* algorithm, CAS size distributions calculated from the PbP forward detector data are used with a refractive index of water (m=1.33+0.0i). The CIP size distributions are calculated using the binned data from the standard time-series product.

2.2.2. Campaigns

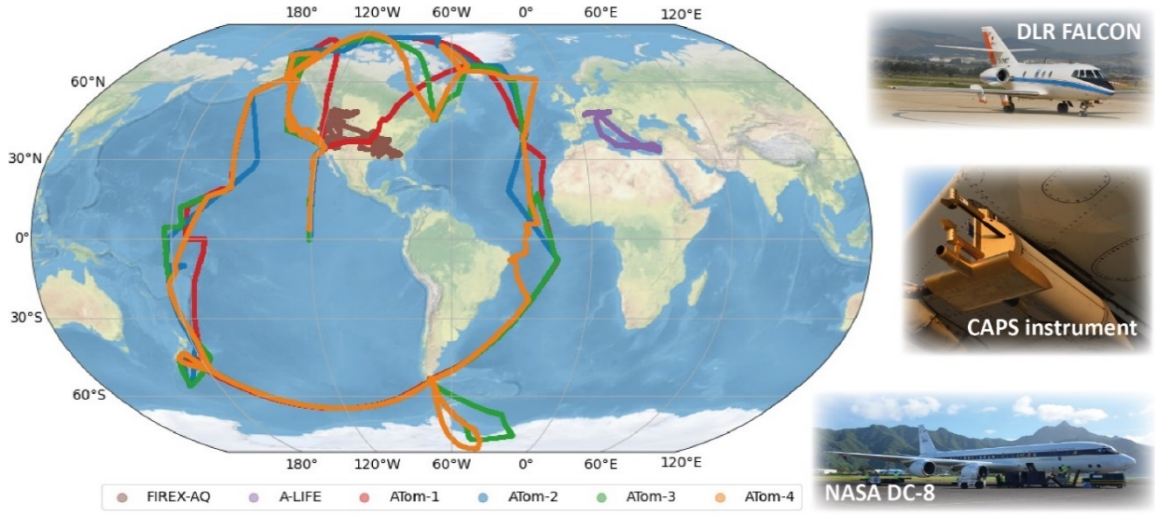

Figure II 2-3. Map with flight tracks of the FIREX-AQ (brown), A-LIFE (purple) and the four ATom (red, blue, green, orange) deployments. Images on the right depict the German Aerospace Center (DLR) research aircraft Falcon 20 E-5, the second-generation Cloud, Aerosol, and Precipitation Spectrometer (CAPS) instrument of the University of Vienna mounted under the wing of the NASA DC-8 aircraft, and the NASA research aircraft DC-8.

Figure II 2-3 presents a map of flight tracks: the four ATom deployments (ATom-1, ATom-2, ATom-3, and ATom-4), A-LIFE, and FIREX-AQ. An overview of the time periods for each campaign, deployed instrumentation used for the observation of size distributions in the relevant size range starting at 0.5 µm, relative humidity, and temperature for each mission is given in Table II 2-1. All missions together total 639 h of airborne measurements.

Table II 2-1. Overview of field campaigns and instrumentation used for the *Cloud Indicator* algorithm. Included are the total flight hours as well as the number of hours in-cloud (i.e., using the "cloudflag"). The instrumentation used in the algorithm for the size distribution, temperature, and relative humidity for each campaign are also listed.

Campaign	Time period	Location	Flight hours (cloudflag)	Instrumentation		
				Size distribution	Temperature	Relative humidity
ATom-1	Jul-Aug 2016	Global	91 (10)	UNIVIE-CAPS	MMS	DLH
ATom-2	Jan-Feb 2017	Global	94 (13)	UNIVIE-CAPS	MMS	DLH
A-LIFE	Mar-Apr 2017	Mediterranean	74 (3)	UNIVIE-CAPS	CMET	CMET
ATom-3	Sep-Oct 2017	Global	114 (18)	UNIVIE-CAPS	MMS	DLH
ATom-4	Apr-May 2018	Global	115 (13)	UNIVIE-CAPS	MMS	DLH
FIREX-AQ	Jul-Sep 2019	USA	151 (4)	UNIVIE-CAPS	MMS	DLH

2.2.2.1. ATom

The NASA-funded Atmospheric Tomography Mission (ATom) aimed to investigate the distribution of aerosols and trace gases in the remote global atmosphere between 2016 and 2018 (Thompson et al., 2022; Wofsy et al., 2021). The NASA DC-8 aircraft was equipped with an extensive gas and aerosol payload, providing approximately 700 different meteorological, trace gas, aerosol, and cloud parameters. The profiling flights took place in latitudes between nearly 90°N and 90°S up to 13 km altitude above the Pacific and Atlantic Oceans and were conducted in

each of the four seasons. A total of about 301000 km and 645 vertical profiles were flown, providing 53h of measurements inside clouds.

From the extensive ATom instrumentation, data from the UNIVIE-CAPS instrument, a Diode Laser Hygrometer (DLH), and the Meteorological Measurement System (MMS) are relevant for this study. DLH measures water vapor by detecting individual rotation-vibration lines of H_2O using wavelength modulated differential absorption spectroscopy (Diskin et al., 2002). For the *Cloud Indicator* algorithm, relative humidity with respect to water and ice is used from the DLH product. Measurements of GPS position, true airspeed, pressure, temperature, and three-dimensional wind were performed with the Meteorological Measurement System (MMS, Scott et al., 1990; Chan et al., 1998). MMS uses high-precision sensors for air motion sensing and a separate internal navigation system for accurate wind calculations. Temperature measurements from MMS are also used for the *Cloud Indicator* algorithm. Additionally, the true airspeed data is used for the calculations of the CAS and CIP number size distributions.

2.2.2.2. A-LIFE

The European Research Council (ERC)-funded "Absorbing aerosol layers in a changing climate: aging, lifetime and dynamics (A-LIFE)" project aimed to study the properties of mixtures of absorbing aerosols in the Eastern Mediterranean (Weinzierl and Coauthors, in prep.). During the 74 h of airborne sampling, multiple dust outbreaks from the Saharan and Arabian deserts, pollution layers, mixtures of polluted dust layers, and clouds were measured by in situ and remote sensing techniques. A-LIFE deployed the German Aerospace Center (DLR) Falcon 20 E-5 aircraft to the Eastern Mediterranean Sea with the UNIVIE-CAPS as part of an extensive aerosol and cloud payload between 3 and 30 April 2017. Additional measurements of GPS position and meteorological parameters (i.e., temperature, true airspeed, and pressure) were collected with the meteorological measurement system of the DLR Falcon (CMET).

2.2.2.3. FIREX-AQ

The Fire Influence on Regional to Global Environments Experiment and Air Quality (FIREX-AQ) mission was an extensive, joint NASA and NOAA venture investigating the impact of agricultural fires and wildfires in the US on air quality, weather, and climate using airborne in situ and remote sensing as well as ground-based observations (Warneke and Coauthors, in prep.).

Smoke plumes of agricultural fires and wildfires were sampled and characterized in situ and close to the point of emission with the NASA DC-8 equipped with an extensive payload for measurements of aerosols, trace gases, and clouds. In total, 151h of airborne measurements were conducted, including emissions from approx. 90 agricultural fires, 11 wildfires, and a pyrocumulonimbus event (Peterson et al., 2022).

During FIREX-AQ, the DC-8 also carried the UNIVIE-CAPS instrument, as well as the same DLH and MMS instruments used during Atom (see Section I.2.2.1). The CAPS, DLH, and MMS measurements during FIREX-AQ provided a large data set of in-cloud and cloud-free measurements, which contributed to the development of the *Cloud Indicator* algorithm.

2.2.3. Novel *Cloud Indicator* algorithm

The process of selecting and classifying cloud sequences in airborne in situ observations can be very time-consuming if done manually. Simple detection algorithms, with criteria like thresholds for particle number concentration in selected size ranges, are prone to misclassification, particularly when coarse aerosol particles (> 1 μm) are present. The motivation for the *Cloud Indicator* algorithm is to provide a robust algorithm that automatically detects and classifies clouds with a low number of misclassifications because several airborne in situ measurements are subject to artifacts during measurements inside clouds which commonly get flagged or erased in the post-flight data processing. Furthermore, the algorithm needed to provide cloud information (and, in

particular, a cloud mask) promptly after a measurement flight, which means that the algorithm was optimized for short processing times. This prompt application requirement of the *Cloud Indicator* limits the input data to parameters that are processed fast and excludes parameters with extensive processing, e.g., image analysis.

For the development of the *Cloud Indicator* algorithm, we restricted the used parameters to size distribution measurements from UNIVIE-CAPS, combined with measurements of temperature and relative humidity over water (RH_w) and ice (RH_i). While this algorithm utilizes the UNIVIE-CAPS size distribution, it can be used with any size distribution measurements of aerosol and cloud particles covering the size range from approximately 0.5 to 50 µm. Other potential light-scattering spectrometers covering the required size range, either standalone or in combination, are: the Cloud Droplet Probe (CDP), the Backscatter Cloud Probe (BCP), and the Cloud Particle Spectrometer with Polarized Detection (CPSPD) from Droplet Measurement Technologies (Longmont, USA), the Fast Forward Scattering Spectrometer Probe (FFSSP), Fast Cloud Droplet Probe (FCDP) from SPEC (Boulder, USA) and the Small Ice Detector (SID-2/3) from the University of Hertfordshire (Baumgardner et al., 2017). Additional imaging probes that operate partly in the desired size range but are generally missing the particles below 2µm are the Cloud Particle Imager (CPI) and the two-Dimensional Stereo (2D-S) probe from SPEC, the PHIPS-HALO from Karlsruhe Institute of Technology (KIT) and the Particle-i Imaging System (PI) from Artium (Sunnyvale, USA). It should be noted that an upper size limit of 50 µm is sufficient to apply this algorithm; however, a larger upper limit extending further into the size range of cloud particles reduces the probability of misclassifications due to undetected cloud particles.

The *Cloud Indicator* distinguishes whether measurements were taken inside a cloud, in an Aerosol-Cloud Transition Regime (ACTR), or a cloud-free sequence. For clouds, the algorithm further distinguishes between cirrus, Mixed-Phase Temperature Regime (MPTR), and liquid clouds. The parameters of the *Cloud Indicator* algorithm have been selected to represent basic properties of clouds (e.g., cloud particle number concentration, relative humidity, and temperature) and to distinguish a cloud from an aerosol layer with enhanced concentrations of coarse-mode particles (e.g., mineral dust, sea salt, or biomass burning aerosol). The criteria were tuned empirically by comparing in-field observations (e.g., flight reports, videos, and pictures from the flights) with measured parameters. Table II 2-2 gives an overview of the criteria used in the *Cloud Indicator* algorithm. Criterion 1 describes the temperature and relative humidity thresholds, criterion 2 gives the particle number concentration thresholds, and criterion 3 defines the newly-established cloud-aerosol volume factor (f_{CA}).

Table II 2-2. Overview of criteria used for classification of measurements with the *Cloud Indicator* algorithm. For more details see text.

		Liquid	MPTR (Mixed-Phase Temperature Regime)	Cirrus	ACTR (Aerosol-Cloud Transition Regime)
Criterion 1		$T \geq 273.15$ K $RH_w \geq 60\%$	273.15 K > T > 235.15 K $RH_i \geq 40\%$	$T \leq 235.15$ K $RH_i \geq 40\%$	No cloud
Criterion 2	**Case 2.1**	$RH_w \geq 60\%$ $N_{(D>25\ \mu m)} > 10^{-3}$ cm^{-3}	$RH_i \geq 40\%$ $N_{(D>25\ \mu m)} > 10^{-3}$ cm^{-3}	$RH_i \geq 40\%$ $N_{(D>25\ \mu m)} > 10^{-3}$ cm^{-3}	$RH_w \geq 60\%$ | $RH_i \geq 40\%$ $N_{(D>25\ \mu m)} > 10^{-5}$ cm^{-3}
	Case 2.2	$RH_w \geq 90\%$ $N_{(D>14\ \mu m)} > 10^{-3}$ cm^{-3}	$RH_i \geq 90\%$ $N_{(D>14\ \mu m)} > 10^{-3}$ cm^{-3}	$RH_i \geq 90\%$ $N_{(D>14\ \mu m)} > 10^{-3}$ cm^{-3}	$RH_i \geq 90\%$ $N_{(D>14\ \mu m)} > 10^{-5}$ cm^{-3}
	Case 2.3	$RH_w \geq 95\%$ $N_{(D>5\ \mu m)} > 10^{-3}$ cm^{-3}	$RH_i \geq 95\%$ $N_{(D>5\ \mu m)} > 10^{-3}$ cm^{-3}	$RH_i \geq 95\%$ $N_{(D>5\ \mu m)} > 10^{-3}$ cm^{-3}	$RH_i \geq 95\%$ $N_{(D>5\ \mu m)} > 10^{-5}$ cm^{-3}
Criterion 3		$f_{CA} = V_{(D>5\ \mu m)}/V_{(D<3\ \mu m)} > 100$			---

Criterion 1 of the *Cloud Indicator* algorithm uses temperature and relative humidity to assign cloud type (liquid, MPTR, or cirrus). Sequences with temperatures of 273.15 K or higher and RH_w at 60% or higher are classified as liquid clouds, whereas sequences at 235.15 K or colder are classified as cirrus clouds. MTPR clouds have temperatures between 235.15 K and 273.15 K and can consist of pure liquid, mixed-phase, or cirrus clouds (Costa et al., 2017). For the cirrus and MPTR class, RH_i must be 40% or higher.

The particle number concentration thresholds (criterion 2) are based on three different cloud particle number concentrations which are further differentiated in three sub-cases (2.1, 2.2, and 2.3), representing total number concentrations $N_{(D>5\mu m)}$, $N_{(D>14\mu m)}$ and $N_{(D>25\mu m)}$ with lower particle size limits of 5µm, 14µm, and 25µm, respectively. Depending on the relative humidity during a particular measurement, a different number concentration is applicable. For increasing relative humidity, the lower limit of the particle size decreases. For a liquid cloud, the corresponding RH_w thresholds are 60%, 90%, and 95% for the sub-cases 2.1, 2.2, and 2.3, respectively. For MPTR and cirrus clouds, RH_i is considered with thresholds of 40%, 90%, and 95% for sub-case 2.1, 2.2, and 2.3, respectively.

Criterion 3 is independent of the type of cloud (liquid, MPTR, or cirrus) and aims to avoid misclassifications of aerosol layers with enhanced concentrations of coarse-mode particles as clouds. The criterion is based on a cloud-aerosol volume factor (f_{CA}) developed in this study. The f_{CA} is a ratio between volume concentrations of the size ranges dominated by aerosol and cloud particles. The cloud particle-dominated volume concentration $V_{(D>5\mu m)}$ is defined as the integral volume concentration of all particles larger than 5µm, whereas the aerosol particle-dominated volume concentration $V_{(D<3\mu m)}$ covers the size range between approximately 0.5µm and 3µm. The volume ratio reflects typical processes in the atmosphere. That is, disregarding the nucleation, Aitken, and accumulation modes, atmospheric aerosol layers generally have a decreasing number concentration with an increasing particle size above ~ 0.5µm. Especially for aerosol layers with an enhanced coarse-mode, this behavior is particularly true for the size range above 0.5 µm (Brock et al., 2021; Weinzierl et al., 2017, 2009). In the case of the *Cloud Indicator* concentrations, the characteristics of atmospheric aerosol layers typically have $N_{(D<3\mu m)} >> N_{(D>5\mu m)}$ and $V_{(D<3\mu m)} \sim V_{(D>5\mu m)}$. This behavior can be seen in the left plot of Figure II 2-4, which presents an example volume size distribution of an aerosol layer (mineral dust). For clouds, the volume size distribution shows a different characteristic. In contrast to aerosol layers, the cloud number concentration is not generally decreasing with increasing size above 0.5 µm particle diameter but can have a mode diameter around 10 µm or larger (Heymsfield et al., 2017; Korolev et al., 2017).

This behavior leads to a very different volume size distribution that results in $V_{(D<3\mu m)} << V_{(D>5\mu m)}$, typically by several orders of magnitude for measurements inside clouds. The volume size distribution of the right plot of Figure II 2-4 demonstrates the significant difference between the red-shaded aerosol-particle dominated $V_{(D<3\mu m)}$ and blue-shaded cloud-particle dominated $V_{(D>5\mu m)}$ volume concentrations. To classify a sequence as a cloud, f_{CA} must exceed a threshold of 100. This value can be considered as a conservative threshold and was determined empirically by observations of mineral dust, biomass burning aerosol, and sea salt layers in the ATom, A-LIFE, and FIREX data sets.

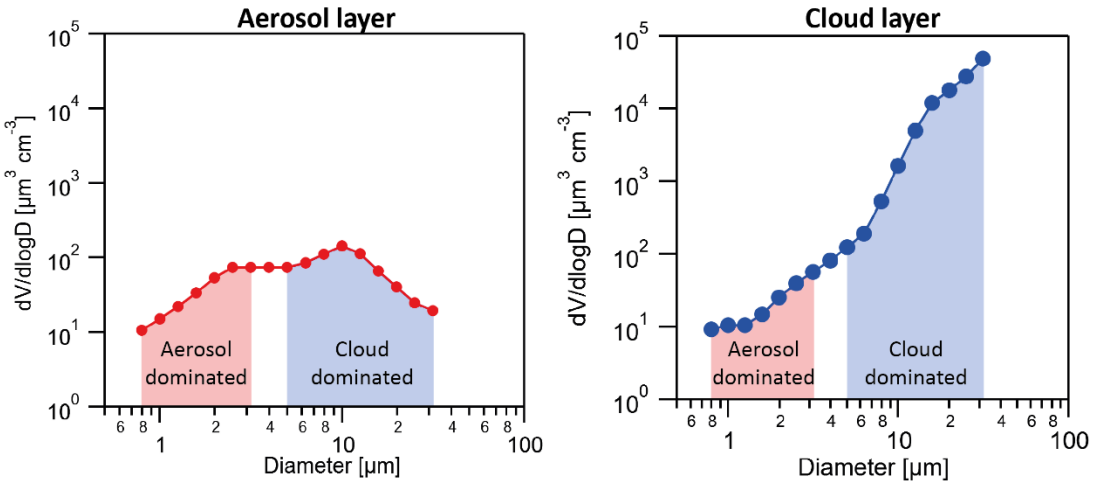

Figure II 2-4. Visualization of the cloud-aerosol volume factor (f_{CA}). The size range below 3µm is aerosol-particle dominated and the red-colored area represents the aerosol-particle dominated volume concentration. The size range above 5µm is considered cloud-particle dominated, and the blue shaded area defines the corresponding volume concentration. Left: Volume size distribution for an aerosol layer. This situation would result in $f_{CA} < 100$, and criterion 3 would not be satisfied (mineral dust layer, A-LIFE, 20 April 2017). Right: Volume size distribution for measurements inside a cloud (A-LIFE, 29 April 2017).

The Aerosol-Cloud Transition Regime (ACTR) is an additional category of the *Cloud Indicator*, considering sequences in an intermediate stage between aerosol layer and cloud, e.g., the twilight zone, which is a region of droplet/ice crystal formation and evaporation between clouds and cloud-free areas (Charlson et al., 2007; Hirsch et al., 2014; Koren et al., 2007). Table II 2-2 summarizes the two criteria for classifying a measurement as an ACTR sequence. The first criterion holds if a sequence is not classified as cirrus, MTPR, or liquid cloud. The second criterion has three sub-cases with lower particle size limits of 5µm, 14µm, and 25µm. The relative humidity thresholds are $RH_w \geq 60\%$ or $RH_i \geq 40\%$ for sub-case 2.1, $RH_i \geq 90\%$ for sub-case 2.2, and $RH_i \geq 95\%$ for sub-case 2.3. To fulfill criterion 2, a non-zero number concentration needs to be measured[1].

One additional purpose of the *Cloud Indicator* algorithm is to provide a data product ("cloudflag") for screening measurement periods inside clouds. To avoid the classification of a cloudy sequence as cloud-free in the "cloudflag" product, measurement periods between two detected clouds with a length of 10s or less are also flagged[2]. However, the "cloudflag" product is only meant to screen sequences inside clouds to avoid cloud artifacts (i.e., liquid droplets and ice crystals impacting at the inlet walls and generating secondary aerosols (Craig et al., 2014)). For the analysis of sequences inside clouds, the initial *Cloud Indicator* output should be used.

[1] A non-zero number concentration depends on the lower detection limit of the instrument. For the UNIVIE-CAPS, we use a threshold of 10^{-5} #/cm³

[2] For *Cloud Indicator* products prior to the year 2022, no "cloudflag" product existed and the linking between consecutive cloud detections less than 10s apart was performed for liquid, MPTR and cirrus clouds.

2.3. Results

In this section, the application of the *Cloud Indicator* algorithm is presented based on two different case studies from ATom and A-LIFE. Section 2.3.1 presents a case study in which the algorithm classified all cloud types in a short measurement sequence during ATom-1 above the Atlantic Ocean. The second case study is described in Section 2.3.2 and showcases clouds embedded in a mineral dust layer, which was measured during A-LIFE.

2.3.1. Case study 1: Sequence of clouds in the central Atlantic during ATom-1

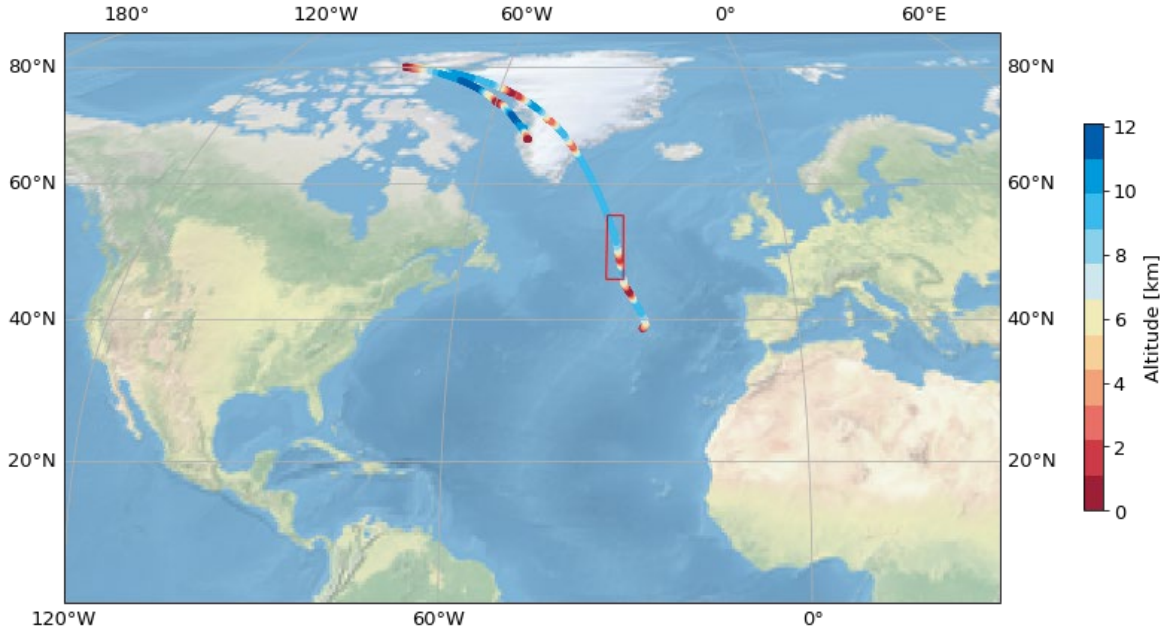

Figure II 2-5. Track of the ATom-3 flight from Terceira, Azores to Kangerlussuaq, Greenland on 20 August 2016. The flight altitude is color-coded. The measurement period marked with the red box was investigated in detail in case study 1.

Figure II 2-5 presents the flight track of the ATom-1 mission flight from Terceira, Azores, to Kangerlussuaq, Greenland, on 20 August 2016. A period of approximately 1 h, highlighted by the red box in Figure II 2-5, is used to present the classification scheme of the *Cloud Indicator*. All three cloud types (liquid, MPTR, and cirrus), as well as ACTR, were measured during this period.

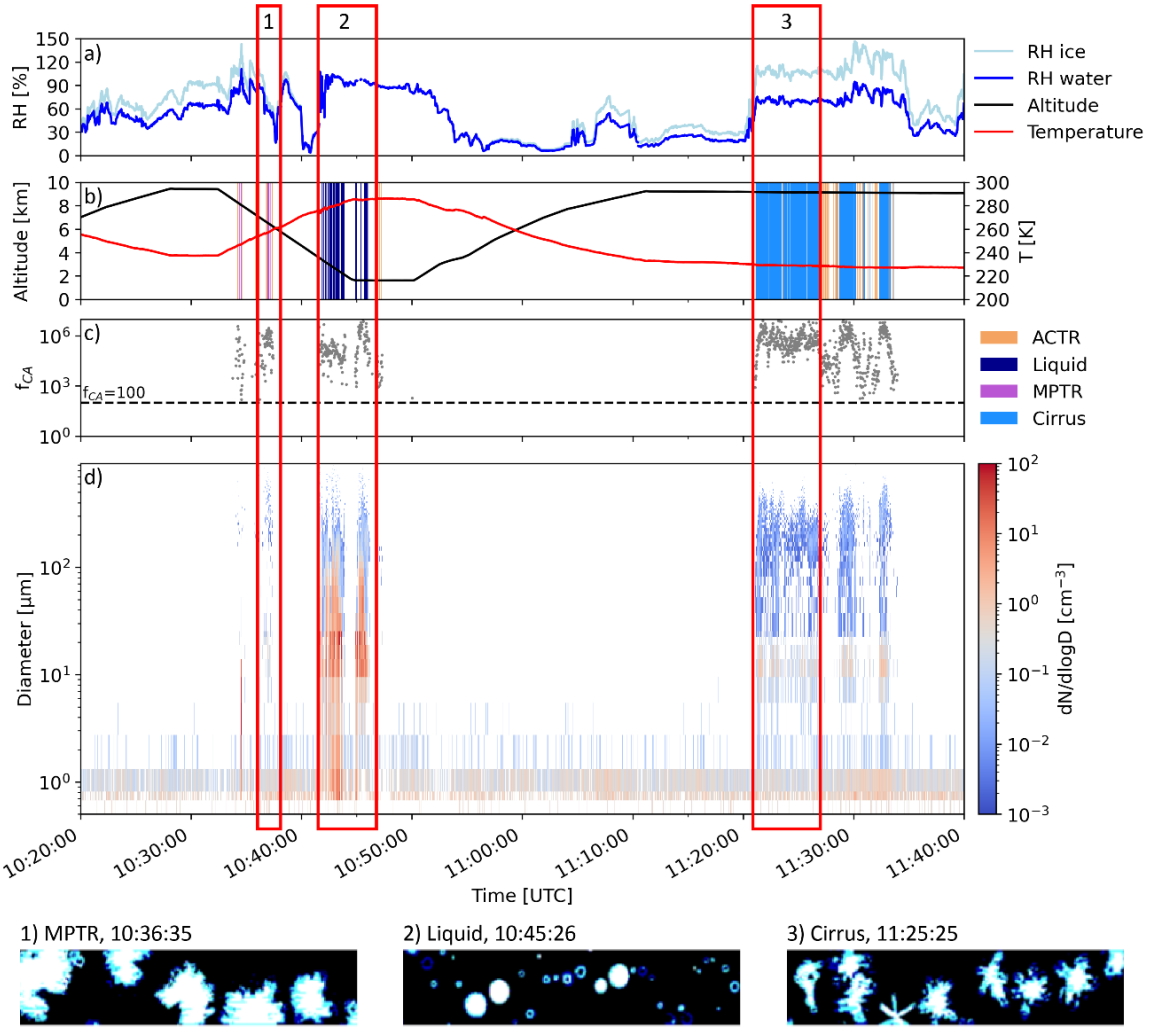

Figure II 2-6. Time series of a) RHi and RHw, b) altitude, temperature, and *Cloud Indicator* classification, c) cloud-aerosol volume factor (f_{CA}), and d) particle size distribution in the size range 0.6 to 25 µm (CAS data) and 25 to 930 µm (CIP data) for the ATom-1 flight on 20 August 2016. For the three red-marked boxes, CIP shadow images of the detected particles are shown.

Figure II 2-6 depicts a time series of the relevant measurement period: Panel a) visualizes RH_w and RH_i in dark blue and light blue, respectively. Panel b) presents the flight altitude in km on the left y-axis and the ambient temperature in K on the right y-axis using black and red lines, respectively. The classification derived by the *Cloud Indicator* is presented with colored strips, where ACTR is shown in yellow, liquid clouds in dark blue, MPTR clouds in purple, and cirrus clouds in light blue. The grey markers in panel c) show the f_{CA}, where the threshold of f_{CA}=100 is highlighted by the dashed, horizontal line. Panel d) presents the time series of CAPS size distributions. Particle diameters are shown on the y-axis and dN/dlogD is color-coded. For the size range between 0.6 and approximately 25 µm, CAS data are used, and for the size range between approximately 25 and 930 µm, CIP data are used. Between 10:36 and 10:37, an MPTR cloud was sampled (red box with number 1). The ambient temperature of this period increased from 254 to 258 K, and the particle size distribution indicates the presence of particles covering the entire size range of CAPS. The average cloud particle number concentrations $N_{(D>5µm)}$, $N_{(D>14µm)}$, and $N_{(D>25µm)}$ are 0.040, 0.026, 0.006 cm^{-3}, respectively, and RH_i decreases from 105% to 62% with an average of 81%. The values of temperature, relative humidity, and cloud particle number concentrations fulfill criteria 1 and 2 of the MPTR *Cloud Indicator* classification. The average f_{CA} is more than 10^6, which satisfies the cloud criterion 3. The MPTR cloud detected between 10:36 and 10:37 is

enclosed by ACTR-classified periods, most likely representing the edges of the cloud where cloud particle number concentrations were too low to fulfill criterion 2. Starting around 10:42, liquid clouds were measured. Between 10:45 and 10:46 (box 2), RH_w is rather constant with an average of 96% at 285 K, fulfilling criterion 1 for a liquid cloud. The size distribution for this time period clearly shows a mode between 10 and 20 µm with dN/dlogD reaching more than 100 cm^{-3} in this size range. The corresponding f_{CA} ranges between 10^6 and 10^7, satisfying criterion 3. The $N_{(D>5µm)}$ is on average 7.9 cm^{-3}, fulfilling sub-case 2.3. After 10:46, the concentration of cloud particles decreases, and criterion 2 of the *Cloud Indicator* is not fulfilled. Towards the end of the presented case study, a succession of cirrus clouds was observed, starting around 11:21. The measurement period between 11:21 and 11:27 (Figure II 2-6, box 3) has an average RH_i of 107% at 229 K, satisfying criterion 1 for a cirrus cloud. With a minimum RH_i of 96% and $N_{(D>5µm)}$ of 0.09 cm^{-3}, sub-case 2.3 is also fulfilled. The size distribution time series between 11:21 and 11:27 shows a high concentration of particles larger than 5µm, which leads to an average f_{CA} value exceeding 10^6, satisfying criterion 3. In summary, case study 1 showcases the ability of the *Cloud Indicator* to successfully distinguish liquid, MPTR, and cirrus cloud types as well ACTR in one flight sequence using our well-defined classification criteria.

2.3.2. Case study 2: Cloud embedded in dust layer during A-LIFE

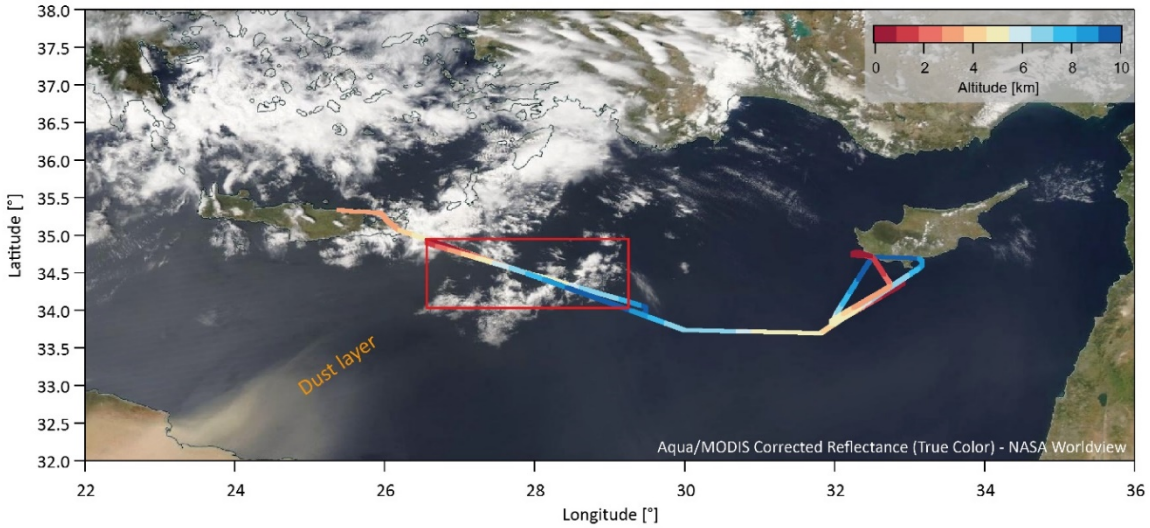

Figure II 2-7. Flight track of A-LIFE flight from Heraklion, Crete, to Paphos, Cyrus, on 20 April 2017. The flight altitude is color-coded and underlaid with a true color corrected reflectance image taken with MODIS on the Aqua satellite on the same day. Besides clouds, the satellite image shows a pronounced African dust outbreak with dust being transported in a northeasterly direction. The flight track framed with the red box is investigated in further detail and a time series is presented in Figure II 2-8. (NASA Worldview, https://go.nasa.gov/3ljMWG9)

Case study 2 presents a cloud embedded in a mineral dust layer during the A-LIFE mission. The flight from Heraklion, Crete to Paphos, Cyprus on 20 April 2017 is shown in Figure II 2-7, where the MODIS satellite image shows the presence of clouds in the western portion of the flight and a Saharan dust outflow moving in a north-eastern direction from Northern Africa across the Mediterranean Sea. During the flight, multiple vertical profiles were performed between near sea level and approximately 10 km altitude. One selected vertical profile (Figure II 2-7, red box) highlights clouds embedded in a Saharan dust layer. The corresponding time series of aerosol, cloud and meteorological measurements are presented in Figure II 2-8. The aircraft descended into the dust layer at approximately 15:30 and 8km altitude, indicated by an increasing amount and size of aerosol particles. During further descent at an altitude of about 6.1 km and around 15:40, the upper edge of the cloud layer was reached, which is confirmed by an increasing RH_i to

more than 80% and an increased concentration of particles larger than 100 µm. The cloud edge sequence is classified by the *Cloud Indicator* as ACTR. During further descent, the central part of the cloud was entered as RH_i increased to values larger than 100% and particles exceeding the upper CAPS size detection limit were measured. With all three criteria fulfilled and temperatures between 255 K at the top of the cloud to 274 K at the bottom, the *Cloud Indicator* detects and classifies this sequence as an MPTR cloud. Around 15:50 at 3.8km altitude, the lower edge of the cloud is reached and the *Cloud Indicator* classification first changes from MPTR to ACTR, and later to cloud-free. Below the cloud layer (approximately 15:50 and later), a dense dust layer with particles up to 100 µm are present.

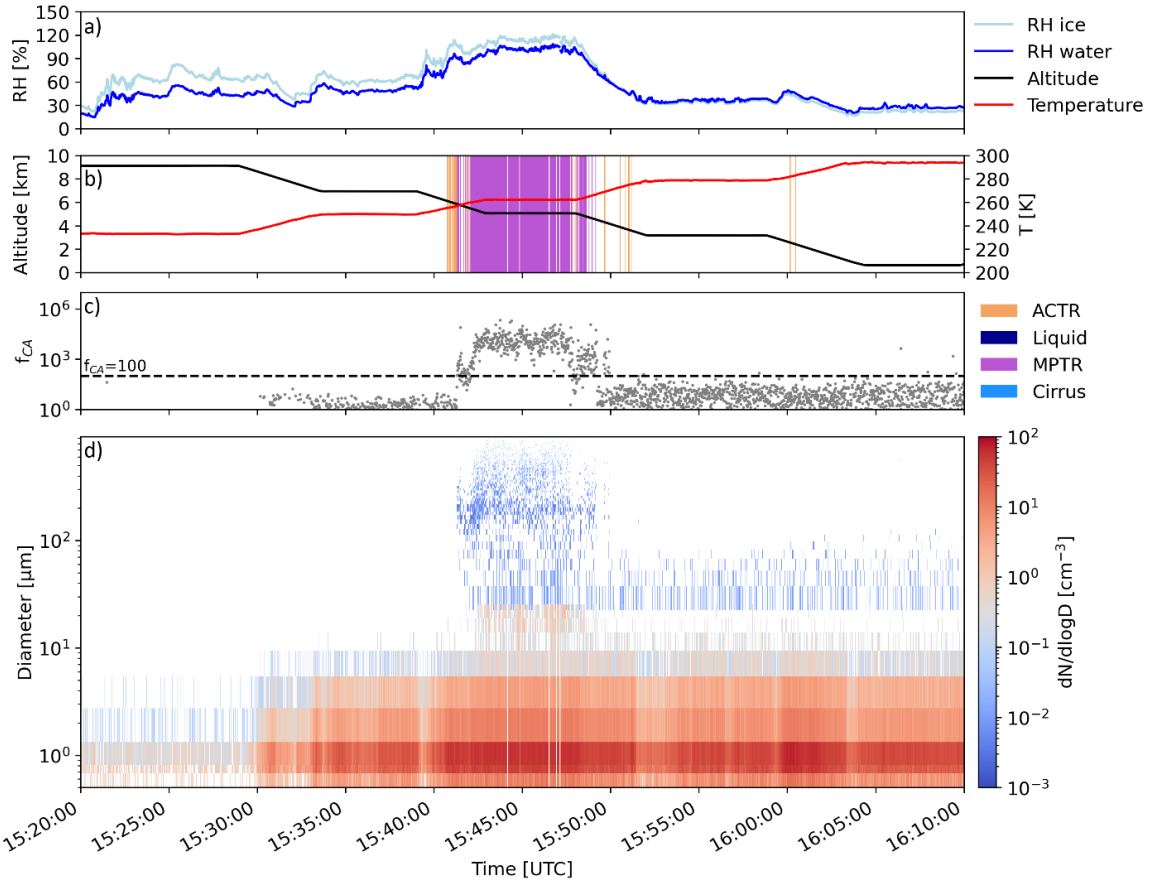

Figure II 2-8. Same representation as Figure II 2-6, but for measurements during the A-LIFE flight 20170420b on 20 April 2017.

Case study 2 depicts the performance and ability of the *Cloud Indicator* algorithm to detect and differentiate clouds from layers with enhanced concentrations of coarse-mode aerosol, which represents an extreme case with a cloud embedded in a mineral dust layer.

2.4. Discussion

The following section discusses the performance of the *Cloud Indicator* algorithm and verifies the two case studies with independent and concurrent measurements (Section 2.4.1). Section 2.4.2 reviews the thresholds chosen for the *Cloud Indicator* criteria in the context of published values in the literature.

2.4.1. Verification of classification with independent measurements

Since the *Cloud Indicator* algorithm is based on relative humidity, temperature, and volume and number concentrations, the CIP, which records shadow images of particles larger than 15 µm, can be used as an independent verification of the classification.

Below the time series in Figure II 2-6 (case study 1), corresponding images of cloud particles taken during the analyzed sequences of MPTR, liquid, and cirrus clouds are shown. All three sets of particle images independently confirm the *Cloud Indicator* classification and show the presence of ice crystals for the MPTR and cirrus classifications as for spherical droplets for periods classified as a liquid cloud.

For case study 2, a more detailed analysis of the vertical structure is shown in Figure II 2-9, where the considered period is presented in a vertically-resolved boxplot showing number concentrations of all particles larger than 5µm. The vertical profile is resolved in 200 m altitude bins. For each *Cloud Indicator* class, a single boxplot is created, i.e., if there are multiple classifications in one altitude bin, a boxplot for each classification exists in this altitude bin. The colors red, grey, and blue of the boxplots represent the *Cloud Indicator* classifications cloud-free, ACTR, and cloud (cloud represents liquid, MPTR, or cirrus clouds), respectively. For the verification of the *Cloud Indicator* and the analysis of the dust-embedded cloud, the data can be vertically separated into five relevant altitude layers: dust layer from 0 to 3.8 km, cloud base of dust-embedded cloud from 3.8 to 4.4 km, embedded cloud from 4.4 to 5.8 km, cloud top from 5.8 to 6 km, and dust layer at 6 km and above. On the right side of Figure II 2-9, randomly chosen CIP images of aerosol and cloud particles in the respective altitudes are shown. Each image is labeled in the top left corner as “dust” or “ice”. Particles in the dust layer above the cloud are too small to be resolved by the CIP. The mineral dust layer between 0 and 3.8 km carries a substantial amount of coarse-mode aerosol particles with diameters up to 100 µm visible in the size distribution time series in Figure II 2-8 and in Figure II 2-9 with an increased concentration of particles larger than 5µm (median number concentrations between 0.06 and 0.32 cm^{-3}). CIP images of these non-spherical dust particles at the bottom right side of Figure II 2-9 show diameters between approximately 15 and 70 µm. The *Cloud Indicator* algorithm classifies most of the dust layer as “cloud-free” with some “ACTR” classifications, which is also consistent with visual observations during the flight. The measurements in the “cloud base” area between 3.8 and 4.4 km are characterized as a transition region between dust layer and cloud. The randomly chosen images for this layer show ice crystals as well as dust particles, which supports the classifications of the *Cloud Indicator*. Inside the cloud, between 4.4 and 5.6 km, all altitudes have an MPTR cloud classification as also supported by the CIP images showing only large ice crystals. The median number concentration of cloud particles larger than 5 µm rises with increasing altitude from 0.11 cm^{-3} to a maximum of 0.34 cm^{-3} at 5.0 km. From 5.0 km to 5.6 km, the concentration decreases to 0.07 cm^{-3}. The cloud top altitude bins between 5.8 and 6.0 km are classified as cloud and ACTR, which agrees with the assumption that this region is the transition between the aerosol layer and the cloud embedded into this aerosol layer. While the CIP images of ice crystals support the cloud classification, the particles are smaller than the ice crystals within the cloud below. Above 6.2 km, the number concentration of particles larger than 5µm decreases towards 0 cm^{-3} with increasing altitude. The size distribution along the flight path, as shown in Figure II 2-8, shows that the mineral dust layer extends above the cloud top to an altitude of approximately 8 km, with

diameters of mineral dust particles decreasing with increasing altitude. The *Cloud Indicator* classifies this mineral dust layer correctly as “cloud-free” with some “ACTR” contribution in the altitude bin directly above the cloud top.

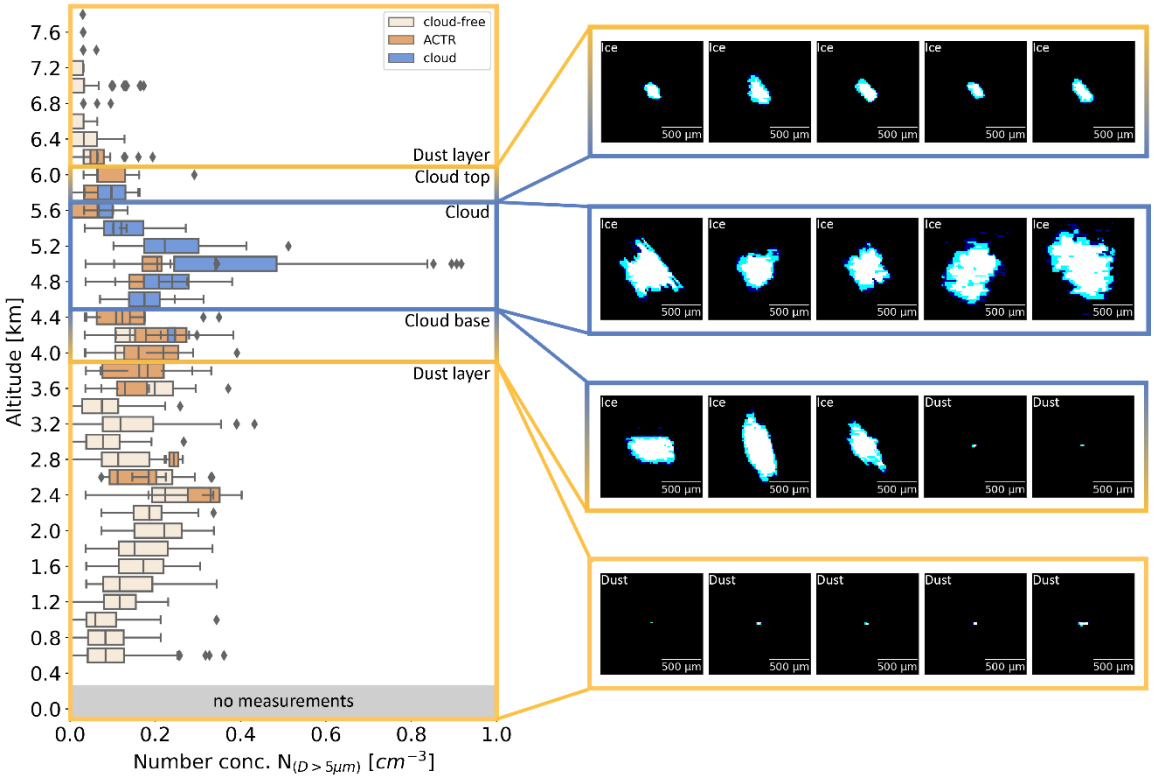

Figure II 2-9. Vertical profile of particle number concentration for particles larger than 5µm. Data were averaged over 200m bins, and box-and-whisker plots represent the variability, where the median and upper and lower quartiles are indicated with the box, “whiskers” show the lower and upper extreme values, and outliers are visualized with markers. The color of the boxes represents the classification of the *Cloud Indicator*. In the case of multiple classifications in the same altitude bin, a boxplot is generated for each category. For altitude ranges, randomly chosen CIP images visualize the detected particles. Altitude layers are grouped (lower part of the dust layer, cloud base, cloud, cloud top, and upper part of dust layer) with colored rectangles, where orange and blue represent the presence of dust and cloud particles, respectively.

Figure II 2-9 shows that the particle number concentrations within the cloud and in the dust layer section are relatively comparable. Here, a simple, number concentration-based cloud detection algorithm may lead to misclassifications of the dust layer as a cloud. In the case of the *Cloud Indicator* algorithm, the particular combination of number concentration thresholds and the cloud-aerosol volume factor (f_{CA}) reduces the possibility of misclassifications of the mineral dust as a cloud. Case study 2, in particular, depicts the ability of the f_{CA} to clearly separate the dust layer and the embedded cloud, as f_{CA} differs by several orders of magnitude within the cloud section compared to the dust layer section.

For both case studies 1 and 2, CIP images of particles captured during corresponding time periods support the ability of the *Cloud Indicator* algorithm to detect clouds and successfully separate layers with enhanced coarse-mode aerosol concentrations from cloud periods. Additionally, the images validate the type classification of the *Cloud Indicator* algorithm with spherical droplets captured during a liquid cloud classification and ice crystals during MPTR and cirrus cloud classifications.

2.4.2. *Cloud Indicator* in the context of literature

The criteria for the *Cloud Indicator* algorithm were established empirically from measurements during the ATom, A-LIFE, and FIREX-AQ missions, where in-field observations were used to iteratively improve the criteria. In the following section, we discuss the *Cloud Indicator* threshold values for the relative humidity and number concentration criteria.

Relative humidity with respect to water (RH_w) inside liquid clouds generally has a relatively narrow distribution around 100% (Korolev and Isaac, 2006). Korolev and Isaac (2006) used the data from three aircraft field campaigns to investigate relative humidity distributions in liquid, mixed-phase, and ice clouds. For liquid clouds, they determined 97% as the lower RH_w threshold. According to the authors, sequences with smaller RH_w are either measured near cloud boundaries or consist of supercooled large droplets and drizzle measured underneath the cloud base. In both cases, mixing with dry air decreases the measured RH_w. The *Cloud Indicator* algorithm considers such cases with a conservatively lower RH_w threshold of 60%. However, sequences with relative humidity as low as 60% are only classified as liquid clouds if they also fulfill the criteria of the cloud-aerosol volume factor (f_{CA}) and the number concentration of particles larger than 25µm. Depending on the formation process, clouds in the mixed-phase temperature regime (MPTR) can consist entirely of ice crystals or liquid droplets (i.e. supercooled liquid clouds) or a mixture of liquid droplets and ice particles (mixed-phase clouds) (Costa et al., 2017). Korolev and Isaac (2006) also investigated the RH_i distributions inside clouds as a function of temperature and found supersaturated clouds with lower temperatures and a broad distribution of RH_i. Specifically, they found supersaturated clouds with RH_i between 60-80% and some as low as 20%. These findings support the RH_i threshold of 40% of the *Cloud Indicator* algorithm for MPTR clouds. For cirrus clouds at temperatures below 235.15 K, the RH_i threshold of 40% is in good agreement with previously published investigations of RH_i inside cirrus clouds, where the frequency of detected cirrus clouds starts to increase at RH_i between 30 and 50% (Diao et al., 2013; Korolev and Isaac, 2006; Krämer et al., 2020; Ovarlez et al., 2002; Patnaude et al., 2021; Petzold et al., 2017; Spichtinger et al., 2004).

Operational weather forecasting defines a cloud as an aggregation of liquid droplets and/or ice crystals suspended in air, which becomes a visible cloud if the cloud particle number concentration is sufficiently large (Lohmann et al., 2016). However, there are no accepted thresholds of cloud microphysical and optical properties which define a cloud (Spänkuch et al., 2022). Analysis of large cloud data sets can be used to quantify the question, “How many cloud particles make a cloud?”. Krämer et al. (2020) and Patnaude et al. (2021) each present an analysis of large data sets containing measurements from multiple campaigns covering tropical, mid-latitude, and Arctic regions. Besides other parameters, these studies provide investigations of ice particle number concentration in cirrus clouds. The cloud definition in Krämer et al. (2020) considers all particles with a diameter larger than 3µm, which is smaller than the lowest size criterion of the *Cloud Indicator* at 5 µm. Krämer et al. (2020) report in-cloud number concentrations with a 10^{th} and 25^{th} percentile of 0.002 and 0.007 cm^{-3}, respectively. The reported particle number concentrations in Patnaude et al. (2021) contain all particles larger than 25µm, coinciding very well with the size limit of case 2.1 of the *Cloud Indicator*, which is applicable for RH_i between 40 and 90%. For cirrus clouds with RH_i between 40 and 90%, Patnaude et al. (2021) report mean number concentrations between 0.0001 and 0.001 cm^{-3}. Both Krämer et al. (2020) and Patnaude et al. (2021) report smaller number concentrations compared to the thresholds of 0.001 cm^{-3} used in the *Cloud Indicator* algorithm. However, the *Cloud Indicator* accounts for sequences with particle number concentrations lower than 0.001 cm^{-3} with the additional ACTR class.

The relative humidity thresholds show remarkable agreement with published studies, and the number concentration threshold compares well particularly because the ACTR class of the *Cloud Indicator* covers cases of number concentrations lower than 0.001 cm^{-3}.

2.5. Summary

Clouds play an important role in the Earth's climate system, but cloud feedbacks and aerosol-cloud interaction still pose the largest uncertainties in current climate predictions. Precise detection and classification of clouds in in situ data sets is therefore crucial to improve the understanding of numerous physical processes in the atmosphere.

In this study, we presented a novel algorithm, called the *Cloud Indicator*, for automatic cloud and cloud phase detection in (airborne) in-situ observations. In-cloud sequences are classified into liquid clouds, clouds in the Mixed-Phase Temperature Regime (MPTR), cirrus clouds, or Aerosol-Cloud Transition Regime (ACTR). The main characteristics of the novel *Cloud Indicator* algorithm are:

- Classification of cloud encounters and cloud phase based on particle number concentrations in three size ranges, relative humidity over water and ice, and temperature (see Table II 2-2)
- Application of the algorithm is flexible and allows the usage of measurements from a variety of instruments
- Tuned and evaluated to successfully differentiate cloud sequences from those with enhanced concentrations of coarse-mode particles (e.g., mineral dust, sea salt, or biomass burning layers)
- Introduction of a novel cloud-aerosol volume factor (f_{CA}), allowing precise and robust distinction between clouds and aerosol layers, thereby reducing misclassifications
- Fast application provides cloud screening information during or shortly after a measurement flight

The algorithm was developed in the framework of three international airborne field campaigns: ATom (Atmospheric Tomography; 2016-2018), A-LIFE (Absorbing aerosol layers in a changing climate: aging, lifetime and dynamics; 2017), and FIREX-AQ (Fire Influence on Regional to Global Environments Experiment and Air Quality; 2019). During each of the three field campaigns, the University of Vienna second-generation Cloud, Aerosol, and Precipitation Spectrometer (UNIVIE-CAPS) was part of the aircraft payload and served as the central instrument of this study. The measurements from the UNIVIE-CAPS were processed with a novel calibration and a data evaluation procedure also introduced in this study. The novel procedure allows in-field CAPS calibrations over the entire size range and provides a refractive index-independent calibration result. Furthermore, it uses statistical methods to consider instrumental uncertainties.

We presented the performance of the *Cloud Indicator* with two case studies during ATom and A-LIFE. The ATom case demonstrates the general performance of the *Cloud Indicator*, where, during approximately 1 h of measurements, all classifications were observed, including liquid clouds, clouds in the Mixed-Phase Temperature Regime (MPTR), cirrus clouds, Aerosol-Cloud Transition Regime (ACTR), and cloud-free cases. The A-LIFE sample was characterized by a complex mixture of clouds embedded in a mineral dust layer, showcasing the unique ability of the *Cloud Indicator* to successfully differentiate between layers of enhanced coarse-mode aerosol concentrations and clouds. Shadow images of cloud and aerosol particles taken with the CAPS during the two case studies served as an independent validation and confirmed the detection and classification of the *Cloud Indicator* algorithm. The parameter thresholds of the *Cloud Indicator* criteria were also discussed in the context of values in the literature and showed a good agreement.

In summary, the *Cloud Indicator* allows precise cloud screening of (airborne) in situ data sets key to investigations of aerosol and gas-phase processes in the atmosphere. It sets the foundation for homogenized cloud data sets crucial to advance the understanding of cloud microphysical properties and aerosol-cloud interactions. Ongoing work closely examines the formation of clouds

in Saharan mineral dust during A-LIFE and assesses the homogenized ATom, A-LIFE, and FIREX-AQ cloud data set with respect to ice cloud properties in pristine and aerosol-impacted environments.

3. Paper III: Brock et al. (2021) - Ambient aerosol properties in the remote atmosphere from global-scale in situ measurements

Brock, C. A., Froyd, K. D., **Dollner, M.**, Williamson, C. J., Schill, G., Murphy, D. M., Wagner, N. J., Kupc, A., Jimenez, J. L., Campuzano-Jost, P., Nault, B. A., Schroder, J. C., Day, D. A., Price, D. J., Weinzierl, B., Schwarz, J. P., Katich, J. M., Wang, S., Zeng, L., Weber, R., Dibb, J., Scheuer, E., Diskin, G. S., DiGangi, J. P., Bui, T., Dean-Day, J. M., Thompson, C. R., Peischl, J., Ryerson, T. B., Bourgeois, I., Daube, B. C., Commane, R., and Wofsy, S. C.

Published 2021 in *Atmospheric Chemistry and Physics*, 21, 15023–15063

DOI: https://doi.org/10.5194/acp-21-15023-2021

Abstract

In situ measurements of aerosol microphysical, chemical, and optical properties were made during global-scale flights from 2016–2018 as part of the Atmospheric Tomography Mission (ATom). The NASA DC-8 aircraft flew from ∼ 84° N to ∼ 86° S latitude over the Pacific, Atlantic, Arctic, and Southern oceans while profiling nearly continuously between altitudes of ∼ 160 m and ∼ 12 km. These global circuits were made once each season. Particle size distributions measured in the aircraft cabin at dry conditions and with an underwing probe at ambient conditions were combined with bulk and single-particle composition observations and measurements of water vapor, pressure, and temperature to estimate aerosol hygroscopicity and hygroscopic growth factors and calculate size distributions at ambient relative humidity. These reconstructed, composition-resolved ambient size distributions were used to estimate intensive and extensive aerosol properties, including single-scatter albedo, the asymmetry parameter, extinction, absorption, Ångström exponents, and aerosol optical depth (AOD) at several wavelengths, as well as cloud condensation nuclei (CCN) concentrations at fixed supersaturations and lognormal fits to four modes. Dry extinction and absorption were compared with direct in situ measurements, and AOD derived from the extinction profiles was compared with remotely sensed AOD measurements from the ground-based Aerosol Robotic Network (AERONET); this comparison showed no substantial bias.

The purpose of this work is to describe the methodology by which ambient aerosol properties are estimated from the in situ measurements, provide statistical descriptions of the aerosol characteristics of different remote air mass types, examine the contributions to AOD from different aerosol types in different air masses, and provide an entry point to the ATom aerosol database. The contributions of different aerosol types (dust, sea salt, biomass burning, etc.) to AOD generally align with expectations based on location of the profiles relative to continental sources of aerosols, with sea salt and aerosol water dominating the column extinction in most remote environments and dust and biomass burning (BB) particles contributing substantially to AOD, especially downwind of the African continent. Contributions of dust and BB aerosols to AOD were also significant in the free troposphere over the North Pacific. Comparisons of lognormally fitted size distribution parameters to values in the Optical Properties of Aerosols and Clouds (OPAC) database commonly used in global models show significant differences in the mean diameters and standard deviations for accumulation-mode particles and coarse-mode dust. In contrast, comparisons of lognormal parameters derived from the ATom data with previously published shipborne measurements in the remote marine boundary layer show general agreement. The data set resulting from this work can be used to improve global-scale representation of climate-relevant aerosol properties in remote air masses through comparison

with output from global models and assumptions used in retrievals of aerosol properties from both ground-based and satellite remote sensing.

Author contributions

This publication combines the measurements from the CAS component of the UNIVIE-CAPS with in-cabin measurements of size distributions also using aerosol composition measurements conducted during ATom for the calculation of intensive and extensive aerosol properties. The CAS component has a significant contribution to the study since it covers the entire coarse-mode and some of the accumulation mode of the combined size distributions.

I played a major role in the preparation of CAPS for the aircraft field experiments and performed the CAPS measurements during a large number of flights of the four ATom deployments. I performed the quality assurance and processing of the CAPS measurements, including the processing of the *Cloud Indicator* product. The *Cloud Indicator* was used to select periods relevant for the analysis of this publication. I computed and analyzed the CAS size distributions with the novel size distribution retrieval developed in the framework of this dissertation (Section II.4.2.2.3, page 39). Charles Brock (first author) and I discussed intensively and worked together to combine the size distributions from the in-cabin instruments and CAS, focusing on a good agreement in the overlapping size range of the in-cabin instruments and CAS.

Relevance for the dissertation

This publication has a significant contribution to the scientific question of this dissertation. The analysis within this publication has an important contribution to the assessment of the global distribution of atmospheric coarse-mode aerosol. One result of the paper is the significance and abundance of atmospheric coarse-mode aerosol, which is one significant achievement of this dissertation.

4. Paper IV: Dollner et al. (2022b, in prep.) - Aerosol-cloud interactions in Saharan mineral dust over the Eastern Mediterranean

Dollner, M., Gasteiger, J., Kandler, K., Schöberl, M., Sudharaj, A., Witaschs, B. and Weinzierl, B.
In preparation 2022

Abstract

Mineral dust is one of the largest contributors to the total atmospheric aerosol load by mass. However, despite this large contribution, atmospheric processes connected to mineral dust are still not well understood. Ongoing research investigates the aerosol-cloud interactions of mineral dust. Laboratory experiments have been conducted to determine the ability of minerals dust to act as cloud condensation nuclei (CCN) and ice nucleating particles (INPs). However, atmospheric measurements about the CCN and INP ability of mineral dust are rare.

In this study, we present unique in situ and remote sensing observations of dust-embedded clouds measured in the Mediterranean on 20 April 2017 during the A-LIFE campaign. In situ observations of shadow images and size distributions of aerosol and cloud particles, measurements of relative humidity and liquid water content (LWC), and remote sensing measurements with a Doppler wind lidar were used to characterize microphysical dust and cloud properties. A central instrument of this study is the second-generation Cloud, Aerosol, and Precipitation Spectrometer (CAPS), which captured the shadow images and recorded the size distributions of the coarse-mode aerosol and cloud particles. For the CAS, the optical spectrometer in CAPS, a novel size distribution retrieval was developed and is introduced in this study. The retrieval considers instrumental uncertainties and utilizes a Monte Carlo method to report particle sizes as geometric diameters and takes the non-sphericity and the refractive index of the measured particles into account. The hotwire sensor of the CAPS, responsible for the LWC measurements, was calibrated with a newly developed machine learning (ML) method also introduced in this study.

The study presents detailed analyses of the clouds embedded in a dense mineral dust layer, revealing two separate aerosol-cloud interaction processes occurring in the dust-embedded clouds. First, cloud top ice crystal measurements and size distributions from the mineral dust layer were used to investigate the hypothesis that the ice crystals of the embedded clouds formed via heterogeneous ice nucleation. These results were compared with findings from laboratory experiments and commonly used INP parameterization providing a good agreement and confirming the hypothesis. The second process observed in the dust-embedded cloud describes the small-scale CCN activation of mineral dust particles to small liquid droplets (~10 µm). The analysis showed that mineral dust particles with an activation diameter as small as 0.13 to 0.23 µm acted as CCN and activated into cloud droplets. Comparisons of the laboratory studies of mineral dust activation diameters revealed an excellent agreement. Observations with the DWL confirmed small-scale vertical lifting as the reason for the significant increase in water supersaturation, providing the appropriate environment to initiate the CCN activation of mineral dust.

Author contributions

This publication was designed and written by myself, with contributions and comments from coauthors. All figures incorporated in this paper are prepared by myself, except Figure II 4-10,

which was provided by Dr. Benjamin Witschas and modified by myself. I developed the novel CAS size distribution retrieval and the new machine learning (ML) method for the CAPS hotwire calibration. I played a major role in the preparation of CAPS for the A-LIFE field experiment and performed the CAPS measurements during a number of A-LIFE flights. I performed the quality assurance and processing of the A-LIFE CAPS measurements and performed the complete analysis for this publication. Discussions with coauthors triggered ideas leading to the current content of the paper.

Relevance for the dissertation

The findings of this publication contribute significantly to this dissertation. The newly developed CAS size distribution retrieval and the novel ML method for the CAPS hotwire calibration contribute to the enhancement of CAPS measurements capabilities for coarse-mode aerosol and cloud particles, which represents one significant achievement of this dissertation. Furthermore, the results from the investigation of the dust-embedded clouds are one major result of this dissertation.

4.1. Introduction

Although approx. 70% of the atmospheric aerosol mass consists of mineral dust (Huneeus et al., 2011; Kinne et al., 2006), it remains a significant contributor to the uncertainties of predictions of the Earth's energy budget (Adebiyi and Kok, 2020). The direct impact of mineral dust on the atmospheric energy budget depends on the size of the particles. Fine dust has a predominantly cooling effect by scattering shortwave solar radiation, whereas coarse dust warms the atmosphere by absorbing solar and terrestrial radiation (Miller et al., 2006). Global climate models tend to underestimate the amount of coarse-mode mineral dust particles. This misrepresentation overestimates the cooling effect by 0.15 W m^{-2} (0.1 to 0.24 W m^{-2}) and increases the likelihood of a general warming effect of mineral dust (Adebiyi and Kok, 2020).

Besides the direct interaction with radiation, mineral dust also affects the Earth's atmosphere with its ability to act as cloud condensation nuclei (CCN) and ice nucleating particles (INPs). CCNs are aerosol particles that activate and grow to liquid cloud droplets within a water vapor supersaturated environment (Seinfeld and Pandis, 2006). The CCN ability of a particular aerosol particle depends on its size and chemical composition. A widely used parameterization of this dependency is the κ-Köhler theory, which uses the parameter κ to describe this relative humidity-dependent growth of aerosol particles for different compositions and particle sizes (Petters and Kreidenweis, 2007). The CCN activity of mineral dust has been studied by several laboratory studies. Tang et al. (2016) provide a comprehensive literature review of these studies, revealing a good agreement throughout the different laboratory observations. Single component mineral dust (e.g., illite, kaolinite, montmorillonite) appears to have a very low CCN activity, which can be described with κ<0.01. However, authentic samples of North African, Saharan, and Asian dust are reported with slightly higher κ in the range between 0.01 and 0.023 (Tang et al., 2016).

INPs are the fundamental component of heterogeneous ice nucleation, which is the mechanism of primary ice formation at temperatures > 235 K. There are different modes of heterogeneous ice nucleation and definitions have been subject to change in the past (Kanji et al., 2017). Vali et al. (2015) describe the heterogeneous ice nucleation modes as follows. Deposition nucleation is the growth via direct deposition of supersaturated vapor on an INP, whereas freezing nucleation includes a liquid state. Freezing nucleation can be separated into immersion freezing, contact freezing, and condensation freezing. For immersion and contact freezing, the ice nucleation is initiated by an INP, with the difference that the INP is immersed within the liquid droplet for immersion freezing. Condensation freezing is defined as the concurrent initiation of the liquid

droplet formation process and the freezing process, where the droplet formation happens at conditions below the melting point of ice.

Numerous laboratory studies investigated the ice nucleation ability of mineral dust. Kanji and Abbatt (2006) investigated the deposition mode nucleation of mineral dust in the temperature range between 263 and 218 K. For a Saharan dust sample with particle sizes ranging from 0.5 to 5 µm, they found an ice onset relative humidity with respect to ice (RH_i) between 102 and 108% with no strong dependency on temperature. Findings from Kanji and Abbatt (2006) were confirmed by other studies of ice nucleation of super micron dust (Hoose and Möhler, 2012). However, current global-climate models underestimate the effect of dust aerosol on cloud formation. A model-tuning study used the hemispheric and seasonal contrast of cloud top phase from satellite observations to constrain the dust-driven droplet freezing in a global-climate model (Villanueva et al., 2021). They revealed an effect of 0.14 ± 0.13 W m^{-2} due to dust-based immersion freezing of droplets between 30°N and 60°N.

Airborne in situ observations are used to improve the understanding of atmospheric CCNs and INPs. However, atmospheric in situ measurements of CCN activation and ice nucleation events are difficult to measure since it is challenging to predict the exact moment and region of the microphysical process. A method to measure the ice nucleation ability of aerosol particles directly in the atmosphere was conducted during recent airborne in situ investigations (Cziczo et al., 2017). Residuals of evaporated ice crystals (i.e., particles remaining after the evaporation of the ice crystal) revealed information about the chemical composition and size of the aerosol particles that initiated the ice crystal formation. The analysis of the residuals can be done either offline using optical and other microscopy techniques (more details in section c) of Cziczo et al., 2017) or online with instruments like a real-time mass spectrometer (e.g., Eidhammer et al., 2010). A study using such an online method found mineral dust and metallic particles as the dominant INP of the measured ice crystals (Cziczo et al., 2013). Induced nucleation of ambient aerosol in a portable chamber of controlled temperature and saturation is another in situ method to investigate the cloud condensation and ice nucleation properties of the ambient aerosol. In situ measurements are often combined with model simulations and satellite observations to learn about the nucleation process and responsible INPs (e.g. Jensen et al., 2018). Such a combined approach of global-scale airborne in situ measurements of dust aerosol in the upper troposphere and detailed cirrus-formation simulations determined the dominant role of dust aerosol in the cirrus formation process in the northern hemispherical extra-tropics in all seasons (Froyd et al., 2022). However, such atmospheric in situ observations are rare and more investigations are necessary to reduce knowledge gaps connected to atmospheric CCN and INP processes.

This study presents, to our knowledge, the first in situ observations of clouds embedded in a mineral dust layer measured during the A-LIFE field campaign in the Mediterranean. Airborne in situ measurements of mineral dust, pollution, and clouds were conducted with the German Aerospace Center (DLR) Falcon 20 E-5, equipped with an extensive aerosol and cloud payload and a Doppler wind lidar (DWL). On 20 April 2017, in situ measurements of a mineral dust layer and clouds revealed two separated processes of aerosol-cloud interactions in the dust-embedded clouds. First, the hypothesis that heterogeneous ice nucleation of mineral dust particles formed the cloud-top ice crystals of the dust-embedded cloud was investigated. Second, the unique capture of small-scale activation and growth of mineral dust particles to liquid droplets within the embedded cloud was analyzed comprehensively.

4.2. Method

This chapter introduces the methods relevant for analyzing of the aerosol-cloud interactions in the mineral dust layer. The chapter is structured as follows: section 4.2.1 describes the A-LIFE field experiment, and section 4.2.2 follows with an introduction of the second-generation Cloud, Aerosol, and Precipitation Spectrometer (CAPS) and its associated CAPS data analysis algorithms. The presented algorithms include the *Cloud Indicator* for cloud detection and classification, a novel size distribution retrieval, and a newly developed calibration method for the CAPS hotwire sensor for liquid water content (LWC). This chapter ends with information on the offline chemical analysis of particles collected from the mineral dust layer and the introduction of the Doppler Wind Lidar (DWL) in sections 4.2.3 and 4.2.4, respectively.

4.2.1. A-LIFE field campaign

The "Absorbing aerosol layers in a changing climate: aging, lifetime and dynamics (A-LIFE)" project was funded by the European Research Council (ERC) to investigate the properties of mixtures of absorbing aerosols in the Eastern Mediterranean (Weinzierl and Coauthors, in prep.). Furthermore, properties and lifetime of coarse-mode aerosol particles and the processes allowing these large particles to remain lofted were particularly interesting for the project. The A-LIFE project deployed the German Aerospace Center (DLR) Falcon 20 E-5 aircraft in the Eastern Mediterranean between 3 and 30 April 2017. The aircraft was equipped with an extensive aerosol and cloud payload, instruments for meteorological parameters, and a Doppler Wind Lidar (DWL). In total 22 flights with 74h of airborne sampling were conducted, including measurements of multiple dust outbreaks from the Saharan and Arabian deserts, pollution layers, and mixtures of pollution and dust. Cloud observations were focused primarily on the dust-cloud interactions. The airborne in situ observations were assisted and extended by simulations from the Lagrangian transport and dispersion model FLEXPART (Pisso et al., 2019; Seibert and Frank, 2004; Stohl et al., 2005, 1998; Tipka et al., 2020).

4.2.2. Second-generation Cloud, Aerosol, and Precipitation Spectrometer

The second-generation Cloud, Aerosol, and Precipitation Spectrometer (CAPS, Droplet Measurement Technologies, Longmont, CO, USA) is a wing-mounted optical spectrometer and optical array probe for measurements of aerosol and cloud particles in the nominal size range between 0.5 and 930 µm. The CAPS was deployed during the A-LIFE field campaign and measurements provided input for two algorithms used in this study. First, the *Cloud Indicator* algorithm was used to separate periods inside clouds from cloud-free sequences (Dollner et al., 2022a, in prep.). Furthermore, a novel algorithm was developed to calculate particle size distributions, which considers instrumental uncertainties and reports the particle sizes in geometric diameters. Section 4.2.2.1 describes the components of the CAPS instrument and gives a brief overview of the standard data products. The *Cloud Indicator* algorithm, the size distribution retrieval, and the hotwire calibration method are specified in chapters 4.2.2.2, 4.2.2.3, and 4.2.2.4, respectively.

4.2.2.1. Instrument description

The CAPS has two main components: the Cloud and Aerosol Spectrometer (CAS) and the Cloud Image Probe (CIP) (Baumgardner et al., 2001). Additionally, CAPS supplies measurements of true airspeed, pressure, relative humidity, temperature, and liquid water content with supporting sensors. The CAPS from the University of Vienna (UNIVIE-CAPS) is the main instrument used for this study. A detailed description of the UNIVIE-CAPS and the procedure used to calibrate the instrument can be found in section II.2.2.1.2 (page 15) (Dollner et al., 2022a, in prep.).

CAS is an optical spectrometer that sizes aerosol or cloud particles based on the principle of light scattering of single particles intersecting with a laser beam (wavelength 658 nm). The CAS from the UNIVIE-CAPS measures the scattered light in the forward direction (4.2° – 13.2°) and covers a size range between approximately 0.5 and 50 µm. Additional detectors also measure backscattered light. However, only measurements from the forward detector are used for this study.

The Cloud Image Probe (CIP) is an optical array probe (OAP) (Knollenberg, 1970) that extends the size range of UNIVIE-CAPS to larger particles. It covers the nominal size range between 15 and 930 µm of aerosol and cloud particles passing a 658 nm collimated laser beam and records shadow images with a linear array of 64 photodiodes. The CIP of the UNIVIE-CAPS is a greyscale version reporting images of measured particles with three intensity levels.

4.2.2.2. The *Cloud Indicator* algorithm

The *Cloud Indicator* is an algorithm that automatically detects and classifies measurement periods inside clouds (Dollner et al., 2022a, in prep.). The algorithm distinguishes periods in cloud-free, Aerosol-Cloud Transition Regime (ACTR), liquid clouds, clouds in the Mixed-Phase Temperature Regime (MPTR), and cirrus clouds. Furthermore, it utilizes size distribution, relative humidity, and temperature measurements to automatically detect and classify the cloud type of flight periods in clouds. An additional cloud-aerosol volume factor (f_{ca}) is used to ensure a robust distinction of aerosol layers with an enhanced coarse-mode concentration (e.g., a mineral dust layer) from clouds and, hence, reduces misclassification of the two. In general, the size distribution data is not restricted to any specific instrument; however, the size distribution input to the *Cloud Indicator* algorithm should cover the range between approx. 0.5 µm and at least 50 µm. For this study, size distribution measurements were taken from the UNIVIE-CAPS.

4.2.2.3. Size distribution retrieval

Particle size distributions are commonly reported with equivalent optical diameters (e.g., spherical ammonium sulfate equivalent), where reported diameters represent the size of a particle of the equivalent material having the same measured signal. The new retrieval reports particle sizes as geometric diameter and applies a Monte Carlo method (Metropolis and Ulam, 1949) for the consideration of instrumental uncertainties, as well as refractive indices and non-sphericity of the measured aerosol. The general measurement principle of optical spectrometers like the CAS is the collection of light scattered by single particles intersecting a light beam, e.g., from a laser (Kulkarni et al., 2011). The scattered light is collected with photodetectors and recorded as a digital signal, where the amplitude of the signal (i.e., scattering signal amplitude) corresponds to the intensity of the detected light. Calibrations are used to determine the instrument-specific relationship between the scattering signal amplitude and the theoretical scattering cross-section (Szymanski et al., 2009; Walser et al., 2017). The calibration procedure introduced in Dollner et al. (2022a, in prep.) provides this relationship independent of the used calibration material's refractive index of the used calibration material and is the foundation for the size distribution retrieval explained in this section.

The main input for the size distribution retrieval consists of scattering signal amplitudes from the CAS particle-by-particle data (PbP-data), information about the type of the measured particles, and the scattering cross-section functions representing the different particle types and shapes.

Particle classes and scattering cross-section functions

To select the correct scattering cross-section functions for the size distribution retrieval, information about contributing particle types in a measured airmass is necessary. There are several possibilities to retrieve this information and one way is with in situ measurements. For

example, mass-spectrometers can provide information about the chemical composition of the aerosol particles in an airmass(e.g., Brock et al., 2021). For the A-LIFE data set, aerosol type was obtained using FLEXPART simulation of mass fractions of different chemical components. The simulation output was processed to provide time series of number fractions of the contributing aerosol types: mineral dust (dust), sea salt (SS), sulfates (SO4), organics (OM), and black carbon (BC). Additionally, water and ice were added as types for clouds. The seven types build the set of particle classes for the size distribution retrieval (see Table II 4-1). Ensembles of scattering cross-section functions were calculated for each of the seven classes, representing a possible range of refractive indices. Figure II 4-1 visualizes the refractive index ensembles of all seven classes. For SS, SO4, and OM, water update was also considered for the refractive indices and the particle densities using a volume weighting and the κ-dependent growth factor (Petters and Kreidenweis, 2007; Zieger et al., 2013). Table II 4-1 summarizes the refractive index ranges, used hygroscopicity values κ, and particle densities for the corresponding classes as they are used in the size distribution retrieval (Bond and Bergstrom, 2006; Brock et al., 2021; Froyd et al., 2019; Kandler et al., 2011; Koehler et al., 2009; Michel Flores et al., 2012; Moise et al., 2015; Petters and Kreidenweis, 2007; Svenningsson et al., 2006; Tang, 1996; Zieger et al., 2017). For dust, the refractive indices were used from Kandler et al. (2011), which represent composition-dependent refractive indices for different mineral dust components. Scattering cross-section functions for SO4, OM, BC, hydrated SS, and water, are calculated for spherical particles, whereas for dust, dry SS, and ice, non-spherical particles were assumed, and their scattering cross-section ensembles also considered different particle shapes and orientations.

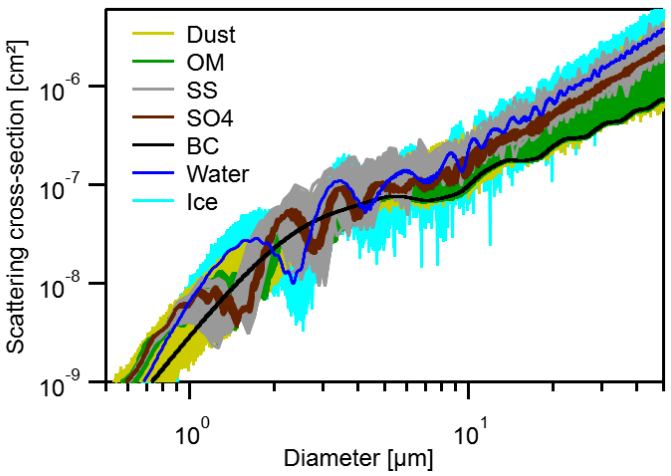

Figure II 4-1. Scattering cross-section ensembles of particle classes for CAS geometry used in the novel size distribution retrieval.

Table II 4-1. Refractive index ranges, κ and density of the different particle classes of the size distribution retrieval. The ensemble of 'dust' refractive indices is used as explained in Kandler et al. (2011).

Class	Refractive index		κ	Particle density [kg/m³]
	n	k		
Dust	Kandler et al. (2011)		0.03	2500
SS	1.541	0	1.1	1800
SO4	1.5-1.53	0	0.483	1770
OM	1.44-1.61	0-0.03	0.163	1350
BC	1.75-1.95	0.63– 0.79	0	1000
Water	1.33	0	-	1000
Ice	1.31	0	-	917

Binning, "perfect diameter", and "slope correction"

The size distribution retrieval presented here applies the "perfect diameter" method (Rosenberg et al., 2012), which is briefly described here. A more detailed description of the

procedure can be found in Rosenberg et al. (2012). First, the scattering cross-section values corresponding to the CAS detection range are divided to generate a binning for the size distribution retrieval. Because scattering cross-section functions for the geometry of the CAS optics are non-monotonic (see Figure II 4-1), one scattering cross-section bin may be split across the corresponding diameter space, depending on the specific scattering cross-section function. However, equations 11 and 12 from Rosenberg et al. (2012) calculate bin center diameters and bin widths taking these non-monotonic effects into account. This approach provides bins with representative diameters and bin widths for the CAS-specific scattering response. The method is applied to the scattering cross-section function ensembles of the different classes leading to ensembles of bin center diameters and bin widths for each class.

Depending on the scattering cross-section function, some bins need to be large to avoid errors from scattering cross-section ambiguities. However, the bin center diameter varies with respect to the shape of the size distribution due to the bin interval weighting of particle sizes. Thus, for a bin in a section of the size distribution where the number concentration decreases with increasing diameters (i.e., negative slope), a smaller bin center diameter should be used to avoid oversizing. The opposite is also true: for an increasing number concentration with increasing diameters (i.e., positive slope), a larger bin center diameter should be implemented to avoid under-sizing. The bin center diameter can be approximated with a sigmoidal function to correct for over- and under-sizing, depending on the slope of the size distribution at the bin location.

Size distribution retrieval

Figure II 4-2 shows a flowchart of the size distribution retrieval, where the core of the retrieval is within the grey shaded box. For the size distribution calculations of a selected time period, measurements of scattering signal amplitudes are taken from the corresponding PbP data and converted to scattering cross-sections using a calibration valid for the measurement period (Dollner et al., 2022a, in prep.). The retrieved scattering cross-section values are sorted into the scattering cross-section bins of the specific particle class, which returns a count distribution for the selected time period. The count distribution is converted into particle size distributions (i.e., dN/dlogD in cm^{-3}) at STP conditions[3] using the following equations:

$$\overline{N_i} = \frac{\sum_j^n \frac{N_{i,j} * (f_{PbP})_j * (f_{STP})_j}{\Delta t_j * TAS_j * SA}}{n} \quad \textbf{(1)}$$

$$\frac{dN}{dlogD} = \frac{\overline{N_i} * \varepsilon}{w_i} * \ln(10) * D_i \quad \textbf{(2)}$$

Here, $N_{i,j}$ represents the counts of the i-th bin for a specific data point j, $\overline{N_i}$ is the average bin concentration for the selected time period, n is the number of used data points in the time period. For a specific data point j, f_{PbP} is the PbP-factor[4], f_{STP} is the STP-factor, Δt is the sampling time in seconds, and TAS the true airspeed in cm s^{-1}. SA the sample area of the CAS in cm^2. For equation (2), ε represents a systematic deviation that covers uncertainties of TAS, temperature, and pressure measurements. D_i and w_i are the bin center diameters and bin widths, respectively, using the "perfect diameter" method as described above. The resulting particle size distributions are corrected for the slope-dependent over- and under-sizing, followed by a sampling efficiency correction of flow-induced undercounting of small particles (Spanu et al., 2020). Measurements of CAPS are at near ambient conditions; hence, the calculated particle size distributions represent

[3] STP: corrected to conditions at standard pressure (1013.25 hPa) and standard temperature (273.15 K)

[4] PbP recordings are limited to a certain number of particles. If the number concentration is larger than this limit a scaling factor is applied.

the aerosol at ambient relative humidity. The retrieval applies a numerical solution of the κ - Köhler theory to obtain the particle size distribution at dry relative humidity conditions (Brock et al., 2016).

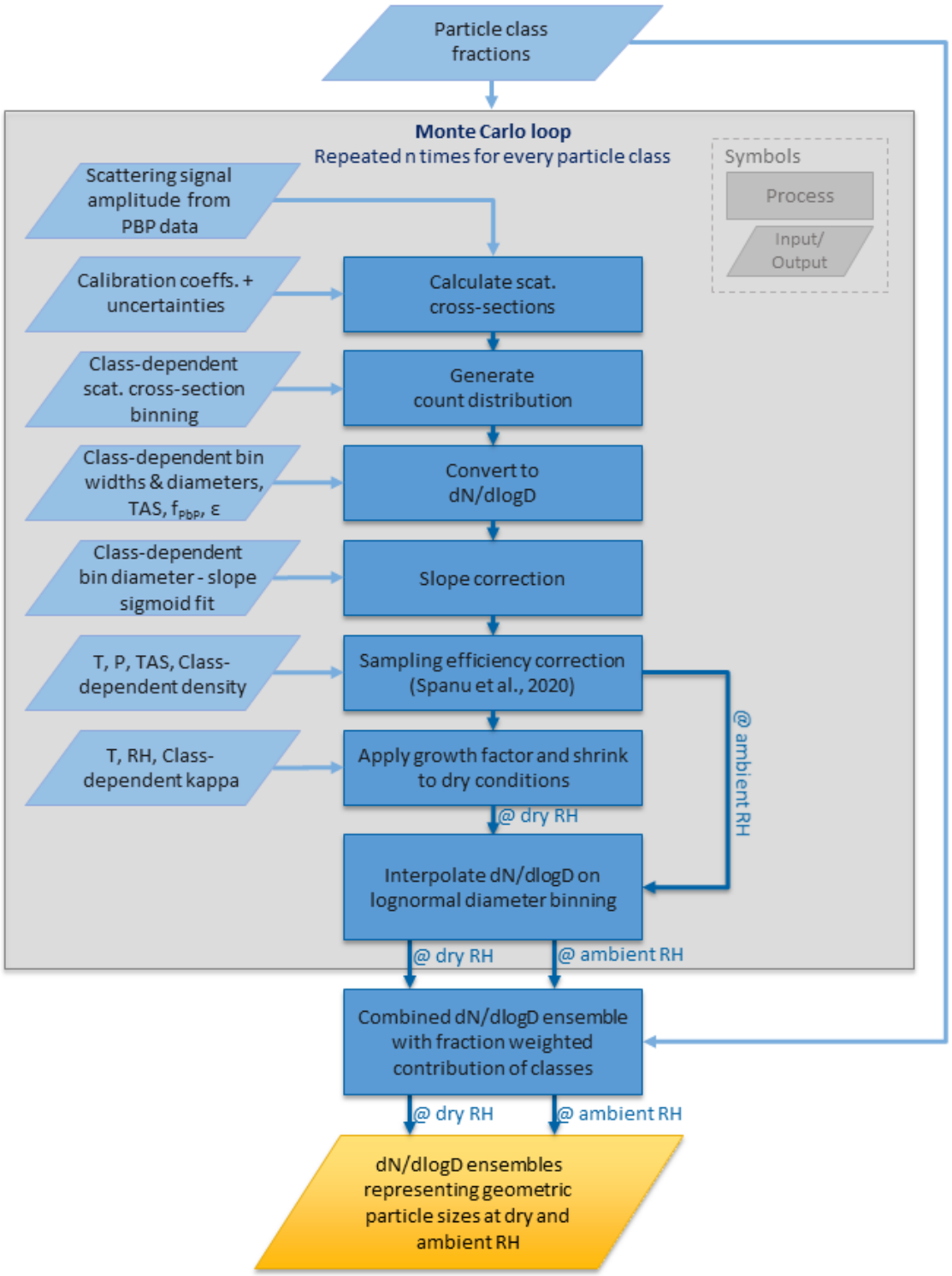

Figure II 4-2. Flowchart of the novel size distribution retrieval. Rectangles represent processes and rhomboids inputs and outputs of the retrieval, where the golden rhomboid indicates the final dN/dlogD output. The part inside the grey box is calculated for all particle classes separately and represents the Monte Carlo loop of the retrieval. ε represents a systematic uncertainty and f_{PbP} is the PbP-factor. For further details, see text.

The presented process is part of the Monte Carlo simulation and is repeated numerous times[5]. For each repetition, the following input values are randomly selected:

- Scattering signal amplitudes from the PbP data of the selected time period
- Calibration coefficients generated from the reported calibration uncertainties
- Bin center diameter (D_i) and bin width (w_i) from an ensemble for the corresponding particle class
- Systematic deviations (ε) of up to 20%, covering uncertainties of TAS, temperature, and pressure measurements

The output of the Monte Carlo simulation is an ensemble of size distributions for one particle class. Calculations for all classes, which have contributing particles in the airmass of the selected period, constitute a set of size distribution ensembles.

Since the binning of the different classes is unequal, an interpolation on a lognormal diameter grid is applied for the size distribution ensembles of all classes, followed by the combination of the size distribution ensembles of the different classes based on their proportional contribution to the observed air mass. The final outputs of the retrieval are two ensembles of size distributions reflecting instrumental uncertainties and covering the range of geometric sizes of the measured particle composition for dry and ambient relative humidity conditions. In summary, this approach enables a more reliable and precise measurement and quantification of atmospheric coarse-mode aerosol and cloud particles.

4.2.2.4. Novel machine learning method for hotwire calibration

The liquid water content sensor used in the CAPS instruments is a King probe hotwire sensor (King et al., 1978). Baumgardner et al. (2017) describe the measurement principle as the energy, in the form of electrical current, required to keep a cylindrical wire (called the hotwire) at a constant temperature. At the hotwire, energy is lost due to radiation, convection, and evaporation of droplets. The radiation component has only a minor contribution and is neglected for the calculations, which leaves convection and evaporation as the only two major energy sinks. After the subtraction of the convection term from the measured energy consumption, the remaining contribution results from the evaporation of liquid water at the hotwire. The remaining energy consumption due to evaporation can be used to calculate the LWC of the measured liquid droplets.

Generally, there are two ways to estimate the convection term: a) averaging the power consumption measured before and after a targeted cloud, or b) using the airspeed and air density at the location of measurement. The optimum parameterization method (OPM) presented in McFarquhar et al. (2017) provides a method to iteratively approximate parameters for calculating the convection term. For the OPM method, measurements outside of clouds, where only the convection determines the measured energy consumption, are used to optimize the parameters by reducing the error between calculated and measured convection. The Machine Learning (ML) method introduced in this study is partly comparable to the OPM method since it also utilizes the measured power outside of clouds. However, instead of iteratively optimizing parameters, we utilize a neural network to determine the convection component only using three input parameters: the temperature, pressure, and airspeed at the probe location[6]. Using the measured power outside of clouds, the neural network trains a model to predict the convection component based on these three input parameters. This trained model is then applied to predict the

[5] The number of Monte Carlo repetitions depends on computing power of the setup. A good range is between 200 and 1000 repetitions.

[6] Information on how to convert ambient temperature, pressure and true airspeed to values at the location of the instrument can be found in Spanu et al. (2020).

convective loss for measurements inside clouds. A subtraction of the predicted convective loss from the measured power leaves the evaporation due to the liquid droplets. According to King et al. (1978), measurements with a hotwire LWC sensor are attributed with a minimum threshold of 0.05 g m^{-3} and an uncertainty of ±0.05 g m^{-3}. Cober et al. (2001) reported an uncertainty of 15% and a baseline drift of up to 0.02 g m^{-3}. The application of the novel ML method to the A-LIFE measurement flight from this study provides an average baseline of 0.0028 ± 0.0093 g m^{-3}.
Even though Hotwire LWC sensors are constructed to only measure the water content of liquid droplets, they also respond to the ice crystals with a measurement of 10-20% of the ice mass (Cober et al., 2001; Field et al., 2004; Korolev et al., 2017, 1998b). It is important to take this ice crystal-induced signal into account when analyzing measurements in mixed-phase or ice clouds.

4.2.3. Chemical analysis of sample measurements

Aerosol chemical composition and single-particle characteristics were studied on samples collected inside the Falcon behind an inlet with an average cut-off diameter of 2.5 µm. Particles were collected on pre-treated transmission electron microscope (TEM) grids and analyzed by scanning electron microscopy coupled with energy-dispersive X-ray spectroscopy (SEM-EDX) for their morphology and chemical composition. For this study, the sample collected on 20 April 2017 at 15:55 (see Figure II 4-4) was prepared and quality checked, leaving 172 single particles in the size range of 100 nm to 2.5 µm for the analysis.

The normalized atomic concentrations of 18 elements and their element ratios were used to derive a set of rules and thereby classify each particle into various groups and classes. Due to measurement limitations, organic matter could not be investigated quantitatively using this method. The current classification schemes include 40 particle groups generally observed in various geographical environments which are then classified under seven major classes, including dust, sea salt, sulfates, nitrates, biomass-burning type, C-dominated, and mixtures. Particles that did not fit into these schemes were grouped under 'other' particles. The relative abundance of each class for a sample is calculated with respect to the total number of particles analyzed. The rule sets for major particle groups and classes can be found in Kandler et al. (2018, 2011, 2009, 2009) and the references therein. The class 'dust' is constituted by silicate-like particles, clay minerals (mainly illite, kaolinite, chlorite), feldspar-like (K, Na, and Ca types), carbonates, and Fe particles as oxides and hydroxides.

4.2.4. DLR Doppler wind lidar

The Doppler wind lidar (DWL), installed in the Falcon for the A-LIFE campaign, operates a coherent laser at a 2 µm wavelength and uses the Doppler shift of the reflected signal from aerosol and cloud particles to obtain information about atmospheric wind (Köpp et al., 2004). The DLR DWL can operate in two modes: conical scanning, which enables the calculation of the three-dimensional wind, and nadir-pointing mode, which offers precise information about the vertical wind but no information about the horizontal wind (Chouza et al., 2016; Smalikho, 2003). While measurement from the DLR DWL can be used to calculate calibrated aerosol backscatter (Chouza et al., 2015), the uncalibrated backscatter signal can be used as a surrogate for the location of aerosol layers and clouds. For this study, DLR DWL measurements of the vertical wind and uncalibrated backscatter are used.

4.3. Results

In this section, the methods introduced in section 4.2 are applied to the A-LIFE measurements from 20 April 2017 to assess the formation process for the ice crystals in the cloud-top of the dust-embedded clouds. Furthermore, small-scale CCN activation events, where mineral dust activation and growth led to a large number of small liquid droplets, will be studied.

Introduction of the case study

Particular weather patterns regularly transport mineral dust from African or Arabian deserts to the Mediterranean. The satellite image of Figure II 4-3 visualizes such a mineral dust transport event from the coast of Africa with a northeasterly flow direction on 20 April 2017. The image also shows clouds covering parts of Southern Europe and the Mediterranean Sea. The color-coded line shows the A-LIFE science flight from Heraklion, Crete, to Paphos, Cyprus. The flight extensively sampled a region of the simultaneous presence of a mineral dust layer and clouds embedded into this dust layer on 20 April 2017 south-east of Crete, highlighted with a red rectangle in Figure II 4-3.

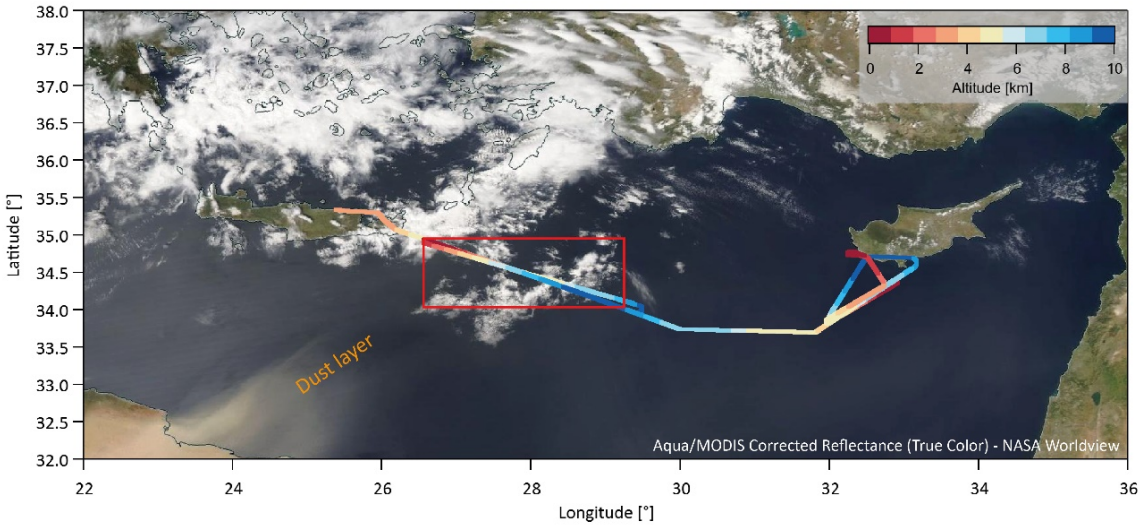

Figure II 4-3. This figure is taken from Dollner et al. (2022a, in prep.). It shows a true color-corrected reflectance satellite image (MODIS; Aqua) of the Mediterranean on 20 April 2017. The satellite image shows mineral dust transported from Africa moving in a northeasterly direction. Clouds predominantly cover the north-western part of the presented region. The altitude-colored line represents the Falcon flight track on 20 April 2017 from Heraklion, Crete, to Paphos, Cyrus. The red frame highlights the region where the mineral dust layer and clouds intersect and represents the region of interest for this study. (NASA Worldview, https://go.nasa.gov/3ljMWG9)

Figure II 4-4 depicts a timeseries of meteorological and cloud-relevant parameters from the red-marked region in Figure II 4-3: a) relative humidity with respect to water (dark blue line) and ice (light blue line); b) flight altitude (black line), ambient temperature (red line) and classification of the *Cloud Indicator* with the Aerosol-Cloud Transition Regime (ACTR) shown in yellow, liquid clouds in dark blue, Mixed-Phase Temperature Regime (MPTR) clouds in purple, and cirrus clouds in light blue; c) liquid water content (LWC) measured with the CAPS hotwire sensor (grey dotted line); d) timeseries of the CAPS size distribution with particle diameter on the y-axis and color-coded dN/dlogD concentrations.

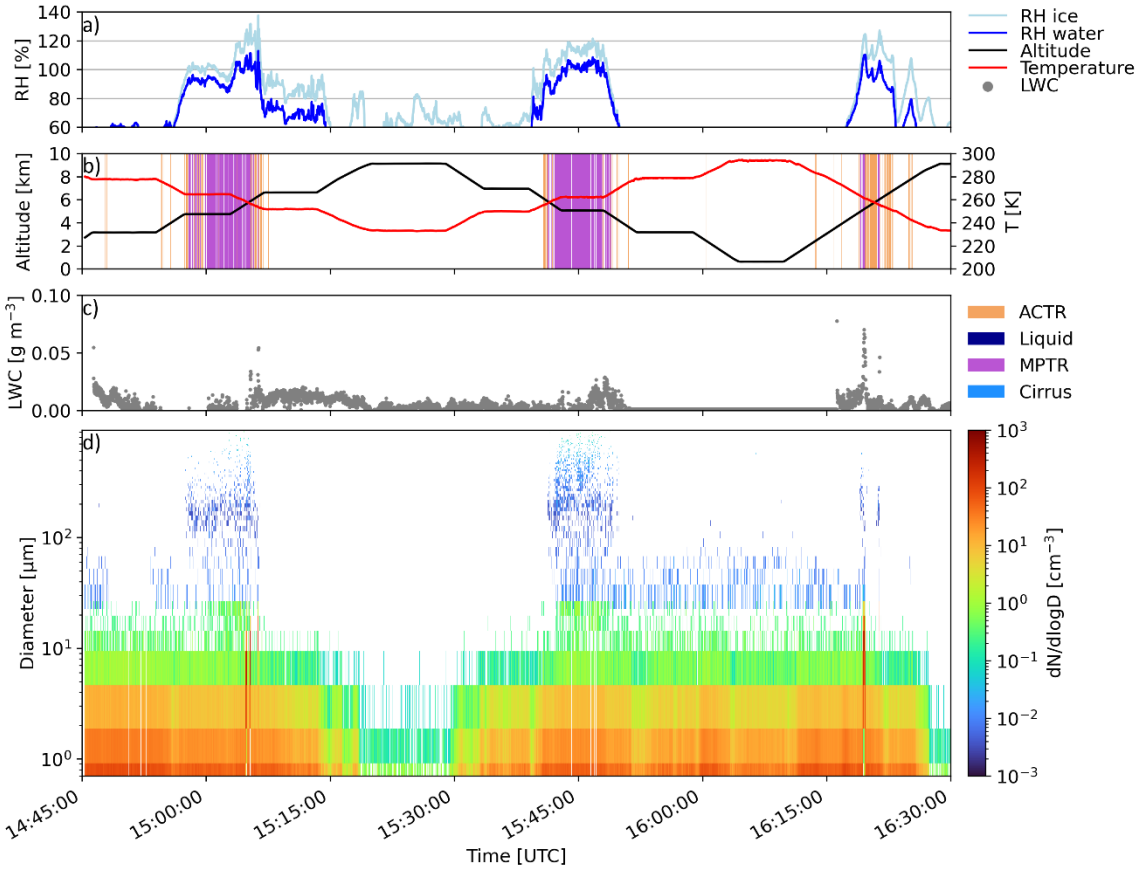

Figure II 4-4. Time series of a) relative humidity with respect to water and ice, b) altitude, temperature, and *Cloud Indicator* classification, c) liquid water content (LWC) measured with the CAPS hotwire sensor, and d) particle size distribution in the size range 0.8 to 25 µm (CAS data) and 25 to 930 µm (CIP data) for the region of interest (red box in Figure II 4-3) of the A-LIFE flight on 20 April 2017.

The measurement period shown in Figure II 4-4 characterized the presence of mineral dust with embedded clouds. According to the three vertical profile measurements presented in Figure II 4-4, the mineral dust layer extends from near the surface to approximately 8 km with a significant number of coarse-mode particles, including particle sizes exceeding 30 µm. Between 15:53:35 and 15:56:35 at an altitude of 3.2 km, particles were collected for single-particle chemical composition analysis. The composition, presented in Figure II 4-5, is dominated (89%) by mineral dust. The remaining particles consist of sea salt, sulfates, nitrates, and others. Approximately one-third of the mineral dust particles consist of silicates, one-third of chlorites, and the remaining particles are kaolinite, illite, feldspar, carbonate, or other oxides/hydroxides.

During the three vertical profiles between an altitude of 0.6 and 9.1 km, clouds embedded into the dust layer were sampled and classified by the *Cloud Indicator* as Mixed-Phase Temperature Regime (MPTR) clouds with sporadic periods of Aerosol-Cloud Transition Regime (ACTR) (see Figure II 4-4). All three cloud measurements are characterized by elevated relative humidity values, where relative humidity with respect to water (RH_w) and ice (RH_i) mostly exceed 90% and 100%, respectively.

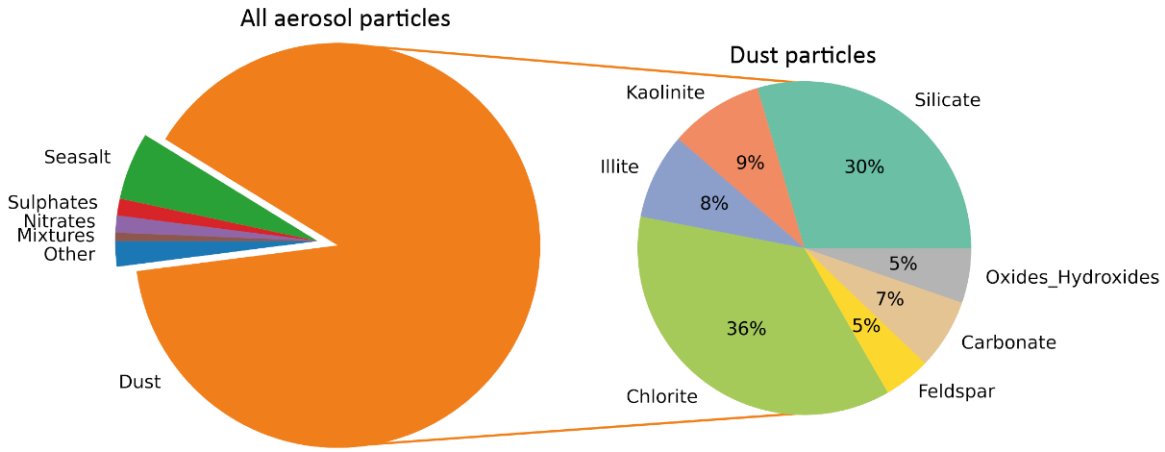

Figure II 4-5. Chemical composition of particles sampled in mineral dust layer between 15:53:35 and 15:56:35 during the flight 20 April 2017.

Investigation of ice crystals in the dust-embedded cloud

Figure II 4-6 presents the vertical profile of the cloud between 15:40 and 15:49 with panel a) showing the number concentration of particles larger than 30 µm ($N_{D>30\mu m}$) and panel b) displaying the ratio between $N_{D>30\mu m}$ and predicted INPs calculated with the parameterizations for general aerosol from DeMott et al. (2010) (D10, red dots) and the parameterization for dust aerosol from DeMott et al. (2015) (D15, orange dots). A ratio of 1, corresponding to a perfect agreement between predicted INP and measured ice crystal number concentration $N_{D>30\mu m}$, is highlighted with the vertical dashed line. Panel c) depicts RH_w (blue) and RH_i (light-blue), with the dashed vertical line representing a relative humidity of 100%.

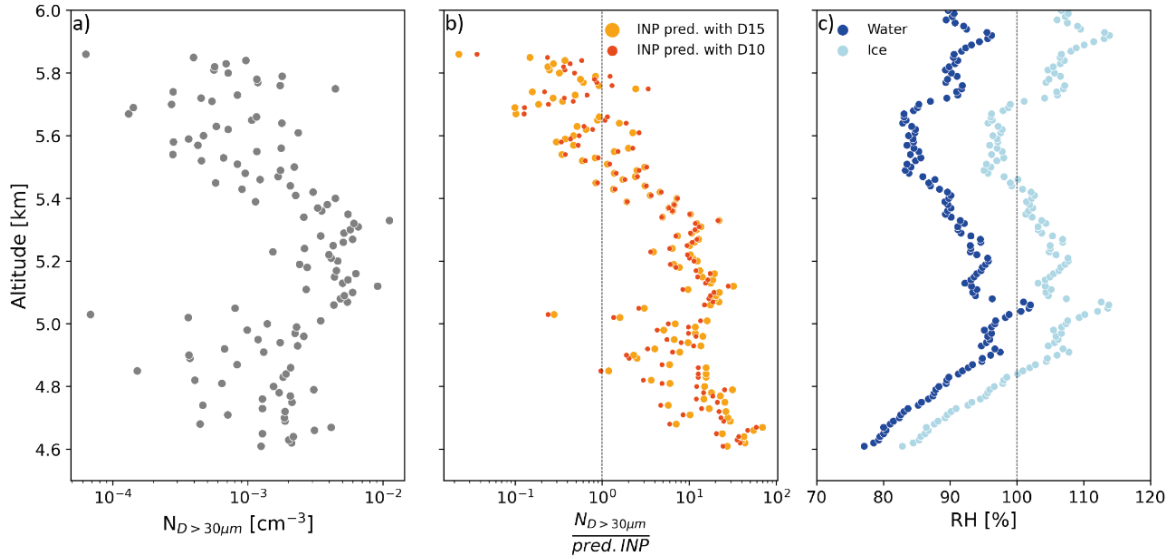

Figure II 4-6. Averaged vertical profile with 100 m resolution for measurements inside the cloud period between 15:40 and 15:50. Panels show: a) Number concentrations for particles larger than 30µm, b) ratio of number concentration of particles larger than 30µm and predicted INP using parametrization from DeMott et al. (2010) D10 and DeMott et al. (2015) D15, and c) relative humidity with respect to water and ice.

For the lower part of the cloud between 4.6 and 5.0 km, $N_{D>30\mu m}$ is on average 0.002 cm^{-3}, and ratios between $N_{D>30\mu m}$ and the predicted INP number concentrations are mostly above 10. Both

RH_w and RH_i are sub-saturated at 4.6km and increase with increasing altitude. At an altitude of approx. 4.8 km, RH_i reaches 100% and continues to increase up to 106%. Between approx. 5.0 and 5.3 km, the cloud is supersaturated with respect to ice, and the highest $N_{D > 30\mu m}$ of the cloud was observed (average: 0.004 cm^{-3}). From approx. 5.3 to 5.6 km, the airmass is sub-saturated with respect to water and ice, and $N_{D > 30\mu m}$ decreases from generally above 10^{-3} cm^{-3} to smaller values. With increasing altitude, $N_{D > 30\mu m}$ and the number concentration of predicted INP trend towards equality, as shown with a ratio around 1. Until the top of the cloud, $N_{D > 30\mu m}$ stays on average below 10^{-3}, whereas the ratio between $N_{D > 30\mu m}$ and predicted INP number concentration decreases to values below 1. Above about 5.7 km up to the cloud top, the cloud is again super saturated with respect to ice. Generally, in the upper half of the cloud, ratios calculated with the D10-INP parameterization exceed the ones with D15. In contrast, in the lower half of the cloud, this trend changes, where D15 ratios are larger than D10.

Figure II 4-7 gives insight into the cloud microphysical properties. Measurements inside the cloud are vertically split into seven vertical bins with a resolution of 0.2 km, starting from the cloud base at 4.6 km to the cloud top at 5.8 km. With increasing altitude, the cloud temperature decreases. Average temperatures for the vertical bins are indicated next to the altitude information. Each row of images shows examples of the ice crystals recorded within the corresponding altitude bin, and the histograms on the right side show the normalized probability distribution of area equivalent diameters of all recorded ice crystals for that bin. To avoid uncertainties at the lower detection limit of the CIP, only images of particles with an equivalent diameter larger than 30 µm are considered and out-of-focus images are rejected.

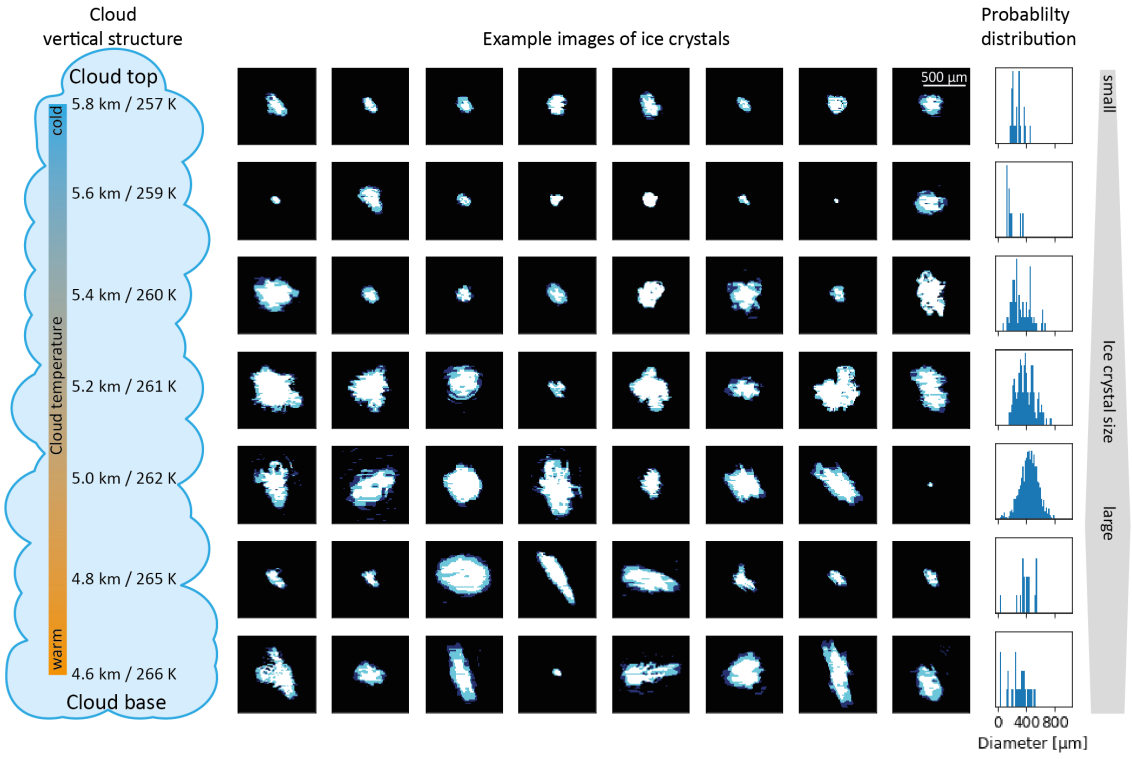

Figure II 4-7. Vertical structure of the cloud embedded in a dust layer sampled between 15:40 and 15:50. The sketch on the left side illustrates each altitude bin with a corresponding average temperature. Each row of images shows examples of ice crystals at the corresponding altitude bin. Normalized probability distributions present the area equivalent diameters of imaged particles within the corresponding altitude bin. Note: only images of ice crystals larger than 30 µm are considered and out-of-focus images are rejected.

Images and probability distributions of the ice crystals in the upper part of the cloud (5.6 and 5.8 km) are small compared to the particles located toward the middle part of the cloud (5.0 and 5.2 km). In the lowest section of the cloud (4.6 and 4.8 km), the sizes of the ice crystals decrease slightly compared to the altitude bins above.

Growth of small liquid cloud droplets

Figure II 4-8 is a magnified region of Figure II 4-4 and shows the measurements inside clouds for the periods between 15:04:40 and 15:05:30 and between 16:19:04 and 16:19:50. During these periods, significant changes in the particle number size distributions – particularly in the size range below approx. 40 to 50 µm are visible. The count median diameter (CMD) calculated for the CAS measurements (black-dotted line in panel d) demonstrates the change in the size distribution very clearly.

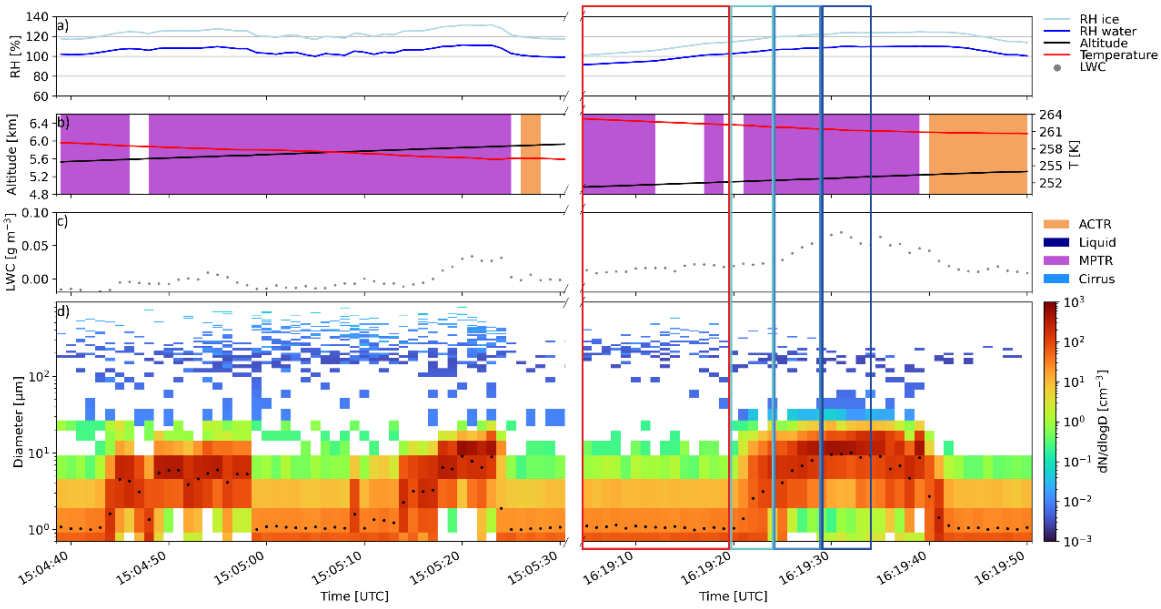

Figure II 4-8. Magnified region of Figure II 4-4 into two time periods: 15:04:40 – 15:05:30 and 16:19:04 – 16:19:50. The black dotted line in panel d) represents the count median diameter (CMD) for the size distribution measured with the CAS. Colored boxes represent different stages of the growth event between 16:19:04 – 16:19:50 used for the size distributions in Figure II 4-9.

Three activation events, with an increase of CMD from approx. 1 µm to values around 10 µm, are visible. During these periods, the particle number concentrations peak at approx. 10 µm with dN/dlogD between 10^2 and 10^3 cm^{-3}. Furthermore, significantly lower concentrations are observed in the size range around 1 µm compared to the size distributions during periods outside the events. All three events are accompanied by increasing relative humidity values, leading to supersaturation with respect to water and ice. Average temperatures during the three events are 258, 256, and 261 K.

To analyze particle growth in more detail, size distribution measurements from the CAS were processed with the size distribution retrieval presented in section 4.2.2.3. Figure II 4-9 illustrates the results of the calculations for the last activation case (16:19:04 - 16:19:50). The dotted lines represent the size distributions at different stages during the particle growth event, which are indicated with the colored boxes in Figure II 4-8. The dotted red line represents the size distribution measured preceding the growth event. The blue curves are from the different stages during the growth process, with the increasing darkness of blue indicating a more advanced growth. The continuous red line represents the size distribution of the same mineral dust layer measured outside of clouds between 14:46 and 14:53. The blue shaded area below the dark blue

curve in Figure II 4-9 visualizes the number concentration of last stage in the observed growth, which we define as the small cloud particle number concentration ($N_{cloud,\ small}$), i.e., 88.7 cm^{-3}. The red shaded area represents the integration of the mineral dust layer size distribution, starting from the largest to smaller sizes until the obtained number concentration equals the number concentration of grown particles. The left end of this area defines the maximum activation diameter ($D_{act,\ max}$), which is 0.29 µm for the presented case. The 50% activation diameter ($D_{act,\ 50}$) represents the case that only 50% of all particles in the dust layer start to grow (red shaded area with dots) and is smaller (0.17 µm) than $D_{act,\ max}$.

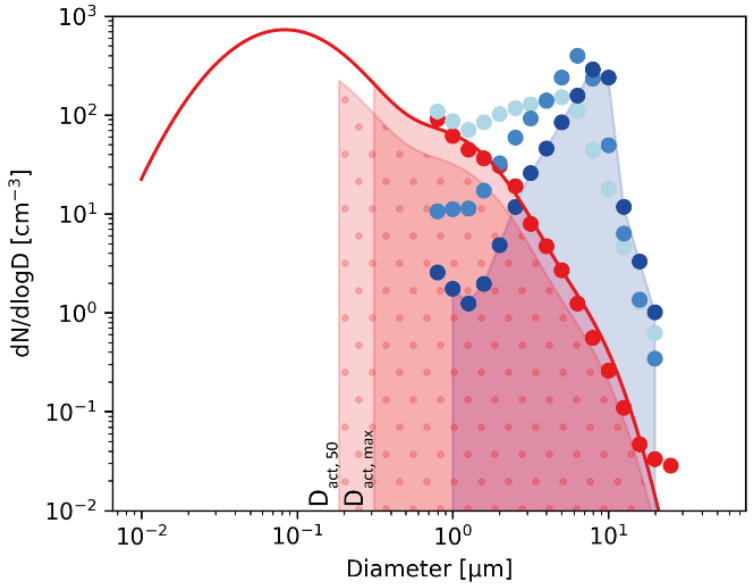

Figure II 4-9. Particle number size distribution for the growth event (16:19:04 – 16:19:50). The blue dots represent the size distributions at different stages during the particle growth (increasing darkness of blue indicating more advanced growth) and correspond to the same colored boxes in Figure II 4-8. The blue shaded area below the dark blue dotted curve represents the total number of small droplets which had been grown during the CCN activation event. The red line represents the complete size distribution of the mineral dust layer. Maximum activation diameter ($D_{act,\ max}$) and 50% activation diameter ($D_{act,\ 50}$) are indicated by the left ends of the red shaded area and red shaded area with dots, respectively.

The results from calculations for all three events are summarized in Table II 4-2. The average small cloud particle number concentration is 119.7cm^{-3}. Average values for $D_{act,\ 50}$ and $D_{act,\ max}$ are 0.14 and 0.23, respectively.

Table II 4-2. Number concentration of small cloud particles ($N_{cloud,\ small}$) and corresponding maximum activation diameter ($D_{act,\ max}$), 50% activation diameter ($D_{act,\ 50}$), and liquid water content (LWC) calculated from the size distribution for particles larger than 1 µm for all three events. The calculations are restricted to the measurements from the CAS instrument and values are calculated for STP conditions.

Event Time [UTC]	$N_{cloud,\ small}$ [cm^{-3}]	$D_{act,\ max}$ [µm]	$D_{act,\ 50}$ [µm]	LWC_{SD} [g m^{-3}]
15:04	121.2	0.22	0.13	0.01
15:05	149.2	0.19	0.11	0.02
16:19	88.7	0.29	0.17	0.03
Average	119.7	0.23	0.14	0.02

Measurements from the DWL can be used to retrieve information about the three-dimensional wind and the location of aerosol layers and clouds in the vertical column below the aircraft. For this study, Figure II 4-10 presents the uncalibrated backscatter (panel a) and the vertical wind

(panel b) for the first vertical profile (approx. 15:00 to 15:20) of the time series presented in Figure II 4-4.

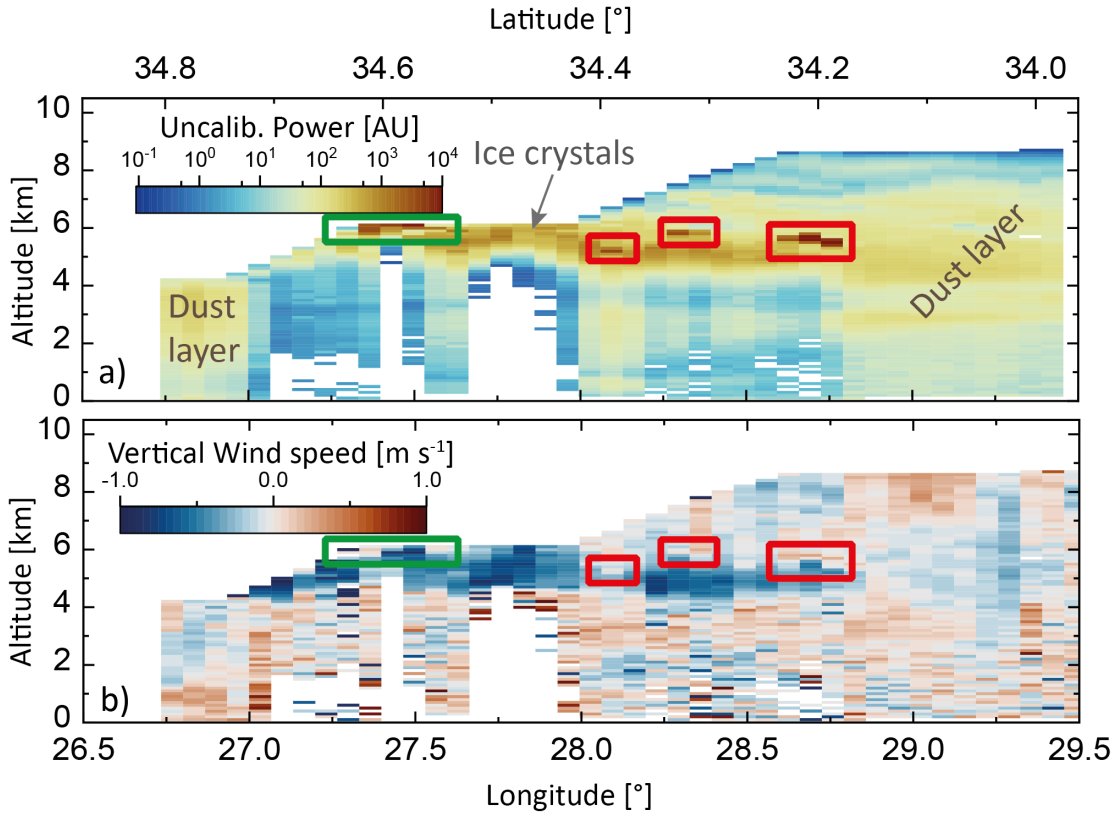

Figure II 4-10. a) Uncalibrated backscatter and b) vertical wind speed from the DLR Doppler wind lidar (DWL) measured during the vertical profile between approx. 15:00 and 15:20. Panel a) indicates the dust layer and clouds with ice crystals with grey labels. Green and red boxes in a) and b) represent locations of CCN activation events.

The uncalibrated backscatter in panel a) visualizes the mineral dust layer with elevated signals of measured power around 10^2 AU at latitudes between 26.75° and 27.0° and 28.75° and 29.5°. Between 28.75° and 29.5°, the mineral dust layer extends from near the surface to altitudes near 8km, with the most intense layer between 4 and 5km altitude. At latitudes between 27.25° and 28.75°, the uncalibrated backscatter signal shows a layer of elevated power with values around 10^3 AU between 5 and 6 km. This layer represents the clouds also visible in the in situ measurements shown in Figure II 4-4. The green and red boxes highlight locations of very high (10^4) backscatter signals, where the green box represents the region of in situ sampling of the growth events between 15:04:40 – 15:05:30 presented in Figure II 4-8. The location of the green and red boxes is also indicated in panel b), which represents the vertical wind velocity with blue and red represent descending and ascending motion, respectively.

4.4. Discussion

Two separate processes of aerosol-cloud interactions have been observed within the dust-embedded cloud on 20 April 2017. This chapter will examine the two processes separately and is structured as follows: In section 4.4.1, the hypothesis that heterogeneous ice nucleation of mineral dust particles is responsible for the cloud-top ice crystals is discussed and compared with results from laboratory experiments and commonly used parameterizations. Section 4.4.2 examines the activation of mineral dust particles to small liquid droplets and compares the findings from this study to a laboratory experiment.

4.4.1. Heterogeneous ice nucleation of mineral dust particles

In the previous section, ice crystals with sizes between approx. 30 and 930 µm were observed in a cloud embedded in a mineral dust layer. Figure II 4-6 and Figure II 4-7 revealed the cloud top as the location of the smallest ice crystals. Assuming that this is also the formation location of these cloud particles and no significant processes other than the growth of the ice crystals happened since the formation, we formulate the hypothesis that super micron mineral dust particles formed these ice crystals via heterogeneous ice nucleation.

The mineral dust layer, extending from near the surface into altitudes above the top of the investigated cloud, provides a significant reservoir of super micron mineral dust particles ($N_{dust,\ D>1\mu m,\ STP}$ = 17.52). At the top of the cloud (5.8 km), the RH_i conditions were supersaturated with an average of 105.9 % (±1.0 %). Based on results from laboratory studies from Kanji and Abbatt (2006), the observed RH_i is within the range of ice onset relative humidity of super micron Saharan dust (102 - 108 %) for deposition freezing. Hence, these findings suggest favorable conditions for the ice particle nucleation on the mineral dust, potentially due to deposition freezing. A common metric to compare the ice nucleation ability of different aerosols is the ice-active surface site density n_s. Following the description for polydisperse aerosol in Kanji et al. (2017) $n_s = N_{ice}/A_{total}$ where N_{ice} is the number of ice crystals in cm^{-3} and A_{total} is the surface area of the aerosol size distribution in $cm^2\ cm^{-3}$. The average number concentration of ice crystals larger than 30 µm are $N_{D>30\mu m}$ = 0.0010 ± 0.0005 cm^{-3} and $N_{D>30\mu m,\ STP}$ = 0.0019 ± 0.0009 cm^{-3} at STP conditions. Since the measurements of the ice crystals and the mineral dust layer were performed at different pressure and temperature conditions, the $N_{D>30\mu m,\ STP}$ is utilized for the N_{ice} term. For A_{total}, only the super micron aerosol of the investigated mineral dust layer is considered. A_{total} at STP conditions is $2.67 \times 10^{-6}\ cm^2\ cm^{-3}$ and results in an average n_s = 699 ± 348 cm^{-2}. This value is in good agreement with reported values for K-feldspar summarized in Kanji et al. (2017), which also agrees with the contribution of feldspar to the chemical composition of the sampled mineral dust layer (see Figure II 4-5). Niemand et al. (2012) and Atkinson et al. (2013) provide temperature-dependent parameterizations of n_s for mineral dust based on the results from laboratory measurements. The applications of the two parameterizations in the cloud top region results in $n_{s,\ Niemand}$ = 2899 ± 392 cm^{-2} and $n_{s,\ Atkinson}$ = 4014 ± 1081 cm^{-2}. Both parametrizations are in good agreement with n_s calculated from the measured ice crystal concentration, especially when considering that the entire range of possible n_s values spans over 12 magnitudes. The comparison of predicted INP concentrations from two commonly used parameterizations for general aerosol (D10) and dust aerosol (D15) with the observed $N_{D>30\mu m}$ was shown in panel b) of Figure II 4-6. In the cloud top region at 5.8 km, the average predicted INPs and $N_{D\ >\ 30\mu m}$ agree by a factor of 0.67 and 0.43 for D10 and D15, respectively, which is an adequate consistency.

Comparisons of the ice-active surface site density n_s and commonly used INP parametrizations D10 and D15 with the observed ice crystal concentration $N_{D>30\mu m}$, show good agreement. However, for all comparisons, $N_{D>30\mu m}$ slightly underestimates the parameterizations. The sedimentation of ice crystals may have an effect, since ice crystals with a diameter of 100 µm are approximated to fall with 0.1 m s^{-1} with increased velocity for larger ice crystals (Gasparini et al., 2017; Spichtinger and Gierens, 2009). Figure II 4-10 provides evidence for the sedimentation of the ice crystals. Panel a) shows the cloud layer with ice crystals in a light red color with an uncalibrated power of approx. 10^3 AU and a grey label “Ice crystals”. The corresponding area in panel b) shows negative vertical velocity in blue, which indicates a falling motion of the particles. Consequently, between the formation of the ice crystals and the measurements of $N_{D<30\mu m}$, some ice crystals have already fallen into lower altitude layers and, therefore, $N_{D<30\mu m}$ does not completely reflect all ice crystals nucleated from the mineral dust particles. Nevertheless, the comparison of the ice crystal measurements at the cloud top with parameterizations and laboratory results of ice onset relative

humidity and INP strengthens the hypothesis that super micron mineral dust particles are INPs, which nucleated potentially via deposition mode freezing to the observed ice crystals.

4.4.2. Mineral dust as CCN

Sudden growth events of a large number of aerosol particles to sizes in the range around 10 µm were observed in the time periods between 15:04:40 and 15:05:30 and between 16:19:04 and 16:19:50 (see Figure II 4-8). The analysis of these events is depicted in Figure II 4-9 and revealed an average number concentration of newly formed droplets of 119.7 cm^{-3} (Table II 4-2). The presence of droplets is indicated with measurements of the CAPS hotwire LWC-sensor, showing an increased LWC during the three events (see Figure II 4-8 panel c). The first event at 15:04 shows only a minor increase to a maximum LWC of 0.009 g m^{-3}. For the second (15:05) and third (16:19) events, a more significant increase with a maximum LWC_{hot} of 0.034 g m^{-3} and 0.070 g m^{-3}, respectively, were measured. A comparison with the LWC_{SD} values calculated from the CAS size distributions for all particles larger than 1µm (Table II 4-2) reveals larger values for the hotwire measurements. However, because the hotwire sensor also measures about 10-20% of the ice crystal mass, the agreement of LWC_{hot} and LWC_{SD} confirms that the particles at 10 µm are small droplets. The three events show that the aerosol particles in the mineral dust layer act as cloud condensation nuclei forming the small droplets. The integration of the mineral dust layer size distribution starting from the largest to smaller sizes obtained an average activation diameter between $D_{act,\ 50}$ = 0.14 µm and $D_{act,\ max}$ = 0.23 µm. This range of potential activation diameters is in excellent agreement with laboratory studies, which found the activation of Saharan mineral dust particles larger than approx. 0.2 µm already at low (0.2-0.3%) supersaturation (Herich et al., 2009; Koehler et al., 2009). A rough approximation of the RH_w values for the start of the observed CCN activation can be seen in Figure II 4-11, which depicts the count median diameter (CMD) as a function of the RH_w for the three CCN activation events at 15:04 (blue), 15:05 (orange) and 16:19 (green). CMD values start to increase at RH_w between 102 and 104% and continue to increase to approx. 10 µm with increasing RH_w. These RH_w values, corresponding to supersaturation between 2 and 4%, are higher than the results from the laboratory studies. However, it is likely that mineral dust particles sporadically activate at lower supersaturations but the temporal and instrumental resolution of the airborne instrumentation of this study does not allow such a precise investigation. The largest RH_w values of the three events are at 111% (see Figure II 4-11). Such high supersaturations can occur when saturated airmasses are lifted since adiabatic cooling decreases the saturation pressure with respect to water and, hence, increases the relative humidity (Wallace and Hobbs, 2006). The observed high-supersaturation values during the CCN activation events lead to the second hypothesis of this study, namely, that sudden small-scale vertical lifting events initiated the observed CCN activation.

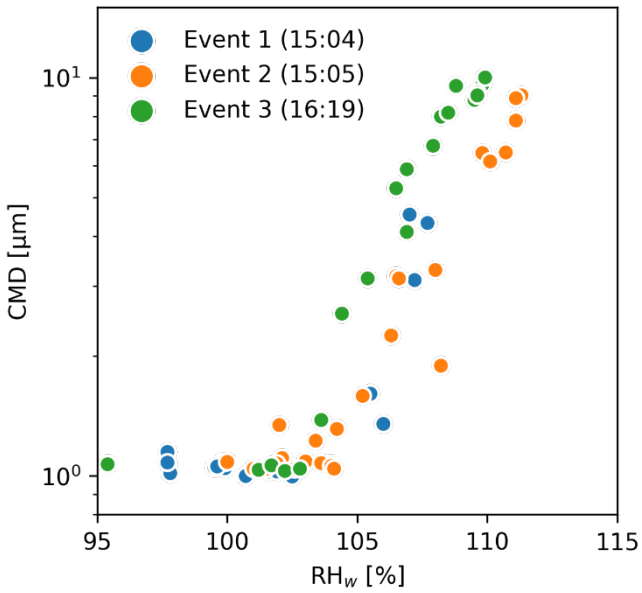

Figure II 4-11. Count median diameter (CMD) as a function of RH_w for the three CCN activation events at 15:04 (blue), 15:05 (orange) and 16:19 (green) presented in Figure II 4-9.

Measurements from DWL can be utilized to investigate the vertical motion of the airmasses. Panel a) of Figure II 4-10 indicates the region of the first (15:04) and second (15:05) CCN activation event with a green box where the uncalibrated power shows an intense signal. More of such intense signal events in the DWL measurements are visible within the dust-embedded clouds – highlighted in red boxes. Like the observed CCN activation events, these events occur at comparable altitudes inside the mineral dust layer. Hence, we conclude that they are also events of CCN activation. All of these potential CCN activation events are connected to vertical lifting, which can be seen by the positive vertical wind speed in the green and red boxes in panel b).

Bringing together the findings from the DWL measurements and the three analyzed CCN activation events, there is evidence to support the hypothesis that small-scale adiabatic lifting events are responsible for the CCN activation of mineral dust particles into supercooled liquid droplets with a mode diameter of approximately 10 µm. The lower limit of activation diameter is approximated to be between 0.14 and 0.23 µm, which is in very good agreement with laboratory experiments. Some of these newly formed liquid droplets may also turn into ice crystals if freezing is initiated through, e.g., immersion or contact freezing.

4.5. Summary

During the A-LIFE field campaign, unique measurements were conducted of clouds embedded in an intense African mineral dust plume in the Mediterranean on 20 April 2017. In situ measurements of meteorological parameters and liquid water content (LWC), aerosol and cloud particle size distributions, and airborne Doppler wind lidar (DWL) observations were utilized to investigate these clouds concerning the CCN and INP properties of mineral dust. The aerosol and cloud particle size distributions were obtained from the CAS optical spectrometer of the Cloud, Aerosol, and Precipitation Spectrometer (CAPS) and processed with a novel size distribution retrieval introduced in this study. Considering instrumental uncertainties, this algorithm reports particle sizes in geometric diameters taking non-sphericity and refractive indices of the measured aerosol into account. Furthermore, LWC measurements from the hotwire sensor of CAPS were calibrated with a new method utilizing a machine-learning-based method presented in this manuscript. These new algorithms provided the tools for the detailed analysis of the dust-embedded clouds, which revealed two separate aerosol-cloud interactions processes occurring in the dust-embedded clouds:

- Ice nucleating particle (INP) closure reveals mineral dust particles serving as nuclei for the ice crystals observed in the dust-embedded cloud, most likely via deposition mode freezing.
- Mineral dust particles activated and grew to small liquid droplets during CCN activation events, initiated by water supersaturated environments due to vertical lifting events.

For the INP closure, cloud-top ice crystal number concentrations and the particle size distribution of the mineral dust layer were used to role of the mineral dust in the ice crystal formation of the observed dust-embedded cloud. The ice crystal number concentration was considered as a surrogate for the INP concentration during the nucleation of the ice crystals. Comparisons of cloud top relative humidity with ice onset relative humidity measurements from laboratory experiments revealed an overlapping agreement and confirmed deposition mode freezing as the potential nucleation mechanism. Commonly used INP parameterizations were applied to the size distribution of the mineral dust layer and exhibited a slight overestimation when compared to the cloud top ice crystal concentration. However, sedimentation effects removing larger ice crystals into lower levels of the cloud may explain this overestimation.

For the second aerosol-cloud interaction process, size distributions and LWC observations of three CCN activation events were analyzed confirming the CCN activation and growth of mineral dust into liquid droplets with a modal diameter of approx. 10 µm. The calculated activation

diameter of the mineral dust particles (i.e., the smallest particle diameter that can act as a nucleus for the growth of a liquid droplet) was between 0.13 and 0.23 µm, providing excellent agreement with laboratory studies. Observations with the Doppler wind lidar (DWL) revealed small-scale vertical lifting as the reason for the significantly high water vapor supersaturation, providing the conditions for CCN activation of the mineral dust particles. The potential freezing of some of the small droplets may have also contributed to the observed ice crystals.

Chapter 3

III. Summary and Conclusion

An incomplete understanding of atmospheric aerosol-cloud interaction processes is one of the most significant contributors to the uncertainties of predictions of the Earth's changing climate - one of the greatest challenges for humanity in this century. The investigation of aerosol-cloud interactions belongs to the list of high-priority research topics in atmospheric sciences. Significant efforts have been made to close the gaps of understanding aerosol impacts on clouds using model simulations, laboratory investigations, and ground-based and airborne observations.

This cumulative dissertation focused on assessing the global distribution of coarse-mode aerosol and clouds with large-scale in situ aircraft observations, including laboratory experiments, theoretical simulations, and significant algorithm developments. The methodological developments and scientific analyses were based on the observations from three international airborne field observations: Atmospheric Tomography (ATom; 2016-2018), Absorbing aerosol layers in a changing climate: aging, lifetime, and dynamics (A-LIFE; 2017), and Fire Influence on Regional to Global Environments Experiment - Air Quality (FIREX-AQ; 2019)

Results from this cumulative dissertation were presented based on four publications, and contributed to additional 17 publications (see pages 5-9). In the following, the main achievements of this dissertation and the corresponding publications are summarized:

a. *Next-generation measurements of coarse-mode aerosol and cloud particles (Paper I, II, IV)*: Novel characterizations and techniques set the foundation for more reliable and precise measurements and quantifications of atmospheric coarse-mode aerosol and cloud particles.

b. *A novel algorithm for automatic detection and classification of clouds (Paper II)*: The newly developed algorithm for automatic detection and classification of periods inside clouds opens the door to greatly expanded analysis of the scientific drivers of cloud processes like aerosol-cloud interactions.

c. *Significance of coarse-mode aerosol (Paper III)*: Global-scale airborne in situ measurements were processed with the novel size distribution retrieval and revealed the importance of coarse-mode aerosol. Furthermore, the analysis demonstrated the significant atmospheric abundance of coarse-mode aerosol over large regions of the globe reaching deep into the free troposphere.

d. *The formation of dust-impacted clouds (Paper IV)*: Detailed investigations of measurements of clouds embedded in a dense mineral dust layer revealed mineral dust as the source for heterogeneous ice nucleation and, thereby, confirmed laboratory measurements and ice nucleating particle (INP) parameterizations. Additional precise analysis of a unique CCN activation event within these clouds shows to be initiated by vertical lifting events.

Figure III 1 schematically summarizes this dissertation, where items and text in blue indicate the achievements emerging from this dissertation. The yellow sketch visualizes the second-generation Cloud, Aerosol, and Precipitation Spectrometer (CAPS), which is the central instrument of this dissertation.

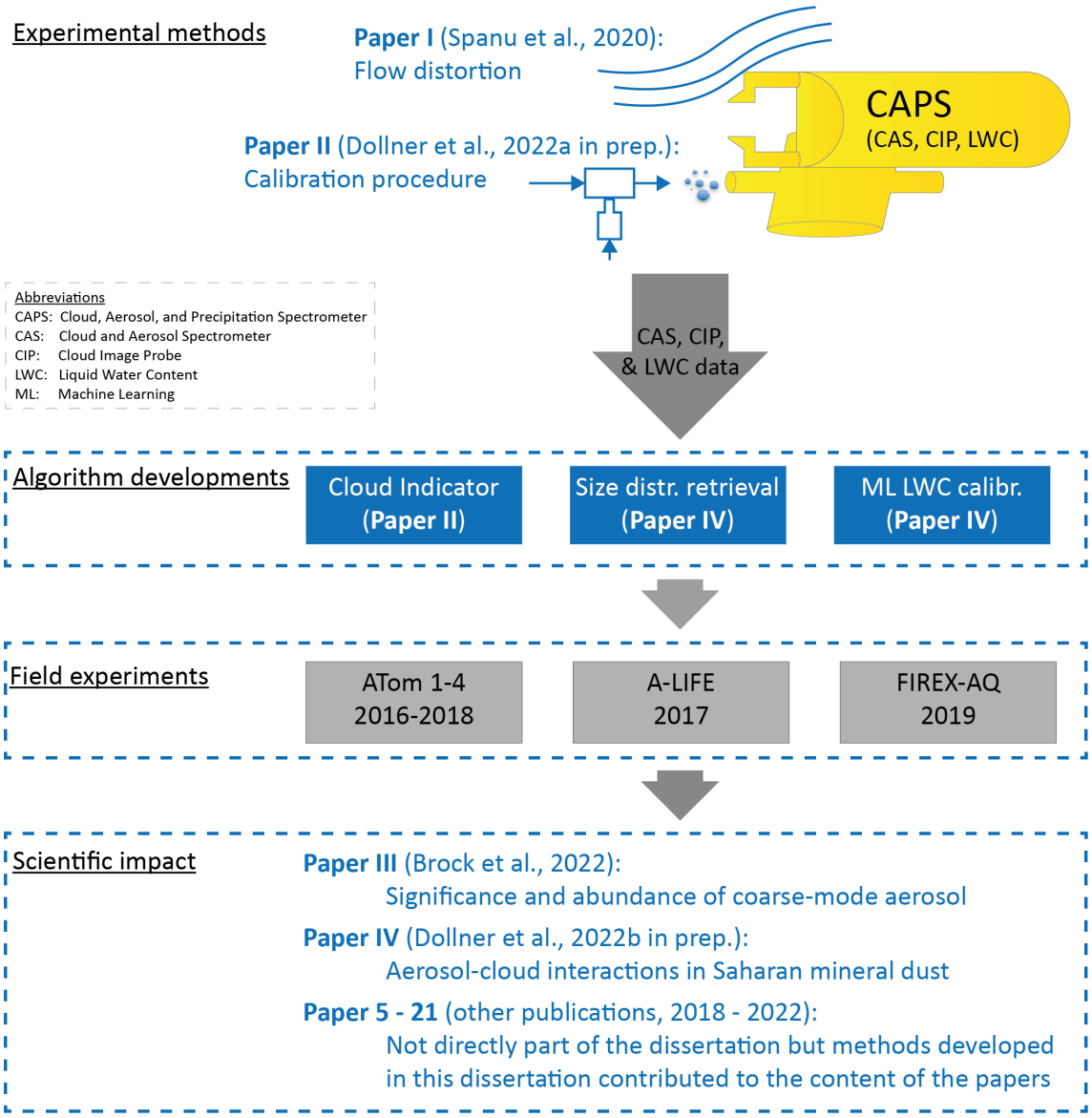

Figure III 1. Schematic summarizing the dissertation. Items and text in blue represent the achievements of this dissertation.

Ad (a): The second-generation Cloud, Aerosol, and Precipitation Spectrometer (CAPS) is the central instrument of this dissertation. CAPS is a wing-mounted optical spectrometer and optical array probe measuring aerosol and cloud particles in the nominal size range between 0.5 and 930 µm. Spanu et al. (2020) is the first paper (Paper I) contributing to the results of this dissertation and revealed the effects of mounting location-dependent flow distortions on airborne in situ measurements of aerosols and clouds. The study provided particle size-dependent correction schemes for these flow distortions, which have been successfully tested and applied to the measurements of CAPS. Paper II (Dollner et al., 2022a, in prep.) introduced a novel calibration process, including an updated calibration setup. The setup enables the calibration of the entire size range of the optical spectrometer CAS of CAPS (nominally 0.5 – 50 µm) not only in the lab but also in the field. The calibration process involves a new procedure for the calibration analysis, which reports a refractive index-independent calibration output with uncertainties. This calibration output sets the foundation for the newly developed size distribution retrieval presented in Paper IV (Dollner et al., 2022b, in prep.). The size distribution retrieval applies Monte

Carlo simulations and provides particle sizes in geometric diameters taking non-sphericity and refractive indices of the measured aerosol and instrumental uncertainties into account. Furthermore, a new method was introduced in Paper IV, which utilizes a machine learning (ML) approach for calibrating the LWC measurements from the hotwire sensor of CAPS. The approach is a further development of the existing optimum parameterization method (OPM), which is used to derive the baseline of a hotwire LWC sensor.

Ad (b): The main focus of Paper II represents the second major achievement of this dissertation: The *Cloud Indicator* algorithm. The algorithm automatically detects and classifies clouds and cloud phase in (airborne) in-situ observations. In-cloud sequences are further separated into liquid clouds, clouds in the Mixed-Phase Temperature Regime (MPTR), cirrus clouds, or Aerosol-Cloud Transition Regime (ACTR). The algorithm's criteria are based on particle number concentrations in three size ranges, relative humidity over water and ice, and temperature. A cloud-aerosol volume factor f_{CA} introduced in this dissertation allows the precise and robust distinction between clouds and aerosol layers with enhanced concentrations of coarse-mode particles (e.g., mineral dust, sea salt, or biomass burning layers) thereby reducing the number of misclassifications. The *Cloud Indicator* was presented with detailed analysis of two case studies during ATom and A-LIFE. The algorithm was validated with independent measurements showing a good performance for ACTR, liquid, MPTR and cirrus clouds during the ATom flight above the northern Atlantic. For the A-LIFE case, which was characterized by a complex mixture of clouds embedded into a mineral dust layer, the *Cloud Indicator* proved its capability to distinguish mineral dust layers from clouds.

Ad (c): The third major achievement of this dissertation demonstrates the significance and atmospheric abundance of coarse-mode aerosol. This result was accomplished by applying the methodological developments from (a) and (b) to the CAPS measurements conducted during ATom and A-LIFE. High-quality CAPS size distributions processed with the new size distribution retrieval were combined with aircraft in-cabin measurements yielding unique combined composition-resolved size distributions covering the entire aerosol size range from the nucleation mode to the coarse-mode (0.003 - 50 µm). Paper III (Brock et al., 2021) presents the one-of-a-kind global-scale data set of extensive and intensive aerosol properties calculated from the ATom combined size distributions. The calculations demonstrated the importance of precise coarse-mode aerosol measurements for a correct representation of atmospheric aerosol properties. A hemispheric comparison of the abundance of coarse-mode aerosol from continental origins in the lower and free troposphere revealed a substantially higher amount in the northern compared to the southern hemisphere. Furthermore, Paper III showed that the Aerosol Optical Depth (AOD) from dust and biomass burning aerosol is relevant above the Atlantic downwind of the major source in Africa and contributes significantly to the free troposphere above the Northern Pacific.

Ad (d): The fourth and last major achievement is presented in Paper IV (Dollner et al., 2022b, in prep.), which investigated a cloud embedded in a dense mineral dust layer. The application of the algorithms and techniques developed in (a) and (b) (i.e., the *Cloud Indicator*, the size distribution retrieval, and the machine learning-based LWC calibration method) enabled a detailed analysis of the interactions between the mineral dust layer and the embedded clouds. A closure between the mineral dust size distribution and the ice crystal number concentration at the top of the embedded cloud identified the mineral dust particles as the source of the heterogeneous ice nucleation. Furthermore, the closure analysis confirmed commonly used INP parameterizations and agreed with results from laboratory measurements. The observations of the mineral dust embedded clouds captured several unique CCN activation events, where mineral dust particles activated and grew to small liquid droplets. Detailed analysis of these growth events exhibited a particle activation diameter between 0.13 and 0.23 µm which was in excellent agreement with laboratory studies of the CCN ability of mineral dust at supersaturations between 0.2 and 0.3%. Combined with concurrent vertical motion measurements of a Doppler Wind Lidar (DWL), these

findings revealed vertical lifting events as the initiator for a super saturated environment leading to the sudden CCN activation. In summary, the observations of the clouds embedded in the mineral dust layer showed two interactions of the mineral dust and the embedded clouds: heterogenous ice nucleation responsible for the formation of ice crystals and small-scale CCN activation events leading to many small liquid droplets.

In summary, the results of this dissertation improved the capabilities of airborne in situ measurements, offering more reliable and precise observations and quantifications of atmospheric coarse-mode aerosol and cloud particles. The algorithms developed in the framework of this thesis are not limited to the presented applications, but can also be used for analysis of data from past and upcoming field experiments. The novel *Cloud Indicator* algorithm provides robust and automatic detections and classifications of cloud, which establishes the foundation for extended investigations of cloud processes like aerosol-cloud interactions. These newly developed algorithms and techniques enabled the analysis of global-scale airborne in situ aerosol observations and revealed the importance and extensive atmospheric abundance of coarse-mode aerosol. Furthermore, investigations of clouds embedded in a dense mineral dust layer demonstrated two processes of aerosol-cloud interactions: heterogeneous ice nucleation leading to ice crystals and small-scale vertical lifting induced CCN activation and growth of small liquid droplets. The unique observation of these two processes in the atmosphere confirm findings from laboratory experiments.

The unique airborne in situ observations from the ATom, A-LIFE and FIREX-AQ field campaigns provide valuable data sets of aerosol and cloud observations indispensable to improving the understanding of processes like aerosol-cloud interactions. However, continuing airborne in situ observations and technological enhancements of measurement and data analysis techniques are essential in order to push the observational limits and close knowledge gaps in atmospheric processes like aerosol-cloud interactions.

IV. References

Adebiyi, A.A., Kok, J.F., 2020. Climate models miss most of the coarse dust in the atmosphere. Sci. Adv. 6, eaaz9507. https://doi.org/10.1126/sciadv.aaz9507

Afchine, A., Rolf, C., Costa, A., Spelten, N., Riese, M., Buchholz, B., Ebert, V., Heller, R., Kaufmann, S., Minikin, A., Voigt, C., Zöger, M., Smith, J., Lawson, P., Lykov, A., Khaykin, S., Krämer, M., 2018. Ice particle sampling from aircraft – influence of the probing position on the ice water content. Atmospheric Measurement Techniques 11, 4015–4031. https://doi.org/10.5194/amt-11-4015-2018

Ahn, E., Huang, Y., Chubb, T.H., Baumgardner, D., Isaac, P., de Hoog, M., Siems, S.T., Manton, M.J., 2017. In situ observations of wintertime low-altitude clouds over the Southern Ocean. Quarterly Journal of the Royal Meteorological Society 143, 1381–1394. https://doi.org/10.1002/qj.3011

Atkinson, J.D., Murray, B.J., Woodhouse, M.T., Whale, T.F., Baustian, K.J., Carslaw, K.S., Dobbie, S., O'Sullivan, D., Malkin, T.L., 2013. The importance of feldspar for ice nucleation by mineral dust in mixed-phase clouds. Nature 498, 355–358. https://doi.org/10.1038/nature12278

Balkanski, Y., Schulz, M., Claquin, T., Guibert, S., 2007. Reevaluation of Mineral aerosol radiative forcings suggests a better agreement with satellite and AERONET data. Atmos. Chem. Phys. 7, 81–95. https://doi.org/10.5194/acp-7-81-2007

Barker, H.W., Cole, J.N.S., Li, J., von Salzen, K., 2016. A parametrization of 3-D subgrid-scale clouds for conventional GCMs: Assessment using A-Train satellite data and solar radiative transfer characteristics. Journal of Advances in Modeling Earth Systems 8, 566–597. https://doi.org/10.1002/2015MS000601

Barker, H.W., Stephens, G.L., Partain, P.T., Bergman, J.W., Bonnel, B., Campana, K., Clothiaux, E.E., Clough, S., Cusack, S., Delamere, J., Edwards, J., Evans, K.F., Fouquart, Y., Freidenreich, S., Galin, V., Hou, Y., Kato, S., Li, J., Mlawer, E., Morcrette, J.J., O'Hirok, W., Räisänen, P., Ramaswamy, V., Ritter, B., Rozanov, E., Schlesinger, M., Shibata, K., Sporyshev, P., Sun, Z., Wendisch, M., Wood, N., Yang, F., 2003. Assessing 1D Atmospheric Solar Radiative Transfer Models: Interpretation and Handling of Unresolved Clouds. Journal of Climate 16, 2676–2699. https://doi.org/10.1175/1520-0442(2003)016<2676:ADASRT>2.0.CO;2

Baumgardner, D., Abel, S.J., Axisa, D., Cotton, R., Crosier, J., Field, P., Gurganus, C., Heymsfield, A., Korolev, A., Krämer, M., Lawson, P., McFarquhar, G., Ulanowski, Z., Um, J., 2017. Cloud Ice Properties: In Situ Measurement Challenges. Meteorological Monographs 58, 9.1-9.23. https://doi.org/10.1175/amsmonographs-d-16-0011.1

Baumgardner, D., Jonsson, H., Dawson, W., O'Connor, D., Newton, R., 2001. The cloud, aerosol and precipitation spectrometer: a new instrument for cloud investigations. Atmospheric Research, 13th International Conference on Clouds and Precipitation 59–60, 251–264. https://doi.org/10.1016/S0169-8095(01)00119-3

Baumgardner, D., Korolev, A., 1997. Airspeed Corrections for Optical Array Probe Sample Volumes. Journal of Atmospheric and Oceanic Technology 14, 1224–1229. https://doi.org/10.1175/1520-0426(1997)014<1224:acfoap>2.0.co;2

Bond, T.C., Bergstrom, R.W., 2006. Light Absorption by Carbonaceous Particles: An Investigative Review. Aerosol Science and Technology 40, 27–67. https://doi.org/10.1080/02786820500421521

Boucher, O. (Ed.), 2013. Clouds and Aerosols, in: Climate Change 2013 the Physical Science 1 Basis: Working Group I Contribution to the Fifth Assessment Report of the Intergovernmental Panel on Climate Change [Stocker, T.F., D. Qin, G.-K. Plattner, M. Tignor, S.K. Allen, J. Boschung, A. Nauels, Y. Xia, V. Bex, and P.M. Midgley (Eds.)]. Cambridge University Press, Cambridge, pp. 571–658. https://doi.org/10.1017/CBO9781107415324.016

Boutle, I.A., Abel, S.J., Hill, P.G., Morcrette, C.J., 2014. Spatial variability of liquid cloud and rain: observations and microphysical effects: Cloud and Rain Variability. Q.J.R. Meteorol. Soc. 140, 583–594. https://doi.org/10.1002/qj.2140

Brock, C.A., Froyd, K.D., Dollner, M., Williamson, C.J., Schill, G., Murphy, D.M., Wagner, N.J., Kupc, A., Jimenez, J.L., Campuzano-Jost, P., Nault, B.A., Schroder, J.C., Day, D.A., Price, D.J., Weinzierl, B., Schwarz, J.P., Katich, J.M., Wang, S., Zeng, L., Weber, R., Dibb, J., Scheuer, E., Diskin, G.S., DiGangi, J.P., Bui, T., Dean-Day, J.M., Thompson, C.R., Peischl, J., Ryerson, T.B., Bourgeois, I., Daube, B.C., Commane, R., Wofsy, S.C., 2021. Ambient aerosol properties in the remote atmosphere from global-scale in situ measurements. Atmos. Chem. Phys. 21, 15023–15063. https://doi.org/10.5194/acp-21-15023-2021

Brock, C.A., Wagner, N.L., Anderson, B.E., Attwood, A.R., Beyersdorf, A., Campuzano-Jost, P., Carlton, A.G., Day, D.A., Diskin, G.S., Gordon, T.D., Jimenez, J.L., Lack, D.A., Liao, J., Markovic, M.Z., Middlebrook, A.M., Ng, N.L., Perring, A.E., Richardson, M.S., Schwarz, J.P., Washenfelder, R.A., Welti, A., Xu, L., Ziemba, L.D., Murphy, D.M., 2016. Aerosol optical properties in the southeastern United States in summer – Part 1: Hygroscopic growth. Atmos. Chem. Phys. 16, 4987–5007. https://doi.org/10.5194/acp-16-4987-2016

Cesana, G.V., Del Genio, A.D., 2021. Observational constraint on cloud feedbacks suggests moderate climate sensitivity. Nat. Clim. Chang. 11, 213–218. https://doi.org/10.1038/s41558-020-00970-y

Chakrabarty, R.K., Beres, N.D., Moosmüller, H., China, S., Mazzoleni, C., Dubey, M.K., Liu, L., Mishchenko, M.I., 2014. Soot superaggregates from flaming wildfires and their direct radiative forcing. Sci Rep 4, 5508. https://doi.org/10.1038/srep05508

Chan, K.R., Dean-Day, J., Bowen, S.W., Bui, T.P., 1998. Turbulence measurements by the DC-8 Meteorological Measurement System. Geophysical Research Letters 25, 1355–1358. https://doi.org/10.1029/97GL03590

Chang, D.Y., Lelieveld, J., Steil, B., Yoon, J., Yum, S.S., Kim, A.-H., 2021. Variability of aerosol-cloud interactions induced by different cloud droplet nucleation schemes. Atmospheric Research 250, 105367. https://doi.org/10.1016/j.atmosres.2020.105367

Charlson, R.J., Ackerman, A.S., Bender, F.A.-M., Anderson, T.L., Liu, Z., 2007. On the climate forcing consequences of the albedo continuum between cloudy and clear air. Tellus B: Chemical and Physical Meteorology 59, 715–727. https://doi.org/10.1111/j.1600-0889.2007.00297.x

Chouza, F., Reitebuch, O., Groß, S., Rahm, S., Freudenthaler, V., Toledano, C., Weinzierl, B., 2015. Retrieval of aerosol backscatter and extinction from airborne coherent Doppler wind lidar measurements. Atmospheric Measurement Techniques 8, 2909–2926. https://doi.org/10.5194/amt-8-2909-2015

Chouza, F., Reitebuch, O., Jähn, M., Rahm, S., Weinzierl, B., 2016. Vertical wind retrieved by airborne lidar and analysis of island induced gravity waves in combination with numerical models and in situ particle measurements. Atmos. Chem. Phys. 16, 4675–4692. https://doi.org/10.5194/acp-16-4675-2016

Cober, S.G., Isaac, G.A., Korolev, A.V., Strapp, J.W., 2001. Assessing cloud-phase conditions. J. Appl. Meteorol. 40, 1967–1983. https://doi.org/10.1175/1520-0450(2001)040<1967:acpc>2.0.co;2

Costa, A., Meyer, J., Afchine, A., Luebke, A., Günther, G., Dorsey, J.R., Gallagher, M.W., Ehrlich, A., Wendisch, M., Baumgardner, D., Wex, H., Krämer, M., 2017. Classification of Arctic, midlatitude and tropical clouds in the mixed-phase temperature regime. Atmos. Chem. Phys. 17, 12219–12238. https://doi.org/10.5194/acp-17-12219-2017

Craig, L., Moharreri, A., Rogers, D.C., Anderson, B., Dhaniyala, S., 2014. Aircraft-Based Aerosol Sampling in Clouds: Performance Characterization of Flow-Restriction Aerosol Inlets. Journal of Atmospheric and Oceanic Technology 31, 2512–2521. https://doi.org/10.1175/JTECH-D-14-00022.1

Cziczo, D.J., Froyd, K.D., Hoose, C., Jensen, E.J., Diao, M.H., Zondlo, M.A., Smith, J.B., Twohy, C.H., Murphy, D.M., 2013. Clarifying the Dominant Sources and Mechanisms of Cirrus Cloud Formation. Science 340, 1320–1324. https://doi.org/10.1126/science.1234145

Cziczo, D.J., Ladino, L., Boose, Y., Kanji, Z.A., Kupiszewski, P., Lance, S., Mertes, S., Wex, H., 2017. Measurements of Ice Nucleating Particles and Ice Residuals. Meteorological Monographs 58, 8.1-8.13. https://doi.org/10.1175/amsmonographs-d-16-0008.1

D'Alessandro, J.J., Diao, M., Wu, C., Liu, X., Chen, M., Morrison, H., Eidhammer, T., Jensen, J.B., Bansemer, A., Zondlo, M.A., DiGangi, J.P., 2017. Dynamical conditions of ice supersaturation and ice nucleation in convective systems: A comparative analysis between in situ aircraft observations and WRF simulations. Journal of Geophysical Research: Atmospheres 122, 2844–2866. https://doi.org/10.1002/2016JD025994

D'Alessandro, J.J., Diao, M., Wu, C., Liu, X., Jensen, J.B., Stephens, B.B., 2019. Cloud Phase and Relative Humidity Distributions over the Southern Ocean in Austral Summer Based on In Situ Observations and CAM5 Simulations. Journal of Climate 32, 2781–2805. https://doi.org/10.1175/JCLI-D-18-0232.1

DeMott, P.J., Prenni, A.J., Liu, X., Kreidenweis, S.M., Petters, M.D., Twohy, C.H., Richardson, M.S., Eidhammer, T., Rogers, D.C., 2010. Predicting global atmospheric ice nuclei distributions and their impacts on climate. PNAS 107, 11217–11222. https://doi.org/10.1073/pnas.0910818107

DeMott, P.J., Prenni, A.J., McMeeking, G.R., Sullivan, R.C., Petters, M.D., Tobo, Y., Niemand, M., Möhler, O., Snider, J.R., Wang, Z., Kreidenweis, S.M., 2015. Integrating laboratory and field data to quantify the immersion freezing ice nucleation activity of mineral dust particles. Atmos. Chem. Phys. 15, 393–409. https://doi.org/10.5194/acp-15-393-2015

Diao, M., Bryan, G.H., Morrison, H., Jensen, J.B., 2017. Ice Nucleation Parameterization and Relative Humidity Distribution in Idealized Squall-Line Simulations. Journal of the Atmospheric Sciences 74, 2761–2787. https://doi.org/10.1175/JAS-D-16-0356.1

Diao, M., Jensen, J.B., Pan, L.L., Homeyer, C.R., Honomichl, S., Bresch, J.F., Bansemer, A., 2015. Distributions of ice supersaturation and ice crystals from airborne observations in relation to upper tropospheric dynamical boundaries. Journal of Geophysical Research: Atmospheres 120, 5101–5121. https://doi.org/10.1002/2015JD023139

Diao, M., Zondlo, M.A., Heymsfield, A.J., Avallone, L.M., Paige, M.E., Beaton, S.P., Campos, T., Rogers, D.C., 2014. Cloud-scale ice-supersaturated regions spatially correlate with high water vapor heterogeneities. Atmospheric Chemistry and Physics 14, 2639–2656. https://doi.org/10.5194/acp-14-2639-2014

Diao, M., Zondlo, M.A., Heymsfield, A.J., Beaton, S.P., Rogers, D.C., 2013. Evolution of ice crystal regions on the microscale based on in situ observations. Geophysical Research Letters 40, 3473–3478. https://doi.org/10.1002/grl.50665

Diskin, G.S., Podolske, J.R., Sachse, G.W., Slate, T.A., 2002. Open-path airborne tunable diode laser hygrometer, in: Fried, A. (Ed.), . Presented at the International Symposium on Optical Science and Technology, Seattle, WA, p. 196. https://doi.org/10.1117/12.453736

Dollner, M., Gasteiger, J., Schöberl, M., Gattringer, A., Beres, N.D., Diskin, G.S., Bui, T.P., Weinzierl, B., 2022a, in prep. The Cloud Indicator: A novel algorithm for automatic detection and classification of clouds using airborne in situ observations.

Dollner, M., Weinzierl, B., Gasteiger, J., Schöberl, M., Kandler, K., Sudharaj, A., Witschas, B., Coauthors, 2022b, in prep. Aerosol-cloud interactions of Saharan mineral dust over the Eastern Mediterranean.

Dusek, U., Frank, G.P., Hildebrandt, L., Curtius, J., Schneider, J., Walter, S., Chand, D., Drewnick, F., Hings, S., Jung, D., Borrmann, S., Andreae, M.O., 2006. Size Matters More Than Chemistry for Cloud-Nucleating Ability of Aerosol Particles. Science 312, 1375–1378. https://doi.org/10.1126/science.1125261

Eidhammer, T., DeMott, P.J., Prenni, A.J., Petters, M.D., Twohy, C.H., Rogers, D.C., Stith, J., Heymsfield, A., Wang, Z., Pratt, K.A., Prather, K.A., Murphy, S.M., Seinfeld, J.H., Subramanian, R., Kreidenweis, S.M., 2010. Ice Initiation by Aerosol Particles: Measured and Predicted Ice Nuclei Concentrations versus Measured Ice Crystal Concentrations in an Orographic Wave Cloud. Journal of the Atmospheric Sciences 67, 2417–2436. https://doi.org/10.1175/2010JAS3266.1

Elsaesser, G.S., Genio, A.D.D., Jiang, J.H., Lier-Walqui, M. van, 2017. An Improved Convective Ice Parameterization for the NASA GISS Global Climate Model and Impacts on Cloud Ice Simulation. Journal of Climate 30, 317–336. https://doi.org/10.1175/jcli-d-16-0346.1

Field, P.R., Hogan, R.J., Brown, P.R.A., Illingworth, A.J., Choularton, T.W., Kaye, P.H., Hirst, E., Greenaway, R., 2004. Simultaneous radar and aircraft observations of mixed-phase cloud at the 100 m scale. Q. J. R. Meteorol. Soc. 130, 1877–1904. https://doi.org/10.1256/qj.03.102

Froyd, K.D., Cziczo, D.J., Hoose, C., Jensen, E.J., Diao, M.H., Zondlo, M.A., Smith, J.B., Twohy, C.H., Murphy, D.M., 2013. Cirrus Cloud Formation and the Role of Heterogeneous Ice Nuclei. Aip Conf Proc 1527, 976–978. https://doi.org/10.1063/1.4803436

Froyd, K.D., Murphy, D.M., Brock, C.A., Campuzano-Jost, P., Dibb, J.E., Jimenez, J.-L., Kupc, A., Middlebrook, A.M., Schill, G.P., Thornhill, K.L., Williamson, C.J., Wilson, J.C., Ziemba, L.D., 2019. A new method to quantify mineral dust and other aerosol species from aircraft platforms using single-particle mass spectrometry. Atmospheric Measurement Techniques 12, 6209–6239. https://doi.org/10.5194/amt-12-6209-2019

Froyd, K.D., Yu, P., Schill, G.P., Brock, C.A., Kupc, A., Williamson, C.J., Jensen, E.J., Ray, E., Rosenlof, K.H., Bian, H., Darmenov, A.S., Colarco, P.R., Diskin, G.S., Bui, T., Murphy, D.M., 2022. Dominant role of mineral dust in cirrus cloud formation revealed by global-scale measurements. Nat. Geosci. 1–7. https://doi.org/10.1038/s41561-022-00901-w

Gasparini, B., Münch, S., Poncet, L., Feldmann, M., Lohmann, U., 2017. Is increasing ice crystal sedimentation velocity in geoengineering simulations a good proxy for cirrus cloud seeding? Atmos. Chem. Phys. 17, 4871–4885. https://doi.org/10.5194/acp-17-4871-2017

Gasteiger, J., Wiegner, M., 2018. MOPSMAP v1.0: a versatile tool for the modeling of aerosol optical properties. Geoscientific Model Development 11, 2739–2762. https://doi.org/10.5194/gmd-11-2739-2018

Glen, A., Brooks, S.D., 2013. A new method for measuring optical scattering properties of atmospherically relevant dusts using the Cloud and Aerosol Spectrometer with Polarization (CASPOL). Atmos. Chem. Phys. 13, 1345–1356. https://doi.org/10.5194/acp-13-1345-2013

Grosvenor, D.P., Choularton, T.W., Lachlan-Cope, T., Gallagher, M.W., Crosier, J., Bower, K.N., Ladkin, R.S., Dorsey, J.R., 2012. In-situ aircraft observations of ice concentrations within clouds over the Antarctic Peninsula and Larsen Ice Shelf. Atmospheric Chemistry and Physics 12, 11275–11294. https://doi.org/10.5194/acp-12-11275-2012

Guan, H., Cober, S.G., Isaac, G.A., 2001. Verification of Supercooled Cloud Water Forecasts with In Situ Aircraft Measurements. Weather and Forecasting 16, 145–155. https://doi.org/10.1175/1520-0434(2001)016<0145:VOSCWF>2.0.CO;2

Herich, H., Tritscher, T., Wiacek, A., Gysel, M., Weingartner, E., Lohmann, U., Baltensperger, U., Cziczo, D.J., 2009. Water uptake of clay and desert dust aerosol particles at sub- and supersaturated water vapor conditions. Phys. Chem. Chem. Phys. 11, 7804–7809. https://doi.org/10.1039/B901585J

Heymsfield, A.J., Krämer, M., Luebke, A., Brown, P., Cziczo, D.J., Franklin, C., Lawson, P., Lohmann, U., McFarquhar, G., Ulanowski, Z., Van Tricht, K., 2017. Cirrus Clouds. Meteorological Monographs 58, 2.1-2.26. https://doi.org/10.1175/AMSMONOGRAPHS-D-16-0010.1

Hirsch, E., Koren, I., Levin, Z., Altaratz, O., Agassi, E., 2014. On transition-zone water clouds. Atmospheric Chemistry and Physics 14, 9001–9012. https://doi.org/10.5194/acp-14-9001-2014

Hoose, C., Möhler, O., 2012. Heterogeneous ice nucleation on atmospheric aerosols: a review of results from laboratory experiments. Atmospheric Chemistry and Physics 12, 9817–9854. https://doi.org/10.5194/acp-12-9817-2012

Huang, Y., Siems, S.T., Manton, M.J., 2021. Wintertime In Situ Cloud Microphysical Properties of Mixed-Phase Clouds Over the Southern Ocean. Journal of Geophysical Research: Atmospheres 126, e2021JD034832. https://doi.org/10.1029/2021JD034832

Huneeus, N., Schulz, M., Balkanski, Y., Griesfeller, J., Prospero, J., Kinne, S., Bauer, S., Boucher, O., Chin, M., Dentener, F., Diehl, T., Easter, R., Fillmore, D., Ghan, S., Ginoux, P., Grini, A., Horowitz, L., Koch, D., Krol, M.C., Landing, W., Liu, X., Mahowald, N., Miller, R., Morcrette, J.-J., Myhre, G., Penner, J., Perlwitz, J., Stier, P., Takemura, T., Zender, C.S., 2011. Global dust model intercomparison in AeroCom phase I. Atmospheric Chemistry and Physics 11, 7781–7816. https://doi.org/10.5194/acp-11-7781-2011

IPCC, 2021. Summary for Policymakers, in: Masson-Delmotte, V., Zhai, P., Pirani, A., Connors, S.L., Péan, C., Berger, S., Caud, N., Chen, Y., Goldfarb, L., Gomis, M.I., Huang, M., Leitzell, K., Lonnoy, E., Matthews, J.B.R., Maycock, T.K., Waterfield, T., Yelekçi, O., Yu, R., Zhou, B. (Eds.), Climate Change 2021: The Physical Science Basis. Contribution of Working Group I to the Sixth Assessment Report of the Intergovernmental Panel on Climate Change. Cambridge University Press.

Jensen, E.J., Kaercher, B., Ueyama, R., Pfister, L., Bui, T.V., Diskin, G.S., DiGangi, J.P., Woods, S., Lawson, R.P., Froyd, K.D., Murphy, D.M., 2018. Heterogeneous Ice Nucleation in the Tropical Tropopause Layer. J. Geophys. Res.-Atmos. 123, 12210–12227. https://doi.org/10.1029/2018JD028949

Jourdan, O., Oshchepkov, S., Gayet, J.-F., Shcherbakov, V., Isaka, H., 2003. Statistical analysis of cloud light scattering and microphysical properties obtained from airborne measurements. Journal of Geophysical Research: Atmospheres 108. https://doi.org/10.1029/2002JD002723

Kandler, K., Lieke, K., Benker, N., Emmel, C., Küpper, M., Müller-Ebert, D., Ebert, M., Scheuvens, D., Schladitz, A., Schütz, L., Weinbruch, S., 2011. Electron microscopy of particles collected at Praia, Cape Verde, during the Saharan Mineral Dust Experiment: particle chemistry, shape, mixing state and complex refractive index. Tellus B: Chemical and Physical Meteorology 63, 475–496. https://doi.org/10.1111/j.1600-0889.2011.00550.x

Kandler, K., Schneiders, K., Ebert, M., Hartmann, M., Weinbruch, S., Prass, M., Pöhlker, C., 2018. Composition and mixing state of atmospheric aerosols determined by electron microscopy: method development and application to aged Saharan dust deposition in the Caribbean boundary layer. Atmos. Chem. Phys. 18, 13429–13455. https://doi.org/10.5194/acp-18-13429-2018

Kandler, K., SchüTZ, L., Deutscher, C., Ebert, M., Hofmann, H., JäCKEL, S., Jaenicke, R., Knippertz, P., Lieke, K., Massling, A., Petzold, A., Schladitz, A., Weinzierl, B., Wiedensohler, A., Zorn, S., Weinbruch1, S., 2009. Size distribution, mass concentration, chemical and mineralogical composition and derived optical parameters of the boundary layer aerosol at Tinfou, Morocco, during SAMUM 2006. Tellus B: Chemical and Physical Meteorology 61, 32–50. https://doi.org/10.1111/j.1600-0889.2008.00385.x

Kanji, Z.A., Abbatt, J.P.D., 2006. Laboratory studies of ice formation via deposition mode nucleation onto mineral dust and n-hexane soot samples. Journal of Geophysical Research: Atmospheres 111. https://doi.org/10.1029/2005JD006766

Kanji, Z.A., Ladino, L.A., Wex, H., Boose, Y., Burkert-Kohn, M., Cziczo, D.J., Krämer, M., 2017. Overview of Ice Nucleating Particles. Meteorological Monographs 58, 1.1-1.33. https://doi.org/10.1175/amsmonographs-d-16-0006.1

King, W.D., Parkin, D.A., Handsworth, R.J., 1978. A Hot-Wire Liquid Water Device Having Fully Calculable Response Characteristics. Journal of Applied Meteorology 17, 1809–1813. https://doi.org/10.1175/1520-0450(1978)017<1809:ahwlwd>2.0.co;2

Kinne, S., Schulz, M., Textor, C., Guibert, S., Balkanski, Y., Bauer, S.E., Berntsen, T., Berglen, T.F., Boucher, O., Chin, M., Collins, W., Dentener, F., Diehl, T., Easter, R., Feichter, J., Fillmore, D., Ghan, S., Ginoux, P., Gong, S., Grini, A., Hendricks, J., Herzog, M., Horowitz, L., Isaksen, I., Iversen, T., Kirkevåg, A., Kloster, S., Koch, D., Kristjansson, J.E., Krol, M., Lauer, A., Lamarque, J.F., Lesins, G., Liu, X., Lohmann, U., Montanaro, V., Myhre, G., Penner, J., Pitari, G., Reddy, S., Seland, O., Stier, P., Takemura, T., Tie, X., 2006. An AeroCom initial assessment – optical properties in aerosol component modules of global models. Atmospheric Chemistry and Physics 6, 1815–1834. https://doi.org/10.5194/acp-6-1815-2006

Knollenberg, R.G., 1970. The Optical Array: An Alternative to Scattering or Extinction for Airborne Particle Size Determination. Journal of Applied Meteorology 9, 86–103. https://doi.org/10.1175/1520-0450(1970)009<0086:toaaat>2.0.co;2

Koehler, K.A., Kreidenweis, S.M., DeMott, P.J., Petters, M.D., Prenni, A.J., Carrico, C.M., 2009. Hygroscopicity and cloud droplet activation of mineral dust aerosol. Geophysical Research Letters 36. https://doi.org/10.1029/2009GL037348

Köhler, H., 1936. The nucleus in and the growth of hygroscopic droplets. Trans. Faraday Soc. 32, 1152–1161. https://doi.org/10.1039/TF9363201152

Kok, J.F., Ridley, D.A., Zhou, Q., Miller, R.L., Zhao, C., Heald, C.L., Ward, D.S., Albani, S., Haustein, K., 2017. Smaller desert dust cooling effect estimated from analysis of dust size and abundance. Nature Geosci 10, 274–278. https://doi.org/10.1038/ngeo2912

Köpp, F., Rahm, S., Smalikho, I., 2004. Characterization of Aircraft Wake Vortices by 2-µm Pulsed Doppler Lidar. Journal of Atmospheric and Oceanic Technology 21, 194–206. https://doi.org/10.1175/1520-0426(2004)021<0194:COAWVB>2.0.CO;2

Koren, I., Remer, L.A., Kaufman, Y.J., Rudich, Y., Martins, J.V., 2007. On the twilight zone between clouds and aerosols: CLOUDS TWILIGHT ZONE. Geophys. Res. Lett. 34. https://doi.org/10.1029/2007GL029253

Korolev, A., Isaac, G., 2006. Relative Humidity in Liquid, Mixed-Phase, and Ice Clouds. Journal of The Atmospheric Sciences - J ATMOS SCI 63, 2865–2880. https://doi.org/10.1175/JAS3784.1

Korolev, A., McFarquhar, G., Field, P.R., Franklin, C., Lawson, P., Wang, Z., Williams, E., Abel, S.J., Axisa, D., Borrmann, S., Crosier, J., Fugal, J., Krämer, M., Lohmann, U., Schlenczek, O., Schnaiter, M., Wendisch, M., 2017. Mixed-Phase Clouds: Progress and Challenges. Meteorological Monographs 58, 5.1-5.50. https://doi.org/10.1175/AMSMONOGRAPHS-D-17-0001.1

Korolev, A.V., Isaac, G.A., Cober, S.G., Strapp, J.W., Hallett, J., 2003. Microphysical characterization of mixed-phase clouds. Quarterly Journal of the Royal Meteorological Society 129, 39–65. https://doi.org/10.1256/qj.01.204

Korolev, A.V., Strapp, J.W., Isaac, G.A., 1998a. Evaluation of the Accuracy of PMS Optical Array Probes. J. Atmos. Oceanic Technol. 15, 708–720. https://doi.org/10.1175/1520-0426(1998)015<0708:EOTAOP>2.0.CO;2

Korolev, A.V., Strapp, J.W., Isaac, G.A., Nevzorov, A.N., 1998b. The Nevzorov Airborne Hot-Wire LWC–TWC Probe: Principle of Operation and Performance Characteristics. Journal of Atmospheric and Oceanic Technology 15, 1495–1510. https://doi.org/10.1175/1520-0426(1998)015<1495:TNAHWL>2.0.CO;2

Krämer, M., Rolf, C., Spelten, N., Afchine, A., Fahey, D., Jensen, E., Khaykin, S., Kuhn, T., Lawson, P., Lykov, A., Pan, L.L., Riese, M., Rollins, A., Stroh, F., Thornberry, T., Wolf, V., Woods, S., Spichtinger, P., Quaas, J., Sourdeval, O., 2020. A microphysics guide to cirrus – Part 2:

Climatologies of clouds and humidity from observations. Atmospheric Chemistry and Physics 20, 12569–12608. https://doi.org/10.5194/acp-20-12569-2020

Kulkarni, P., Baron, P.A., Willeke, K. (Eds.), 2011. Aerosol Measurement: Principles, Techniques, and Applications. John Wiley & Sons, Inc., Hoboken, NJ, USA. https://doi.org/10.1002/9781118001684

Lachlan-Cope, T., Listowski, C., O'Shea, S., 2016. The microphysics of clouds over the Antarctic Peninsula – Part 1: Observations. Atmos. Chem. Phys. 16, 15605–15617. https://doi.org/10.5194/acp-16-15605-2016

Liu, S., Zhao, C., Zhou, Y., Wu, Z., Hu, Z., 2022. Multi-Case Analysis of Ice Particle Properties of Stratiform Clouds Using In Situ Aircraft Observations in Hebei, China. Atmosphere 13, 200. https://doi.org/10.3390/atmos13020200

Loeb, N.G., Wielicki, B.A., Doelling, D.R., Smith, G.L., Keyes, D.F., Kato, S., Manalo-Smith, N., Wong, T., 2009. Toward Optimal Closure of the Earth's Top-of-Atmosphere Radiation Budget. Journal of Climate 22, 748–766. https://doi.org/10.1175/2008jcli2637.1

Lohmann, U., Lüönd, F., Mahrt, F., 2016. An Introduction to Clouds: From the Microscale to Climate. Cambridge University Press, Cambridge. https://doi.org/10.1017/CBO9781139087513

Luebke, A.E., Afchine, A., Costa, A., Grooß, J.U., Meyer, J., Rolf, C., Spelten, N., Avallone, L.M., Baumgardner, D., Krämer, M., 2016. The origin of midlatitude ice clouds and the resulting influence on their microphysical properties. Atmos. Chem. Phys. 16, 5793–5809. https://doi.org/10.5194/acp-16-5793-2016

Ma, X., von Salzen, K., Li, J., 2008. Modelling sea salt aerosol and its direct and indirect effects on climate. Atmospheric Chemistry and Physics 8, 1311–1327. https://doi.org/10.5194/acp-8-1311-2008

McFarquhar, G.M., Baumgardner, D., Bansemer, A., Abel, S.J., Crosier, J., French, J., Rosenberg, P., Korolev, A., Schwarzoenboeck, A., Leroy, D., Um, J., Wu, W., Heymsfield, A.J., Twohy, C., Detwiler, A., Field, P., Neumann, A., Cotton, R., Axisa, D., Dong, J.Y., 2017. Processing of Ice Cloud In Situ Data Collected by Bulk Water, Scattering, and Imaging Probes: Fundamentals, Uncertainties, and Efforts toward Consistency, in: Baumgardner, D., McFarquhar, G.M., Heymsfield, A.J. (Eds.), Ice Formation and Evolution in Clouds and Precipitation: Measurement and Modeling Challenges, Meteorological Monographs. Amer Meteorological Society, Boston. https://doi.org/10.1175/amsmonographs-d-16-0007.1

Meehl, G.A., Boer, G.J., Covey, C., Latif, M., Stouffer, R.J., 2000. The Coupled Model Intercomparison Project (CMIP). Bulletin of the American Meteorological Society 81, 313–318. https://doi.org/10.1175/1520-0477(2000)081<0313:TCMIPC>2.3.CO;2

Meehl, G.A., Senior, C.A., Eyring, V., Flato, G., Lamarque, J.-F., Stouffer, R.J., Taylor, K.E., Schlund, M., 2020. Context for interpreting equilibrium climate sensitivity and transient climate response from the CMIP6 Earth system models. Sci. Adv. 6, eaba1981. https://doi.org/10.1126/sciadv.aba1981

Metropolis, N., Ulam, S., 1949. The Monte Carlo Method. Journal of the American Statistical Association 44, 335–341. https://doi.org/10.1080/01621459.1949.10483310

Michel Flores, J., Bar-Or, R.Z., Bluvshtein, N., Abo-Riziq, A., Kostinski, A., Borrmann, S., Koren, I., Koren, I., Rudich, Y., 2012. Absorbing aerosols at high relative humidity: linking hygroscopic growth to optical properties. Atmospheric Chemistry and Physics 12, 5511–5521. https://doi.org/10.5194/acp-12-5511-2012

Mie, G., 1908. Beiträge zur Optik trüber Medien, speziell kolloidaler Metallösungen. Ann. Phys. 330, 377–445. https://doi.org/10.1002/andp.19083300302

Miller, R.L., Cakmur, R.V., Perlwitz, J., Geogdzhayev, I.V., Ginoux, P., Koch, D., Kohfeld, K.E., Prigent, C., Ruedy, R., Schmidt, G.A., Tegen, I., 2006. Mineral dust aerosols in the NASA Goddard Institute for Space Sciences ModelE atmospheric general circulation model.

Journal of Geophysical Research: Atmospheres 111. https://doi.org/10.1029/2005JD005796

Miller, R.M., McFarquhar, G.M., Rauber, R.M., O'Brien, J.R., Gupta, S., Segal-Rozenhaimer, M., Dobracki, A.N., Sedlacek, A.J., Burton, S.P., Howell, S.G., Freitag, S., Dang, C., 2021. Observations of supermicron-sized aerosols originating from biomass burning in southern Central Africa. Atmos. Chem. Phys. 21, 14815–14831. https://doi.org/10.5194/acp-21-14815-2021

Moise, T., Flores, J.M., Rudich, Y., 2015. Optical Properties of Secondary Organic Aerosols and Their Changes by Chemical Processes. Chem. Rev. 115, 4400–4439. https://doi.org/10.1021/cr5005259

Niemand, M., Möhler, O., Vogel, B., Vogel, H., Hoose, C., Connolly, P., Klein, H., Bingemer, H., DeMott, P., Skrotzki, J., Leisner, T., 2012. A Particle-Surface-Area-Based Parameterization of Immersion Freezing on Desert Dust Particles. Journal of the Atmospheric Sciences 69, 3077–3092. https://doi.org/10.1175/JAS-D-11-0249.1

Ovarlez, J., Gayet, J.-F., Gierens, K., Ström, J., Ovarlez, H., Auriol, F., Busen, R., Schumann, U., 2002. Water vapour measurements inside cirrus clouds in Northern and Southern hemispheres during INCA. Geophysical Research Letters 29, 60-1-60–4. https://doi.org/10.1029/2001GL014440

Patnaude, R., Diao, M., 2020. Aerosol Indirect Effects on Cirrus Clouds Based on Global Aircraft Observations. Geophysical Research Letters 47, e2019GL086550. https://doi.org/10.1029/2019gl086550

Patnaude, R., Diao, M., Liu, X., Chu, S., 2021. Effects of thermodynamics, dynamics and aerosols on cirrus clouds based on in situ observations and NCAR CAM6. Atmospheric Chemistry and Physics 21, 1835–1859. https://doi.org/10.5194/acp-21-1835-2021

Peterson, D.A., Thapa, L.H., Saide, P.E., Soja, A.J., Gargulinski, E.M., Hyer, E.J., Weinzierl, B., Dollner, M., Schöberl, M., Papin, P.P., Kondragunta, S., Camacho, C.P., Ichoku, C., Moore, R.H., Hair, J.W., Crawford, J.H., Dennison, P.E., Kalashnikova, O.V., Bennese, C.E., Bui, T.P., DiGangi, J.P., Diskin, G.S., Fenn, M.A., Halliday, H.S., Jimenez, J., Nowak, J.B., Robinson, C., Sanchez, K., Shingler, T.J., Thornhill, L., Wiggins, E.B., Winstead, E., Xu, C., 2022. Measurements from inside a Thunderstorm Driven by Wildfire: The 2019 FIREX-AQ Field Experiment. Bulletin of the American Meteorological Society 1. https://doi.org/10.1175/BAMS-D-21-0049.1

Petters, M.D., Kreidenweis, S.M., 2007. A single parameter representation of hygroscopic growth and cloud condensation nucleus activity. Atmos. Chem. Phys. 7, 1961–1971. https://doi.org/10.5194/acp-7-1961-2007

Petzold, A., Krämer, M., Neis, P., Rolf, C., Rohs, S., Berkes, F., Smit, H.G.J., Gallagher, M., Beswick, K., Lloyd, G., Baumgardner, D., Spichtinger, P., Nédélec, P., Ebert, V., Buchholz, B., Riese, M., Wahner, A., 2017. Upper tropospheric water vapour and its interaction with cirrus clouds as seen from IAGOS long-term routine in situ observations. Faraday Discuss. 200, 229–249. https://doi.org/10.1039/C7FD00006E

Pincus, R., Klein, S.A., 2000. Unresolved spatial variability and microphysical process rates in large-scale models. Journal of Geophysical Research: Atmospheres 105, 27059–27065. https://doi.org/10.1029/2000JD900504

Pisso, I., Sollum, E., Grythe, H., Kristiansen, N.I., Cassiani, M., Eckhardt, S., Arnold, D., Morton, D., Thompson, R.L., Groot Zwaaftink, C.D., Evangeliou, N., Sodemann, H., Haimberger, L., Henne, S., Brunner, D., Burkhart, J.F., Fouilloux, A., Brioude, J., Philipp, A., Seibert, P., Stohl, A., 2019. The Lagrangian particle dispersion model FLEXPART version 10.4. Geosci. Model Dev. 12, 4955–4997. https://doi.org/10.5194/gmd-12-4955-2019

Purcell, E.M., Pennypacker, C.R., 1973. Scattering and Absorption of Light by Nonspherical Dielectric Grains. The Astrophysical Journal 186, 705–714. https://doi.org/10.1086/152538

Rosenberg, P.D., Dean, A.R., Williams, P.I., Dorsey, J.R., Minikin, A., Pickering, M.A., Petzold, A., 2012. Particle sizing calibration with refractive index correction for light scattering optical particle counters and impacts upon PCASP and CDP data collected during the Fennec campaign. Atmospheric Measurement Techniques 5, 1147–1163. https://doi.org/10.5194/amt-5-1147-2012

Schumann, U. (Ed.), 2012. Atmospheric Physics: Background – Methods – Trends, Research Topics in Aerospace. Springer Berlin Heidelberg, Berlin, Heidelberg. https://doi.org/10.1007/978-3-642-30183-4

Scott, S.G., Bui, T.P., Chan, K.R., Bowen, S.W., 1990. The Meteorological Measurement System on the NASA ER-2 Aircraft. Journal of Atmospheric and Oceanic Technology 7, 525–540. https://doi.org/10.1175/1520-0426(1990)007<0525:TMMSOT>2.0.CO;2

Seibert, P., Frank, A., 2004. Source-receptor matrix calculation with a Lagrangian particle dispersion model in backward mode. Atmos. Chem. Phys. 4, 51–63. https://doi.org/10.5194/acp-4-51-2004

Seinfeld, J.H., Bretherton, C., Carslaw, K.S., Coe, H., DeMott, P.J., Dunlea, E.J., Feingold, G., Ghan, S., Guenther, A.B., Kahn, R., Kraucunas, I., Kreidenweis, S.M., Molina, M.J., Nenes, A., Penner, J.E., Prather, K.A., Ramanathan, V., Ramaswamy, V., Rasch, P.J., Ravishankara, A.R., Rosenfeld, D., Stephens, G., Wood, R., 2016. Improving our fundamental understanding of the role of aerosol−cloud interactions in the climate system. Proceedings of the National Academy of Sciences 113, 5781–5790. https://doi.org/10.1073/pnas.1514043113

Seinfeld, J.H., Pandis, S.N., 2006. Atmospheric chemistry and physics: from air pollution to climate change, 2nd ed. ed. J. Wiley, Hoboken, N.J.

Sherwood, S.C., Bony, S., Dufresne, J.-L., 2014. Spread in model climate sensitivity traced to atmospheric convective mixing. Nature 505, 37–42. https://doi.org/10.1038/nature12829

Smalikho, I., 2003. Techniques of Wind Vector Estimation from Data Measured with a Scanning Coherent Doppler Lidar. Journal of Atmospheric and Oceanic Technology 20, 276–291. https://doi.org/10.1175/1520-0426(2003)020<0276:TOWVEF>2.0.CO;2

Sokolik, I.N., Winker, D.M., Bergametti, G., Gillette, D.A., Carmichael, G., Kaufman, Y.J., Gomes, L., Schuetz, L., Penner, J.E., 2001. Introduction to special section: Outstanding problems in quantifying the radiative impacts of mineral dust. J. Geophys. Res. 106, 18015–18027. https://doi.org/10.1029/2000JD900498

Spänkuch, D., Hellmuth, O., Görsdorf, U., 2022. What is a cloud? Toward a more precise definition? Bulletin of the American Meteorological Society 1. https://doi.org/10.1175/BAMS-D-21-0032.1

Spanu, A., Dollner, M., Gasteiger, J., Bui, T.P., Weinzierl, B., 2020. Flow-induced errors in airborne in situ measurements of aerosols and clouds. Atmospheric Measurement Techniques 13, 1963–1987. https://doi.org/10.5194/amt-13-1963-2020

Spichtinger, P., Gierens, K., Smit, H.G.J., Ovarlez, J., Gayet, J.F., 2004. On the distribution of relative humidity in cirrus clouds. Atmos. Chem. Phys. 4, 639–647. https://doi.org/10.5194/acp-4-639-2004

Spichtinger, P., Gierens, K.M., 2009. Modelling of cirrus clouds – Part 1a: Model description and validation. Atmos. Chem. Phys. 9, 685–706. https://doi.org/10.5194/acp-9-685-2009

Stohl, A., Forster, C., Frank, A., Seibert, P., Wotawa, G., 2005. Technical note: The Lagrangian particle dispersion model FLEXPART version 6.2. Atmos. Chem. Phys. 5, 2461–2474. https://doi.org/10.5194/acp-5-2461-2005

Stohl, A., Hittenberger, M., Wotawa, G., 1998. Validation of the lagrangian particle dispersion model FLEXPART against large-scale tracer experiment data. Atmospheric Environment 32, 4245–4264. https://doi.org/10.1016/S1352-2310(98)00184-8

Stubenrauch, C.J., Rossow, W.B., Kinne, S., Ackerman, S., Cesana, G., Chepfer, H., Girolamo, L.D., Getzewich, B., Guignard, A., Heidinger, A., Maddux, B.C., Menzel, W.P., Minnis, P., Pearl, C., Platnick, S., Poulsen, C., Riedi, J., Sun-Mack, S., Walther, A., Winker, D., Zeng, S., Zhao, G., 2013. Assessment of Global Cloud Datasets from Satellites: Project and Database Initiated by the GEWEX Radiation Panel. Bulletin of the American Meteorological Society 94, 1031–1049. https://doi.org/10.1175/bams-d-12-00117.1

Svenningsson, B., Rissler, J., Swietlicki, E., Mircea, M., Bilde, M., Facchini, M.C., Decesari, S., Fuzzi, S., Zhou, J., Mønster, J., Rosenørn, T., 2006. Hygroscopic growth and critical supersaturations for mixed aerosol particles of inorganic and organic compounds of atmospheric relevance. Atmos. Chem. Phys. 6, 1937–1952. https://doi.org/10.5194/acp-6-1937-2006

Szymanski, W.W., Nagy, A., Czitrovszky, A., 2009. Optical particle spectrometry—Problems and prospects. Journal of Quantitative Spectroscopy and Radiative Transfer 110, 918–929. https://doi.org/10.1016/j.jqsrt.2009.02.024

Tang, I.N., 1996. Chemical and size effects of hygroscopic aerosols on light scattering coefficients. J. Geophys. Res. 101, 19245–19250. https://doi.org/10.1029/96JD03003

Tang, M., Cziczo, D.J., Grassian, V.H., 2016. Interactions of Water with Mineral Dust Aerosol: Water Adsorption, Hygroscopicity, Cloud Condensation, and Ice Nucleation. Chem. Rev. 116, 4205–4259. https://doi.org/10.1021/acs.chemrev.5b00529

Tegen, I., 2003. Modeling the mineral dust aerosol cycle in the climate system. Quaternary Science Reviews 22, 1821–1834. https://doi.org/10.1016/S0277-3791(03)00163-X

Thompson, C.R., Wofsy, S.C., Prather, M.J., Newman, P.A., Hanisco, T.F., Ryerson, T.B., Fahey, D.W., Apel, E.C., Brock, C.A., Brune, W.H., Froyd, K., Katich, J.M., Nicely, J.M., Peischl, J., Ray, E., Veres, P.R., Wang, S., Allen, H.M., Asher, E., Bian, H., Blake, D., Bourgeois, I., Budney, J., Bui, T.P., Butler, A., Campuzano-Jost, P., Chang, C., Chin, M., Commane, R., Correa, G., Crounse, J.D., Daube, B., Dibb, J.E., DiGangi, J.P., Diskin, G.S., Dollner, M., Elkins, J.W., Fiore, A.M., Flynn, C.M., Guo, H., Hall, S.R., Hannun, R.A., Hills, A., Hintsa, E.J., Hodzic, A., Hornbrook, R.S., Huey, L.G., Jimenez, J.L., Keeling, R.F., Kim, M.J., Kupc, A., Lacey, F., Lait, L.R., Lamarque, J.-F., Liu, J., McKain, K., Meinardi, S., Miller, D.O., Montzka, S.A., Moore, F.L., Morgan, E.J., Murphy, D.M., Murray, L.T., Nault, B.A., Neuman, J.A., Nguyen, L., Gonzalez, Y., Rollins, A., Rosenlof, K., Sargent, M., Schill, G., Schwarz, J.P., Clair, J.M.St., Steenrod, S.D., Stephens, B.B., Strahan, S.E., Strode, S.A., Sweeney, C., Thames, A.B., Ullmann, K., Wagner, N., Weber, R., Weinzierl, B., Wennberg, P.O., Williamson, C.J., Wolfe, G.M., Zeng, L., 2022. The NASA Atmospheric Tomography (ATom) Mission: Imaging the Chemistry of the Global Atmosphere. Bulletin of the American Meteorological Society 103, E761–E790. https://doi.org/10.1175/BAMS-D-20-0315.1

Tipka, A., Haimberger, L., Seibert, P., 2020. Flex_extract v7.1.2 – a software package to retrieve and prepare ECMWF data for use in FLEXPART. Geosci. Model Dev. 13, 5277–5310. https://doi.org/10.5194/gmd-13-5277-2020

Touzé-Peiffer, L., Barberousse, A., Le Treut, H., 2020. The Coupled Model Intercomparison Project: History, uses, and structural effects on climate research. WIREs Climate Change 11, e648. https://doi.org/10.1002/wcc.648

Twomey, S., 1974a. Pollution and the planetary albedo. Atmospheric Environment (1967) 8, 1251–1256. https://doi.org/10.1016/0004-6981(74)90004-3

Twomey, S., 1974b. Pollution and the planetary albedo. Atmospheric Environment (1967) 8, 1251–1256. https://doi.org/10.1016/0004-6981(74)90004-3

Vali, G., DeMott, P.J., Möhler, O., Whale, T.F., 2015. Technical Note: A proposal for ice nucleation terminology. Atmospheric Chemistry and Physics 15, 10263–10270. https://doi.org/10.5194/acp-15-10263-2015

Villanueva, D., Neubauer, D., Gasparini, B., Ickes, L., Tegen, I., 2021. Constraining the Impact of Dust-Driven Droplet Freezing on Climate Using Cloud-Top-Phase Observations.

Geophysical Research Letters 48, e2021GL092687. https://doi.org/10.1029/2021GL092687

Wallace, J.M., Hobbs, P.V., 2006. Atmospheric science: an introductory survey, 2nd ed. ed, International geophysics series. Elsevier Academic Press, Amsterdam ; Boston.

Walser, A., Sauer, D., Spanu, A., Gasteiger, J., Weinzierl, B., 2017. On the parametrization of optical particle counter response including instrument-induced broadening of size spectra and a self-consistent evaluation of calibration measurements. Atmos. Meas. Tech. 10, 4341–4361. https://doi.org/10.5194/amt-10-4341-2017

Wang, C., Soden, B.J., Yang, W., Vecchi, G.A., 2021. Compensation Between Cloud Feedback and Aerosol-Cloud Interaction in CMIP6 Models. Geophysical Research Letters 48, e2020GL091024. https://doi.org/10.1029/2020GL091024

Warneke, C., Coauthors, in prep. Fire Influence on Regional to Global Environments Experiment and Air Quality (FIREX-AQ) Overview.

Waterman, P.C., 1965. Matrix formulation of electromagnetic scattering. Proceedings of the IEEE 53, 805–812. https://doi.org/10.1109/PROC.1965.4058

Weinzierl, B., Ansmann, A., Prospero, J.M., Althausen, D., Benker, N., Chouza, F., Dollner, M., Farrell, D., Fomba, W.K., Freudenthaler, V., Gasteiger, J., Groß, S., Haarig, M., Heinold, B., Kandler, K., Kristensen, T.B., Mayol-Bracero, O.L., Müller, T., Reitebuch, O., Sauer, D., Schäfler, A., Schepanski, K., Spanu, A., Tegen, I., Toledano, C., Walser, A., 2017. The Saharan Aerosol Long-Range Transport and Aerosol–Cloud-Interaction Experiment: Overview and Selected Highlights. Bull. Amer. Meteor. Soc. 98, 1427–1451. https://doi.org/10.1175/BAMS-D-15-00142.1

Weinzierl, B., Coauthors, in prep. The A-LIFE field experiment in the Eastern Mediterranean: highlights from the airborne observations and insights into properties of absorbing aerosol mixtures.

Weinzierl, B., Petzold, A., Esselborn, M., Wirth, M., Rasp, K., Kandler, K., SchüTZ, L., Koepke, P., Fiebig, M., 2009. Airborne measurements of dust layer properties, particle size distribution and mixing state of Saharan dust during SAMUM 2006. Tellus B: Chemical and Physical Meteorology 61, 96–117. https://doi.org/10.1111/j.1600-0889.2008.00392.x

Wendisch, M., Brenguier, J. (Eds.), 2013. Airborne Measurements for Environmental Research: Methods and Instruments, 1st ed. Wiley. https://doi.org/10.1002/9783527653218

Wofsy, S.C., Afshar, S., Allen, H.M., Apel, E.C., Asher, E.C., Barletta, B., Bent, J., Bian, H., Biggs, B.C., Blake, D.R., Blake, N., Bourgeois, I., Brock, C.A., Brune, W.H., Budney, J.W., Bui, T.P., Butler, A., Campuzano-Jost, P., Chang, C.S., Chin, M., Commane, R., Correa, G., Crounse, J.D., Cullis, P.D., Daube, B.C., Day, D.A., Dean-Day, J.M., Dibb, J.E., DiGangi, J.P., Diskin, G.S., Dollner, M., Elkins, J.W., Erdesz, F., Fiore, A.M., Flynn, C.M., Froyd, K.D., Gesler, D.W., Hall, S.R., Hanisco, T.F., Hannun, R.A., Hills, A.J., Hintsa, E.J., Hoffman, A., Hornbrook, R.S., Huey, L.G., Hughes, S., Jimenez, J.L., Johnson, B.J., Katich, J.M., Keeling, R.F., Kim, M.J., Kupc, A., Lait, L.R., McKain, K., Mclaughlin, R.J., Meinardi, S., Miller, D.O., Montzka, S.A., Moore, F.L., Morgan, E.J., Murphy, D.M., Murray, L.T., Nault, B.A., Neuman, J.A., Newman, P.A., Nicely, J.M., Pan, X., Paplawsky, W., Peischl, J., Prather, M.J., Price, D.J., Ray, E.A., Reeves, J.M., Richardson, M., Rollins, A.W., Rosenlof, K.H., Ryerson, T.B., Scheuer, E., Schill, G.P., Schroder, J.C., Schwarz, J.P., St.Clair, J.M., Steenrod, S.D., Stephens, B.B., Strode, S.A., Sweeney, C., Tanner, D., Teng, A.P., Thames, A.B., Thompson, C.R., Ullmann, K., Veres, P.R., Wagner, N.L., Watt, A., Weber, R., Weinzierl, B.B., Wennberg, P.O., Williamson, C.J., Wilson, J.C., Wolfe, G.M., Woods, C.T., Zeng, L.H., Vieznor, N., 2021. ATom: Merged Atmospheric Chemistry, Trace Gases, and Aerosols, Version 2. https://doi.org/10.3334/ORNLDAAC/1925

Wood, R., Field, P.R., 2011. The Distribution of Cloud Horizontal Sizes. Journal of Climate 24, 4800–4816. https://doi.org/10.1175/2011JCLI4056.1

Woods, S., Lawson, R.P., Jensen, E., Bui, T.P., Thornberry, T., Rollins, A., Pfister, L., Avery, M., 2018. Microphysical Properties of Tropical Tropopause Layer Cirrus. Journal of Geophysical Research: Atmospheres 123, 6053–6069. https://doi.org/10.1029/2017jd028068

Wu, C., Liu, X., Diao, M., Zhang, K., Gettelman, A., Lu, Z., Penner, J.E., Lin, Z., 2017. Direct comparisons of ice cloud macro- and microphysical properties simulated by the Community Atmosphere Model version 5 with HIPPO aircraft observations. Atmos. Chem. Phys. 17, 4731–4749. https://doi.org/10.5194/acp-17-4731-2017

Zieger, P., Fierz-Schmidhauser, R., Weingartner, E., Baltensperger, U., 2013. Effects of relative humidity on aerosol light scattering: results from different European sites. Atmos. Chem. Phys. 13, 10609–10631. https://doi.org/10.5194/acp-13-10609-2013

Zieger, P., Väisänen, O., Corbin, J.C., Partridge, D.G., Bastelberger, S., Mousavi-Fard, M., Rosati, B., Gysel, M., Krieger, U.K., Leck, C., Nenes, A., Riipinen, I., Virtanen, A., Salter, M.E., 2017. Revising the hygroscopicity of inorganic sea salt particles. Nat Commun 8, 15883. https://doi.org/10.1038/ncomms15883

APPENDIX A

Enclosed papers

Atmos. Meas. Tech., 13, 1963–1987, 2020
https://doi.org/10.5194/amt-13-1963-2020

Atmospheric Measurement Techniques
Open Access
EGU

Flow-induced errors in airborne in situ measurements of aerosols and clouds

Antonio Spanu[1], **Maximilian Dollner**[1], **Josef Gasteiger**[1], **T. Paul Bui**[2], **and Bernadett Weinzierl**[1]

[1]University of Vienna (UNIVIE), Faculty of Physics, Aerosol Physics and Environmental Physics, Vienna, Austria
[2]NASA Ames Research Center, Mountain View, CA, USA

Correspondence: Antonio Spanu (antonio.spanu@univie.ac.at)

Received: 23 January 2019 – Discussion started: 5 February 2019
Revised: 11 February 2020 – Accepted: 25 February 2020 – Published: 17 April 2020

Abstract. Aerosols and clouds affect atmospheric radiative processes and climate in many complex ways and still pose the largest uncertainty in current estimates of the Earth's changing energy budget.

Airborne in situ sensors such as the Cloud, Aerosol, and Precipitation Spectrometer (CAPS) or other optical spectrometers and optical array probes provide detailed information about the horizontal and vertical distribution of aerosol and cloud properties. However, flow distortions occurring at the location where these instruments are mounted on the outside of an aircraft may directly produce artifacts in detected particle number concentration and also cause droplet deformation and/or breakup during the measurement process.

Several studies have investigated flow-induced errors assuming that air is incompressible. However, for fast-flying aircraft, the impact of air compressibility is no longer negligible. In this study, we combine airborne data with numerical simulations to investigate the flow around wing-mounted instruments and the induced errors for different realistic flight conditions. A correction scheme for deriving particle number concentrations from in situ aerosol and cloud probes is proposed, and a new formula is provided for deriving the droplet volume from images taken by optical array probes. Shape distortions of liquid droplets can either be caused by errors in the speed with which the images are recorded or by aerodynamic forces acting at the droplet surface caused by changes of the airflow when it approaches the instrument. These forces can lead to the dynamic breakup of droplets causing artifacts in particle number concentration and size. An estimation of the critical breakup diameter as a function of flight conditions is provided.

Experimental data show that the flow speed at the instrument location is smaller than the ambient flow speed. Our simulations confirm the observed difference and reveal a size-dependent impact on particle speed and concentration. This leads, on average, to a 25 % overestimation of the number concentration of particles with diameters larger than 10 µm diameter and causes distorted images of droplets and ice crystals if the flow values recorded at the instrument are used. With the proposed corrections, errors of particle number concentration and droplet volume, as well as image distortions, are significantly reduced by up to 1 order of magnitude.

Although the presented correction scheme is derived for the DLR Falcon research aircraft (Saharan Aerosol Long-range Transport and Aerosol-Cloud-Interaction Experiment (SALTRACE) campaign) and validated for the DLR Falcon (Absorbing aerosol layers in a changing climate: aging, lifetime and dynamics mission conducted in 2017 (A-LIFE) campaign) and the NASA DC-8 (Atmospheric Tomography Mission (ATom) campaigns), the general conclusions hold for any fast-flying research aircraft.

1 Introduction

Aerosol–cloud–radiation interactions are one of the largest uncertainties in current climate predictions (Stocker et al., 2014). The size distribution of cloud and aerosol particles is a crucial parameter for aerosol–radiation and aerosol–cloud interaction (Albrecht, 1989; Rosenfeld and Lensky, 1998; Pruppacher and Klett, 2010). For example, an increase of the fraction of coarse particles can modify the direct radiative

forcing of desert dust from cooling to warming (Kok et al., 2017) and also increase the reservoir of ice-nucleating particles (e.g., DeMott et al., 2010).

Airborne in situ measurements are fundamental to extend our knowledge of cloud and aerosol distributions, especially in the coarse mode. Instruments typically used by the aerosol and cloud community, for measuring coarse particles, are open-path or passive-inlet[1] optical particle counters (OPCs) and optical array probes (OAPs). OPCs and OAPs measure particle flux as they record, within a time interval, the number of particles passing through a specific region named sampling area. The flux is later converted into a concentration using the airflow speed. Therefore, errors in the flow speed are directly affecting the calculated particle and cloud hydrometeor concentrations. For example, a too-low flow speed leads to a higher calculated particle concentration. Since the aircraft itself can influence the surrounding air and the flow measurements (Kalogiros and Wang, 2002), airborne measurements are challenging. Flow distortion caused by the fuselage and wings not only impacts the flow velocity but also modifies air temperature, pressure, and density as compared to free stream conditions, thereby further affecting the aerosol and cloud measurements. For example, a higher air density leads to a higher number concentration of aerosol particles if the particles are sufficiently small to be able to follow the airflow. Furthermore, large droplets may be deformed or may even break up during high-speed sampling due to aerodynamic forces acting on the droplet surface, as studied by Szakall et al. (2009); Vargas and Feo (2010). Whereas droplet deformation does not change the detected number concentrations, breakup results in enhanced droplet number concentrations (Weber et al., 1998). These shattering artifacts may originate not only from aerodynamic forces but also from impaction breakup of cloud droplets and ice particles in and around the aerosol inlet (Korolev and Isaac, 2005; Craig et al., 2013). In contrast to these effects, droplets may appear as deformed on the OAP images, but they are not deformed in reality. This is the case if the camera does not use the correct particle velocity for taking the images.

Generally, the degree of the artifact depends on the mounting position of the instrument at the aircraft and also on the flight conditions. Effects of a disturbed flow field on observed particle concentrations have been studied for an incompressible flow (e.g., King, 1984; King et al., 1984; Drummond and MacPherson, 1985; Norment, 1988). However, the assumption that air is incompressible does not hold for measurements on fast-flying aircraft ($> 100\,\mathrm{m\,s^{-1}}$). Computational fluid dynamics (CFD) models are a powerful tool to study aircraft inlets (e.g., Korolev et al., 2013; Moharreri et al., 2013, 2014; Craig et al., 2013, 2014) and sensors (Laucks and Twohy, 1998; Cruette et al., 2000) but are computationally expensive. That is why many studies considered only the instrument itself but not the combined effect of the aircraft and the instrument.

Recently, Weigel et al. (2016) proposed a more general correction method for particle concentrations measured by an underwing instrument. Its first component is a compression correction factor that is based on thermodynamical calculations using simultaneous measurements of the instrument's pitot tube. Its second component is a size-dependent correction factor that corrects the effect of the inertia of particles with diameters larger than 70 µm but not for smaller particles.

In the present study, the influence of airflow distortion caused by the aircraft wing and the instrument is characterized for airborne aerosol and cloud measurements using CFD simulations with a compressible airflow. Furthermore, we investigate how different flight conditions affect particle concentrations depending on size. We propose a correction strategy valid for different aircraft configurations and passive-inlet instruments. Moreover, we investigate how water droplets deform when approaching a wing-mounted instrument on a fast-flying aircraft. Errors affecting the estimation of the droplet volume from OAP images are studied using different approximating formulas. Numerical results are compared with in situ measurements collected with a Cloud and Aerosol Spectrometer with Depolarization Detection (CAS-DPOL, Droplet Measurement Techniques (DMT) Inc., Longmont, CO, USA; Baumgardner et al., 2001) and a second-generation Cloud, Aerosol and Precipitation Spectrometer (CAPS). The analysis is valid for a variety of wing-mounted OPC and OAP instruments used by the aerosol and cloud community. Other potential error sources affecting OPC and OAP measurements like calibration method (Walser et al., 2017), optical misalignment (Lance et al., 2010), or size-dependent sampling area (Hayman et al., 2016) are not considered in this paper.

The paper is organized as follows: Sect. 2 introduces the methodology. For clarity, we divided the presentation of the results into two parts: the first part (Sect. 3.1) analyzes flow changes around wing-mounted instruments and their effects on derived particle concentrations. Also, a correction strategy is described. The second part (Sect. 3.2) describes a method that provides a corrected particle speed for OAP measurements. It includes an evaluation of a parameterization of the droplet breakup process, as well as the verification of numerical results with experimental data. Different formulas for calculating the droplet volume and the undisturbed droplet diameter from OAP images are evaluated. The paper closes with recommendations (Sect. 4) helping to reduce errors in airborne aerosol and cloud measurements and a summary of findings (Sect. 5).

[1] Instruments with passive inlets are not actively sampling the air with a pump; instead, they rely on the airflow resulting from the wind or the aircraft motion.

2 Methodology

The correction strategy presented in this paper is based on numerical simulations of airflow and particle motion and field data collected in 2013 during the Saharan Aerosol Long-range Transport and Aerosol-Cloud-Interaction Experiment (SALTRACE; Weinzierl et al., 2017). The primary purpose is to quantify flow-induced measurement errors and to present a particle concentration correction scheme. The proposed correction scheme is later tested with independent datasets collected during two field campaigns, the Absorbing aerosol layers in a changing climate: aging, lifetime and dynamics mission conducted in 2017 (A-LIFE; https://a-life.at, last access: 5 March 2020) and the Atmospheric Tomography Mission over the years 2016–2018 (ATom-1 through ATom-4; Wofsy et al., 2018).

2.1 Airborne meteorological and aerosol measurements aboard the DLR Falcon and the NASA DC-8 research aircraft

The primary analysis focuses on the DLR research aircraft Dassault Falcon 20E (registration D-CMET) and is later applied to the NASA DC-8 (registration N817NA).

Figure 1 shows a sketch of the DLR Falcon with a wing-mounted instrument, such as the CAPS. Table 1 gives an overview of the specifications of Falcon and DC-8 including the range of typical aircraft cruise speeds and instruments used for this study. The typical altitude range covered by the DLR Falcon is below 12 800 m, and the true air speed (TAS), which is the speed of the aircraft relative to the air mass flown through, ranges from $80\,\mathrm{m\,s^{-1}}$ at low altitude to $220\,\mathrm{m\,s^{-1}}$ at higher altitude (see Table 1). The DLR Falcon is equipped with a Rosemount five-hole pressure probe model 858 on the tip of the nose boom (see Fig. 1), referred to as the CMET system in our study. The CMET system measures air speed and direction and has been calibrated using a cone trail (Bögel and Baumann, 1991). Bögel and Baumann (1991) estimate static pressure errors during pilot-induced maneuvers being smaller than 1 %, which converts to a 0.5 % error in derived air speed.

The NASA DC-8 can fly at altitudes up to 13 800 m with TAS between 90 and $250\,\mathrm{m\,s^{-1}}$. During the ATom mission, the NASA DC-8 was equipped with the Meteorological Measurement System (MMS; Scott et al., 1990). The MMS hardware consists of three major systems: an air-motion sensing system to measure air speed and direction with respect to the aircraft, an aircraft-motion sensing system to measure the aircraft velocity with respect to the earth, and a data acquisition system to sample, process, and record the measured quantities (Chan et al., 1998; Scott et al., 1990). The uncertainty of the MMS pressure sensors is estimated to be less than 2 %.

2.1.1 Aerosol and cloud instruments

In this section, we describe the instruments used for aerosol and cloud measurements during the different campaigns. For SALTRACE, the DLR Falcon was equipped with a CAS-DPOL mounted under the aircraft wing, hereafter named CAS. CAS is a passive-inlet OPC (Baumgardner et al., 2001). Other similar open-path and passive-inlet instruments are the Forward Scattering Spectrometer Probe (FSSP type 100 and 300), the Cloud Droplet Probe (CDP), and the Cloud Particle Spectrometer with Polarization Detection (CPSPD) (Knollenberg, 1976; Lance et al., 2010; Baumgardner et al., 2014). The general measurement mechanism of an OPC is the following: when a particle passes through the laser beam, it scatters light, which is collected by an optical system and detected by a photo-detector. The resulting signal is then recorded and converted to the instrument-specific scattering cross section. Using scattering theory the particle size can be inverted from this cross section (e.g., Walser et al., 2017).

During A-LIFE and the ATom missions, CAPS was used as the aerosol and cloud instrument. CAPS is an instrument consisting of a second generation CAS and a Cloud Imaging Probe (CIP). CIP is an OAP. OAP were introduced by Knollenberg (1970) and extensively used for droplet and ice-crystal measurements. OAPs measure particle size indirectly with a linear array of photodiodes (64 in the case of CIP) by detecting the shadow formed by the particle passing through a collimated laser beam ($\lambda = 658$ nm in the case of CIP). The CIP acquires 2D images of the particles and hydrometeors by assembling sequences of image slices. In order to reconstruct the correct length of a particle along flow direction it is critical that the particle speed assumed for image creation, hereafter named OAP reference speed, represents the real particle speed. The image acquisition frequency, i.e., the speed with which the CIP records image slices, is usually set according to the OAP reference speed such that each image pixel represents in both dimensions the same lengths. CIP's working mechanism is similar to those of other OAPs like 2D-S or HVPS (Knollenberg, 1981; Lawson et al., 2006).

2.1.2 Measurement of airflow and flow distortion caused by the aircraft

The DLR Falcon is equipped with four hard points under the aircraft wings to carry up to four instruments inside standard canisters (developed by Particle Measuring Systems). Canisters have an outer diameter of ~ 0.177 m with a 1.25 m length and are mounted with 3.5° angle with respect to the wing (see the green arrow in Fig. 1).

As we described, OPC and OAP measurements depend on the flow, therefore wing-mounted instruments are sometimes equipped with flow sensors to constrain local flow conditions. Commonly used sensors are pitot-static tubes, hereafter referred to as pitot tubes (Letko, 1947; Garcy, 1980). Pitot tubes are usually located to measure flow conditions

Table 1. Aircraft configuration details and instruments used in this study. The DLR CAS (UNIVIE CAPS) is equipped with a 17 cm (24 cm) long pitot tube.

Campaign	Aircraft	Max. altitude	Typ. cruise speed	Default flow sensors	Wing instrument	Reference
SALTRACE	DLR Falcon	12 800 m	80–220 m s^{-1}	CMET system	DLR CAS	Weinzierl et al. (2017)
A-LIFE	DLR Falcon	12 800 m	80–220 m s^{-1}	CMET system	UNIVIE CAPS	https://a-life.at (last access: 5 March 2020)
ATom	NASA DC-8	13 800 m	90–250 m s^{-1}	MMS	UNIVIE CAPS	Wofsy et al. (2018)

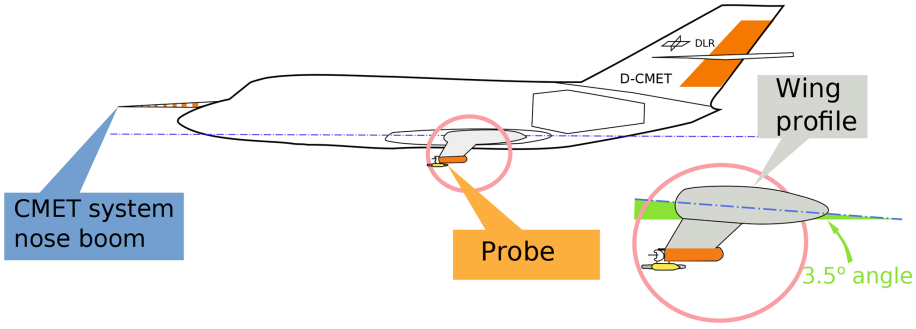

Figure 1. The DLR Falcon research aircraft equipped with the meteorological sensors in the nose boom (also referred to as the "CMET system" in this study) and a probe mounted under the wing for the detection of coarse-mode aerosols and cloud droplets/ice crystals.

representative of the sampling area. A pitot tube measures total pressure p_{tot} and the static pressure p_s. p_{tot} is the sum of the static and the dynamic pressure q_c and is a measure of the total energy per unit volume. Consequently, p_{tot} should not change around the aircraft if dissipative processes, such as a shock wave, do not occur. Table A1 summarizes the different velocities referred to in this study. At small Mach numbers ($M = U/U_{sound} < 0.3$, approximately corresponding to 100 m s^{-1} at sea level), air speed U can be derived using the incompressible form of Bernoulli's equation. When the air speed increases ($M > 0.3$), air density cannot be considered independent of velocity. For this reason, a generalized Bernoulli equation is needed, which is given by

$$\int_{p_1}^{p_s} \frac{\mathrm{d}p}{\rho_{air}} + \frac{U^2}{2} = \text{const.} \tag{1}$$

p_1 is a static reference pressure and the air density ρ_{air} is a function of pressure. Using the heat capacity ratio γ and the sound speed $U_{sound} = \sqrt{\gamma\, p_s/\rho_{air}}$ for an adiabatically expanding gas, the following expression can be derived:

$$\frac{p_{tot}}{p_s} = \left(1 + \frac{\gamma - 1}{2} M^2\right)^{\frac{\gamma}{\gamma-1}}. \tag{2}$$

It is assumed that the pitot tube is oriented parallel to the airflow. Eq. (2) can be converted to obtain the airflow speed:

$$U = \sqrt{\frac{2\gamma}{\gamma - 1}\frac{p_s}{\rho_{air}}\left(\left(\frac{p_{tot}}{p_s}\right)^{\frac{\gamma-1}{\gamma}} - 1\right)}. \tag{3}$$

Equation (3) shows that errors of pressure-based air speed measurements are related to the static pressure as well as to the dynamic pressure (Nacass, 1992). Static pressure errors are typically introduced by disturbances in the flow field around the aircraft and mainly depend on the location and design of the pitot tube (Garcy, 1980). The amount by which the local static pressure at a given point in the flow field differs from the free stream static pressure is the so-called position error.

Errors in the measured dynamic pressure may occur due to airflow disturbances caused by the aircraft or by excessive flow angularity, for example when flying with a large angle of attack ($> 10°$), i.e., a large angle between the flow and the probe axis. A large angle of attack may occur during fast ascent or descents or steep turns of the aircraft. In that case, the fluid stream is no more parallel to the instrument head and errors occur in both, total and static pressure readings (Sun et al., 2007; Masud, 2010). When the DLR Falcon flies under typical operating conditions during research flights the angle of attack is small enough to have only a negligible contribution to the error of the dynamic pressure.

The TAS, i.e., the speed of the air in the free stream, can deviate from the probe air speed (PAS), i.e., the air speed at the location of the probe which may have a flow sensor as described above. King (1984) estimated the difference between TAS and PAS being smaller than 10 % and varying as the inverse square of the scaled distance from the aircraft nose. However, the estimation of King (1984) relies on an incompressible fluid, but using Bernoulli's equation for incompressible flow leads to a 10 % overestimation of air

speed (as compared with a compressible flow) with an 8 % error in pressure as the aircraft approaches transonic speeds ($M \sim 0.8$). Therefore, because of the air compressibility, differences between TAS and PAS can be larger than 10 % in reality.

The CAS is equipped with a 17 cm pitot tube, whereas the CAPS has a 24 cm long one to represent the conditions in the CIP sampling area. Pressure sensors have been statically calibrated by the manufacturer. Comparisons of the total pressure p_{tot} measured by the pitot tube of the wing-mounted instrument (CAS or CAPS) with corresponding measured p_{tot} of the aircraft system (CMET or MMS) reveal deviations of less than 2 %. Therefore, the position error can be estimated using the deviations between the CMET or MMS measurements, representing the free stream conditions, and the wing-mounted instrument reading. Figure 2 shows a statistical comparison between temperature (a), dynamic pressure (b) and static pressure (c) values recorded by the CMET system at the nose boom (free stream) and by the CAS instrument during SALTRACE. In Fig. 2d TAS_{CMET} is compared with the PAS calculated using the pitot tube data according to Eq. (3). Pixels are color coded with the statistical frequency of the binned data. Red lines in Fig. 2a–c are linear fits of the data with calculated R^2 values.

As indicated by the deviation from the 1 : 1 line (dashed), wing-mounted instruments experience an overpressure on their static sensors (Fig. 2b). Since the total pressure is constant along the aircraft (within the pressure sensors errors), a higher static pressure p_s results in a lower dynamic pressure q_c (Fig. 2c). Consequently, the calculated PAS is on average 30 % lower than TAS, with a 35 % maximum relative deviation at higher speed (Fig. 2d). In the Appendix, analogous comparisons of static pressure p_s and dynamic pressure q_c measured by CAPS and the DC-8 MMS system are shown for ATom-1 (Fig. A1). To understand the differences between PAS and TAS, we use a numerical model.

2.2 Numerical models

2.2.1 Flow model

As mentioned earlier, the assumption of incompressibility of air is not valid for fast-flying aircraft ($M > 0.3$) such as the DLR Falcon and the NASA DC-8. A more general model including air compressibility is needed. Here, we use a numerical CFD model based on the time-averaged Navier–Stokes equation for compressible flows (Johnson, 1992). The numerical solution is obtained using a modified version of the rhoSimpleFoam solver from the finite volume code OpenFOAM v4.0.x (Weller et al., 1998). The solver calculates a steady state solution with a segregated approach using a SIMPLE loop, with the latter solution solved using the Reynolds-averaged Navier–Stokes equations (RANS) with a Launder-SharmaKE (Launder and Spalding, 1974) turbulence model. Nakao et al. (2014) successfully used OpenFOAM for simulating the airflow on a two-dimensional NACA (National Advisory Committee for Aeronautics) wing profile under different attack angles.

In our study, we use a simplified three-dimensional model of the Falcon wing equipped with a probe measurement system, which consists of a pylon and a cylindrical canister mounted under the wing (see Fig. 1). The tube of the CAS with the passive inlet was not modeled since preliminary simulations showed that the effect of the CAS tube on the concentrations measured by CAS is smaller than 5 %. For simplicity, we reduced the complexity of the parameter space using a constant angle of attack of 4° which is the median value derived from the flight conditions (see Figs. A2 and A3 in the Appendix). We adopt a comparatively large model domain with edge lengths of 10 times the instrument length to minimize the effects of the domain boundaries. The model mesh comprises 8×10^6 elements. The dependency of the results on the number of mesh elements was tested, using different meshes (created with snappyhexmesh Montorfano, 2017), until we found convergence of the results. To separate CFD results from the statistical analyses conducted over the measured dataset we refer to the simulated velocity as U being the absolute value of the three-dimensional velocity vector. U_0 is the velocity in the free stream of the simulations. With this notation U_0 is equal to TAS.

Note that the aircraft fuselage was not included in the model domain because of limitations of computational resources and its limited effect on the flow at the mounting point of the CAS (1.5 m distance from the fuselage during SALTRACE) as shown below in Sect. 3.1.1. Different aircraft types, e.g., DC-8, or different mounting locations may affect the airflow at the instrument. However, as will be shown below, our flow model, with the CAS mounted on the Falcon wing, can be used for general conclusions because particle concentrations depend only on the ratio between the local airflow and the free stream airflow.

2.2.2 Particle motion

To describe particle motion, we adopt an Eulerian–Lagrangian approach: the Eulerian continuum equations are solved for the fluid phase (see Sect. 2.2.1), whereas Newton's equations describe the particle motion determining their trajectories. We assume spherical particles with a density $\rho_p = 2.5\,g\,cm^{-3}$ for mineral dust and $\rho_p = 1\,g\,cm^{-3}$ for water droplets. We use a one-way coupling; i.e., we consider flow-induced drag forces on the particles. According to Elghobashi (1991), ignoring the effect of particle motion on the flow itself (two-way coupling) and inter-particle collisions (four-way coupling) is a reasonable assumption for volumetric particle fractions smaller than 10^{-6}. For dust particles, this corresponds to atmospheric concentrations lower than $2.5\,g\,m^{-3}$. This value is at least 2 orders of magnitude larger than concentrations measured in dense desert dust aerosol layers (e.g., Kandler et al., 2009; Weinzierl et al., 2009, 2011;

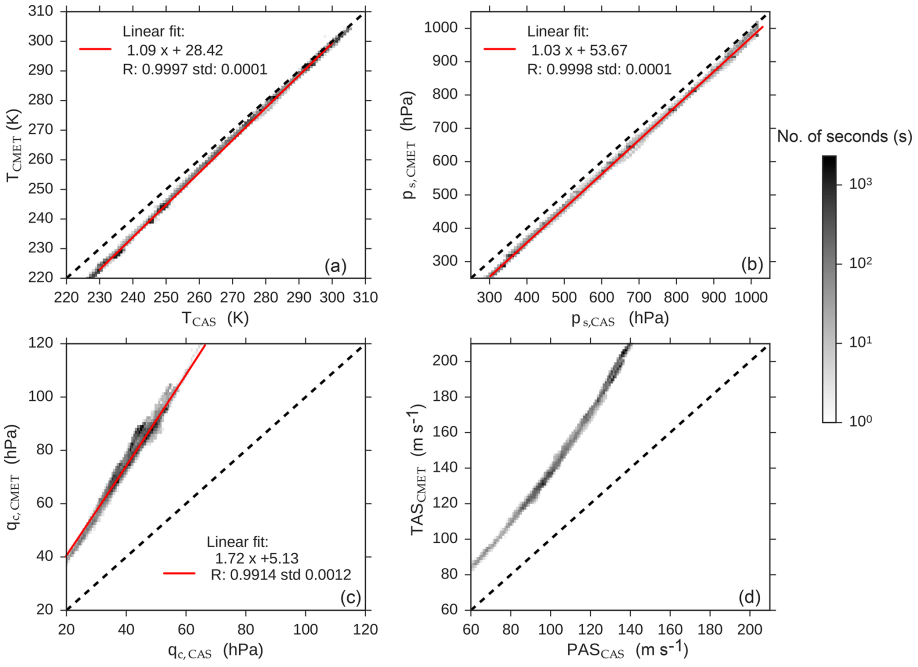

Figure 2. Statistical comparison between values recorded by the CMET system and the CAS pitot tube during SALTRACE: temperature **(a)**, static pressure **(b)**, dynamic pressure **(c)**, and air speed **(d)**. The histogram color map refers to the number of seconds of data at 1 Hz. Dashed lines represent the 1 : 1 line and the red lines linear fits.

Solomos et al., 2017) or volcanic ash layers (e.g., Barsotti et al., 2011; Poret et al., 2018). Single particle motion is resolved using a Lagrangian model where motion equations are integrated in time. The considered forces acting on a particle are the pressure gradient, the drag force, and the gravity.

2.2.3 Droplet distortion model

As described in the introduction, fast changes in the airflow can modify the shape of water droplets causing droplet breakup and consequently strongly affecting the measured number concentration. Here, we use a droplet deformation model to describe how the flow affects the shape of water droplets measured by OAP instruments mounted underwing. A large body of research exists on droplet deformation and breakup (Rumscheidt and Mason., 1961; Rallison, 1984; Marks, 1998). The droplet dynamics is crucial for estimating the icing hazard of supercooled droplets on an aircraft wing (e.g., Tan and Papadakis, 2003). Flow changes experienced around the wing can have important consequences especially when sampling supercooled droplets, for example, in the case of mixed-phase clouds. Jung et al. (2012) observed how shear could cause almost instantaneous freezing in supercooled droplets. Vargas and Feo (2010); Vargas (2012) used laboratory observations to investigate the deformation and breakup of water droplets near the leading edge of an airfoil. Droplet breakup, as an effect of the instability caused by shear on the droplet surface, was early studied by Pilch and Erdman (1987) and Hsiang and Faeth (1992). Different analytical models exist for describing a droplet in a uniform flow such as the Taylor Analogy Breakup (TAB) model (O'Rourke and Amsden, 1987), Clark's model (Clark, 1988) and the droplet deformation and breakup (DDB) model by Ibrahim et al. (1993). Vargas (2012) modifies the DDB model to include the effect of a changing airflow. However, this model does not fully agree with the experimental data especially for particles with diameters larger than 1000 µm. Here we use a volume of fluid (VOF) method (Noh and Woodward, 1976) to determine droplet deformations as a function of droplet size and flight conditions (p_s, T, TAS). Droplets are initially assumed to be spherical with diameter d_0. Similar to the TAB model a simplified problem is considered assuming that droplets are radially symmetric along the flow.

Sampled droplets experience a change of slip velocity U_{slip} (speed of particle relative to the air around it) when approaching the instrument. For this reason, we simulate a transitional state where the air speed varies from zero (still air) to its final value TAS minus PAS (when the droplet is passing through the sampling area). The applied velocity values are calculated along the simulated trajectory of the droplet (of given d_0) and imposed as boundary conditions. Similar to Vargas (2012) we assume that the droplet does not exchange heat with its surroundings and the only forces involved in the deformation of the droplet are viscous, pressure and surface tension forces.

Table 2. Flight conditions (p_s, T, TAS) used to initialize the numerical flow simulation test cases.

Test name	TAS ($m\,s^{-1}$)	p_s (hPa)	T (K)
u75_p1000	75	990	295
u100_p900	100	900	300
u125_p700	125	700	295
u125_p900	125	900	300
u150_p650	150	650	280
u150_p550	150	550	270
u150_p450	150	450	260
u150_p330	150	330	245
u175_p400	175	400	240
u175_p330	175	330	245
u200_p250	200	250	220

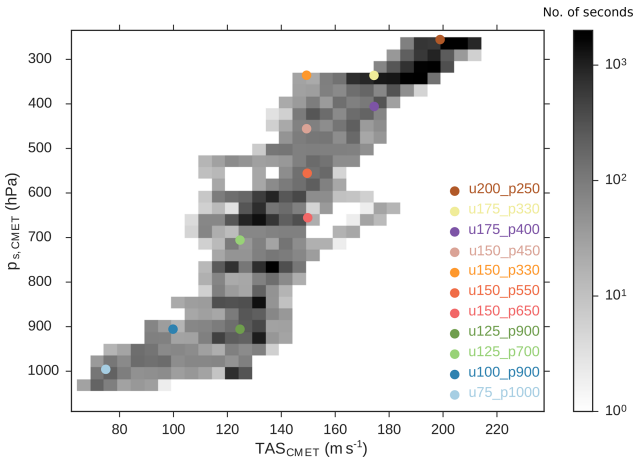

Figure 3. A 2-D histogram of flight conditions (pressure and TAS) recorded at 1 Hz by the CMET system at the nose boom during SALTRACE. Pixels are color coded with the number of seconds spent in the corresponding condition. Colored dots represent the selected test cases for the CFD investigations described in Table 2.

The numerical method relies on the solver InterFoam included in OpenFOAM. Numerical schemes for solving the flow are second-order implicit schemes both in the spatial and in the temporal discretization (Rhie and Chow, 1982). The Courant number, i.e., the flow speed multiplied by time resolution and divided by space resolution, is limited to 0.8 globally and to 0.2 at the interface, and the domain size is 10 times larger than the droplet, as suggested by Yang et al. (2017). The simulations have been performed with a water to air density ratio of 1000 : 1. Surface tension decreases with temperature from $\sigma = 0.75\,N\,m^{-1}$ at $T = 278\,K$ to $\sigma = 0.70\,N\,m^{-1}$ at $T = 305\,K$ (Vargaftik et al., 1983). The effect of a change in droplet surface tension due to the presence of impurities is not considered which seems to be a reasonable assumption given that salts increase the surface tension of seawater only by less than 1 % (Nayar et al., 2014).

3 Results and discussion

3.1 Airflow distortion, particle concentration, and OAP reference speed

Aerosol concentrations are usually expressed as particle number (or mass) per unit volume. Since the aerosol particles are embedded in the air, and the air density depends on pressure and temperature, the aerosol concentration depends as well on these parameters. Therefore, sampling conditions, e.g., the flight level pressure or the flow-induced pressure distortion at the measurement location, influence the concentration measurement directly.

3.1.1 Measured and simulated airflow

To understand the effect of different flight conditions on the measurements, we selected 11 test cases (see Table 2) for the simulations with initial data (p_s, T, TAS) chosen from flight conditions recorded during SALTRACE. Figure 3 shows a frequency histogram of the static pressure p_s and the TAS recorded by the CMET system during the SALTRACE campaign. The colored dots represent the 11 selected cases. Only certain combinations of p_s and TAS represent typical flight conditions for the DLR Falcon. For example, low pressure (high altitude) is associated with higher aircraft speed (when air density is lower, the aircraft needs to fly with a higher speed to have the same lift). As an example for all test cases, we first analyze the result for the specific test case u100_p900 ($TAS = 100\,m\,s^{-1}$ and $p_s = 900\,hPa$; see Table 2). Figure 4 shows the simulated airflow in a vertical plane through the Falcon wing where the simplified probe is mounted (white region). The local pressure (a) and the local air speed (b) are expressed as relative deviations (in percent) from free stream conditions. During flight, the pressure above the aircraft wing is lower than in the free stream, while the pressure below the wing is higher, resulting in a lower air speed at the wing-mounted probe compared to free stream conditions (Fig. 4b). Pressure and velocity changes in front of an obstacle are a function of the distance from the obstacle. In the case of an incompressible flow, Stokes provided an analytical expression for the velocity field in front of a sphere. However, in the case of a compressible flow, a necessary assumption for a fast-flying aircraft ($TAS > 150\,m\,s^{-1}$), analytical solutions have not been found yet. Figure 5 shows the ratio between the local conditions near the probe and free stream conditions for pressure (a) and air speed (b) as a function of the distance from the instrument head. The different colors represent a selection of test cases with different TAS (increasing from light-blue to brown). The gray round shape symbolizes the simplified instrument mounted in a canister below the aircraft wing. The pitot tube is sketched in dark gray. The location of the static port is marked with a vertical red line, whereas the location of the tip of the pitot tube is marked

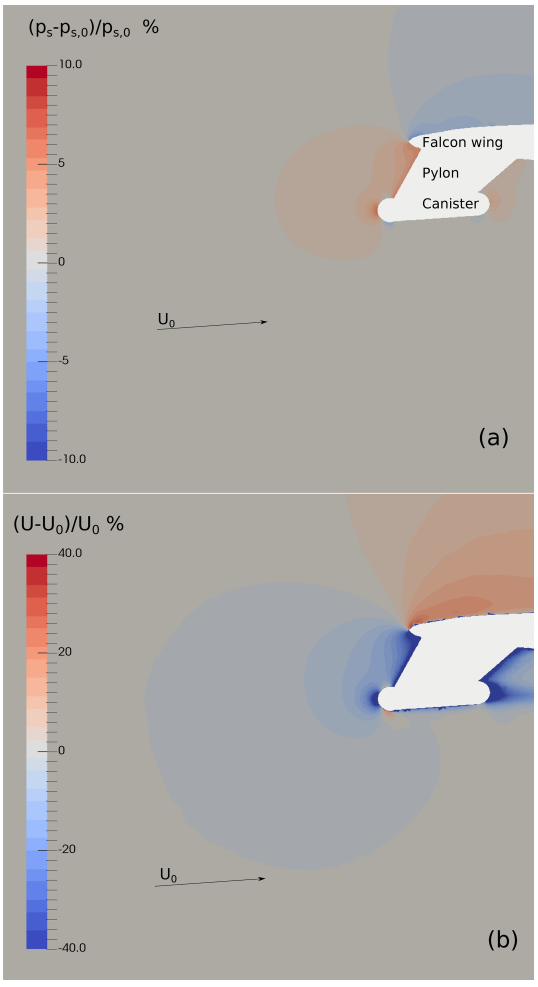

Figure 4. Vertical slice through the probe center and along the flow direction for the simulated test case u100_p900. The white area represents the aircraft wing with the pylon and the probe installed. Colored contours illustrate the static pressure p_s **(a)** and the velocity field **(b)** expressed as the ratio compared to the free stream values. The overpressure in front of the probe is slowing down the flow field.

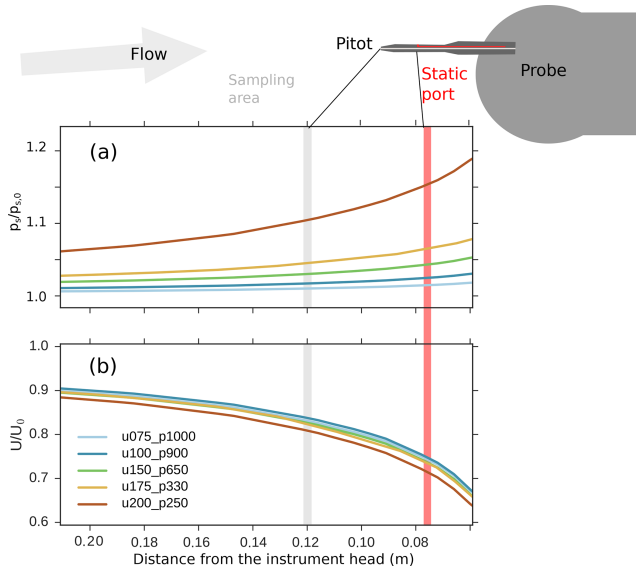

Figure 5. Static pressure and velocity normalized by the free stream values calculated along a streamline as a function of the distance from the instrument head. Different colors represent different tests described in Table 2. The gray area marks the pitot tube location, while the red area marks the static port location. The pitot tube was designed to measure the pressure conditions representative of the sampling area of the instrument.

with a light gray line. Note, that the sampling area of the instrument is located at the same horizontal distance from the instrument head as the tip of the pitot tube, thus conditions at the light gray line should be representative of the location of the aerosol measurement. Contrary to the incompressible case, where the ratio U/U_0 is independent of the air speed U_0 (TAS), here due to compressibility the ratio is changing with U_0. An incompressible case in Fig. 5b would be similar to the u75_p1000 simulation where the compression effect is still small. As visible in this figure, the relative air speed difference between the free stream and the instrument location increases with TAS.

Errors in the pressure measurement can arise due to the position of the static port relative to the tip of the pitot tube. For a pitot tube in a laminar flow, errors are a function of the pitot tube length and the static port distance from the tip (Barlow et al., 1999). For CAS, the static port is located 44 mm downstream of the tip. According to Fig. 5a this difference will lead to a deviation in the pressure since the pressure is decreasing exponentially as a function of the distance from the probe head. However, these differences are still small compared to the position error. For example, considering the numerical test case u100_p900 (see Fig. 5), a CAS pitot tube reading will overestimate p_s by 2.5 % and underestimate air speed by 26 % as compared to the free stream values.

To understand the differences between the free stream conditions and the conditions at the wing-mounted instrument, we analyzed the data collected during SALTRACE and compared them with the results from the numerical simulations. Figure 6 shows a statistical analysis of ratios between values read by the CAS pitot tube and the CMET system during SALTRACE for temperature (a), static pressure (b) and air speed (c). The histogram color map refers to the number of seconds of available 1 Hz data of these ratios as function of specific T_{CMET}, $p_{\mathrm{s,CMET}}$, $\mathrm{TAS}_{\mathrm{CMET}}$. The different marker colors indicate the selected simulation test cases described in Table 2. The simulation results in Fig. 6 are valid for the pitot tube static port location. The temperature difference between free stream conditions and the probe is decreasing from 3.5 % to 0.5 % with increasing temperature. This effect is a response to a lower aircraft speed at low altitude (see Fig. 3). Also, the trend of the pressure difference in Fig. 6b shows a similar behavior decreasing from 20 % at high to

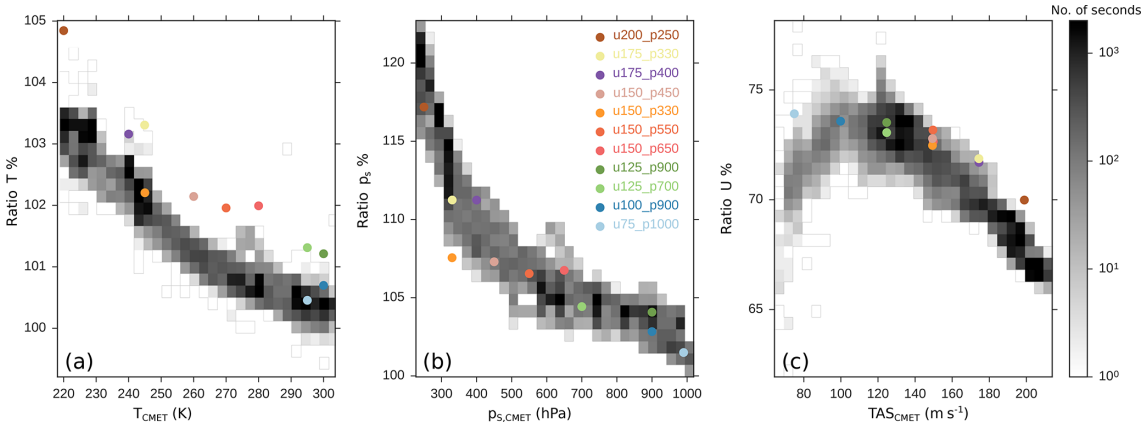

Figure 6. Statistical analysis of ratios between values read by the CAS pitot tube and the CMET system during SALTRACE. The histogram color map refers to the number of seconds of data at 1 Hz. Colored dots represent the selected test cases for the CFD simulations described in Table 2.

1 %–2 % at low altitude. Local conditions differ from free stream also for air speed as shown in Fig. 6c with air speed being 25 % to 35 % lower at the probe location compared to the free stream. In this context, it is worth mentioning that a longer pitot tube, as in the case of CAPS (as compared to the CAS used during SALTRACE), will reduce the position error because the deviation of the pressure in front of the probe from the free stream pressure is exponentially decreasing with increasing distance from the probe head. Indeed, the differences between TAS_{CMET} and PAS_{CAPS} are only 15 % to 20 % (see the Appendix, Fig. A4).

The simulated conditions at the pitot tube location well represent the measured data from the SALTRACE campaign with small deviations (see Fig. 6). These comparisons indicate that our simplified instrument model geometry and the exclusion of the fuselage in the simulations introduce an uncertainty of less than 5 %. The deviation of U for u75_p1000 (Fig. 6c) from the measurements may be related to changes of the aircraft configuration at low altitude when the flaps are used. The systematic differences in temperature (Fig. 6a) need a separate explanation. Like pressure also the temperature is increasing near the probe head. For this reason, temperature measurements are sensitive to the measurement location. In the CAS and CAPS instruments, the temperature sensor is installed in the back (see CAPS photograph in the Appendix, Fig. A5), and the temperature measurement is corrected using the Bernoulli equation to obtain the temperature at the pitot tube. Consequently, errors in pressure will lead to an error in the temperature. This provides a possible explanation for the 1 % difference between the temperature values obtained from the instrument and the simulations (Fig. 6a). The temperature bias is probably due to a combination of static pressure bias, instrumental uncertainty, and model parameterization. Nevertheless, an error of 1 % in T will lead, according to Eq. (3), to a PAS error of about 0.5 %. Thus, the uncertainty of the temperature has only a very small contribution to the uncertainty of the PAS and is therefore negligible.

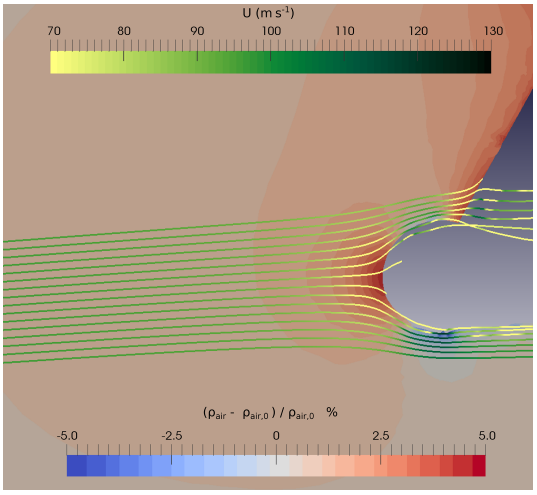

Figure 7. Relative deviation of air density ρ_{air} around the probe from the air density $\rho_{air,0}$ in the free stream for the test case u100_p900 as contours in the background (color code at the bottom). Lines in the foreground represent streamlines colored with the local airflow velocity U (color code at the top).

3.1.2 Simulated particle concentration and sampling efficiency

In this section, we use simulated flow fields (Sect. 2.2.2) to study how the airflow around a wing-mounted instrument affects the particles. For each class of particles with a different density ρ_p and diameter d_p, we release 2×10^5 particles upstream the instrument at the domain border and calculate the sampling efficiency f_{eff} as the ratio between particles passing through the sampling area and particles released at the domain border. Counting the particles is done using

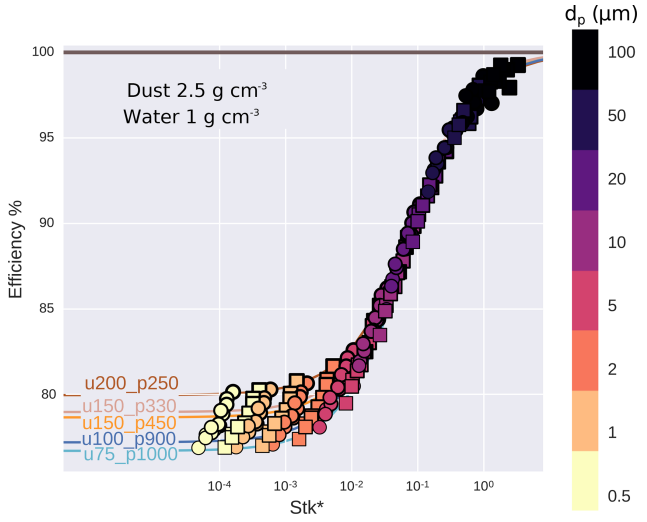

Figure 8. Sampling efficiency calculated as a function of modified Stokes number (see Eq. 4) for selected numerical test cases of Table 2. Each marker represents a run where we released 2×10^5 particles of a specific diameter (colors) and density (dust: squares; water: circles) in front of the probe in the computed flow field. Sampling efficiency is defined as the ratio between particles released and particles passing through the sampling area, renormalized by the corresponding areas. Curves are obtained by fitting the data with a sigmoid function (see text).

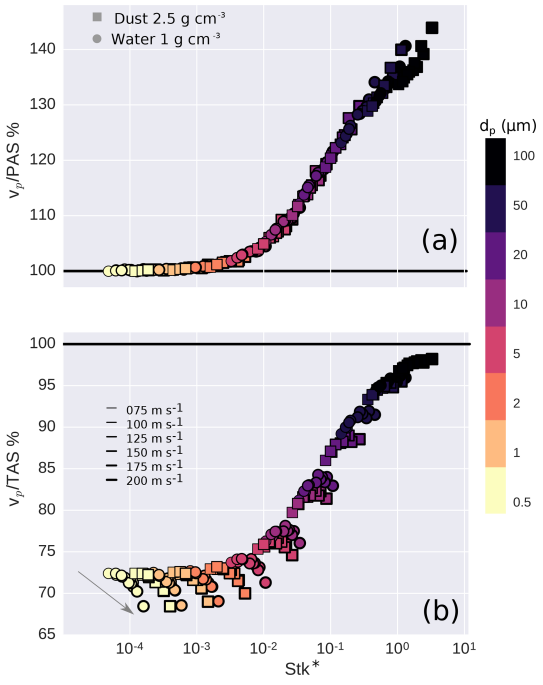

Figure 9. Particle velocity v_p normalized by PAS_{CAS} **(a)** and TAS_{CMET} **(b)** as a function of modified Stokes number Stk^*. The contour thickness of the markers increases with TAS. Colors denote particle diameters.

a Gaussian kernel that reduces the dependency of the estimated particle concentration on the computational grid (Silverman, 1986). These numbers are normalized by the ratio of the releasing area to the sampling area. Figure 7 shows an example of streamlines around the wing-mounted instrument. Contours are color coded with density ρ_{air} and streamlines with air speed U. Air speed decreases in the vicinity of the probe and streamlines are bent due to the flow distortion caused by the overpressure. This effect has been observed already by King (1984). The ability of particles to adapt to flow changes is expressed by the Stokes number Stk. The Stokes number represents the ratio of particle's response time to the characteristic fluid timescale. Particles with a small Stokes number react immediately to flow changes and consequently follow the streamlines, as in the case of submicron-sized particles. To generalize the analysis according to Israel and Rosner (1982) into the non-laminar flow regime, we use instead of the original Stokes number Stk a modified Stokes number Stk^*, which is defined as

$$Stk^* = \frac{\rho_p U d_p^2}{L 18 \mu_{air}} \psi(Re_p) \text{ where } Re_p = \frac{p_s U d_p}{T \mu_{air} R_s}. \quad (4)$$

μ_{air} is the dynamic viscosity of air, R_s is the specific gas constant of air (287.1 J kg^{-1} K^{-1}) and ψ the additional correction factor as a function of particle Reynolds number Re_p varying from 1 in the laminar case to values smaller than 0.1 in the case of fully turbulent flow (see Fig. 3 of Israel and Rosner, 1982 or Eq. 36a of Wessel and Righi, 1988 for $\psi(Re_p)$). L is a characteristic fluid length, here fixed to 1 m. The TAS is used for U in Eq. (4). Figure 8 shows the sampling efficiency as a function of the Stokes number Stk^*. Different symbol colors represent particle diameters whereas the differently colored lines represent fits of sigmoid functions to the Stokes numbers of the selected test cases. The sampling efficiency f_{eff} is well approximated by the sigmoid fits. In the Appendix, Table A3 presents the sampling efficiencies of the selected test cases for different particle diameters and densities. For large Stokes numbers, the simulated droplet concentration at the probe is minimally affected by the flow. For example, $f_{eff} > 95\,\%$ holds for diameters larger than 100 µm. For small particles with less inertia, the effect caused by the flow is more evident, and it leads to a sampling efficiency of $\sim 77\,\%$ (test case u100_p900). This effect appears less marked for test cases at higher TAS and lower pressure, e.g., for u200_p250, where 80 % of the small particles reach the sampling area. It is worth mentioning that simulations considering only the wing itself without the instrument (not shown) result in f_{eff} values around 91 %–92 % for small Stk^* illustrating that both the wing and the instrument affect the flow at the sampling location.

The change of particle inertia as a function of particle diameter plays a significant role also for particle velocity. As King (1984) reported, particle speed v_p may significantly differ from the local air speed depending on their Stokes

number. Figure 9 shows the particle speed v_p normalized by PAS (a) and TAS (b) for the selected test cases. Different colors represent different particle diameters and marker thickness is a function of the TAS. For each simulated case, particle speed is calculated as an average of the sampled particles. For diameters smaller than 5 µm, PAS is a reasonable approximation of particle speed. Larger particles with a higher Stokes number, are less influenced by the airflow change due to their inertia. For this reason the particle velocity v_p for diameters $d_p > 50$ µm can be well approximated using the TAS with an error smaller than 10 % (see Fig. 9b). Figure 9b also shows that at higher TAS (see gray arrow) the normalized particle speed is lower, especially for smaller particles, because of the lower normalized air speed (Fig. 5).

3.1.3 Compressibility effect on particle concentration: a correction strategy

The PAS is lower than TAS (during SALTRACE, PAS/TAS $\simeq$ 70 %; see Fig. 6c). Thus, for a given number of particle counts per time interval, particle number concentrations calculated using PAS as a reference speed are larger than values obtained using TAS. Furthermore, the temperature and the pressure at the probe are higher than in the free stream as shown in Fig. 6a and b. Wrong temperature and pressure values will lead to errors of the concentration values after conversion to other conditions, e.g., those in the free stream. A higher pressure value leads to a lower calculated concentration, whereas it is directly proportional to the temperature value used.

Weigel et al. (2016) provide a method to derive ambient number concentration from data of underwing instruments that is primarily based on the concept that the air compression near the instrument causes a corresponding densification of the number concentration of airborne particles. Subsequently, they take into account a size-dependent correction factor that corrects the effect of the inertia of large particles. Their inertia correction is mainly assessed on the basis of the circularity of droplet images taken by an OAP at a resolution of 15 µm. Weigel et al. (2016) conclude that particles with diameters $d_p < 70$ µm follow the airflow and thus require no inertia correction. On the contrary, our simulations (see, e.g., Fig. 9) show a notable impact of the particle inertia already for particle diameters $d_p = 10$ µm (their speed is about 10 % higher than the air speed; particle density 1 g m^{-3}) and a strong impact for 50 µm particles (about 25 % faster than air). These particle simulations are consistent with results (not shown) from a simplified numerical particle motion model using the simulated flow fields (Sect. 3.1.1) as input and Eq. (3.5) of Hinds (1999) (which is based on Clift et al., 1978) to calculate the drag force on the particles. Therefore, we conclude that inertia needs to be taken into consideration for particles larger than about $d_p > 5$–10 µm.

The main idea of our concentration correction strategy is to express the sampling efficiency f_{eff} as a function of the Stokes number and a parameter α describing the difference between the probe and the free stream conditions:

$$\alpha = \frac{p_{s,probe}}{p_{s,free}} \frac{T_{free}}{T_{probe}} \frac{PAS}{TAS}. \quad (5)$$

Using α as variable, the sampling efficiency f_{eff} (in %) can be approximated with the sigmoid equation:

$$f_{eff}(\alpha, Stk^*) = k_0 + \frac{100\,\% - k_0}{1 + e^{k_1} \cdot (Stk^*)^{k_2}}. \quad (6)$$

The sampling efficiency values from the simulations for different flight conditions and for different distances from the probe were used to fit the coefficients in Eq. (6), finding $k_0 = 83.7\,\% \cdot \alpha + 14.6\,\%$, $k_1 = 1.86 \cdot \alpha - 3.66$, and $k_2 = -0.87$. Equation (6) allows correcting particle concentrations as a function of the modified Stokes number and flight conditions. For each particle diameter d_p, the first step of the correction is to estimate the corresponding modified Stokes number (Eq. 4) using free stream conditions (p_s, T, TAS) and a range of particle densities. Secondly, the sampling efficiency f_{eff} is calculated using the Eq. (6). Finally, the ambient number concentration N_i in each diameter bin i (covering the diameter interval from $d_{p,i}$ to $d_{p,i+1}$) is calculated as follows:

$$N_i = \frac{\text{number of detected particles in bin } i}{\text{size of sampling area} \cdot \text{TAS} \cdot \text{measurement duration} \cdot f_{eff}(d_p)}. \quad (7)$$

Note that Eq. (6) is an extension of the formula by Belyaev and Levin (1974) where the deviation of the sampling efficiency from unity was found (via a direct method) to be a sigmoid function of the Stokes number and to be proportional to (PAS/TAS – 1).

Figure 10 compares estimated sampling efficiencies with sampling efficiencies obtained directly from the simulations. Two different estimation methods are considered to illustrate the benefit of the new correction strategy proposed here. In the "old method" (Fig. 10a) concentrations are calculated using PAS as reference speed, which are then corrected with an adiabatic expansion between the probe and free stream conditions. In contrast, the "new method" (Fig. 10b) uses TAS as reference speed and the fitted sampling efficiency f_{eff} sigmoid function from Eq. (6). The concentrations calculated with the "old method" are correct for describing the behavior of small particles (see Fig. 10a). Small particles exhibit enough mobility to follow the airflow. In contrast, using probe conditions (PAS) and an adiabatic expansion overestimates the particle number concentration by up to 25 % for coarse-mode particles ($d_p > 2$ µm). This difference will grow even larger if PAS deviates more from TAS. The "new method" (Fig. 10b) shows good agreement with deviations smaller than 2 % for the complete size range. The "new method" not only has the advantage of reducing concentration errors but it also reduces the size dependence of these errors.

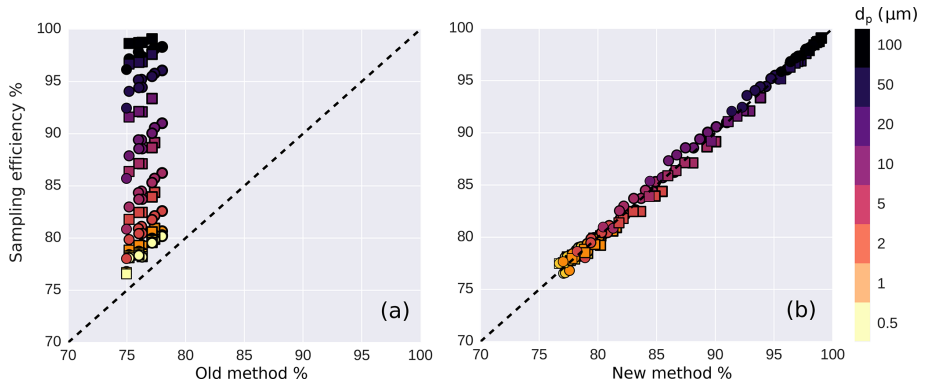

Figure 10. Simulated sampling efficiency f_{eff} versus sampling efficiencies estimated from the simulations using the "old method" **(a)** and the "new method" **(b)**. Different markers indicate different numerical test cases, while the colors refer to the particle diameter. For the "old method", the concentration is calculated using the probe conditions and using an adiabatic expansion to free stream conditions. For the "new method", the concentration is calculated using free stream conditions and corrected for the flow distortion by applying Eq. (6). To obtain the sampling efficiency, concentrations from both methods are divided by concentration assumed in the free stream.

3.1.4 Reducing OAP errors related to OAP reference speed

The OAP reference speed is usually derived from measurements with a pitot tube being part of the OAP, thus by default represent local conditions. As explained in Sect. 2.1.1 the OAP reference speed is critical for the correct reconstruction of the particle size in the direction of the flow. OAP instruments mainly cover particle diameters larger than 30 µm. Figure 9b shows that particle speed v_{p} in this size range is close to TAS, i.e., v_{p} is minimally affected by the flow around the aircraft. Thus, using the PAS as a OAP reference speed will result in images flattened along the flow direction, with a relative error proportional to the relative offset of PAS from TAS. On the contrary, TAS is a good approximation for the OAP reference speed minimizing image distortion errors. Therefore, the basis of the correction method proposed here is to calibrate the pressure sensors such that the pitot tube of the OAP reports TAS instead of PAS. This can be achieved by performing a similar analysis as presented in Fig. 2. In our case, the CAPS pitot tube was re-calibrated using data from the CMET system together with simultaneous measurements of CAPS during some test flights. A linear fit[2] between the free stream conditions from the CMET system and the probe conditions from CAPS is performed for q_{c} and p_{s}. A similar analysis was conducted using NASA DC-8 data provided by the MMS for ATom-2, ATom-3, and ATom-4.

[2]For DMT's instruments, like the CAPS, the pitot tube calibration can be done modifying in the PADS acquisition software the file "config.ini" with the coefficients obtained with the linear fit. Since in PADS temperature measurements are derived using the Bernoulli equation, reported values depend on the dynamic pressure. Consequently, the temperature and PAS values need to be recalculated during the post-processing, using the dynamic pressure at the probe obtained by inverting the fit coefficients.

Figure 11 shows the ratio of the air speed reported by the CAPS instrument and the TAS during the NASA DC-8 campaigns ATom-1 (a, 2016), ATom-2 (b, 2017), and the Falcon campaign A-LIFE (c, 2017). Whereas during ATom-1 the CAPS pitot tube calibration was based on the manufacturer settings reporting PAS, the CAPS pitot tube was calibrated to match free stream conditions reporting TAS during ATom-2 and A-LIFE. The obtained air speed during ATom-2 and A-LIFE, named hereafter TAS_{CAPS}, shows on average a 2 % deviation from the TAS_{CMET} and 3 % from TAS_{MMS}. Contrary, during ATom-1, the uncorrected PAS_{CAPS} shows an offset with the TAS_{MMS} larger than 15 % (see Fig. 11a).

3.2 Droplet deformation

The recorded shape of droplets using an OAP is a combination of the real particle shape influenced by the sampling conditions and, as discussed above, instrumental effects such as those resulting from the settings to calculate v_{p}. In the following we evaluate OAP image distortions along the flow direction to estimate the correctness of the assumed particle speed v_{p} and to investigate aerodynamic effects on the real droplet shape. Since ice crystals mostly present irregular shapes, we limit our analysis to liquid droplet images.

Figure 12 shows sequences of gray-scale images taken with the CIP in cloud passages during the ATom-4 campaign. The vertical dimension (y axis) of these images is the dimension of the optical array (being perpendicular to airflow direction) and the horizontal dimension (x axis) initially is the time dimension, which is converted to length using the OAP reference speed. As discussed, using PAS would result in particles flattened in the horizontal dimension since for particles in the OAP size range v_{p} is higher than PAS (Fig. 9). For the particles shown in Fig. 12 pressure and temperature conditions recorded during the passages ensure droplets being in a liquid state. Image colors are the three levels of shadow

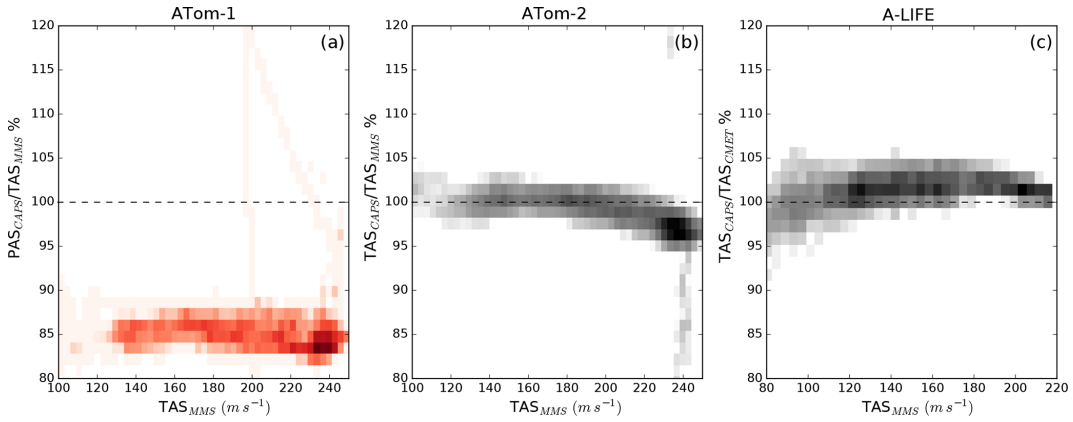

Figure 11. Air velocity recorded by CAPS normalized by air velocity recorded by the default aircraft systems. Data from ATom-1 **(a)**, ATom-2 **(b)**, and A-LIFE **(c)** are shown. While the CAPS pitot tube was calibrated to match PAS during ATom-1, it was calibrated to match the TAS during ATom-2 and A-LIFE. The pixels are color coded with the number of seconds of data at 1 Hz.

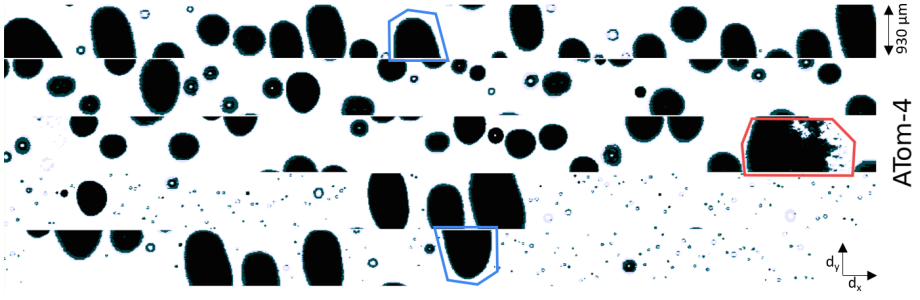

Figure 12. CIP gray-scale images collected in a liquid cloud during the ATom-4 campaign. Colors are the three levels of shadow recorded on each photodetector. The vertical scale is 62 pixels of 15 µm, while the horizontal axis represents the timeline. The red contour indicates splashes due to a droplet breakup. Blue contours highlight examples of large particles that are not fully recorded.

recording on each photo-detector. The vertical scale is 62 pixels, where each pixel represents an area of 15 µm · 15 µm. Images were taken using the TAS_{CAPS} as reference speed. TAS_{CAPS} is obtained as explained in Sect. 3.1.4. The smaller droplet images are nearly circular, whereas larger droplets show deformed shapes, with the deformation becoming increasingly visible with increasing size. The red contour highlights droplet breakup and the blue ones indicate examples of large deformed droplets that are not fully recorded by the array.

To better understand the droplet deformation and v_p deviations from TAS we performed a statistical analysis of droplet images. Figure 13 compares the deformation ratio, defined as the ratio between main droplet axes d_y/d_x for the different droplet images. To extend our analysis, we included datasets collected during different campaigns (as indicated by the marker colors). The images were taken during selected flight sequences where liquid droplets were encountered. Following Korolev (2007), we choose droplet images showing only a small Fresnel effect and entirely contained in the field of view of the CIP, except for the ATom-4 data marked in light blue (Fig. 13b) where also particles which were not fully recorded were included. Image analyses were conducted using the image processing library OpenCV (Bradski, 2000) (using a contours threshold of 0.8). Error bars in both directions are calculated according to the CIP size resolution of one pixel, corresponding to 15 µm and solid lines indicate the mean value of each campaign. Red markers refer to measurements during ATom-1 with the PAS_{CAPS} set as reference speed for particles. Dark blue markers refer to ATom-2 when the TAS_{CAPS} was used after re-calibration of the pitot tube (Fig. 11b). In the case of ATom-1 (red markers), the use of the PAS causes a squeezing effect in the images along the flow direction, i.e., $d_y/d_x > 1$ for most droplets. Contrary, during ATom-2, ATom-4, and A-LIFE the ratio d_y/d_x is more evenly distributed around 1 illustrating the benefit of using TAS_{CAPS} as reference speed. For small droplets (< 150 µm) the large scattering is due to the limited instrument resolution (see error bars). For larger droplets, error bars expressing the instrumental resolution cannot explain the data scattering. The scattering also cannot be explained by air speed errors only. A possible explanation is the instability effect on the surface of the droplets, as presented in Szakall et al. (2009), and dis-

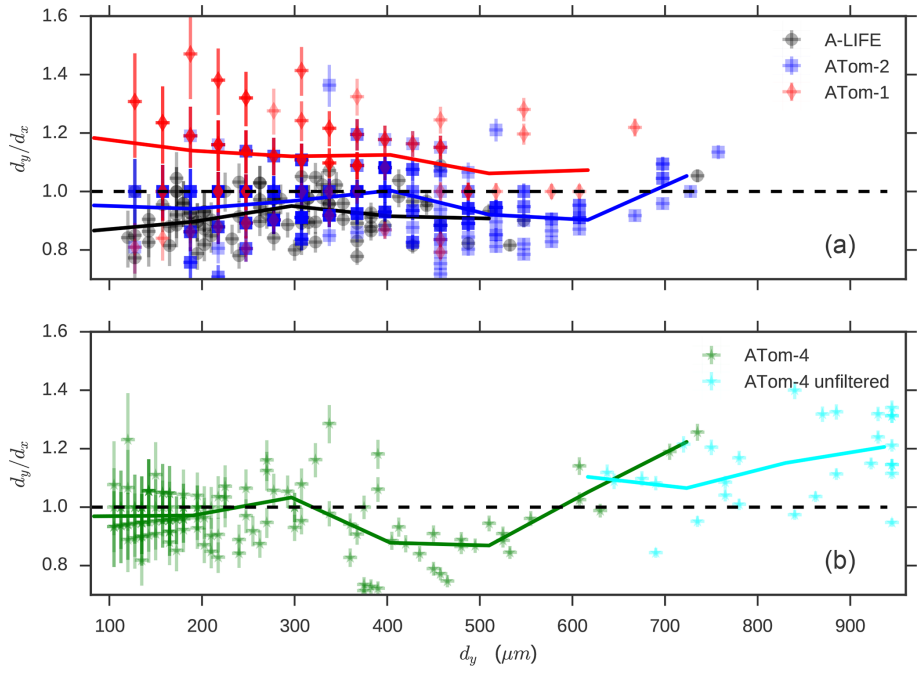

Figure 13. Ratio between the main axis lengths (d_y/d_x) of droplets recorded by the CIP during different campaigns (indicated by color). Error bars represent the CIP pixel resolution (15 µm). Considered are only particles recorded during cloud passages where the temperature ensures a liquid droplet state. Red markers in the upper panel show data from the ATom-1 mission where the CAPS pitot tube, and thus the OAP reference velocity, was calibrated to match PAS, whereas the data of the other campaigns (shown in dark blue, black, green, light blue) were collected when the CAPS pitot tube was calibrated to match TAS (see also Fig. 11). Lines indicate the mean values of each campaign within several wider size intervals. Data from ATom-4 (green), including particles not fully covered by CIP (light blue), are shown in the lower panel.

cussed below. To better understand these phenomena, we extend our study by using a droplet deformation model.

3.2.1 Quantification of droplet deformation

Before analyzing the results of the droplet deformation model, we test the numerical results by comparison with data from the experimental work of Vargas (2012). We selected the experiments of Vargas (2012) where they observed a 1032 µm water droplet approaching an aircraft wing as test for our simulations. The selected experiment consisted of a droplet that is vertically falling on a horizontally rotating arm with an attached wing profile. The wing profile rotated with a speed of 90 m s^{-1}. In Fig. 14 selected images at different points of time in the Vargas (2012) experiment (upper half of the upper panel) are compared with the corresponding simulation results (lower half of the upper panel). Since the flow circulating around the particle is changing with time, the lower panel also shows the corresponding slip velocity values U_{slip} defined as the droplet speed relative to the suspending air. To have a more explicit comparison of the change of droplet shape, the lower panel of Fig. 14 shows the lengths of the droplet's axes of the experimental data (dots) and those simulated (lines) as a function of time and relative speed U_{slip}. The lengths of the axes of individual droplet images are determined using the length and width of a circumscribing rectangle (as sketched in the Fig. 14). As visible in the upper panel, when the droplet approaches the airfoil, U_{slip} increases and the droplet starts to be squeezed along the flow direction, until the breakup process occurs at the droplet edges for $U_{\mathrm{slip}} \sim 60\,\mathrm{m\,s^{-1}}$. The model reproduces the behavior of the droplet over time qualitatively well with deviations smaller than 2 times the uncertainties of the experimental data. To extend our result to different droplet diameters and flight conditions, we use the Weber number We which represents the ratio of the aerodynamic forces to the surface tension forces. We is defined as

$$We = \frac{d_{\mathrm{p}} \rho_{\mathrm{air}} U_{\mathrm{slip}}^2}{\sigma}. \tag{8}$$

σ is the surface tension and d_{p} the droplet diameter. In our case, U_{slip} is changing with time from zero when the droplet is in still air, to its maximum value when the droplet is recorded (U_{slip} =TAS – PAS for large Stokes numbers).

To understand the data deviation found in Fig. 13 we simulated different droplet diameters. The results are shown in Fig. 15 where the deformation ratio is plotted for the simulated droplets as a function of the We. Different marker colors represent different test cases where we varied droplet diameters. As a droplet approaches the airfoil, the relative

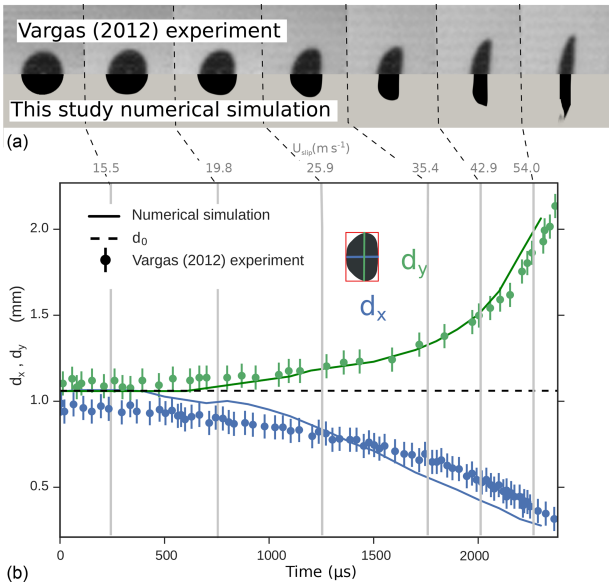

Figure 14. Simulations for a test case with a 1032 µm diameter droplet reproducing an experiment by Vargas (2012). In the upper panel, the upper halves display images recorded by Vargas (2012), while the lower halves show corresponding simulated droplets from the present study. The airflow comes from the left. Time and relative air speed increase from the left to the right. The lower panel shows changes of both droplet axes' lengths (d_x and d_y; see inlay image) as a function of time and relative velocity (labeled at the top) for the experiment from Vargas (2012) (dots) and for the simulations (continuous line).

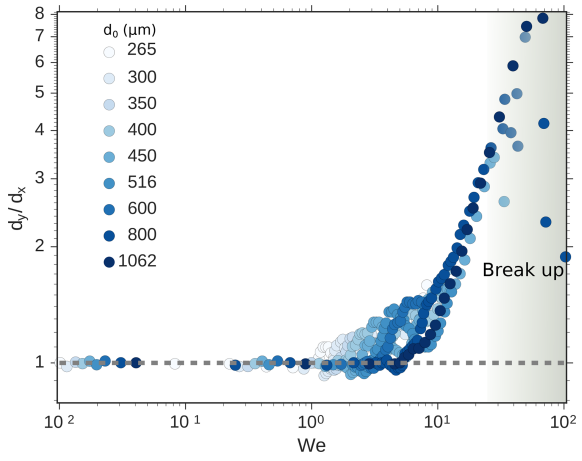

Figure 15. Droplet axis ratio (d_y/d_x) as a function of Weber number (We). Different dots represent different simulations where we increased the initial droplet diameter d_0 from 265 µm (white) to 1062 µm (dark blue). The gray area represents the region where droplet breakup can occur.

speed U_{slip} increases and therefore the We also increases. The mechanism of droplet deformation and breakup is governed by an interplay of aerodynamic, tension and viscous forces. The distortion is primarily caused by the aerodynamic forces, whereas the surface tension and viscous forces, respectively, resist and delay deformation of the droplet. Gravitational forces play a minor role since the ratio of aerodynamic forces over gravitational forces $\rho_{\text{air}} U_{\text{slip}}^2 / \rho_{\text{p}} g d_{\text{p}}$, is much larger than unity. When aerodynamic forces grow larger than the surface tension forces, they deform the droplet causing in the worst case a breakup of the droplet by aerodynamic shattering (Craig et al., 2013). For a droplet approaching an airfoil, the viscous forces are smaller than aerodynamic and surface tension forces and the droplet breakup process is mainly controlled by We. Howarth (1963) and Oertel (2010) showed that a droplet requires a critical Weber number (We_{crit}) for breakup. Wierzba (1990) studied We_{crit} when droplets interact with an instantaneous airflow in a horizontal wind tunnel. Kennedy and Roberts (1990) studied the breakup of droplets subject to an accelerating flow in a vertical wind tunnel.

The critical Weber number We_{crit} from different experimental studies with uniform airflow varies around 11 ± 2. Craig et al. (2013) also assumed $We_{\text{crit}} = 12$ for determining the droplet critical diameter d_{crit} for aerodynamic shattering on an inlet. For a droplet approaching an airfoil, since U_{slip} is changing and droplets can adjust their shape to the changing flow, droplet breakup occurs at larger We compared to the case of a uniform airflow (Vargas, 2012). On the other hand, the rapid change in the flow creates instabilities and droplets show a deformed shape already at $We \sim 1$ (see Fig. 15). Garcia-Magariño et al. (2018) characterized the We_{crit} providing an analytical equation:

$$We_{\text{crit}} = 17.5 + 17.9\tau \text{ where } \tau = \frac{\sqrt{(\rho_{\text{p}} d_{\text{p}}^3 \pi / (6\sigma))}}{U_{\text{slip}} / \frac{\partial U_{\text{slip}}}{\partial t}}. \quad (9)$$

Using the simulated airflow fields and Eqs. (8) and (9), we can express the critical diameter d_{crit} as a function of relative particle speed U_{slip}. U_{slip} is a function of TAS and mounting position (see Fig. 5). Therefore, for a specific configuration, d_{crit} can be expressed as a function of TAS. Figure 16 shows how d_{crit} decreases when TAS increases. The two colors in Fig. 16 refer to the two different mounting configurations for the DLR Falcon and the NASA DC-8. The difference in the mounting configurations between the Falcon and the DC-8 is the main reason for the differences in the relative particle speed U_{slip} for a given droplet diameter d_{p} and TAS, which results in differences in d_{crit} as shown in Fig. 16. Figure 16 also shows that pressure and temperature have only a rather small effect since results for different test cases with same TAS lie on top of each other. Generally, a large difference between the free stream and the probe air speed will increase the slip velocity U_{slip} and consequently the Weber number, reducing the critical diameter for droplet breakup. This explains why critical diameters for the Falcon configuration are smaller than for the DC-8.

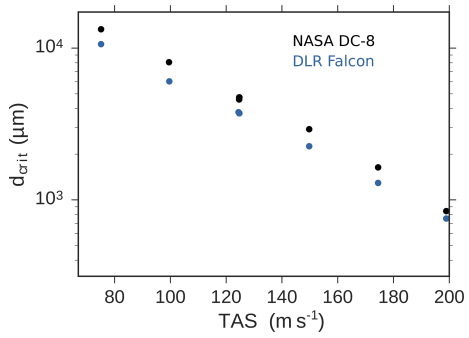

Figure 16. Critical diameter for droplet breakup as a function of TAS for the DLR Falcon and the NASA DC-8 configuration.

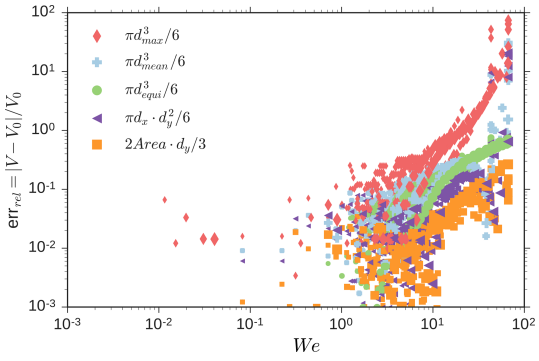

Figure 17. Relative error of the droplet volume as a function of Weber number (We) for different volume approximations (colors). V_0 is the original droplet volume. Different marker sizes represent different simulations where we varied the droplet diameter.

In general, smaller droplets resist deformation more than larger ones because the small diameter translates into a larger curvature. However, relatively small droplets can show instability phenomena where the droplet surface starts to oscillate (called Taylor instability) which are not resolved in our simplified droplet model. This effect can be responsible for some additional scattering of data in Fig. 13.

The aerodynamic deformation of larger droplets, as modeled in Fig. 15, is only partially visible in the statistical analysis presented in Fig. 13, since large droplets have a higher chance to be only partially recorded inside the field of view, and consequently being excluded from the study. However, when considering particles not fully recorded inside the field of view, the deformation becomes visible for particles larger than about 600 µm, as shown for the ATom-4 data in Fig. 13b. Most have ratios $d_y/d_x > 1$ going up to 1.4 which is confirmed by the mean values (lines) being larger than unity. Since the y-extension of these particles is not fully covered by the imaging array, the real ratio d_y/d_x is probably even higher as indicated by the shape of several incomplete droplet images in Fig. 12 (blue contours).

3.2.2 Impact of droplet deformation on particle volume estimation

As observed in Figs. 12, 14, and 15 large liquid droplets show a large distortion with d_y/d_x values around 2 and larger, when measured with an OAP aboard a fast aircraft. This raises the question which diameter should be used to describe the size of deformed droplets. Different diameter definitions exist (Korolev et al., 1998). Here, we use as approximation diameters d_{approx}, the maximum diameter $d_{\text{max}} = \max(d_x, d_y)$, the mean diameter $d_{\text{mean}} = (d_x + d_y)/2$, and the area equivalent diameter $d_{\text{equi}} = 2\sqrt{\text{Area}/\pi}$ where Area is the droplet cross section area calculated from the image. Two additional approximations are used: $d_{\text{spheroid}} = (d_x d_y^2)^{1/3}$ derived assuming a spheroid rotated around the x-axis and $d_{\text{asym}} = (4/\pi \cdot \text{Area} \cdot d_y)^{1/3}$. McFarquhar (2004) noted that inconsistencies in particle size definitions could have significant impacts on mass conversion ratios between different hydrometeor classes used in numerical models. Errors in the droplet volume approximations have a direct effect on the liquid water content (LWC) estimation. We use the numerical simulations analyzed in Fig. 15 to better understand possible errors in the estimation of the droplet volume. The simulated droplet shapes are processed to calculate the different approximation diameters and to estimate the corresponding approximation volumes ($V_{\text{approx}} = d^3_{\text{approx}} \cdot \pi/6$). Results are shown in Fig. 17, where the relative error ($\text{err}_{\text{rel}} = |V_{\text{approx}} - V_0|/V_0$) is plotted as a function of We. V_0 is the actual droplet volume. Using d_{max} (red diamonds), the error increases progressively with We, from 10 % at $We = 1$ until almost a factor of 10 when the breakup process starts. A better approximation is the mean diameter d_{mean} (light blue symbols). In this case, for $We < 20$, on average, the volume is underestimated by 2 % to 20 %. For larger We, the formula overestimates the volume up to a factor of 6. A more stable way to define droplet diameter is based on the equivalent d_{equi} (green circles). Also in this case, errors are growing as a function of We, passing from 3 % to 40 %. A common assumption is considering droplets as spheroids (purple triangles). In this case, using the approximation formula for a spheroid $V_{\text{approx}} = \pi/6 \cdot d_x \cdot d_y^2$ gives errors smaller than 12 % below $We = 34$. For larger We, droplets appear asymmetric, and errors can grow larger than a factor of 7. The best approximation is obtained by using d_{asym} where the volume is obtained from the formula $V_{\text{approx}} = 2/3 \cdot \text{Area} \cdot d_y$. Errors, in this case, are generally ±3 % to ±10 % and in the case of droplet breakup still smaller than a factor of 2.

4 Recommendations

The following list summarizes the proposed correction strategy to reduce flow-induced measurement errors and to express measurement uncertainties for OAP and OPC instruments. OPC and OAP measurement errors directly depend on flow conditions like pressure, air speed, and temperature.

Since free stream conditions differ from conditions at the position where the instrument is mounted on the aircraft, it is fundamental to adopt a correction scheme.

The following are recommended steps for OAPs such as CIP:

1. For imaging probes, covering particle diameters larger than 50 µm, use the TAS as the reference speed in the OAP data acquisition software. If possible, use the TAS recorded by the aircraft. Otherwise, an option could be to re-calibrate the pitot tube installed on the probe to measure free stream conditions (TAS, $p_{s,free}$, and T_{free}; see Sect. 3.1.4 and the Appendix). In this last case, the local probe conditions can be obtained during the data evaluation by inverting the calibration coefficients for p_s, q_c and using Eq. (3) to calculate the PAS.

2. Droplets are deformed by the flow distortion around the wing-mounted instrument even at low TAS, which complicates the volume estimation from OAP images. For the volume estimation, using the formula $V = 2/3 \cdot \text{Area} \cdot d_y$ is recommended.

The following are recommended steps for passive-inlet OPCs such as CAS:

1. Calculate the α parameter (Eq. 5) using the ratio between the free stream and probe conditions[3]. To do so, data from the instrument's pitot tube recording local airflow conditions (PAS, $p_{s,probe}$ and T_{probe}) at the probe are necessary in addition to independent meteorological data covering the free stream condition.

2. Estimate the modified Stokes number Stk^* based on flight conditions (p_s, ($U =$)TAS), particle diameter and density (Eq. 4). If particle density is not known, use a range of possible values to propagate the uncertainty.

3. Use Eq. (6) to calculate the correction factor f_{eff} as function of α and Stk^*.

4. For the derivation of particle number concentration, use free stream conditions (TAS) and the correction factor f_{eff} (see Eq. 7).

5. If steps 1–3 cannot be done, the lookup table in the Appendix (Table A3) can be used instead. These correction values were calculated for different diameters and two reference densities (water and mineral dust).

When designing new mounting systems, the mounting location should be selected such that the deviation between the instrument and free stream conditions, and thus also the flow-induced measurement errors, are minimized.

[3]If the pitot tube of the probe was re-calibrated to measure the free stream conditions, as recommended for OAP, probe conditions need to be obtained by using the inverse of the linear function used for the re-calibration.

5 Conclusions

This study investigated the effect of flow distortion around wing-mounted instruments. The analysis focused on open-path and passive-inlet OPC and OAP instruments. The dataset collected during SALTRACE (Weinzierl et al., 2017) was used to estimate flow differences between the free stream and the aerosol and cloud probes mounted under an aircraft wing. The air speed at the probe location (PAS) was on average 30 % smaller than in the free stream (TAS).

A CFD model was adopted to test different flight conditions. The numerical results matched the recorded differences between free stream conditions and the conditions at the probe location (see Fig. 6). The simulated flow fields were used to estimate changes in concentration for particles of different densities and diameters. Concentrations of particles smaller than about 5 µm can be derived with low error using the probe conditions (PAS, $p_{s,probe}$, and T_{probe}). Therefore, it is highly beneficial to equip wing-mounted instruments covering this size range with measurements of the probe conditions (PAS, $p_{s,probe}$ and T_{probe}). However, the simulations also showed that using probe conditions leads to incorrect particle concentrations with an overestimation of the coarse-mode aerosol amount in the diameter range of 5–100 µm of up to 20 % (see Fig. 10). This inaccuracy can be corrected with the correction scheme proposed in this study which considers the Stokes number depending on particle size and density. The proposed correction scheme was generalized to different aircraft configurations with a simple formula (Eq. 6) based on the ratio between the probe and free stream conditions, reducing concentration errors drastically, from 30 % to less than 2 %.

Wrong OAP recording speeds not only impact the derived particle concentrations but also result in deformed images. Since coarse particles and droplets ($d_p > 50$ µm) move with a speed $v_p \approx$ TAS, TAS was used as the reference speed in the OAP data acquisition software during the A-LIFE and ATom-2 through ATom-4 missions. In our measurements during these missions, the OAP reference speed was taken from the instrument's pitot tube measurements after a re-calibration of the instrument's pitot tube such that it provides TAS. Although the use of TAS as a reference particle speed largely reduced images distortions, large droplets still appeared deformed. To understand the deformation of water droplets, a volume of fluid (VOF) method was used which confirmed that aerodynamic forces are the reason for the deformations. The model well reproduced experimental data from Vargas (2012). Already at Weber number $We = 1$ droplets were deformed (see Figs. 14 and 15). Droplets smaller than 400 µm showed deformed shapes caused by instabilities developing at their surface.

To reduce errors of the estimated LWC derived from OAP size distributions, different definitions of droplet diameter were tested. Using the maximum droplet dimension d_{max} to estimate droplet volume resulted in a 40 % error even

at low aircraft speed with errors dramatically increasing up to 1 order of magnitude with aircraft speed. The best volume approximation was obtained by using the formula $V = 2/3 \cdot d_y \cdot \text{Area}$, where d_y is the particle diameter perpendicular to the flow and Area is the droplet area calculated from the image. Significant differences between air speed in the free stream (TAS) and at the instrument location (PAS) increased the risk, especially for fast flying aircraft, of the breakup of large droplets. Droplet breakup caused measurement artifacts by increasing the number of particles (red contour in Fig. 12). This phenomenon, known also as aerodynamic breakup (Craig et al., 2013), caused shattering of droplets without hitting instrument walls. Extending the result from Garcia-Magariño et al. (2018), we provided an estimate for the critical diameter of droplet breakup as a function of aircraft speed.

Deviations between values of PAS and TAS have been under discussion for some time. In this study, the physical reasons for the observed deviations were explained based on numerical simulations and a new correction method has been proposed. The correction scheme was validated for the DLR Falcon (A-LIFE campaign) and the NASA DC-8 (ATom campaigns) and the general conclusions hold for any fast-flying research aircraft. Using this new method for the analysis of past and upcoming data sets therefore may reduce errors in particle and droplet number concentrations up to 30 % and in the derived LWC up to 1 order of magnitude.

Appendix A

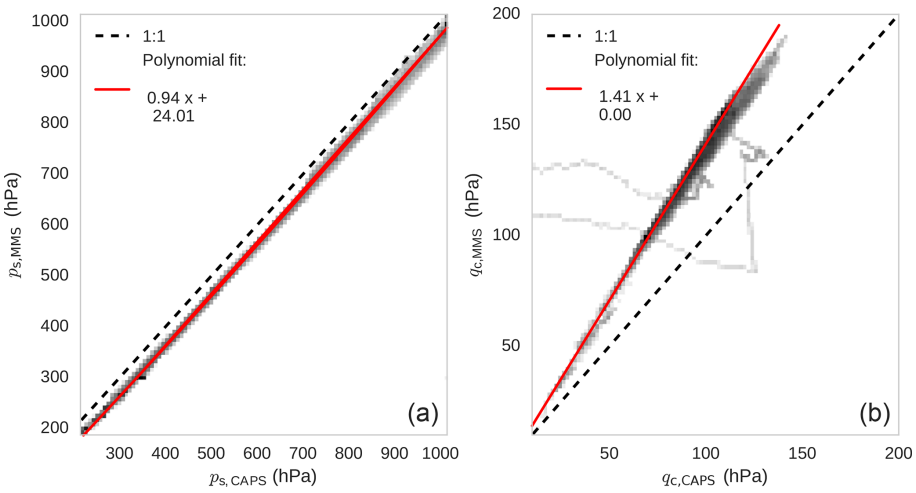

Figure A1. Statistical comparison between values recorded by the MMS and the CAPS pitot tube installed under the aircraft wing during ATom-1: static pressure **(a)** and dynamic pressure **(b)**. The histogram color map refers to number of seconds of data at 1 Hz. Dashed lines represent the 1 : 1 line and red lines linear fits.

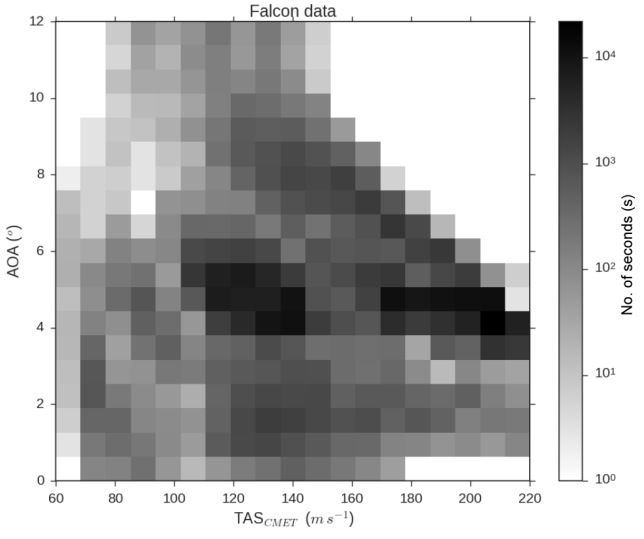

Figure A2. Frequency of angle of attack (AOA) versus TAS during the SALTRACE campaign.

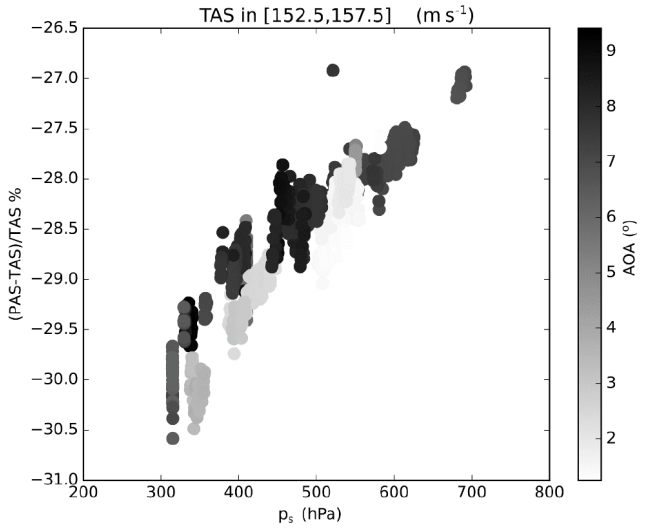

Figure A3. Deviation between PAS and TAS as a function of ambient pressure color coded with the AOA. Markers represent measurements at 1 Hz collected during the SALTRACE campaign covering an arbitrarily chosen TAS range from 152.5 to 157.5 $\mathrm{m\,s^{-1}}$. A TAS range had to be chosen for this figure because the deviation between PAS and TAS depends also on TAS. However, also for other TAS ranges, the data show in a similar way that the AOA has only a minor impact on the measurements; i.e., (PAS–TAS)/TAS changes less than 2 % when the AOA changes.

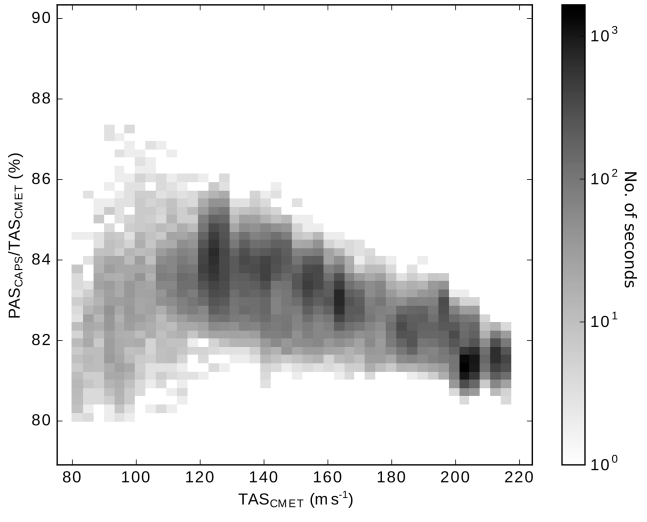

Figure A4. Statistical analysis of differences between air speed in the free stream and at the probe during A-LIFE when CAPS was calibrated to match free stream conditions. $\mathrm{TAS_{CMET}}$ values were obtained by the CMET system and the $\mathrm{PAS_{CAPS}}$ was post-calculated using Eq. (1) and the dynamic and static pressure as well the temperature value at the probe obtained by inverting the relation described in Sect. 3.1.4. The histogram color map refers to the number of seconds of data at 1 Hz.

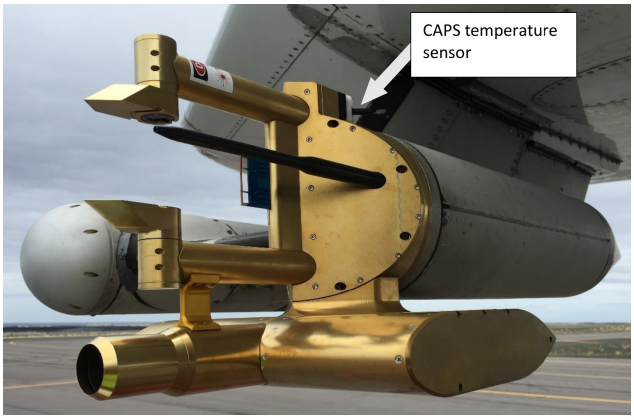

Figure A5. Photograph of the CAPS mounted at the wing of the NASA DC-8 research aircraft during ATom-4. The position of the temperature sensor is marked by the white arrow. (Photograph: Bernadett Weinzierl)

Table A1. Different speeds used.

TAS	True air speed; speed of air mass flown through (relative to aircraft)
$\mathrm{TAS_{CMET}}$	True air speed obtained from CMET system
$\mathrm{TAS_{MMS}}$	True air speed obtained from MMS system
$\mathrm{TAS_{CAPS}}$	True air speed obtained from CAPS instrument after re-calibration to match TAS
PAS	Probe air speed; speed of air at the probe (relative to aircraft, i.e., also relative to probe)
$\mathrm{PAS_{CAS}}$	Probe air speed obtained from CAS instrument
$\mathrm{PAS_{CAPS}}$	Probe air speed obtained from CAPS instrument
U	(Local) air speed; speed of air at a given location (relative to aircraft)
U_0	Free stream velocity; equivalent to TAS
v_p	Particle speed; speed of a particle (relative to aircraft)
U_slip	Slip velocity; speed of a particle relative to the suspending air around the particle
U_sound	Speed of sound
M	Mach number; equal to U/U_sound

Table A2. Abbreviations and symbols used.

AOA	Angle of attack
CFD	Computational fluid dynamics
LWC	Liquid water content
OAP	Optical array probe
OPC	Optical particle counter
VOF	Volume of fluid
d_p	Particle diameter
ρ_p	Particle density
V	Droplet volume
σ	Surface tension
γ	Heat capacity ratio
p_s	Static pressure
p_{tot}	Total pressure
q_c	Dynamic pressure
Stk^*	Modified Stokes number (Eq. 4)
We	Weber number

Table A3. Sampling efficiency f_{eff} (%) for different test cases for different particle diameters d_p and densities ρ_p as shown in Fig. 8.

d_p (µm)	0.5	1	2	5	10	20	50	100
Test case								
$\rho_p = 1\,g\,cm^{-3}$ (water)								
u75_p1000	76.89	76.93	77.09	78.09	80.50	84.99	91.86	95.75
u100_p900	77.30	77.35	77.52	78.76	82.24	88.21	93.96	96.48
u125_p900	77.77	77.81	78.11	79.46	82.55	87.42	93.50	96.25
u150_p650	78.27	78.42	78.76	80.43	83.70	88.50	94.42	97.08
u150_p550	78.18	78.29	78.64	80.32	83.76	88.52	94.44	96.71
u175_p400	79.42	79.52	79.87	81.66	85.20	90.03	95.57	98.62
u175_p330	79.75	79.80	80.14	82.14	85.81	90.66	95.64	98.70
u200_p250	80.16	80.30	80.66	82.60	86.22	91.12	96.18	97.04
$\rho_p = 2.5\,g\,cm^{-3}$ (mineral dust)								
u75_p1000	76.91	77.01	77.40	79.49	83.48	88.93	95.01	97.77
u100_p900	77.32	77.38	77.87	80.47	84.82	90.21	95.86	98.25
u125_p900	77.76	77.93	78.64	81.39	85.89	91.06	96.61	98.70
u150_p650	78.34	78.61	79.28	82.51	87.13	92.25	96.23	99.25
u150_p550	78.24	78.47	79.12	82.51	87.18	92.10	97.49	98.99
u175_p400	79.47	79.74	80.58	84.02	88.62	93.61	98.07	98.94
u175_p330	79.77	80.06	80.88	84.32	89.18	94.40	98.50	99.20
u200_p250	80.26	80.79	81.66	85.20	89.85	94.22	97.97	99.26

Data availability. The data are available from the Oak Ridge National Laboratory Distributed Active Archive Center at https://doi.org/10.3334/ORNLDAAC/1784 (Spanu et al., 2020).

Author contributions. BW and AS designed the study. AS carried out the simulations and the numerical analysis. BW and MD performed the airborne CAPS measurements. MD processed the CAPS data. TPB provided the MMS data. AS analyzed the data with the help of BW and wrote the manuscript with the support of BW and JG. JG, BW, and AS revised the manuscript. All authors commented on the manuscript.

Competing interests. The authors declare that they have no conflict of interest.

Special issue statement. This article is part of the special issue "The Saharan Aerosol Long-range Transport and Aerosol-Cloud-interaction Experiment (SALTRACE) (ACP/AMT inter-journal SI)". It is not associated with a conference.

Acknowledgements. This work was supported by the VERTIGO Marie Curie Initial Training Network, funded through the European Seventh Framework Programme (FP7 2007-2013) under grant agreement no. 607905, and by the European Research Council under the European Community's Horizon 2020 research and innovation framework program/ERC grant agreement no. 640458 (A-LIFE). The authors would also like to acknowledge the contribution of the COST Action inDust (CA16202) supported by COST (European Cooperation in Science and Technology). The SALTRACE aircraft field experiment was funded by the Helmholtz Association (Helmholtz-Hochschul-Nachwuchsgruppe AerCARE, grant agreement no. VH-NG-606) and by DLR. We also would like to acknowledge partial funding through LMU Munich's Institutional Strategy LMUexcellent within the framework of the German Excellence Initiative. The A-LIFE field experiment was funded under ERC grant agreement no. 640458 (A-LIFE). In addition, DLR and two EUFAR projects provided funding for a significant amount of additional flight hours and aircraft allocation days for the A-LIFE aircraft field experiment. The ATom mission and the MMS measurements were funded under National Aeronautics and Space Administration's Earth Venture program (grant NNX15AJ23G). CAPS measurements during ATom were additionally supported by the University of Vienna. We are thankful to Andreas Giez, Volker Dreiling, Christian Mallaun, and Martin Zoeger for providing the meteorological data for SALTRACE and A-LIFE. We would like to thank DMT for the fruitful discussions related to the CAPS instrument. The authors thank the SALTRACE, A-LIFE, and ATom science teams, the pilots, and administrative and technical support teams for their great support before and during the field missions, and for the accomplishment of the unique research flights.

Financial support. This research has been supported by the European Seventh Framework Programme (FP7 2007-2013) (grant no. 607905 VERTIGO Marie Curie Initial Training Network), the European Research Council under the European Community's Horizon 2020 research and innovation framework program/ERC (grant no. 640458 A-LIFE), the National Aeronautics and Space Administration's Earth Venture program (grant no. NNX15AJ23G), and the Helmholtz-Hochschul-Nachwuchsgruppe AerCARE (grant no. VH-NG-606).

Review statement. This paper was edited by Claire Ryder and reviewed by two anonymous referees.

References

Albrecht, B. A.: Aerosols, Cloud Microphysics, and Fractional Cloudiness, Science, 245, 1227–1230, https://doi.org/10.1126/science.245.4923.1227, 1989.

Barlow, J., Rae, W., and Pope, A.: Wind Tunnel Testing, 3rd edition, John Wiley & Sons, New York, US, 1999.

Barsotti, S., Bignami, C., Buongiorno, M., Corradini, S., Doumaz, F., Guerrieri, L., Merucci, L., Musacchio, M., Nannipieri, L., Neri, A., Piscini, A., Silvestri, M., Spanu, A., Spinetti, C., Stramondo, S., and Wegmuller, U.: SAFER Response to Eyjafjallajökull and Merapi Volcanic Eruptions, in: Let's embrace space, Space Research achievements under the 7th Framework Programme, 212–222, https://doi.org/10.2769/1549, 2011.

Baumgardner, D., Jonsson, H., Dawson, W., O'Connor, D., and Newton, R.: The cloud, aerosol and precipitation spectrometer: a new instrument for cloud investigations, Atmos. Res., 59, 251–264, https://doi.org/10.1016/S0169-8095(01)00119-3, 2001.

Baumgardner, D., Newton, R., Krämer, M., Meyer, J., Beyer, A., Wendisch, M., and Vochezer, P.: The Cloud Particle Spectrom-eter with Polarization Detection (CPSPD): A next generation open-path cloud probe for distinguishing liquid cloud droplets from ice crystals, Atmos. Res., 142, 2–14, https://doi.org/10.1016/j.atmosres.2013.12.010, 2014.

Belyaev, S. and Levin, L.: Techniques for collection of representative aerosol samples, J. Aerosol Sci., 5, 325–338, https://doi.org/10.1016/0021-8502(74)90130-X, 1974.

Bradski, G.: The OpenCV Library, Dr. Dobb's Journal of Software Tools, available at: https://www.drdobbs.com/open-source/the-opencv-library/184404319# (last access: 1 April 2020), 2000.

Bögel, W. and Baumann, R.: Test and Calibration of the DLR Falcon Wind Measuring System by Maneuvers, J. Atmos. Ocean. Tech., 8, 5–18, https://doi.org/10.1175/1520-0426(1991)008<0005:TACOTD>2.0.CO;2, 1991.

Chan, K. R., Dean-Day, J., Bowen, S. W., and Bui, T. P.: Turbulence measurements by the DC-8 meteorological measurement system, Geophys. Res. Lett., 25, 1355–1358, https://doi.org/10.1029/97GL03590, 1998.

Clark, M. M.: Drop breakup in a turbulent flow – I. Conceptual and modeling considerations, Chem. Eng. Sci., 43, 671–679, https://doi.org/10.1016/0009-2509(88)87025-8, 1988.

Clift, R., Grace, J. R., and Weber, M. E.: Bubbles, Drops, and Particles, Academic Press, New York, US, 1978.

Craig, L., Moharreri, A., Schanot, A., Rogers, D. C., Anderson, B., and Dhaniyala, S.: Characterizations of Cloud Droplet Shatter

Artifacts in Two Airborne Aerosol Inlets, Aerosol Sci. Tech., 47, 662–671, https://doi.org/10.1080/02786826.2013.780648, 2013.

Craig, L., Moharreri, A., Rogers, D. C., Anderson, B., and Dhaniyala, S.: Aircraft-Based Aerosol Sampling in Clouds: Performance Characterization of Flow-Restriction Aerosol Inlets, J. Atmos. Ocean. Tech., 31, 2512–2521, https://doi.org/10.1175/JTECH-D-14-00022.1, 2014.

Cruette, D., Marillier, A., Dufresne, J. L., Grandpeix, J. Y., Nacass, P., and Bellec, H.: Fast Temperature and True Airspeed Measurements with the Airborne Ultrasonic Anemometer–Thermometer (AUSAT), J. Atmos. Ocean. Tech., 17, 1020–1039, https://doi.org/10.1175/1520-0426(2000)017<1020:FTATAM>2.0.CO;2, 2000.

DeMott, P. J., Prenni, A. J., Liu, X., Kreidenweis, S. M., Petters, M. D., Twohy, C. H., Richardson, M. S., Eidhammer, T., and Rogers, D. C.: Predicting global atmospheric ice nuclei distributions and their impacts on climate, P. Natl. Acad. Sci. USA, 107, 11217–11222, https://doi.org/10.1073/pnas.0910818107, 2010.

Drummond, A. M. and MacPherson, J. I.: Aircraft Flow Effects on Cloud Drop Images and Concentrations Measured by the NAE Twin Otter, J. Atmos. Ocean. Tech., 2, 633–643, https://doi.org/10.1175/1520-0426(1985)002<0633:AFEOCD>2.0.CO;2, 1985.

Elghobashi, S.: Particle-Laden Turbulent Flows: Direct Numerical Simulation and Closure Models, Appl. Sci. Res., 48, 301–314, https://doi.org/10.1007/BF02008202, 1991.

Garcia-Magariño, A., Sor, S., and Velazquez, A.: Droplet Breakup Criterion in Airfoils Leading Edge Vicinity, J. Aircraft, 55, 1867–1876, https://doi.org/10.2514/1.C034631, 2018.

Garcy, W.: Measurement of aircraft speed and altitude, NASA Langley Research Center, Hampton, US, Reference Publication 1046, available at: https://ntrs.nasa.gov/search.jsp?R=19800015804 (last access: 1 April 2020), 1980.

Hayman, M., McMenamin, K. J., and Jensen, J. B.: Response Time Characteristics of the Fast-2D Optical Array Probe Detector Board, J. Atmos. Ocean. Tech., 33, 2569–2583, https://doi.org/10.1175/JTECH-D-16-0062.1, 2016.

Hinds, W. C.: Aerosol technology: properties, behavior, and measurement of airborne particles, John Wiley & Sons, New York, US, 1999.

Howarth, L.: The Scientific Papers of G. I. Taylor. Vol. III. Aerodynamics and the Mechanics of Projectiles and Explosions, J. Fluid Mech., 17, 633–636, https://doi.org/10.1017/S0022112063241554, 1963.

Hsiang, L.-P. and Faeth, G.: Near-limit drop deformation and secondary breakup, Int. J. Multiph. Flow, 18, 635–652, https://doi.org/10.1016/0301-9322(92)90036-G, 1992.

Ibrahim, E. A., Yang, H. Q., and Przekwas, A. J.: Modeling of spray droplets deformation and breakup, J. Propul. Power, 9, 651–654, https://doi.org/10.2514/3.23672, 1993.

Israel, R. and Rosner, D. E.: Use of a Generalized Stokes Number to Determine the Aerodynamic Capture Efficiency of Non-Stokesian Particles from a Compressible Gas Flow, Aerosol Sci. Tech., 2, 45–51, https://doi.org/10.1080/02786828308958612, 1982.

Johnson, C.: Streamline diffusion finite-element method for compressible and incompressible fluid flow, in: Finite Elements in Fluids, edited by: Chung, T. J., 8, 75–96, 1992.

Jung, S., Tiwari, M. K., Doan, N. V., and Poulikakos, D.: Mechanism of supercooled droplet freezing on surfaces, Nat. Commun., 3, 615, https://doi.org/10.1038/ncomms1630, 2012.

Kalogiros, J. A. and Wang, Q.: Aerodynamic Effects on Wind Turbulence Measurements with Research Aircraft, J. Atmos. Ocean. Tech., 19, 1567–1576, https://doi.org/10.1175/1520-0426(2002)019<1567:AEOWTM>2.0.CO;2, 2002.

Kandler, K., Schütz, L., Deutscher, C., Ebert, M., Hofmann, H., Jäckel, S., Jaenicke, R., Knippertz, P., Lieke, K., Massling, A., Petzold, A., Schladitz, A., Weinzierl, B., Wiedensohler, A., Zorn, S., and Weinbruch, S.: Size distribution, mass concentration, chemical and mineralogical composition and derived optical parameters of the boundary layer aerosol at Tinfou, Morocco, during SAMUM 2006, Tellus B, 61, 32–50, https://doi.org/10.1111/j.1600-0889.2008.00385.x, 2009.

Kennedy, J. and Roberts, J.: Rain Ingestion in a Gas Turbine Engine, 4th ILASS-Americas Conference, Hartford, US, 21–23 May 1990.

King, W. D.: Air Flow and Particle Trajectories around Aircraft Fuselages. I: Theory, J. Atmos. Ocean. Tech., 1, 5–13, https://doi.org/10.1175/1520-0426(1984)001<0005:AFAPTA>2.0.CO;2, 1984.

King, W. D., Turvey, D., Williams, D., and Llewellyn, D.: Air flow and particle trajectories around aircraft fuselages. II: Measurements, J. Atmos. Ocean. Tech., 1, 14–21, https://doi.org/10.1175/1520-0426(1984)001<0014:AFAPTA>2.0.CO;2, 1984.

Knollenberg, R.: Techniques for probing cloud microstructure, in: Clouds their Formation, Optical Properties, and Effects, edited by: Hobbs, P. V. and Deepak, A., Academic Press, New York, US, 15–91, https://doi.org/10.1016/b978-0-12-350720-4.50007-7, 1981.

Knollenberg, R. G.: The Optical Array: An Alternative to Scattering or Extinction for Airborne Particle Size Determination, J. Appl. Meteorol., 9, 86–103, https://doi.org/10.1175/1520-0450(1970)009<0086:TOAAAT>2.0.CO;2, 1970.

Knollenberg, R. G.: Three New Instruments for Cloud Physics Measurements: The 2-D Spectrometer, the Forward Scattering Spectrometer Probe, and the Active Scattering Aerosol Spectrometer, in: Proc. Intern. Cloud Physics Conf., Boulder, US, 26–30 June 1976, 554–561, 1976.

Kok, J. F., Ridley, D. A., Zhou, Q., Miller, R. L., Zhao, C., Heald, C. L., Ward, D. S., Albani, S., and Haustein, K.: Smaller desert dust cooling effect estimated from analysis of dust size and abundance, Nat. Geosci., 10, 274–278, https://doi.org/10.1038/ngeo2912, 2017.

Korolev, A.: Reconstruction of the Sizes of Spherical Particles from Their Shadow Images. Part I: Theoretical Considerations, J. Atmos. Ocean. Tech., 24, 376–389, https://doi.org/10.1175/JTECH1980.1, 2007.

Korolev, A. and Isaac, G.: Shattering During Sampling by OAPs and HVPS. Part I: Snow Particles, J. Atmos. Ocean. Tech., 22, 528–542, https://doi.org/10.1175/JTECH1720.1, 2005.

Korolev, A., Emery, E., and Creelman, K.: Modification and Tests of Particle Probe Tips to Mitigate Effects of Ice Shattering, J. Atmos. Ocean. Tech., 30, 690–708, https://doi.org/10.1175/JTECH-D-12-00142.1, 2013.

Korolev, A. V., Strapp, J. W., and Isaac, G. A.: Evaluation of the Accuracy of PMS Optical Array Probes, J. At-

mos. Ocean. Tech., 15, 708–720, https://doi.org/10.1175/1520-0426(1998)015<0708:EOTAOP>2.0.CO;2, 1998.

Lance, S., Brock, C. A., Rogers, D., and Gordon, J. A.: Water droplet calibration of the Cloud Droplet Probe (CDP) and in-flight performance in liquid, ice and mixed-phase clouds during ARCPAC, Atmos. Meas. Tech., 3, 1683–1706, https://doi.org/10.5194/amt-3-1683-2010, 2010.

Laucks, M. and Twohy, C. H.: Size-Dependent Collection Efficiency of an Airborne Counter flow Virtual Impactor, Aerosol Sci. Tech., 28, 40–60, https://doi.org/10.1080/02786829808965511, 1998.

Launder, B. and Spalding, D.: The numerical computation of turbulent flows, Comput. Methods Appl. Mech. Eng., 3, 269–289, https://doi.org/10.1016/0045-7825(74)90029-2, 1974.

Lawson, R. P., O'Connor, D., Zmarzly, P., Weaver, K., Baker, B., Mo, Q., and Jonsson, H.: The 2D-S (Stereo) Probe: Design and Preliminary Tests of a New Airborne, High-Speed, High-Resolution Particle Imaging Probe, J. Atmos. Ocean. Tech., 23, 1462–1477, https://doi.org/10.1175/JTECH1927.1, 2006.

Letko, W.: Investigation of the Fuselage Interference on a Pitot-static Tube Extending Forward from the Nose of the Fuselage, National Advisory Committee for Aeronautics, Langley Aeronautical Lab, Langley Field, US, NACA Technical Note 1496, available at: https://ntrs.nasa.gov/search.jsp?R=19930082152 (last access: 1 April 2020), 1947.

Marks, C. R.: Drop Breakup and Deformation in Sudden Onset Strong Flow, Ph.D. thesis, University of Maryland, College Park, US, available at: http://adsabs.harvard.edu/abs/1998PhDT.....204M (last access: 1 April 2020), 1998.

Masud, J.: Performance Characteristics of Flush Angle-of-Attack Measurement System Integrated on a Pitot Tube, Eng. Appl. Comput. Fluid Mech., 4, 549–557, https://doi.org/10.1080/19942060.2010.11015340, 2010.

McFarquhar, G. M.: A New Representation of Collision-Induced Breakup of Raindrops and Its Implications for the Shapes of Raindrop Size Distributions, J. Atmos. Sci., 61, 777–794, https://doi.org/10.1175/1520-0469(2004)061<0777:ANROCB>2.0.CO;2, 2004.

Moharreri, A., Craig, L., Rogers, D. C., and Dhaniyala, S.: A New Aircraft Inlet for Sampling Interstitial Aerosol: Design Methodology, Modeling, and Wind Tunnel Tests, Aerosol Sci. Tech., 47, 885–894, https://doi.org/10.1080/02786826.2013.800186, 2013.

Moharreri, A., Craig, L., Dubey, P., Rogers, D. C., and Dhaniyala, S.: Aircraft testing of the new Blunt-body Aerosol Sampler (BASE), Atmos. Meas. Tech., 7, 3085–3093, https://doi.org/10.5194/amt-7-3085-2014, 2014.

Montorfano, A.: Mesh generation for HPC problems: the potential of SnappyHexMesh, Workshop HPC Methods for Engineering, Milan, Italy, 19–21 June 2017, https://doi.org/10.13140/RG.2.2.25007.53923, 2017.

Nacass, P.: Theoretical Errors on Airborne Measurements Of: Static Pressure, Impact Temperature, Air Flow Angle, Air Flow Speed, National Center For Atmospheric Research, Boulder, US, Technical Note NCAR/TN-385+STR, https://doi.org/10.5065/D6M61H79, 1992.

Nakao, S., Kashitani, M., Miyaguni, T., and Yamaguchi, Y.: A study on high subsonic airfoil flows in relatively high Reynolds number by using OpenFOAM, J. Therm. Sci., 23, 133–137, https://doi.org/10.1007/s11630-014-0687-5, 2014.

Nayar, K. G., Panchanathan, D., McKinley, G. H., and Lienhard, J. H.: Surface Tension of Seawater, J. Phys. Chem. Ref. Data, 43, 043103, https://doi.org/10.1063/1.4899037, 2014.

Noh, W. F. and Woodward, P.: SLIC (Simple Line Interface Calculation), in: Proceedings of the Fifth International Conference on Numerical Methods in Fluid Dynamics, Twente University, Enschede, Netherlands, 28 June–2 July 1976, 330–340, 1976.

Norment, H. G.: Three-Dimensional Trajectory Analysis of Two Drop Sizing instruments: PMS* OAP and PMS* FSSP, J. Atmos. Ocean. Tech., 5, 743–756, https://doi.org/10.1175/1520-0426(1988)005<0743:TDTAOT>2.0.CO;2, 1988.

Oertel, H. (Ed.): Prandtl's Essentials of Fluid Mechanics, Springer, New York, US, https://doi.org/10.1007/b97538, 2010.

O'Rourke, P. J. and Amsden, A. A.: The Tab Method for Numerical Calculation of Spray Droplet Breakup, in: SAE International Fall Fuels and Lubricants Meeting and Exhibition, 1987, Technical Paper 872089, https://doi.org/10.4271/872089, 1987.

Pilch, M. and Erdman, C. A.: Use of Breakup Time Data and Velocity History Data to Predict the Maximum Size of Stable Fragments for Acceleration-Induced Breakup of a Liquid Drop, Int. J. Multiphase Flow, 13, 741–757, https://doi.org/10.1016/0301-9322(87)90063-2, 1987.

Poret, M., Corradini, S., Merucci, L., Costa, A., Andronico, D., Montopoli, M., Vulpiani, G., and Freret-Lorgeril, V.: Reconstructing volcanic plume evolution integrating satellite and ground-based data: application to the 23 November 2013 Etna eruption, Atmos. Chem. Phys., 18, 4695–4714, https://doi.org/10.5194/acp-18-4695-2018, 2018.

Pruppacher, H. and Klett, J.: Microphysics of Clouds and Precipitation, Springer, Dordrecht, Netherlands, https://doi.org/10.1007/978-0-306-48100-0, 2010.

Rallison, J.: The Deformation of Small Viscous Drops and Bubbles in Shear Flows, Annu. Rev. Fluid Mech., 16, 45–66, https://doi.org/10.1146/annurev.fl.16.010184.000401, 1984.

Rhie, C. and Chow, W.: A numerical study of the turbulent flow past an isolated airfoil with trailing edge separation, 3rd Joint Thermophysics, Fluids, Plasma and Heat Transfer Conference, St. Louis, US, 7–11 June 1982, AIAA-82-0998, https://doi.org/10.2514/6.1982-998, 1982.

Rosenfeld, D. and Lensky, I. M.: Satellite–Based Insights into Precipitation Formation Processes in Continental and Maritime Convective Clouds, B. Am. Meteorol. Soc., 79, 2457–2476, https://doi.org/10.1175/1520-0477(1998)079<2457:SBIIPF>2.0.CO;2, 1998.

Rumscheidt, F. D. and Mason., S. G.: Particle motions in sheared suspensions XII. Deformation and burst of fluid drops in shear and hyperbolic flow, J. Colloid Sci., 16, 238–261, https://doi.org/10.1016/0095-8522(61)90003-4, 1961.

Scott, S., Bui, T. P., Chan, R., and Bowen, S. W.: The Meteorological Measurement System on the NASA ER-2 Aircraft, J. Atmos. Ocean. Tech., 7, 525–540, https://doi.org/10.1175/1520-0426(1990)007<0525:TMMSOT>2.0.CO;2, 1990.

Silverman, B.: Density Estimation for Statistics and Data Analysis, Chapman and Hall, London, UK, 1986.

Solomos, S., Ansmann, A., Mamouri, R.-E., Binietoglou, I., Patlakas, P., Marinou, E., and Amiridis, V.: Remote sensing and modelling analysis of the extreme dust storm hitting the Middle East and eastern Mediterranean in September 2015, At-

mos. Chem. Phys., 17, 4063–4079, https://doi.org/10.5194/acp-17-4063-2017, 2017.

Spanu, A., Dollner, M., Gasteiger, J., Bui, T. P., and Weinzierl, B.: ATom, A-LIFE, SALTRACE: Flow-induced errors in in-situ aerosol and cloud measurements, ORNL DAAC, Oak Ridge, US, https://doi.org/10.3334/ORNLDAAC/1784, 2020.

Stocker, T., Qin, D., Plattner, G. K., Tignor, M., Allen, S., Boschung, J., Nauels, A., Xia, Y., Bex, V., and Midgley, P.: Climate Change 2013 – The Physical Science Basis: Working Group I Contribution to the Fifth Assessment Report of the Intergovernmental Panel on Climate Change, Cambridge University Press, Cambridge, UK, https://doi.org/10.1017/CBO9781107415324, 2014.

Sun, Z., Zhou, J., Zhang, H., and J.A., H.: On the influencing factors in a Pitot tube measurement II. Influence of total and static ports, Chinese Journal of Sensors and Actuators, 20, 941–944, 2007.

Szakall, M., Diehl, K., Mitra, S. K., and Borrmann, S.: A Wind Tunnel Study on the Shape, Oscillation, and Internal Circulation of Large Raindrops with Sizes between 2.5 and 7.5 mm, J. Atmos. Sci., 66, 755–765, https://doi.org/10.1175/2008JAS2777.1, 2009.

Tan, S. and Papadakis, M.: General Effects of Large Droplet Dynamics on Ice Accretion Modeling, in: 41st Aerospace Sciences Meeting and Exhibit, 6–9 January 2003, Reno, US, AIAA 2003-392, 2003.

Vargaftik, N., Volko, B., and Voljak, L.: International Tables of the Surface Tension of Water, J. Phys. Chem. Ref. Data, 12, 817–820, https://doi.org/10.1063/1.555688, 1983.

Vargas, M.: Droplet Deformation Prediction With the Droplet Deformation and Breakup Model (DDB), in: 4th AIAA Atmospheric and Space Environments Conference, New Orleans, US, 25–28 June 2012, AIAA 2012-3131, https://doi.org/10.2514/6.2012-3131, 2012.

Vargas, M. and Feo, A.: Experimental Observations on the Deformation and Breakup of Water Droplets Near the Leading Edge of an Airfoil, in: AIAA Atmospheric and Space Environments Conference, Toronto, Canada, 2–5 August 2010, AIAA 2010-7670, https://doi.org/10.2514/6.2010-7670, 2010.

Walser, A., Sauer, D., Spanu, A., Gasteiger, J., and Weinzierl, B.: On the parametrization of optical particle counter response including instrument-induced broadening of size spectra and a self-consistent evaluation of calibration measurements, Atmos. Meas. Tech., 10, 4341–4361, https://doi.org/10.5194/amt-10-4341-2017, 2017.

Weber, R. J., Clarke, A. D., Litchy, M., Li, J., Kok, G., Schillawski, R. D., and McMurry, P. H.: Spurious Aerosol Measurements when Sampling from Aircraft in the Vicinity of Clouds., J. Geophys. Res., 103, 28337–28346, https://doi.org/10.1029/98JD02086, 1998.

Weigel, R., Spichtinger, P., Mahnke, C., Klingebiel, M., Afchine, A., Petzold, A., Krämer, M., Costa, A., Molleker, S., Reutter, P., Szakáll, M., Port, M., Grulich, L., Jurkat, T., Minikin, A., and Borrmann, S.: Thermodynamic correction of particle concentrations measured by underwing probes on fast-flying aircraft, Atmos. Meas. Tech., 9, 5135–5162, https://doi.org/10.5194/amt-9-5135-2016, 2016.

Weinzierl, B., Petzold, A., Esselborn, M., Wirth, M., Rasp, K., Kandler, K., Schütz, L., Koepke, P., and Fiebig, M.: Airborne measurements of dust layer properties, particle size distribution and mixing state of Saharan dust during SAMUM 2006, Tellus B, 61, 96–117, https://doi.org/10.1111/j.1600-0889.2008.00392.x, 2009.

Weinzierl, B., Sauer, D., Esselborn, M., Petzold, A., Veira, A., Rose, M., Mund, S., Wirth, M., Ansmann, A., Tesche, M., Gross, S., and Freudenthaler, V.: Microphysical and optical properties of dust and tropical biomass burning aerosol layers in the Cape Verde region – an overview of the airborne in situ and lidar measurements during SAMUM-2, Tellus B, 63, 589–618, https://doi.org/10.1111/j.1600-0889.2011.00566.x, 2011.

Weinzierl, B., Ansmann, A., Prospero, J. M., Althausen, D., Benker, N., Chouza, F., Dollner, M., Farrell, D., Fomba, W. K., Freudenthaler, V., Gasteiger, J., Groß, S., Haarig, M., Heinold, B., Kandler, K., Kristensen, T. B., Mayol-Bracero, O. L., Müller, T., Reitebuch, O., Sauer, D., Schäfler, A., Schepanski, K., Spanu, A., Tegen, I., Toledano, C., and Walser, A.: The Saharan Aerosol Long-range Transport and Aerosol-Cloud-Interaction Experiment (SALTRACE): overview and selected highlights, B. Am. Meteorol. Soc., 98, 1427–1451, https://doi.org/10.1175/BAMS-D-15-00142.1, 2017.

Weller, H., Tabor, G., Jasak, H., and Fureby, C.: A tensorial approach to computational continuum mechanics using object-oriented techniques, Comput. Phys., 12, 620–631, https://doi.org/10.1063/1.168744, 1998.

Wessel, R. A. and Righi, J.: Generalized correlations for inertial impaction of particles on a circular cylinder, Aerosol Sci. Tech., 9, 29–60, https://doi.org/10.1080/02786828808959193, 1988.

Wierzba, A.: Deformation and breakup of liquid drops in a gas stream at nearly critical Weber numbers, Exp. Fluids, 9, 59–64, https://doi.org/10.1007/BF00575336, 1990.

Wofsy, S., Afshar, S., Allen, H., Apel, E., Asher, E., Barletta, B., Bent, J., Bian, H., Biggs, B., Blake, D., Blake, N., Bourgeois, I., Brock, C., Brune, W., Budney, J., Bui, T., Butler, A., Campuzano-Jost, P., Chang, C., Chin, M., Commane, R., Correa, G., Crounse, J., Cullis, P., Daube, B., Day, D., Dean-Day, J., Dibb, J., Digangi, J., Diskin, G., Dollner, M., Elkins, J., Erdesz, F., Fiore, A., Flynn, C., Froyd, K., Gesler, D., Hall, S., Hanisco, T., Hannun, R., Hills, A., Hintsa, E., Hoffman, A., Hornbrook, R., Huey, L., Hughes, S., Jimenez, J., Johnson, B., Katich, J., Keeling, R., Kim, M., Kupc, A., Lait, L., Lamarque, J.-F., Liu, J., Mckain, K., Mclaughlin, R., Meinardi, S., Miller, D., Montzka, S., Moore, F., Morgan, E., Murphy, D., Murray, L., Nault, B., Neuman, J., Newman, P., Nicely, J., Pan, X., Paplawsky, W., Peischl, J., Prather, M., Price, D., Ray, E., Reeves, J., Richardson, M., Rollins, A., Rosenlof, K., Ryerson, T., Scheuer, E., Schill, G., Schroder, J., Schwarz, J., St.Clair, J., Steenrod, S., Stephens, B., Strode, S., Sweeney, C., Tanner, D., Teng, A., Thames, A., Thompson, C., Ullmann, K., Veres, P., Vizenor, N., Wagner, N., Watt, A., Weber, R., Weinzierl, B., Wennberg, P., Williamson, C., Wilson, J., Wolfe, G., Woods, C., and Zeng, L.: ATom: Merged Atmospheric Chemistry, Trace Gases, and Aerosols, ORNL DAAC, Oak Ridge, US, https://doi.org/10.3334/ornldaac/1581, 2018.

Yang, W., Jia, M., Che, Z., Sun, K., and Wang, T.: Transitions of deformation to bag breakup and bag to bag-stamen breakup for droplets subjected to a continuous gas flow, Int. J. Heat Mass Tran., 111, 884–894, https://doi.org/10.1016/j.ijheatmasstransfer.2017.04.012, 2017.

Atmos. Chem. Phys., 21, 15023–15063, 2021
https://doi.org/10.5194/acp-21-15023-2021

Atmospheric Chemistry and Physics
Open Access
EGU

Ambient aerosol properties in the remote atmosphere from global-scale in situ measurements

Charles A. Brock[1], Karl D. Froyd[1,2], Maximilian Dollner[3], Christina J. Williamson[1,2], Gregory Schill[1,2], Daniel M. Murphy[1], Nicholas J. Wagner[1,2], Agnieszka Kupc[3], Jose L. Jimenez[2,4], Pedro Campuzano-Jost[2,4], Benjamin A. Nault[2,4], Jason C. Schroder[2,4], Douglas A. Day[2,4], Derek J. Price[2,4], Bernadett Weinzierl[3], Joshua P. Schwarz[1], Joseph M. Katich[1,2], Siyuan Wang[1,2], Linghan Zeng[5], Rodney Weber[5], Jack Dibb[6], Eric Scheuer[6], Glenn S. Diskin[7], Joshua P. DiGangi[7], ThaoPaul Bui[8], Jonathan M. Dean-Day[9], Chelsea R. Thompson[1,2], Jeff Peischl[1,2], Thomas B. Ryerson[1], Ilann Bourgeois[1,2], Bruce C. Daube[10], Róisín Commane[11,a], and Steven C. Wofsy[10]

[1]Chemical Sciences Laboratory, National Oceanic and Atmospheric Administration, Boulder, Colorado 80305, USA
[2]Cooperative Institute for Research in Environmental Sciences, University of Colorado, Boulder, Colorado 80309, USA
[3]Faculty of Physics, Aerosol Physics and Environmental Physics, University of Vienna, Vienna, 1090, Austria
[4]Department of Chemistry, University of Colorado, Boulder, Colorado 80309, USA
[5]School of Earth and Atmospheric Sciences, Georgia Institute of Technology, Atlanta, Georgia 30332, USA
[6]Earth Systems Research Center, Institute for the Study of Earth, Oceans, and Space, University of New Hampshire, Durham, New Hampshire 03824, USA
[7]Langley Research Center, National Aeronautics and Space Administration, Hampton, Virginia 23681, USA
[8]Ames Research Center, National Aeronautics and Space Administration, Moffett Field, California 94035, USA
[9]Bay Area Environment Research Institute, Moffett Field, California 94035, USA
[10]Department of Earth and Planetary Sciences, Harvard University, Cambridge, Massachusetts 02138, USA
[11]School of Engineering and Applied Sciences, Harvard University, Cambridge, Massachusetts 02138, USA
[a]now at: Earth and Environmental Sciences, Lamont–Doherty Earth Observatory, Columbia University, Palisades, New York 10964, USA

Correspondence: Charles A. Brock (charles.a.brock@noaa.gov)

Received: 25 February 2021 – Discussion started: 4 March 2021
Revised: 29 July 2021 – Accepted: 11 August 2021 – Published: 8 October 2021

Abstract. In situ measurements of aerosol microphysical, chemical, and optical properties were made during global-scale flights from 2016–2018 as part of the Atmospheric Tomography Mission (ATom). The NASA DC-8 aircraft flew from ∼ 84° N to ∼ 86° S latitude over the Pacific, Atlantic, Arctic, and Southern oceans while profiling nearly continuously between altitudes of ∼ 160 m and ∼ 12 km. These global circuits were made once each season. Particle size distributions measured in the aircraft cabin at dry conditions and with an underwing probe at ambient conditions were combined with bulk and single-particle composition observations and measurements of water vapor, pressure, and temperature to estimate aerosol hygroscopicity and hygroscopic growth factors and calculate size distributions at ambient relative humidity. These reconstructed, composition-resolved ambient size distributions were used to estimate intensive and extensive aerosol properties, including single-scatter albedo, the asymmetry parameter, extinction, absorption, Ångström exponents, and aerosol optical depth (AOD) at several wavelengths, as well as cloud condensation nuclei (CCN) concentrations at fixed supersaturations and lognormal fits to four modes. Dry extinction and absorption were compared with direct in situ measurements, and AOD derived from the extinction profiles was compared with remotely sensed AOD measurements from the ground-based Aerosol Robotic Network (AERONET); this comparison showed no substantial bias.

Published by Copernicus Publications on behalf of the European Geosciences Union.

The purpose of this work is to describe the methodology by which ambient aerosol properties are estimated from the in situ measurements, provide statistical descriptions of the aerosol characteristics of different remote air mass types, examine the contributions to AOD from different aerosol types in different air masses, and provide an entry point to the ATom aerosol database. The contributions of different aerosol types (dust, sea salt, biomass burning, etc.) to AOD generally align with expectations based on location of the profiles relative to continental sources of aerosols, with sea salt and aerosol water dominating the column extinction in most remote environments and dust and biomass burning (BB) particles contributing substantially to AOD, especially downwind of the African continent. Contributions of dust and BB aerosols to AOD were also significant in the free troposphere over the North Pacific.

Comparisons of lognormally fitted size distribution parameters to values in the Optical Properties of Aerosols and Clouds (OPAC) database commonly used in global models show significant differences in the mean diameters and standard deviations for accumulation-mode particles and coarse-mode dust. In contrast, comparisons of lognormal parameters derived from the ATom data with previously published shipborne measurements in the remote marine boundary layer show general agreement.

The dataset resulting from this work can be used to improve global-scale representation of climate-relevant aerosol properties in remote air masses through comparison with output from global models and assumptions used in retrievals of aerosol properties from both ground-based and satellite remote sensing.

1 Introduction

Atmospheric aerosols are important components of the atmospheric system, interacting chemically and physically with gas-phase components and affecting climate processes through aerosol–radiation and aerosol–cloud interactions (IPCC, 2013). We use the term "aerosol" to indicate a population of non-cloud (non-activated) particles suspended in and interacting with air and its reactive gas-phase constituents. In this terminology, any given air parcel may contain multiple, externally mixed aerosol types (for example, a sea salt aerosol and a dust aerosol may coexist within the same air parcel). Global chemistry–climate models usually represent atmospheric aerosols using bulk, modal, or binned microphysical schemes that apportion various components into size classes. These representations of aerosol properties are often dynamic, allowing for chemical reactions, growth, coagulation, dilution, cloud nucleation, in-cloud production, and dry and wet deposition. To effectively simulate the role of atmospheric aerosol in climate processes, models must adequately represent the mass, composition, and phase of different aerosol types and their distribution amongst particle sizes, the spatial and temporal distribution of the components, their mixing state (existing as external mixtures with different compositions or internal mixtures with blended compositions), their optical properties (often a function of particle size), and their hygroscopic properties and suitability to serve as cloud condensation nuclei (CCN). Underlying these properties are the physical and chemical processes actually being represented in the simulations, including emissions of particles and gas-phase precursors, atmospheric transport, gas-phase, heterogeneous, and aqueous chemistry, cloud processing, evaporation, wet and dry deposition, and transformations such as condensation and coagulation. Simulating these disparate processes and properties is a challenging task for global-scale models, which must balance detailed size-dependent representations of these mechanisms against computational efficiency. There is an imperative for improving aerosol representation in global models: the largest source of uncertainty in understanding climate sensitivity remains aerosol–radiation and aerosol–cloud interactions (the direct and indirect effects, respectively).

Global chemistry–climate models often evaluate their performance based on comparison to remote sensing observations from satellites and from ground-based sensors such as the Aerosol Robotic Network (AERONET; Holben et al., 1998). The satellite products most often used are aerosol optical depth (AOD) from sensors such as the Moderate Resolution Imaging Spectroradiometer (MODIS) on NASA's Aqua and Terra satellites, the Multi-angle Imaging Spectroradiometer (MISR) on Terra, and the Visible Infrared Imaging Radiation Suite (VIIRS) instrument on the Suomi National Polar-orbiting Partnership satellite. Additional information on aerosol characteristics such as the angular dependence of scattered light (the phase function) and single-scatter albedo ω_0 (the ratio of light scattering to the sum of scattering and absorption) can be derived from multi-angle techniques such as from AERONET and MISR, while multi-angle polarimetric data can yield information on the particle size distribution and absorption coefficient (Dubovik et al., 2019). In general, algorithms to generate such additional information on aerosol properties from remote sensing measures require a priori assumptions about aerosol characteristics because the retrievals are under-constrained (e.g., Dubovik et al., 2000). In the case of AERONET, aerosol properties such as column-averaged aerosol phase function and ω_0 can be derived with confidence only in cases in which AOD exceeds 0.4 (Dubovik et al., 2000; Holben et al., 2006), which is much more turbid than is typical of the atmosphere away from large continental sources of pollution, dust, and biomass burning. Extrapolating intensive aerosol properties such as ω_0 from measurements at high AOD values to cleaner regions may lead to substantial biases (Andrews et al., 2017). In a recent overview paper, Kahn et al. (2017) stated that

> at present, it seems unlikely that particle microphysical and chemical properties can be retrieved from remote sensing measurements alone at the level of accuracy required to substantially reduce uncertainties in total direct aerosol radiative forcing (DARF), its anthropogenic component, aerosol–cloud interactions, horizontal material transports, surface–atmosphere aerosol fluxes, and air-quality-related applications.

In this work we make use of in situ measurements made on a research aircraft during the Atmospheric Tomography Mission (ATom), a series of global-scale representative (Katich et al., 2018; Strode et al., 2018) tropospheric observations over the remote Pacific and Atlantic Ocean and portions of the Arctic and Antarctic Ocean, to provide detailed descriptions of the aerosols encountered. We sampled an airstream through an inlet, dried it, and used in-cabin instruments to determine the microphysical and chemical characteristics of the dried aerosol. We then calculated the ambient aerosol properties by accounting for hygroscopic growth to ambient humidity and developed statistics for a number of dry and ambient aerosol properties for the different air mass types encountered. These data, which cover single transects over the two ocean basins in each of four seasons, do not represent a climatology of aerosol characteristics, but provide a representatively sampled "snapshot" of particle properties that can be compared with simulations of these properties to help identify issues in model output and reveal processes that may be inadequately represented. The overarching goal of this paper is to describe how the in situ measurements are combined into a single consistent description of the aerosol microphysical, chemical, hygroscopic, and optical properties listed in Table 1, to present a summary of aerosol properties in different air masses encountered during ATom, and to provide an entry point to the ATom dataset for use in modeling and remote sensing investigations of atmospheric composition and climate.

2 Methods

2.1 The Atmospheric Tomography Mission

The ATom mission was an airborne measurement program that investigated the composition of the remote marine troposphere over four seasons. Science flights took place from 29 July–23 August 2016, 26 January–21 February 2017, 29 September–27 October 2017, and 24 April–21 May 2018, named ATom-1 through ATom-4, respectively (Thompson et al., 2021). The NASA DC-8 aircraft, a large, four-engine, intercontinental-range commercial aircraft adapted for scientific measurements (NASA, 2015), flew from southern California southward to near the Equator and back, then north to the Arctic Ocean, southward over the Pacific Ocean to New Zealand, across the Southern Ocean to Chile, northward to the Azores, across the North American Arctic to Alaska, and back to California (Fig. 1). On ATom-3 and ATom-4, the aircraft flew southward from Chile over the Antarctic Peninsula and Weddell Sea. On ATom-1, the aircraft flew from Greenland to California without crossing the North American Arctic to Alaska. The routes northward across the South Atlantic and across eastern Canada and Greenland varied due to airport availability and weather conditions.

During these flights, the DC-8 made repeated en route ascents and descents from the maximum flight altitude permitted by aircraft performance and air traffic control (ATC) to within ~ 160 m of the surface (visibility and ATC permitting) and back, similar to the HIAPER Pole-to-Pole Observations (HIPPO) study using the smaller National Science Foundation Gulfstream G-V aircraft (Wofsy, 2011). We consider a total of 625 atmospheric profiles, including both descents and ascents, in this study. The DC-8 maintained level flight for several minutes at the lowest and highest altitudes and when required by ATC or to save fuel; at all other times it was constantly ascending or descending at ~ 450 m min^{-1}. The flight routes were pre-planned and not adjusted except to avoid hazardous flight conditions such as deep convection. Pre-planned, multi-level flight patterns were made 12 times in the marine boundary layer (MBL) to investigate vertical fluxes over the remote oceans.

2.2 Instruments

The DC-8 aircraft carried a substantial payload of in situ meteorological, gas-phase, and aerosol instruments as well as limited radiation instruments. Measurements included reactive nitrogen compounds, volatile organic compounds (VOCs), photo-products and oxygenated species, tracers, actinic flux, meteorological parameters, and aerosol composition and size distribution (Thompson et al., 2021). This work focuses exclusively on the aerosol observations and also uses measurements of O_3, CO, pressure, temperature, water vapor, and GPS-derived aircraft location.

The aerosol size distribution instruments and their performance during ATom have been described in detail in several previous publications, which provide comprehensive documentation of the quality of the ATom aerosol dataset. Williamson et al. (2019) detail the function and performance of a multi-channel battery of condensation particle counters (NMASS: nucleation-mode aerosol size spectrometer) used to count and size particles with diameters (D_p) from ~ 3 to ~ 55 nm. Kupc et al. (2018) describe the calibration and performance of an ultrahigh-sensitivity aerosol spectrometer (UHSAS, Droplet Measurement Technologies, Longmont, CO, USA), an optical particle counter that measures the particle size distribution from ~ 60 nm (0.06 µm) to 1.0 µm diameter. Brock et al. (2019) detail how these instruments are combined with a laser aerosol spectrometer (LAS, TSI Inc., St. Paul, MN, USA) to generate continuous, 1 s particle size distribution measurements from 3 nm to 4.8 µm

Table 1. Aerosol properties calculated from the combined aerosol dataset and archived in files.

Parameter	Parameter identifier[a]	Method	Wavelengths	Comments
Dry scattering	*scat_dry_ambpt*	Mie theory from composition-resolved size distribution using refractive indices in Table 2	all[b]	Calculated at ambient pressure and temperature; Sect. 2.7.1
Dry absorption from rBC	*BC_abs_ambPT*	Core–shell Mie theory using air-mass-averaged MAC multiplied by 60 s rBC mass concentration	all[b]	Calculated at ambient pressure and temperature; Sect. 2.7.1
Dry absorption from BrC	*BrC_abs_ambPT*	Bivariate fit between BrC absorption from filter extracts and PALMS biomass burning particles as well as rBC mass concentrations	all[b]	Calculated at ambient pressure and temperature; Sect. 2.7.1; estimated factor of 3 uncertainty
Dry extinction	*ext_dry_ambPT*	Sum of dry scattering and absorption from rBC and BrC	all[b]	Calculated at ambient pressure and temperature
Ambient scattering	*scat_ambRHPT*	κ-Köhler theory to estimate water content; Mie theory to calculate scattering	all[b]	Calculated at ambient pressure and temperature
Ambient extinction	*ext_ambRHPT*	Ambient scattering + dry absorption from rBC and BrC	all[b]	Calculated at ambient pressure and temperature
Dry single-scatter albedo	*SSA_dry*	Dry scattering and extinction	all[b]	Ratio of scattering to extinction
Ambient single-scatter albedo	*SSA_ambRH*	Ambient scattering and extinction	all[b]	Ratio of scattering to extinction
Dry extinction Ångström exponent	*ext_Angstrom_dry*	Fit to dry extinction across all wavelengths[a]	all[b]	Least-squares regression to Eq. (11)
Ambient extinction Ångström exponent	*ext_Angstrom_ambRH*	Fit to ambient extinction at all wavelengths[a]	all[b]	Least-squares regression to Eq. (11)
UV–Vis absorption Ångström exponent	*abs_Angstrom_UV_Vis*	Fit to sum of dry absorption from rBC and BrC	340, 380, 405, 440, 532 nm	Least-squares regression to Eq. (11)
Vis–IR absorption Ångström exponent	*abs_Angstrom_Vis_IR*	Fit to dry absorption from rBC	532, 550, 670, 940, 1020 nm	Least-squares regression to Eq. (11)
Dry mass extinction efficiency	*MEE_dry*	Dry extinction and dry aerosol mass from composition-resolved size distributions and densities in Table 2	all[b]	Ratio of dry extinction to dry aerosol mass
Ambient mass extinction efficiency	*MEE_ambRH*	Ambient extinction and dry aerosol mass	all[b]	Ratio of ambient extinction to dry aerosol mass
Mass absorption cross section	*MAC*	Core–shell Mie theory applied to coated rBC particles	all[b]	Ratio of coated rBC absorption to rBC mass; calculated for air mass averages only; Table S6
Dry asymmetry parameter	*asymmetry_dry*	Mie theory at dry conditions, not including absorbers	all[b]	Eq. (9)
Ambient asymmetry parameter	*asymmetry_ambRH*	Mie theory at ambient conditions, not including absorbers	all[b]	Eq. (9)
Ambient lidar backscatter ratio	*backscat_ratio_ambRH*	κ-Köhler theory to estimate water content; Mie theory to calculate backscattering and scattering	all[b]	Ratio of backscatter to extinction at ambient RH

Table 1. Continued.

Parameter	Parameter identifier[a]	Method	Wavelengths	Comments
Ambient lidar backscatter cross section	*backscat_ambRH*	κ-Köhler theory to estimate water content; Mie theory to calculate backscattering, dry aerosol mass	all[b]	Ratio of backscatter at ambient RH to dry particle mass
Effective radius	*eff_radius*	Integration of size distribution	–	Ratio of third moment of the size distribution to the second moment
Hygroscopicity parameter κ	*kappa_ams*	Volume-weighted sum of κ values from AMS in Table 2	–	Algebraic calculation of electrolytic composition; literature values
$f(\mathrm{RH})_{85\,\%}$	*f_rh_85*	Ratio of calculated extinction at 85 % Rh to that at dry conditions	532 nm only	
κ_{ext}	*kappa_ext*	Fit to calculated extinction at 0 %, 70 %, 80 %, and 85 % RH	532 nm only	Fit to Eq. (10)
CCN concentration	*CCN_005*, *CCN_010*, *CCN_020, CCN_050*, *CCN_100*	Integration of particle size distribution for $D_{\mathrm{p}} > D_{\mathrm{crit,dry}}$	–	Eq. (2), Sect. 2.6; calculated for supersaturations of 0.05 %, 0.1 %, 0.2 %, 0.5 %, and 1.0 %
Lognormal parameters D_{g}, σ_{g}, N	*lognorm_coefs_nucl*, *lognorm_coefs_Aitken*, *lognorm_coefs_accum*, *lognorm_coefs_coarse*	Fits to volume for coarse and accumulation mode and to number for Aitken and nucleation modes	–	Supplement, Tables S2–S4
Mass concentration of sulfate, organics, dust, rBC, BrC, aerosol water	*sulfate, organics*, *nitrate, ammonium*, *sea_salt, dust, BC*, *BrC_est, aerosol_H2O*, *mass_fine, mass_coarse*	Integration of volume size distribution for each component multiplied by density from Table 2, separated into coarse ($D_{\mathrm{p}} \geq 1$ µm) and fine ($D_{\mathrm{p}} < 1$ µm)	–	Ammonium and nitrate from AMS applied to sulfate–organic class across all sizes
Ambient fine-mode extinction fraction η	*FMF*	Coarse- and accumulation-mode compositions applied to lognormal fits to those modes, then Mie theory used to calculate extinctions for each	all[b]	Aerosol water calculated using κ-Köhler theory and values from Table 2

[a] Identifier of variable (short name) in NetCDF file. [b] 340, 380, 405, 440, 532, 550, 670, 870, 940, 1020 nm.

diameter, referred to as the aerosol microphysical property (AMP) size distribution. Brock et al. (2019) also describe the sampling system, uncertainties, and data products associated with these dry particle size distribution measurements and show that data from these instruments are internally consistent and also agree with independently measured aerosol composition and extinction measurements within expected uncertainties.

Section 2.3 below describes in detail how dry size distributions and aerosol composition data from the in-cabin instruments are combined with data from an underwing cloud and aerosol spectrometer (CAS, Droplet Measurement Techniques, Longmont, CO, USA; Baumgardner et al., 2001; Spanu et al., 2020). The CAS is a nearly open-path laser optical particle counter that measures the size distribution of aerosol and cloud particles with diameters from 0.5–50 µm at nearly ambient conditions.

Aerosol composition was determined using two mass spectrometers as well as black and brown carbon measurements. Froyd et al. (2019) provide a detailed description of how data from a single-particle laser ionization mass spectrometer (PALMS; particle analysis by laser mass spectroscopy) are combined with particle size distributions to determine the size-resolved composition and mixing state of particles with D_{p} from 0.14–4.8 µm. In addition, a high-resolution time-of-flight aerosol mass spectrometer (HR-ToF-AMS, hereafter AMS for brevity, Aerodyne Inc., Billerica, USA; DeCarlo et al., 2006; Canagaratna et al., 2007;

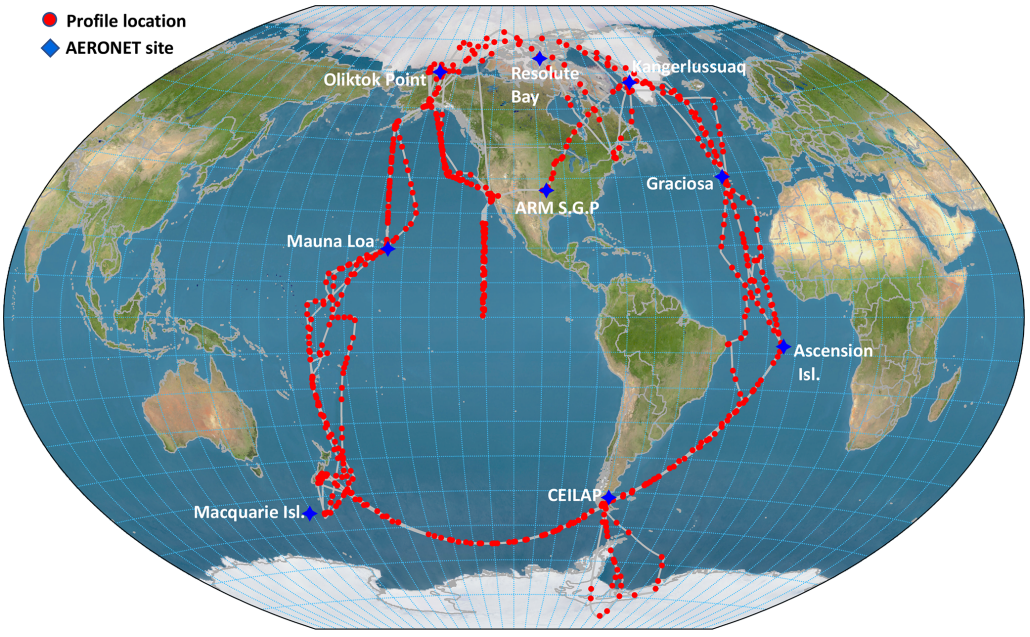

Figure 1. Map showing the flight track of the DC-8 aircraft (gray lines) and midpoint location of each vertical profile (ascent or descent; red circles). Locations and names of AERONET sites against which calculated AOD is compared are shown by blue diamonds and labels. Custom map produced using 1 km digital elevation model data from NOAA (https://www.ngdc.noaa.gov/mgg/topo/globe.html, last access: 3 February 2016).

Schroder et al., 2018; Hodzic et al., 2020), which provides bulk composition of particles with geometric D_p from ~ 0.02 to ~ 0.7 µm with detection efficiencies $> 50\,\%$ between ~ 0.05 and ~ 0.5 µm (Guo et al., 2021), collected data over ~ 46 s every minute and reported with 1 s and 1 min time resolutions (Jimenez et al., 2021). The AMS can also provide size-dependent non-refractory composition information using particle time-of-flight measurement mode, but in the free troposphere this often requires extensive time averaging, which is impractical to apply during the vertical profiles.

Measurements of refractory black carbon (rBC; Petzold et al., 2013) were provided by a single-particle soot photometer (SP2; Gao et al., 2007; Schwarz et al., 2010; Katich et al., 2018). This instrument uses laser-induced incandescence to measure the rBC mass within individual particles from 90 to 550 nm in diameter in the accumulation-mode size range on a 1 s time basis (with frequent null detections at this rate at the concentrations found in ATom). The rBC mass concentration data were corrected to reflect accumulation-mode rBC particles outside the detection range of the instrument by using a lognormal distribution fitted for the average rBC size distribution for each flight, eliminating time periods near takeoff and landing, to calculate a scaling factor. That single correction factor per flight, which increased rBC mass concentrations less than a factor of 1.1 (Katich et al., 2018), was applied to the 1s data for that particular flight. The rBC data were then averaged, with zeros, to the 60 s AMS sampling times, with an uncertainty of $\sim 30\,\%$. Information on the size distribution of the rBC and on the thickness of non-refractory coatings on the rBC particles, which are used to calculate optical properties of the rBC, was obtained by accumulating data over longer time periods (Table S6 in the Supplement).

Brown carbon (BrC) absorption at wavelengths from 300–700 nm was determined by offline analysis of aerosol filter samples collected over times ranging from < 5 min at low altitude to ~ 15 min at high altitude during ATom-2–4 (Zeng et al., 2020). A total of 1074 filters from the ATom mission, including two to three blanks per flight, were analyzed. Water extracts from the filter were further filtered to remove insoluble absorbing particles, then introduced into a liquid waveguide where the spectral absorption was measured with a spectrophotometer. The absorption of BrC by chromophores in the aqueous sample was then converted to aerosol absorption as described in Sect. 2.7.2.

We also use 1 s data from a precision open-path water vapor concentration sensor (Podolske et al., 2003) with an uncertainty of $\pm 5\,\%$ and from the meteorological measurement system (Scott et al., 1990) of temperature measured within uncertainty of ± 0.3 K and of pressure with an uncertainty of ± 0.3 hPa, yielding an uncertainty in relative humidity with respect to water (RH) that ranges from $\pm \sim 7\,\%$ (of the value) in the warm, tropical marine boundary to $\pm \sim 6\,\%$ (of the value) in the cold, dry lower stratosphere. To identify stratospheric air, we use measurements of CO and O_3, which were measured using a multipass optical absorption cell (Mc-

Manus et al., 2005) and chemiluminescence (Ryerson et al., 1998), respectively.

Aerosol measurements can be contaminated by particles resuspended from the inlet walls due to hydrometeor collisions (Murphy et al., 2004). Throughout this analysis, we use data that were obtained only in cloud-free air based on altitude-varying thresholds for RH, T, number concentration, and a measure of the particle volume size distribution in the CAS size range. We include MBL data that are within the CAS "aerosol–cloud transition regime" category as archived in the broader ATom dataset (Wofsy et al., 2018) because excluding data from this category would remove substantial quantities of the data within the moist MBL, which often dominate column-integrated optical properties. All concentration units are reported at standard temperature and pressure (STP; 1013 hPa and 273.15 K); however, extensive optical properties such as extinction and absorption coefficients are reported at ambient temperature and pressure conditions as well as, where indicated, at ambient RH.

2.3 Determining the composition-dependent aerosol size distribution

2.3.1 Overview of methodology

Calculating ambient aerosol properties relies upon combining data from multiple sizing and compositional instruments to develop a comprehensive description of the size-dependent composition and mixing state of the aerosol. From this information the hygroscopic growth and refractive index, which are essential to estimating optical properties of the hydrated aerosol, can be estimated. Figures 2 and 3 show how data from the four size distribution instruments are combined with data from the four composition instruments and compositional and optical models to determine the ambient optical properties. Because the primary purpose of determining the composition-dependent aerosol size distribution is to calculate optical properties, we begin this section by providing an overview of how these size distributions are applied for this purpose using Figs. 2 and 3 as a guide.

The overarching approach is to assign compositions and mixing states to particles within each size bin of the measured particle number size distribution. Once this has been accomplished, refractive index and hygroscopicity for each particle type in each size bin can be estimated, and dry and ambient optical properties can be calculated. There is considerable detail hidden in the first steps shown in the left portion of Fig. 2 – how data from different sizing and composition instruments are combined to produce the composition-resolved size distributions. Figure 3 provides a clearer depiction of this process. For all particle types except rBC, the dry aerosol size distribution is determined from the in-cabin AMP instruments (NMASS+UHSAS+LAS) and the underwing CAS probe. Aerosol volume, surface area, number, and effective diameter can be readily calculated directly from the size distribution. To calculate optical and hygroscopic properties, size-dependent compositional information derived from the AMS and PALMS measurements is mapped to the number size distribution. To be clear, mass concentrations measured by the AMS and PALMS instruments are not directly used; rather, the relative composition as a function of size is applied to the measured number size distributions, which are then used to determine the mass concentration and optical and hygroscopic properties of each component. This represents a marked departure from other datasets and is motivated by the ability of the PALMS instrument to identify the number fractional abundance of externally mixed refractory aerosol types (e.g., sea salt, dust), as well as by its inability to independently provide quantitative information on mass concentrations. The PALMS data, which for ATom provide number fractional abundances of eight particle types (plus an unclassified fraction) in each of four size ranges, must be mapped to independently measured size distributions to quantify the mass concentrations of those particle types (Froyd et al., 2019).

Refractory particles identified by the PALMS instrument are assumed to be present as externally mixed aerosol components, each of which is described by an independent size distribution. In contrast, non-refractory organic–inorganic particles measured by the AMS and PALMS instruments are assumed to be internally mixed using the volume-weighted Zdanovskii–Stokes–Robinson (ZSR) mixing rule (Stokes and Robinson, 1966), assuming no interaction between components, to infer particle hygroscopicity. Light scattering at ambient RH conditions is calculated by estimating the hygroscopic growth factor based on this measured composition, calculating the amount of aerosol water at ambient RH, using the same ZSR mixing rule to estimate ambient refractive index, and applying Mie theory for a homogeneous sphere. As shown in Fig. 3, for particle sizes < 0.05 µm in diameter, the composition of the aerosol is largely unmeasured, but is assumed to be internally mixed and represented by the bulk composition reported by the AMS instrument. From 0.05–0.14 µm diameter, the aerosol is assumed to be internally mixed and the composition is exclusively based on the AMS measurement. This means that any dust, sea salt, or other refractory particles that contribute to this portion of the size distribution are substituted with the AMS composition. (Note that the AMS can measure submicrometer sea salt, but during ATom there was little sea salt detected by the AMS in this size range, and only the PALMS-detected sea salt, primarily in the coarse mode, is considered; Ovadnevaite et al., 2012; Hodzic et al., 2020.) From 0.14–0.25 µm diameter, the size distribution is split into the number fractional contribution of each of eight particle types based on PALMS classification, with AMS composition applied to non-refractory particle types. For particles with diameters from 0.25–$\sim$ 4 µm, the PALMS particle types alone are used, with regional averaging as needed to improve statistics. For particles with diameters from $\sim$ 4–50 µm, there are no compositional mea-

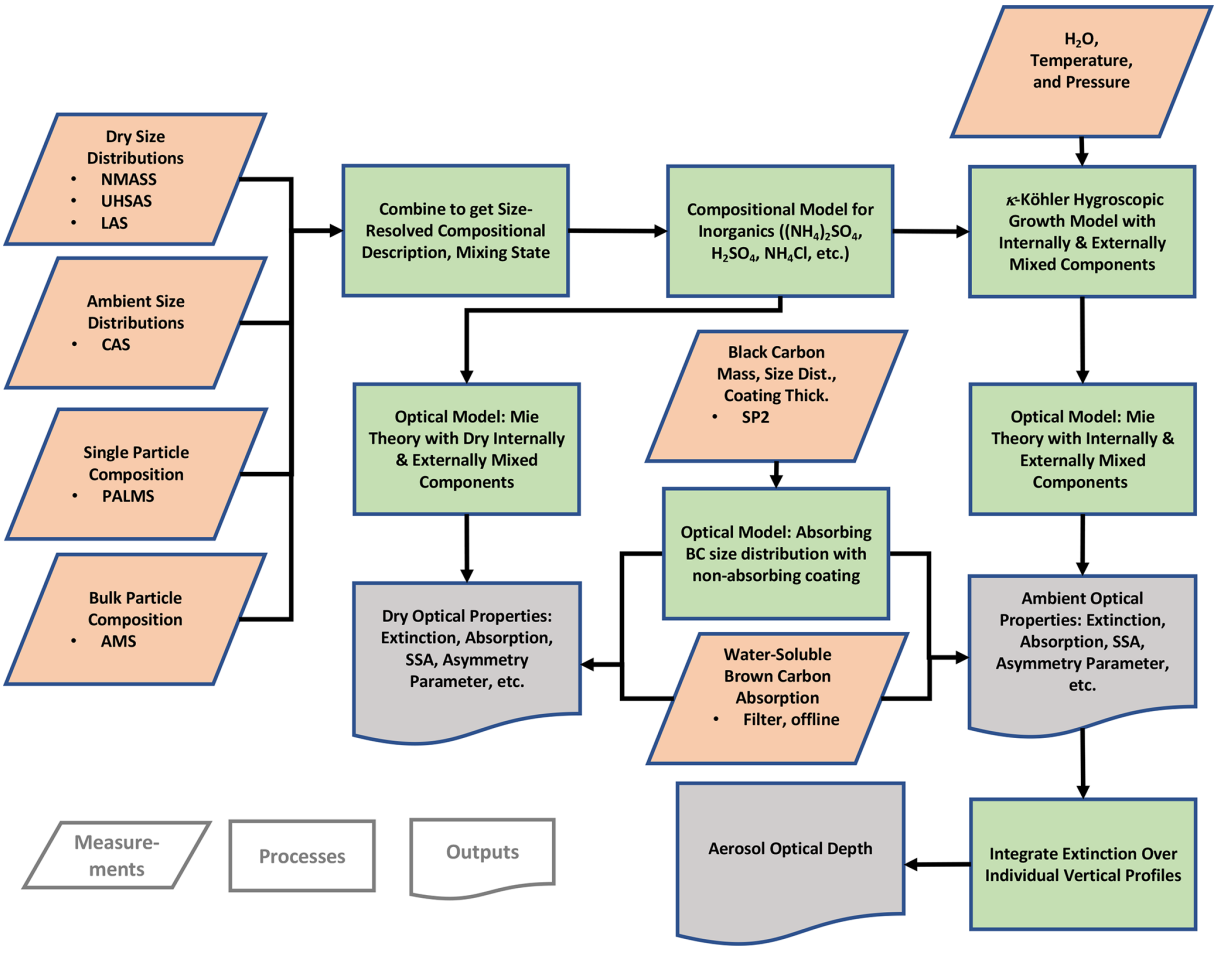

Figure 2. Schematic showing how data from instruments that measure size distribution, particle composition, and meteorological parameters are combined to form a self-consistent description of the composition-dependent size distribution. Compositional, hygroscopic growth, and optical models are combined to determine dry and ambient aerosol optical properties and AOD.

surements due to inlet performance, and the PALMS particle types from the 1.13–$\sim$ 4 µm diameter range are applied.

Three light-absorbing components are assumed to be present: mineral dust, BrC, and rBC (Sect. 2.7.2). Light absorption due to dust is directly calculated from the dust size distribution using Mie theory and an assumed refractive index with a wavelength-dependent imaginary component. Light absorption due to BrC and rBC is treated entirely separately from these calculations. Absorption from BrC is estimated from measurements of water-soluble absorption in aqueous filter extracts, from which a parameterization relating BrC absorption to the abundance of rBC and biomass burning particles is derived. Absorption from BrC is then calculated from the measured abundance of these surrogates using this parameterization. Absorption due to rBC is calculated using core–shell Mie theory applied to air-mass-averaged rBC size distributions and coating thicknesses, from which mass absorption cross sections (MACs) are determined. These MACs, which are assumed to be independent of RH, are then used to estimate absorption from fast-response measurements of rBC mass. Detailed descriptions of the methods used to determine the composition-resolved size distribution and calculate the reported aerosol parameters are given in Sect. 2.3.2 below.

2.3.2 Detailed description of methodology

The PALMS instrument measures mass spectra of ion fragments from the laser-induced thermal desorption of individual aerosol particles (Thomson et al., 2000). Each positive mass spectrum is classified into one of several categories, or types, using spectral signatures based on laboratory calibrations: sea salt, biomass burning, mixed sulfate–organic mixtures (which may also contain nitrate, ammonium, and other inorganic ions), soil dust, heavy fuel oil combustion, meteoric material, alkali salts, elemental carbon (EC), and an unclassified fraction (Froyd et al., 2019). During ATom, particles in the "unclassified" fraction represented 8.8 ± 8.6 % of all the detected particles and are treated as sulfate–organic

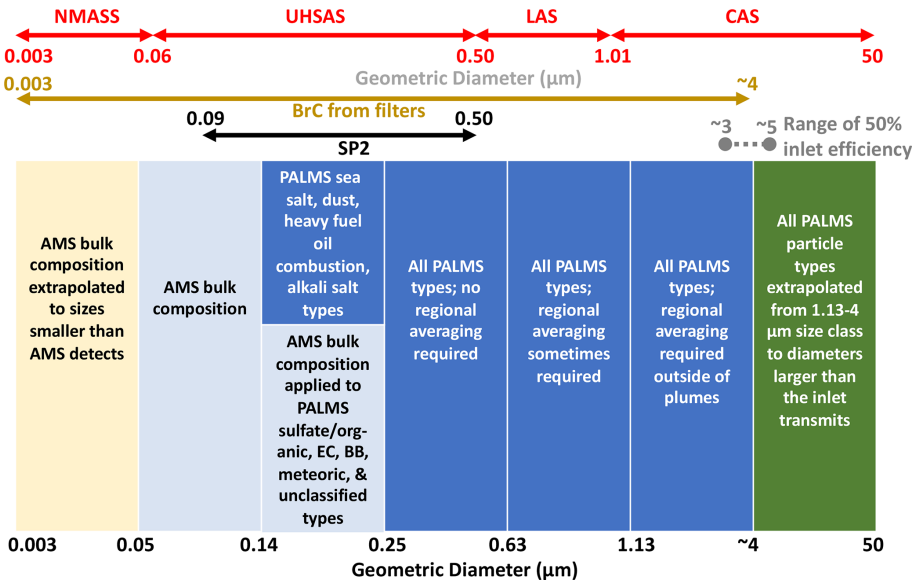

Figure 3. Schematic showing the portions of the size ranges of the particle size distribution instruments that are used and the size ranges over which the composition measurements from the filter measurements, the SP2, the AMS, and PALMS are applied. The approximate range of 50 % inlet transmission efficiency is shown. The needs to average PALMS data to achieve statistically significant descriptions of particle composition are shown, as are the extrapolations of AMS and PALMS data to sizes for which no compositional information is available. The diameter ranges of instrument detection are presented in detail in Guo et al. (2021).

particles in this analysis, resulting in eight total particle types based on the mass spectral signatures. Largely because of variability in the sampling efficiency of particles into the laser beams, by itself the PALMS instrument does not quantify absolute chemical concentrations of the particles (Froyd et al., 2019). Instead, PALMS places particles into compositional categories such as dust, sea salt, and mixed sulfate–organic particles, to which physical characteristics such as refractive index and hygroscopicity are assigned. Based on laboratory calibrations, the sulfate and organic mass fractions of non-refractory particle types (sulfate–organic mixtures, biomass burning particles composed mostly of organic material, and stratospheric meteoric particles composed primarily of sulfuric acid with a small core of condensed meteoric material) can be estimated from the PALMS mass spectra (Froyd et al., 2019). Because each individual particle measured by PALMS is aerodynamically sized prior to laser ablation, each can be classified by both compositional type and size, and the number fraction of each compositional type can be determined for a given particle size range (Froyd et al., 2019). The size-resolved PALMS composition data are converted from aerodynamic to geometric D_p by applying a particle density and shape for each class. However, PALMS cannot directly measure a composition-based size distribution because it is limited by data rate, typically $\sim 4\,s^{-1}$, and because it has size-dependent sampling biases. Instead, a statistical description of aerosol composition in specific size classes determined from PALMS can be combined with independently measured particle size distributions to provide a size distribution for each of the particle types (Froyd et al., 2019). For this analysis, the PALMS particle types were aggregated over four size ranges (0.14–0.25, 0.25–0.63, 0.63–1.13, and $> 1.13\,\mu m$); four bins provide a satisfactory trade-off between number of bins, counting statistics per bin, and spatial resolution for the ATom mission (Froyd et al., 2019). Within each of these size ranges, the different size particles contribute unevenly to the compositional statistics depending on their abundance and the efficiency of detection (Froyd et al., 2019). Depending on ambient concentrations, time averaging may be needed to achieve statistical significance. Once adequate compositional statistics are developed as described below, the accumulated data in the four size ranges are mapped onto the independently measured particle size distributions from the AMP instruments (Fig. 3; Froyd et al., 2019; Murphy et al., 2021).

In the remote troposphere during ATom, the aerosol with $D_p \geq 0.14\,\mu m$ was composed of distinct particle types (with one of the most common types being internally mixed sulfate–organic). Thus, to calculate optical and hygroscopic properties, we do not assume a weighted internal mixture of the chemical components, but rather treat the total aerosol as an externally mixed collection of independent size distributions, each composed of one PALMS compositional type mapped onto the particle size distributions. For particles with $D_p < 0.14\,\mu m$, for which the PALMS instrument provides limited statistics over the averaging times used here, we assume the particles are composed of a non-refractory internal mixture with composition given by the AMS in-

strument, which provides submicron bulk composition measured over $D_p \sim 0.05$–$0.5\,\mu m$ (Guo et al., 2021; Fig. 3). Further, the AMS composition is applied to the sulfate–organic, biomass burning, EC, and meteoric particle types for the 0.14–0.25 µm PALMS size range, the diameters over which the AMS samples with unity efficiency (Guo et al., 2021).

Throughout this work, we average all data to a 60 s time base determined by the AMS reporting interval. The 60 s data frequency we use translates into a vertical resolution of ∼ 450 m given the typical ascent and descent rates in the middle and lower troposphere, with somewhat better vertical resolution at altitudes > 9 km during ascents as climb rates dropped. As noted by Hodzic et al. (2020), in background conditions during ATom a substantial fraction of the AMS organic aerosol (OA) concentrations were below the detection limit and included negative values. We substitute negative AMS values with zeros only when calculating hygroscopic or optical properties (Sect. 2.5 and 2.7, respectively).

The PALMS data presented here were accumulated over 3 min time periods and then interpolated to the same 1 min time interval as the AMS data. However, if fewer than five particles were classified by the PALMS instrument in each PALMS size range over the 3 min period, average compositional information based on much more extensive spatial averaging was applied to that size range. If the time interval in question was in the MBL, typical PALMS compositional statistics from the MBL were applied (Fig. 3). Similarly, if the aircraft was in the lower stratosphere (as identified by CO < 100 ppbv and $O_3 > 100$ ppbv or > 300 ppbv in the southern or northern latitudes, respectively), in a BB plume (tropospheric BB particle number fractions > 0.5 and AMS OA mass $> 1\,\mu g\,m^{-3}$), or a dust plume (dust mass fraction > 0.3 and volume concentration for $D_p > 1\,\mu m$ more than $2\,\mu m^3\,cm^{-3}$), representative compositional statistics from these air masses were applied to the PALMS size range in question.

For PALMS data with poor statistics (fewer than five particles in a PALMS size range) in the free troposphere (FT), regionally averaged particle composition statistics were applied (Fig. 3). This situation most often applied to particles with $D_p > 1.13\,\mu m$, which have very low number concentrations. For the four PALMS size ranges, from smallest to largest, the regionally averaged compositions were applied to 11 %, 3 %, 61 %, and 89 % of the 19 921 60 s samples, respectively. These regionally averaged compositions were separately calculated and applied depending on whether the DC-8 was over the Pacific or Atlantic Ocean and whether it was in Antarctic–Southern Ocean, southern midlatitude, tropical, northern midlatitude, or Arctic air masses. The latitudinal boundaries of these air mass types are provided in the Supplement (Table S1). These same air mass classifications serve as a way to organize the final data products that are the objective of this effort (Sect. 3.3).

Our treatment of the aerosol as an external mixture of discrete aerosol types as quantified by the PALMS, AMS, and SP2 instruments simplifies the actual complex mixing state of the aerosol. Particles identified as dust are assumed to have a sulfate–organic coating, which is accounted for in the density, shape factor, refractive index, and hygroscopicity of the particles (Froyd et al., 2019). But more complex particles composed of mixtures of rBC, dust, and sulfate–organic components may result from coagulation or cloud processes and are not accounted for in this approach. Such complex mixtures of black carbon (BC, not measured with an SP2 instrument), organics, dust, and sulfate have been observed in the continental-scale outflow from Asia (Clarke et al., 2004) and Africa (China et al., 2015). However, based on PALMS mass spectra of individual particles, the simplified treatment of the mixing state of the aerosol in ATom is justified for much of the remote ATom dataset, in which many primary particles have been removed and well-aged, secondary particles dominate (Froyd et al., 2019; Hodzic et al., 2020). We explicitly treat rBC particles with coatings using air-mass-based averages of rBC core size and coating thickness as measured by the SP2 instrument (Sect. 2.7.2). Over all the ATom flights, rBC cores were present in 1.4 % of the aerosol by number over the SP2 size range (90–550 nm), while in identifiable BB plumes 4.3 % of these particles had rBC cores. Sulfate–organic coatings on dust are typically ∼ 5 %–10 % of the dust particle mass (Froyd et al., 2019). The sulfate and organic masses calculated by integrating the composition-resolved size distribution (see the Supplement) were consistent within ∼ 20 % with sulfate and organic masses directly measured by the AMS instrument, with $r^2 > 0.84$ (Fig. S4). This agreement indicates that substantial non-refractory sulfate and organic components were not "hidden" on other particle types (e.g., fine-mode sea salt) and were adequately accounted for in the PALMS classification scheme used here, and it supports our treatment of PALMS particle types as independent, external mixtures.

The aerosol sampling inlet used for the AMP measurements on the DC-8 aircraft, a shrouded solid diffuser inlet designed by A. Clarke (University of Hawaii) and evaluated by McNaughton et al. (2007), excludes most particles with ambient $D_p > 5\,\mu m$ at low altitude, with the 50 % passing efficiency falling to $\sim 3.2\,\mu m$ at ∼ 12 km (McNaughton et al., 2007; Brock et al., 2019). In addition, the LAS optical particle counter, which measures the size distribution of the coarse mode using a red laser, suffers from sizing ambiguities in the size range from ∼ 1 to ∼ 2 µm due to Mie oscillations in the scattering cross section. The LAS also has poor coarse-mode counting statistics due to a sample flow rate of $\sim 1\,cm^3\,s^{-1}$. For these reasons, we use data from the underwing CAS probe, which has an optically defined sample flow rate of $\sim 50\,cm^3\,s^{-1}$ (Spanu et al., 2020), for particles with $D_p > 1.01\,\mu m$. The CAS suffers from similar sizing ambiguities as the LAS. However, a data processing scheme similar to the technique described by Walser et al. (2017), combined with a Monte Carlo method, is used to retrieve a size distribution, with uncertainties, that minimizes these biases. This

methodology will be the subject of a future publication. In this process, a range of possible ambient size distributions that are consistent with the scattering signal and the PALMS-based determination of particle types in the largest size range (1.14 to ∼4.8 µm; Fig. 3) is calculated. For these calculations the refractive indices in Table 2 are used, and water uptake and the non-sphericity of dust are taken into account. Size distributions at dry conditions are then calculated using the hygroscopic growth factors in Table 2. The median size distribution is chosen from the resulting set of possible solutions, and these "dried" CAS data are combined with the AMP measurements to provide the continuous dry size distributions over D_p from 3–50 µm.

Refractory BC particles are treated separately from the rest of the aerosol measured during ATom. The SP2 instrument reports the mass of rBC cores with spherical volume-equivalent diameter from 90–500 nm as a function of time. Statistics regarding the size distribution of the rBC cores, as well as estimates of the average coating thickness on them, can be obtained with extensive averaging at the rBC concentrations found in ATom (outside pollution layers and biomass burning plumes). The size distribution and coating thickness on rBC particles were averaged over the same air mass regions as were the PALMS data when counting statistics were insufficient (Sect. 3.3). As described in Sect. 2.7.2, the averaged, coated size distributions from the SP2 measurements are used to estimate the absorption and other optical properties. However, the rBC size distribution is not combined with the other size distribution measurements, which are assumed to represent the purely scattering aerosol and dust. In other words, we assume two independent types of size distributions: (1) the composition-dependent size distributions, derived from the AMS, PALMS, and size distribution measurements that together describe all non-absorbing aerosol components and dust, and (2) the size distributions of coated rBC particles from the SP2 instrument that are averaged over air mass types and used to calculate MAC values as described in Sect. 2.7.2. (Note that coated rBC particles would also be measured by the size distribution instruments, but would be treated as other particle types – a minor error given low rBC abundance.)

Note that the PALMS instrument reports an "EC" (or "soot") compositional class, which is closely related to the rBC particles measured by the SP2 instrument. However, because PALMS distinguishes only a very small (and uncertain) fraction of all particles containing EC (Murphy et al., 2006), we simply assign all EC particles detected by PALMS to the non-absorbing "sulfate–organic" class for the purpose of calculating aerosol optical and hygroscopic properties (although the EC class is tracked separately in data files in case it might be useful in future analyses). Particles in the EC class are included in the sulfate–organic component in all figures. Light-absorbing rBC particles are assumed to be adequately represented by the more quantitative SP2 measurements alone.

2.4 Modal fits to dry size distributions

In global models, aerosol optical properties depend upon an accurate description of the size-resolved composition of dry particles, which is often described by lognormal parameters that represent different aerosol modes. To compare with these representations, lognormal fits were made to each mode (nucleation, Aitken, accumulation, and coarse) of the dry size distributions measured during ATom. The lognormal equation used is

$$\frac{\mathrm{d}X}{\mathrm{d}\log_{10} D_p} = \frac{X \ln(10)}{\sqrt{2\pi}\ln(\sigma_g)} \exp\left\{-0.5\left(\frac{\ln(D_p/D_{g,x})}{\ln(\sigma_g)}\right)^2\right\}, \quad (1)$$

where the three fitted parameters are X, which represents number or volume, the geometric standard deviation σ_g, and the geometric mean diameter $D_{g,x}$. These fits were made to the volume-weighted size distribution for the coarse ($D_p > 1$ µm) and accumulation ($0.08 > D_p \leq 1$ µm) modes and to the number distribution for the Aitken ($0.012 > D_p \leq 0.08$ µm) and nucleation ($0.03 \geq D_p \leq 0.012$ µm) modes. The fits began with the coarse mode and proceeded toward the nucleation mode. Once fitted, each larger mode was subtracted from the size distribution and the fit of the next smallest mode was made from the residual size distribution. This fitting method is described in more detail in the Supplement, and comparisons of integrated number, surface, and volume for the fitted size distributions and the raw size distributions are given in Tables S2–S4. All descriptions of aerosol properties are based on the measured, rather than fitted, size distributions unless otherwise noted.

2.5 Calculating ambient size distributions

To determine the growth of the dry particles to ambient diameter at the measured ambient water vapor saturation ratio (RH / 100), the hygroscopicity must be estimated for each of the aerosol types. The hygroscopicity of the particles is described by κ using κ-Köhler theory (Petters and Kreidenweis, 2007). In this parameterization, the wet particle diameter D_{drop} can be determined at a given water vapor saturation ratio $S(D_{drop})$ as

$$S(D_{drop}) = \frac{D_{drop}^3 - D_p^3}{D_{drop}^3 - D_p^3(1-k)} \exp\left(\frac{4\sigma_{drop} M_w}{RT\rho_w D_{drop}}\right), \quad (2)$$

where D_p is the diameter of the dry particle, σ_{drop} is the surface tension of the droplet (0.072 J m^{-2}), R is the universal gas constant (8.314 J mol^{-1}), T is the ambient air temperature (K), and ρ_w and M_w are the density and molecular weight of water (1000 kg m^{-3} and 0.018 kg mol^{-1}, respectively). For particles whose non-refractory composition

https://doi.org/10.5194/acp-21-15023-2021

Table 2. Assumed values of the hygroscopicity parameter κ, density ρ, and refractive index.

Instrument: parameter	Hygroscopicity parameter κ[a]	Reference	Density ρ (kg m^{-3})	Reference	Refractive index	Reference
PALMS: sulfate–organic particles	$(1 - F_{org})$[b] $\times 0.73 + F_{org} \times 0.17$[c]	Froyd et al. (2019)	$(1 - F_{org}) \times 1770 + F_{org} \times 1350$[c]	Froyd et al. (2019)	$((1 - F_{org}) \times 1.44 + F_{org} \times 1.48) + 0i$	Froyd et al. (2019)
PALMS: biomass burning, heavy fuel oil combustion, and meteoric	$(1 - F_{org}) \times 0.73 + F_{org} \times 0.17$	Froyd et al. (2019)	$(1 - F_{org}) \times 1770 + F_{org} \times 1350$[c]	Froyd et al. (2019)	$((1 - F_{org}) \times 1.44 + F_{org} \times 1.48) + 0i$	Froyd et al. (2019)
PALMS: soot (assumes small soot core with thick coating)	$(1 - F_{org}) \times 0.73 + F_{org} \times 0.17$	Froyd et al. (2019)	$(1 - F_{org}) \times 1770 + F_{org} \times 1350$[c]	Froyd et al. (2019)	$((1 - F_{org}) \times 1.44 + F_{org} \times 1.48) + 0i$	Froyd et al. (2019)
PALMS: sea salt	1.1	Zieger et al. (2017)	1800[c]	Froyd et al. (2019)	$1.447 + 0i$[d]	Froyd et al. (2019)
PALMS: mineral dust	0.03	Froyd et al. (2019)	2500	Froyd et al. (2019)	530 nm: $1.55 + 0.002i$[e]	Weinzierl et al. (2011)
PALMS: alkali salts	0.5	Froyd et al. (2019)	1500	Froyd et al. (2019)	$1.52 + 0i$	Froyd et al. (2019)
SP2: black carbon	n/a[f]		1800	Park et al. (2004)	$2.26 + 1.26i$	Moteki et al. (2010)
SP2: coating	n/a[f]		n/a[f]		$1.44 + 0i$	mean of AMS for all of ATom
Calculated: H_2O	n/a[f]		1000		$1.33 + 0i$	Hale and Querry (1973)
AMS: $(NH_4)_2SO_4$	0.483	Good et al. (2010)	1760	Hand and Kreidenweis (2002)	$1.527 + 0i$	Hand and Kreidenweis (2002)
AMS: $(NH_4)HSO_4$	0.543	Good et al. (2010)	1780	Hand and Kreidenweis (2002)	$1.479 + 0i$	Hand and Kreidenweis (2002)
AMS: $(NH_4)_3H(SO_4)_2$	0.579	Good et al. (2010)	1830	Hand and Kreidenweis (2002)	$1.53 + 0i$	Hand and Kreidenweis (2002)
AMS: H_2SO_4	0.87	Petters and Kreidenweis (2007)	1800	Hand and Kreidenweis (2002)	$1.408 + 0i$	Hand and Kreidenweis (2002)
AMS: NH_4NO_3	0.597	Good et al. (2010)	1725	Tang (1996)	$1.553 + 0i$	Tang (1996)
AMS: NH_4Cl	0.5	assumed[g]	1519	Haynes et al. (2014)	$1.64 + 0i$	Haynes et al. (2014)
AMS: HNO_3	0.999	Good et al. (2010)	1513	Haynes et al. (2014)	$1.393 + 0i$	Haynes et al. (2014)
AMS: HCl	0.5	assumed	1490	Haynes et al. (2014)	$1.329 + 0i$	Haynes et al. (2014)
AMS: OA	$0.19 \times (O/C) - 0.0048$[h] Mean = 0.179	Rickards et al. (2013)	1550[c]	Guo et al. (2021) average from ATom-1 and ATom-2	$1.48 + 0i$	Varma et al. (2013)

[a] PALMS κ values are applied to refractory and non-refractory components for all $D_p > 0.25$ µm. AMS values are applied to all non-refractory components for $D_p \leq 0.25$ µm. The Zaveri et al. (2005) composition model provides speciation of AMS components. [b] F_{org} is the ratio of organic to organic+sulfate mass in that size class determined by the PALMS instrument. [c] Organic density applied to PALMS is chosen from Froyd et al. (2019) for consistency with other PALMS data products, but is inconsistent with AMS-derived density from Guo et al. (2021) applied here to AMS data. [d] Assumes 27 % residual water by mass (Froyd et al., 2019). [e] Imaginary component of refractive index for mineral dust assumed to vary with wavelength using Eq. (11), with an Ångström exponent of 3. [f] Not applicable: this parameter not used in any calculations. [g] Assumed value is not critical because these species are an insignificant part (< 0.5 %) of the total fine aerosol mass. [h] O / C is the O : C ratio from the HR-ToF-AMS measurements. The O : C ratios are smoothed with a running 10-point binomial filter (across ∼ 10 min of data) before this equation is applied.

is described by the AMS (all particles with $D_p < 0.14\,\mu m$ and the sulfate–organic, biomass burning, meteoric, and EC fractions between 0.14 and 0.25 µm), an algebraic inorganic electrolyte composition model (Zaveri et al., 2005) was used to calculate the concentrations of ammonium sulfate, ammonium bisulfate, letovicite, sulfuric acid, ammonium nitrate, ammonium chloride, nitric acid, and hydrochloric acid from the AMS measurements of sulfate, nitrate, ammonium, and chloride. For this calculation, negative AMS values (which can occur due to background signal subtraction; Jimenez et al., 2021) were set to zero. The κ from these electrolytic species (Table 2) was applied using the volume-weighted ZSR mixing rule to estimate the inorganic κ for each data point. The κ of the OA was estimated using the ratio of O / C reported by the AMS as

$$\kappa_{OA} = 0.19 \times (O/C) - 0.0048, \quad (3)$$

following Rickards et al. (2013). The κ_{OA} values were smoothed with a running 10-point binomial smoothing algorithm to reduce noise. The project-wide average organic κ_{OA} from this method was 0.18 ± 0.03. An analysis of the relationship between κ_{OA} and the O / C ratio (Nakao, 2017) found that volatility and solubility are also key parameters in determining κ_{OA}, but we lack the additional information on such properties needed to provide a revised estimate. The value of $\kappa_{OA} = 0.18$ is higher than those commonly measured or assumed at continental locations. However, in the very remote air masses that comprised the bulk of the ATom sampling, the OA was highly oxidized and chemically processed (Hodzic et al., 2020). The Zaveri–κ-Köhler approach was used successfully to simulate observed aerosol hygroscopic growth over a wide range of aerosol compositions in the southeastern United States (Brock et al., 2016a). For the ATom data, the value of κ was estimated as a volume-weighted sum of the κ values of the non-refractory organic and inorganic components from the AMS measurements and the inorganic composition model using the values listed in Table 2. The ATom project mean value of κ from the AMS measurements was 0.55 ± 0.18 due to the highly oxidized OA and the abundance of acidic sulfate species present.

For particles with $D_p > 0.25\,\mu m$ in the PALMS sulfate–organic, BB, meteoric, and EC compositional classes, κ was estimated using the PALMS-measured organic mass fraction, F_{org},

$$\kappa = \left(1 - F_{org}\right) \times 0.73 + F_{org} \times 0.17, \quad (4)$$

assuming particles were composed of acidic sulfate components, using the project mean inorganic κ from the AMS, and organic material (Froyd et al., 2019). Equation (4) is a mass-weighted implementation of the ZSR mixing rule, again assuming no chemical interactions between the organic and inorganic components. Nitrate mass fraction is not quantified by PALMS for the non-refractory particle classes, but this likely produces only a minor bias in κ because nitrate concentrations were small (Nault et al., 2021). For example, for submicron sizes, the median AMS nitrate mass fraction was 2.4 %, with 25th and 75th percentiles of 0.9 % and 4.6 %, respectively, when total AMS concentrations were positive.

For a pure organic aerosol ($F_{org} = 1$), Eq. (4) yields $\kappa_{org} = 0.17$, which is close to the AMS project-wide value of $\kappa_{org} = 0.18$ from Eq. (3). Using Eq. (4), the project-wide mean value of κ for non-refractory PALMS particle types with $D_p > 0.25\,\mu m$ was 0.52 ± 0.09, which is similar to the AMS value of 0.54 for smaller particles. The κ values for each aerosol type in the largest PALMS size class ($1.13 < D_p \leq 4.8\,\mu m$) were applied to particles with $D_p > 4.8\,\mu m$.

Applying the values of κ listed in Table 2, the RH determined from measured static air temperature and water vapor mixing ratios, and Eq. (2), the dry size distributions for sea salt, BB, sulfate–organic, soil dust, heavy fuel oil combustion, meteoric material, and alkali salts were used to calculate ambient size distributions for each composition class. The contribution of water was calculated from the difference between the wet and dry size distributions for each composition class.

2.6 Calculating cloud condensation nuclei

The concentrations of cloud condensation nuclei (CCN) at several fixed supersaturations were calculated based on the observed dry size distributions and the composition determined from the AMS and the inorganic composition model (Zaveri et al., 2005). To calculate the critical wet diameter, D_{crit}, Eq. (2) was iteratively solved with different D_{drop} using a fixed D_p and a fixed κ determined from the AMS measurements as described in Sect. 2.5 until the maximum supersaturation S_{max} was found. This process was repeated for different D_p until S_{max} matched the supersaturation for which the CCN concentration was being calculated, giving $D_{crit,dry}$, the dry D_p that yielded D_{crit} for a given κ and S_{max}. The number size distribution was then integrated across all $D_p \geq D_{crit,dry}$, yielding the calculated CCN concentration for that minute of flight. The AMS-derived κ values were chosen to infer $D_{crit,dry}$ as these generally fall into the size range in which composition is best constrained by the AMS. For ATom, CCN concentrations were calculated for fixed supersaturations of 0.05 %, 0.1 %, 0.2 %, 0.5 %, and 1.0 %.

2.7 Calculating dry and ambient optical properties

2.7.1 Scattering

Scattering was calculated for each of the composition-based size distributions independently as

$$\sigma_{s,i}(\lambda) = \int_{3\,nm}^{50\,\mu m} \frac{\pi}{4} D_p^2 \alpha_{s,i}\left(D_p, n_i, \lambda\right) N_i\left(D_p\right) d\log_{10}\left(D_p\right), \quad (5)$$

where $\sigma_{s,i}$ is the scattering coefficient (m^{-1}) caused by composition type i (Sect. 2.3), $\alpha_{s,i}$ is the scattering efficiency at wavelength λ calculated from Mie theory using refractive index n_i (Table 2), and N_i is the number concentration (m^{-3}) of particles of composition i within the logarithmic size interval $d\log_{10}(D_p)$. Scattering was calculated for the wavelengths of 340, 380, 405, 440, 532, 550, 670, 870, 940, and 1020 nm, which match common wavelengths for the AERONET sun photometers and satellite measurements of AOD. The refractive indices in Table 2 are not adjusted for wavelength; this is a small potential bias in the context of other assumptions and approximations in the calculation. All particle types are treated as purely scattering, spherical in shape, and internally homogeneous for optical calculations, with the exception of the absorbing components rBC, BrC, and mineral dust, which are described in Sect. 2.7.2. Non-refractory particles with $D_p < 0.25\,\mu m$, and all particles with $D_p < 0.14\,\mu m$, are treated as fully mixed, multi-component mixtures based on the AMS-derived composition and the ZSR mixing state representation introduced in Sect. 2.3.1. The dry particle refractive index is calculated as the volume-weighted mean refractive index of contributing components. This calculation is further simplified for non-refractory particles with $D_p > 0.25\,\mu m$ using just the PALMS organic and sulfate mass fractions (Froyd et al., 2019) and applying organic and sulfate real refractive indices (Table 2) to both of these components. Total scattering is the sum of the scattering from the individual composition-based size distributions $\left(\sigma_{s,tot}(\lambda) = \sum_i \sigma_{s,i}(\lambda)\right)$.

To calculate the scattering coefficient of the aerosol at ambient RH, the effects of hygroscopic growth were considered. The diameter of every particle was adjusted based on growth factors for that aerosol type calculated as described in Sect. 2.5, and the refractive index was adjusted to the volume-weighted mean of dry particle and water refractive indices. Scattering coefficients were also calculated for the particle size distributions at fixed RH values of 70 %, 80 %, and 85 % at the 532 nm wavelength. These values were used to fit a parametric curve describing $f(RH)$, the RH dependence of scattering, as described in Sect. 2.7.4.

2.7.2 Absorption

The aerosol absorption coefficient (σ_a, in m^{-1}) is determined for three aerosol components: refractory black carbon as measured by laser-induced incandescence by the SP2 instrument (rBC), brown carbon (BrC) extrapolated from measurements of liquid absorption in aqueous filter extracts, and absorption due to mineral dust particles identified by the PALMS instrument. The absorption for each of these components is calculated differently. Absorption due to rBC is determined using core–shell Mie theory to calculate regionally representative values of absorption per unit mass (mass absorption cross sections, or MACs) in different air mass types based on the observed size distribution of absorbing cores and the thickness of non-absorbing coatings. These MAC values are then multiplied by the observed 60 s average rBC concentrations to get $\sigma_{a,rBC}$ values. Absorption due to BrC is only roughly approximated using the liquid absorption measured in aqueous extracts from infrequent filter samples, correcting these values for assumed non-soluble BrC and for aerosolization, and developing a proxy relationship between $\sigma_{a,BrC}$ and measured rBC and BB particle concentrations. Neither rBC nor BrC absorbing components are considered in the calculation of optical properties for any of the other particle types, for which we use Mie theory assuming homogeneous uncoated spheres. For mineral dust, a refractive index with a wavelength-dependent imaginary component is applied to the measured 60 s dust size distributions, and $\sigma_{a,dust}$ is explicitly calculated using Mie theory assuming homogeneous spherical particles. Details of the calculations of σ_a for these three absorbing components follow.

Absorption due to rBC was calculated using measurements of rBC core size and coating thickness from the SP2 instrument, averaged over the air mass type. Coating thickness could be determined only from the subset of cores with rBC mass between ~ 2.5 and 6 fg ($\sim$ 140–330 nm volume-equivalent diameter), but this average coating thickness was applied to all rBC cores measured (Gao et al., 2007). The coated size distributions were used to calculate mass absorption cross sections at the same wavelengths of 340, 380, 405, 440, 532, 550, 670, 870, 940, and 1020 nm for each air mass type via core–shell Mie theory (Bohren and Huffman, 1998), assuming that the refractive index of the rBC (Moteki et al., 2010; Table 2) remains constant across these wavelengths (Bond et al., 2013). The calculated regional average MACs were then multiplied by the 60 s averaged rBC mass measured within each respective region to estimate absorption due to the rBC ($\sigma_{a,BC}$) on a 60 s time base. We assume that hygroscopic growth on coated rBC particles does not appreciably change the absorption coefficient through additional lensing effects, since substantial coatings on the aged rBC particles already existed. This assumption is supported by studies that have modeled the effects of coating thicknesses on BC cores that show a saturation effect as coating thickness increases (e.g., Zanatta et al., 2018). It is important to note that this study is not designed to evaluate the characteristics of BC refractive index and morphology (e.g., core–shell) but that these parameters are assumed. These assumptions are discussed in more detail in Sect. 4.1.3.

Absorption due to dust particles ($\sigma_{a,dust}$) was calculated simultaneously with the dust-scattering calculation using the complex refractive indices at three visible wavelengths for Saharan dust provided by Weinzierl et al. (2011). Based on these measurements we use a refractive index of $1.55 + 0.002i$ at a wavelength of 530 nm, with an Ångström coefficient of 3 applied to the imaginary component. We assume that water uptake by dust particles does not change the imaginary component of the refractive index; i.e., the absorbing

minerals are insoluble, and we assume no lensing effects due to coatings or water uptake. However, the real component of the refractive index was allowed to vary with water uptake based on the hygroscopicity of the dust (Table 2). Since this change in real refractive index affects $\sigma_{a,dust}$, this value is slightly different for dry and ambient RH conditions.

In addition to broad-spectrum absorption by rBC and dust, certain organic species absorb light in blue and near-UV wavelengths; these compounds are referred to as brown carbon (BrC). Most of the BrC in the remote atmosphere is believed to originate from biomass burning (e.g., Washenfelder et al., 2015). Absorption due to BrC may change with time from emission due to photo-bleaching of chromophores or to secondary production of absorbing organic species (e.g., Forrister et al., 2015; Liu et al., 2020). Secondary production is believed to take place near combustion sources, while initial bleaching timescales of a day (Forrister et al., 2015; Wang et al., 2016; Wong et al., 2019; Wu et al., 2021). However, there is evidence that high-molecular-weight chromophores may persist in aged biomass burning plumes (Di Lorenzo and Young, 2016; Wong et al., 2017). Absorption from the 300–700 nm wavelength due to water-soluble (WS) BrC was measured during deployments 2–4 of the ATom mission (Zeng et al., 2020). These measurements were made using aqueous extracts from Teflon filters collected over 5–15 min periods. Because of these long sampling periods, it is difficult to directly combine the BrC measurements with the 60 s data used in this analysis. However, we can take advantage of the observed correlations between WS BrC absorption and rBC mass and between WS BrC absorption and the PALMS biomass burning mass (supplemental materials in Zeng et al., 2020) to roughly estimate the WS BrC at 365 nm at 60 s frequency. This proxy WS BrC is calculated from a multivariate linear regression between these parameters and is then multiplied by a factor of 2 to approximately account for unmeasured BrC that is not extractable in water and another factor of 2 to convert from bulk liquid absorption to aerosol absorption (Zeng et al., 2020). The final proxy relationship is

$$\sigma_{a,BrC}(365\,\text{nm}) = 4\,(a_1 M_{BB} + a_2 M_{BC})\,, \quad (6)$$

where a_1 and a_2 are parameters from the multivariate linear regressions from ATom-3–4, and M_{BB} and M_{BC} are the mass concentrations of the PALMS biomass burning particles and the SP2 rBC, respectively. Only values from ATom-3 and ATom-4 were used for Eq. (6) because most BrC measurements during ATom-2 were derived from two regions of burning in Africa and South America, while during ATom-3 and ATom-4, more dilute smoke from a range of geographic regions was sampled. The values of a_1 and a_2 were 0.07 ± 0.06 and $5.4 \pm 1.1\,\text{m}^2\,\text{g}^{-1}$, respectively. A two-sided linear regression between this proxy BrC and the measured values yielded a slope of 0.68 ± 0.06 and $r^2 = 0.40$.

Given the modest ability of the proxy BrC absorption to predict the measured values, as well as the uncertainty in accounting for water-insoluble BrC and in the conversion from liquid to aerosol absorption, this $\sigma_{a,BrC}$ is probably accurate to within only a factor of ~ 3. The absorption coefficients due to BrC at the wavelengths used to calculate scattering and extinction were estimated using an absorption Ångström exponent value of 5 based on the measured liquid absorbance from 300–700 nm (Zeng et al., 2020).

2.7.3 Extinction

Absorption due to BrC, rBC, and dust was summed with total scattering calculated as described in Sect. 2.7.1 to provide total aerosol extinction:

$$\sigma_e(\lambda) = \sigma_{s,tot}(\lambda) + \sigma_{a,dust}(\lambda) + \sigma_{a,BC}(\lambda) + \sigma_{a,BrC}(\lambda). \quad (7)$$

During ATom-4, the SOAP (spectrometers for optical aerosol properties) instrument measured dry aerosol extinction at a wavelength of 532 nm using cavity ring-down spectrometry (Langridge et al., 2011). For comparison with this direct extinction measurement, dry extinction at 532 nm was calculated for a truncated size distribution to match the SOAP instrument, which operated behind a 2 µm aerodynamic diameter impactor. This calculated extinction agreed within experimental uncertainties with the SOAP extinction (Fig. 4a), with a slope of 0.98 and a Pearson's regression coefficient (r^2) of 0.86. Similarly, the absorption calculated from the SP2 measurements at 532 nm as described in Sect. 2.7.2 agreed well with the SOAP photoacoustic absorption spectrometer (Lack et al., 2012) during ATom-4 when the absorption signal was greater than the SOAP noise level of $\sim 2 \times 10^{-6}\,\text{m}^{-1}$ (Fig. 4b), with a slope of 0.88 and $r^2 = 0.71$. These comparisons of the calculations of extinction based on aerosol composition, size distribution, refractive index, and rBC mass and coating thickness with independent, direct measurements of extinction and absorption provide confidence that the calculated optical properties represent the bulk submicron aerosol properties in the atmosphere with good fidelity.

2.7.4 Intensive optical properties

Intensive aerosol properties are those that do not vary with abundance. All intensive optical properties were calculated at wavelengths of 340, 380, 405, 440, 532, 550, 670, 870, 940, and 1020 nm. Single-scatter albedo ω_0 is the ratio of scattering to total extinction ($\sigma_{s,tot}/\sigma_e$). The value of ω_0 was calculated for both the total dry size distributions and those at ambient RH. As described in Sect. 2.7.2, the absorbing component is calculated from regionally averaged MAC values multiplied by the 60 s rBC mass concentrations and from the proxy $\sigma_{a,BrC}(\lambda)$. We do not attempt to model absorption by adjusting the imaginary refractive index of the different components of the composition-resolved size distributions because this would be a severely under-constrained problem.

Mass extinction efficiency is the ratio of extinction to aerosol mass concentration. This parameter is calculated

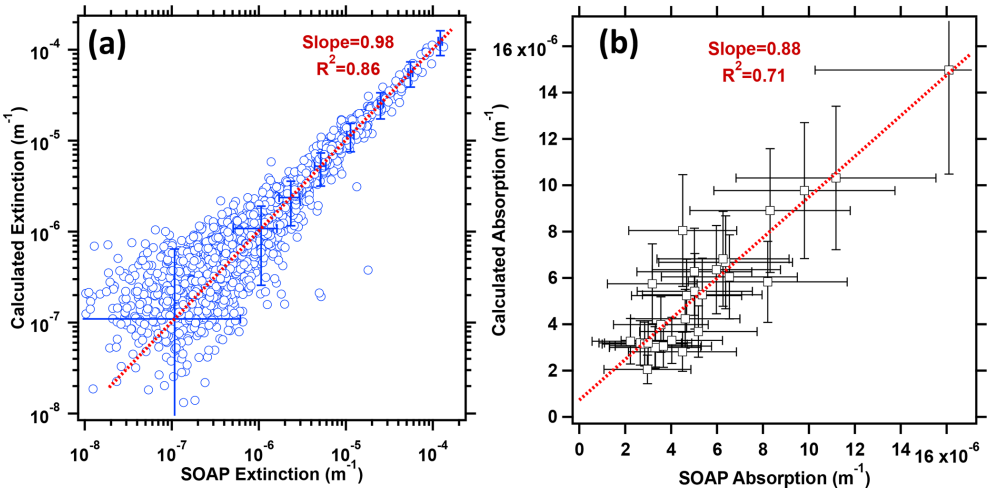

Figure 4. **(a)** Calculated aerosol extinction as a function of measured extinction from the SOAP cavity ring-down spectrometer during ATom-4, showing representative error bars. **(b)** As in **(a)**, but for calculated aerosol absorption and measured absorption from the SOAP photoacoustic spectrometer for cases when absorption $> 2 \times 10^{-6}\,\mathrm{m}^{-1}$ (2× the detection limit). Lines and slopes are from two-sided (orthogonal distance) linear regressions accounting for uncertainties; r^2 values are from one-sided fits. The fitted line in **(a)** was determined from logarithmically transformed data ($\log(y)$ vs. $\log(x)$ regression).

from the dry size distributions using the total dry extinction coefficient σ_e and the total aerosol mass, which is the sum of the aerosol density for each composition component (Table 2) multiplied by the particle volume from the integrated size distribution for that component.

Phase function $P(\theta, \lambda)$ is the normalized angular distribution of light intensity scattered by an aerosol in angle θ relative to the incident radiation. For spherical (Mie) scatterers, it is defined as

$$P_i(\theta, \lambda) = \frac{I_i(\theta, \lambda)}{\int_0^{\pi} I_i(\theta', \lambda) \sin\theta' \mathrm{d}\theta'}, \quad (8)$$

where I is the intensity of the scattered light from an aerosol of composition class i. The asymmetry parameter g is a simplified description of the phase function that is often used in radiative transfer approximations such as the Henyey–Greenstein phase function or the delta-Eddington approach, which are then applied within global-scale models. The asymmetry parameter for an aerosol of composition i is defined as

$$g_i(\lambda) = \frac{1}{2} \int_0^{\pi} \cos\theta\, P_i(\theta, \lambda) \sin\theta \mathrm{d}\theta. \quad (9)$$

As described by Moosmüller and Ogren (2017), practical values of g_i in the atmosphere range from 0 (symmetrically scattered light) to +1 (purely forward-scattered light). Typical values for accumulation-mode-dominated size distributions for mid-visible wavelengths are ∼0.4–0.6, with larger values possible for size distributions with a substantial coarse fraction (e.g., Andrews et al., 2006; Fiebig and Ogren, 2006). We calculate the total aerosol g for both dry and ambient RH conditions from the scattering-weighted sum of the g_i from each composition-based size distribution. The small contribution of rBC and BrC to $P(\theta)$, g, and the scattering coefficient is ignored.

The fine-mode fraction (η) is the fraction of the total extinction that is attributable to the fine mode (e.g., Anderson et al., 2005). This is a parameter that can be retrieved from remote sensing measurements and that apportions the light extinction between the fine (accumulation) mode, whose particles are mostly produced from combustion and secondary processes, and the coarse mode, whose particles are mostly generated by mechanical processes. Because some of the coarse-mode particles extend into the submicron size range (and vice versa), we use the modal fits to the composition-based size distributions to calculate η. The refractive index and hygroscopicity of the coarse and fine modes used to calculate η is calculated from the volume-weighted mean contribution of each composition class within 1 geometric standard deviation of the volume modal diameter of that mode.

The ratio of scattering at wavelength λ at a given RH to that at dry conditions, or $f(\mathrm{RH})_\lambda$, can be parameterized simply using a physically based function,

$$f(\mathrm{RH})_\lambda \equiv \frac{\sigma_{s,\mathrm{tot}}(\lambda, \mathrm{RH})}{\sigma_{s,\mathrm{tot}}(\lambda, \mathrm{RH} = \mathrm{dry})} \simeq 1 + \kappa_{\mathrm{ext}} \frac{\mathrm{RH}}{100 - \mathrm{RH}}, \quad (10)$$

where κ_{ext} is a fitted parameter that is related to, but not identical to, the κ in κ-Köhler theory (Brock et al., 2016a). Because the dry size distributions are assumed to be measured at RH = 0 %, no correction to Eq. (10) to account for residual water (Titos et al., 2016; Kuang et al., 2017; Burgos et al., 2020) is applied. The value of κ_{ext} was calculated for each 60 s data interval by least-squares fitting of Eq. (10) to

the scattering values calculated at the dry condition and at RH values of 70 %, 80 %, and 85 % for each of the 10 wavelengths considered. Separately, the value of $f(\mathrm{RH})$ was calculated for RH = 85 % for comparison with literature values (e.g., Burgos et al., 2020).

The Ångström exponent describes the power-law relationship between extinction, scattering, or absorption and the wavelength of incident light:

$$\frac{\sigma_{x,\lambda}}{\sigma_{x,\lambda_0}} = \left(\frac{\lambda}{\lambda_0}\right)^{-\gamma_x}, \tag{11}$$

where x represents extinction (e), scattering (s), or absorption (a), and λ is the wavelength of incident light; γ is the Ångström exponent, and the naught subscript indicates a reference wavelength. Values of γ_e and γ_s are determined by making a least-squares fit to the calculated values of σ_e and σ_s, respectively, over two wavelength ranges. The first of these, termed the UV–Vis Ångström exponent, is determined by fitting to the values at 340, 380, 405, 440, 532, and 550 nm wavelengths, while the Vis–IR Ångström exponent is calculated at the wavelengths of 670, 870, 940, and 1020 nm. The value of γ_a for $\sigma_{a,BrC}$ is assumed to be 5 at all wavelengths (Zeng et al., 2020). For $\sigma_{a,rBC}$, γ_a is calculated from regionally averaged rBC size distributions using core–shell Mie theory (Sect. 2.7.2) for the UV–Vis and Vis–IR wavelength ranges. Because the raw scattering, extinction, and absorption coefficients at all 10 wavelengths are provided in the archived dataset, additional Ångström exponents using specific wavelength pairs can be readily calculated.

2.8 Calculating aerosol optical depth

During ATom the DC-8 executed repeated en route ascents and descents between ∼ 0.16 and ∼ 12 km approximately every 30–60 min. By integrating ambient extinction or absorption vertically during each ascent or descent, extinction AOD and absorption AOD (AAOD) can be calculated. Because ambient extinction is calculated for each composition class, it is possible to determine the portion of AOD attributable to each of these classes, along with the associated water. This provides a valuable dataset with which to apportion AOD amongst different aerosol types and can be used to compare with model representations of AOD and with assumptions regarding aerosol types used in remote sensing retrieval algorithms.

To adequately represent atmospheric AOD and AAOD, each integrated profile should contain representative measurements in the MBL, where sea salt aerosol often dominates total AOD. The profiles should also contain any optically significant layers, such as biomass burning and dust plumes, that may be present. To ensure that the profiles represent atmospheric AOD, the following rules were used: (1) data were integrated over 1 km thick layers, (2) the profile must have extended from the bottom 1 km layer to at least 8 km in altitude, (3) the bottom two layers (0–2 km) both must have contained valid extinction data, (4) no more than two layers above the required bottom two layers could have been discarded due to cloud screening, and (5) data were interpolated across up to two such discarded layers. There are typically one or two 60 s average data points within each layer for each profile. Of the total 625 oceanic profiles made during ATom, 463 met the criteria listed above. The number of profiles in different latitude regions over the Atlantic and Pacific Ocean is provided in Table S5.

Atmospheric AOD was calculated as

$$\mathrm{AOD}_\lambda = \sum_{j=0}^{N} \overline{\sigma_{e,\lambda,j}}\,\Delta z, \tag{12}$$

where j represents each 1 km thick layer Δz beginning at altitude $z = 0$ km, and $\overline{\sigma_{e,\lambda,j}}$ is the ambient extinction coefficient for wavelength λ averaged from the 60 s data within the layer. Absorption AOD (AAOD) is obtained by substituting σ_a for σ_e.

3 Results

3.1 Aerosol extinction

Aerosol extinction was calculated for both the dry and ambient RH conditions, at STP, and at ambient pressure and temperature. The difference between the ambient RH and dry extinction values provides the extinction due to H_2O. The spatial pattern of ambient total extinction and that due to the aerosol types that dominate AOD – biomass burning, sulfate–organic mixtures, sea salt, dust, and H_2O – is shown in Fig. 5. This figure shows the comprehensive coverage in altitude and latitude of the ATom flights and provides an overview of the spatial patterns of the contribution of different aerosol species to AOD. Total ambient extinction in the remote marine atmosphere (Fig. 5a, b) is dominated by sea salt (Fig. 5g, h) and associated water (Fig. 5k, l) in the MBL, with several notable exceptions. Biomass burning aerosol over the northern subtropical Atlantic, and to a lesser extent over the southern subtropical Atlantic and the tropical and northern midlatitude Pacific, at altitudes < 4 km is an important contributor to dry extinction (Fig. 5c, d; Schill et al., 2020). In general, the Northern Hemisphere has more biomass burning extinction than the Southern Hemisphere. Contributions to extinction from sulfate–organic particles of mostly secondary origin (Fig. 5 e, f; Hodzic et al., 2020) are substantially higher in the Northern than the Southern Hemisphere, especially over the Pacific, due to higher biogenic and anthropogenic emissions in the more continental Northern Hemisphere.

Extinction due to dust is important in the tropics and subtropics of the Atlantic Ocean due mostly to emissions from the Sahara (Fig. 5i, j). There are also significant contributions to extinction from dust in the midlatitudes of the Atlantic and in the free troposphere (FT) of the northern Pacific

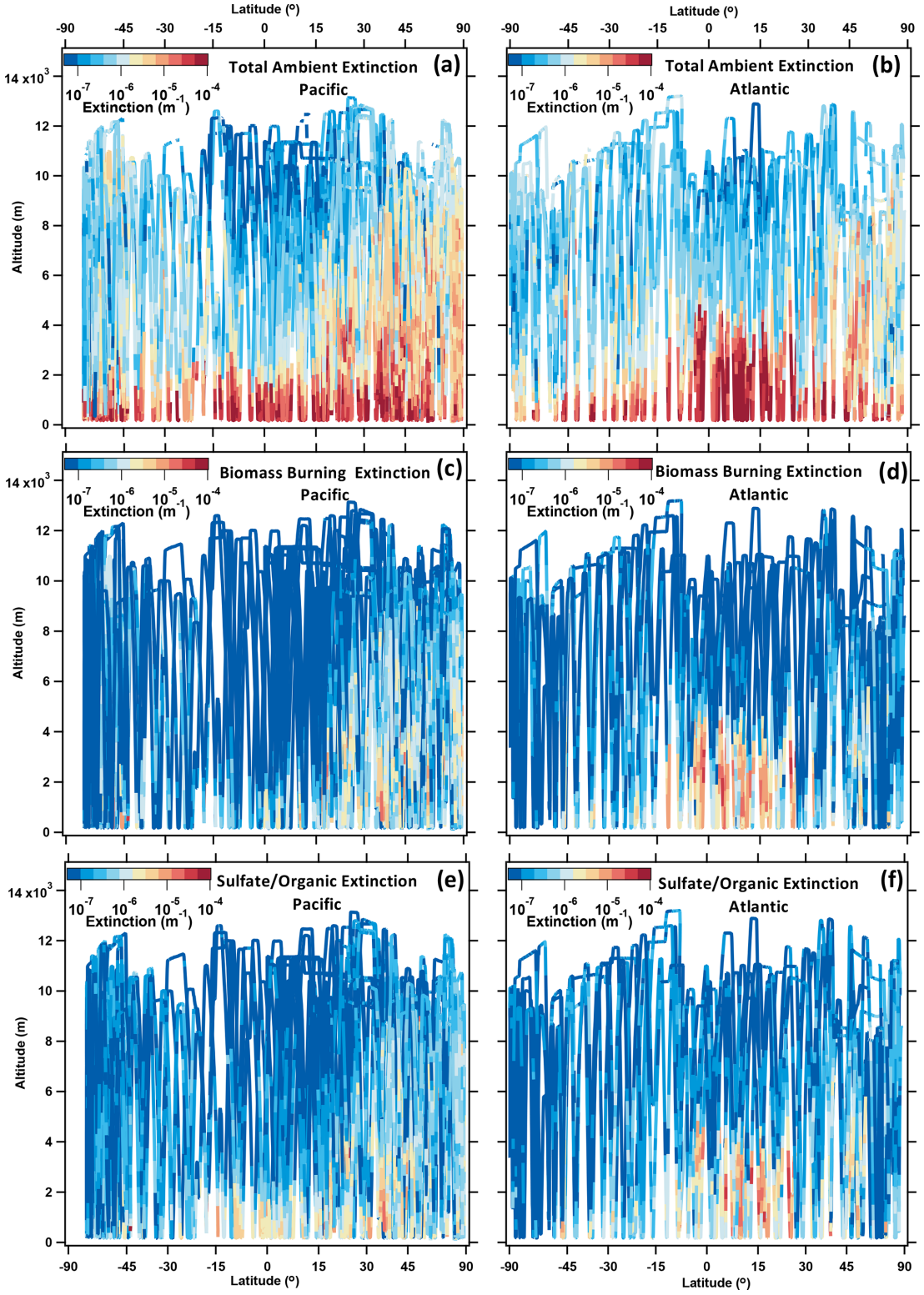
Latitude (°)
-90 -45 -30 -15 0 15 30 45 90
Altitude (m)
14 x10^3
12
10
8
6
4
2
0
Total Ambient Extinction
(a)
Pacific
Extinction (m^-1)
10^-7 10^-6 10^-5 10^-4
Total Ambient Extinction
(b)
Atlantic
Biomass Burning Extinction
(c)
Pacific
Biomass Burning Extinction
(d)
Atlantic
Sulfate/Organic Extinction
(e)
Pacific
Sulfate/Organic Extinction
(f)
Atlantic

Figure 5.

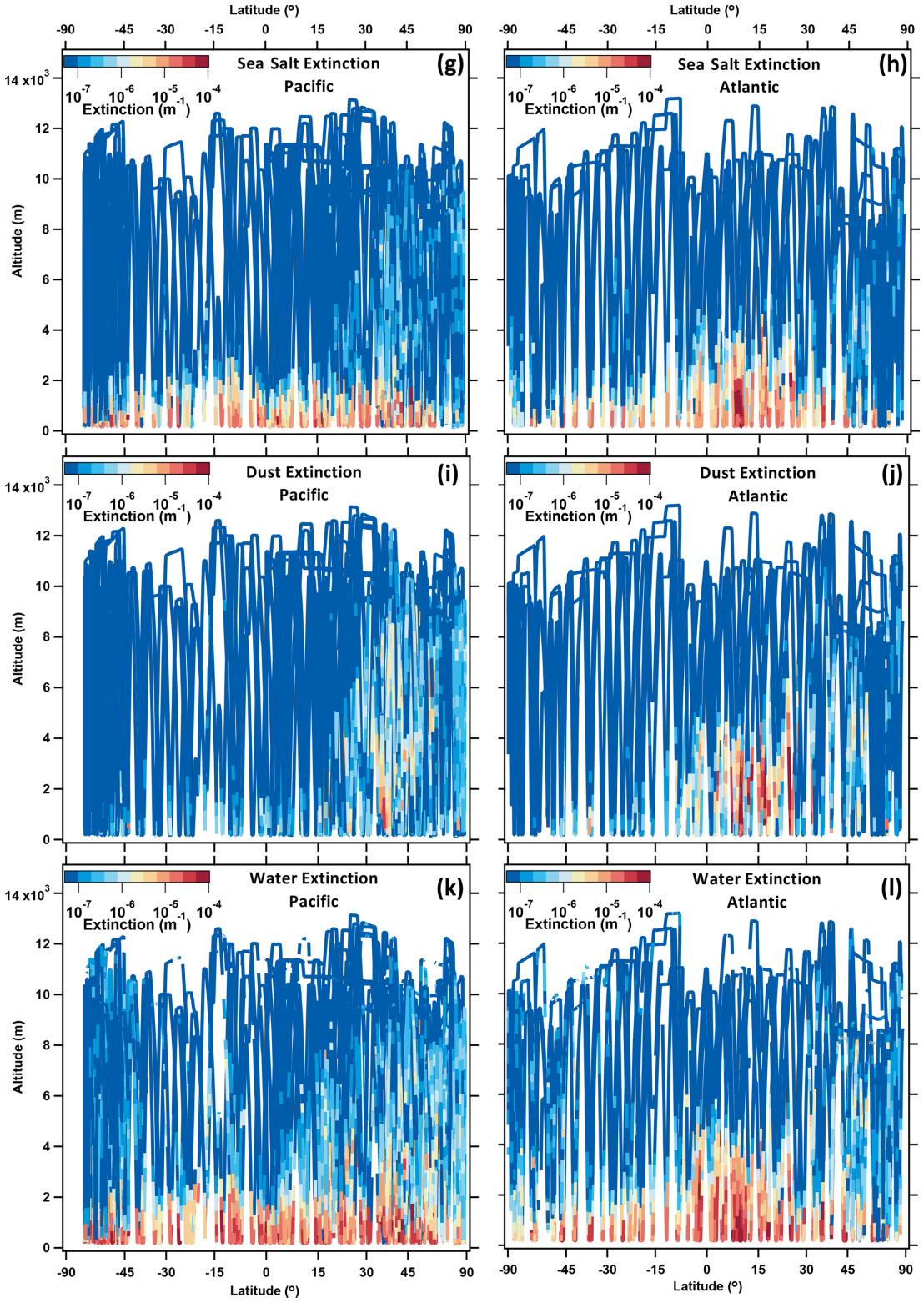

Figure 5. Altitude as a function of latitude color-coded by extinction for all ATom deployments. The x axis is scaled to be proportional to the Earth's surface area. The left column shows measurements made over the Pacific Ocean, western Arctic, and Southern Ocean; the right column is over the Atlantic, eastern Arctic, and Antarctic Peninsula (see Fig. 1). **(a, b)** Total ambient extinction; **(c, d)** dry extinction from biomass burning particles; **(e, f)** dry extinction from mixed sulfate–organic particles; **(g, h)** dry extinction from sea salt particles; **(i, j)** dry extinction from dust particles; **(k, l)** extinction from water associated with all particle types based on the κ-Köhler hygroscopic growth model.

due to dust emitted from Asia and the Sahara (Froyd et al., 2021). There is very little extinction from dust in the Southern Hemisphere at altitudes > 2 km, in sharp contrast with the Northern Hemisphere.

3.2 AOD and comparison with AERONET

The ambient extinction measured during each profile (Fig. 5) was vertically integrated as described in Sect. 2.8 to calculate AOD. Several of these profiles were relatively near AERONET sites. AERONET is an affiliation of ground-based remote sensing sites that use consistent methodologies, calibrations, and instrumentation to make sun photometer measurements of AOD and, in cases of high atmospheric turbidity, aerosol optical and microphysical properties (Holben et al., 1998, 2006). These measurements provide an opportunity to compare AOD calculated through the complex process outlined in Figs. 2 and 3 with directly measured values. Individual profiles were selected for comparison with AERONET if (1) the location of the aircraft at the midpoint in time between the start and end of the profile was within 300 km of the AERONET site and (2) if the midpoint time of the profile was within ± 4 h of an AERONET data record. An exception was made for the Macquarie Island site, as it was the only AERONET site with data in the Southern Ocean. Macquarie Island was 421–601 km from the midpoint of the nearest three DC-8 profiles. There were no matches meeting criteria (1) and (2) between the ATom profiles and the ship-borne Maritime AERONET Network (Smirnov et al., 2009). For comparisons of AOD with the AERONET site at the Mauna Loa Observatory, which lies at 3.4 km of altitude, the DC-8 profile was integrated upward beginning with the 3–4 km altitude bin. Version 3 Level 2.0 AERONET data were used for all comparisons, and the AOD at 532 nm was interpolated from observations at 500 and 675 nm using the Ångström equation (Eq. 11).

The stratospheric aerosol layer contributes ~ 0.005 to ~ 0.01 to mid-visible AOD measured by AERONET (e.g., Yang, 2017) but not to that derived from the DC-8 profiles. The contribution of stratospheric AOD was determined using the Global Space-based Stratospheric Aerosol Climatology (GLOSSAC) v. 2.0 (NASA/LARC/SD/ASDC, 2018; Kovilakam et al., 2020). The mean values of stratospheric AOD at 532 and 1020 nm sampled along the aircraft flight track from the starting to ending location of each profile were spatially interpolated from this dataset and estimated for other wavelengths using Eq. (11). These values were added to the AODs calculated from each ATom profile and are significant contributors to AOD for the profiles with the lowest aerosol burdens.

A two-sided linear regression between the calculated and measured AOD, accounting for estimated uncertainties, produces a slope of 0.86 with $r^2 = 0.76$ (Fig. 6a). A logarithmic plot of the same data shows that values of AOD calculated from the ATom aircraft data are generally lower than those from the AERONET sites, especially for AOD values < 0.05 (Fig. 6b). The normalized mean bias for all of the data points is -0.07, suggesting a slight underestimate by the aircraft compared with the sun photometers. Overall, 22 of the 32 comparison points are within a factor of 2 (Fig. 6b). We note that the average distance between the AERONET sites, excluding Macquarie Island, and the midpoint of the DC-8 profiles was 161 km. Further, the DC-8 performed slantwise profiles spanning ~ 25 min and ~ 300 km horizontally, while the AERONET sites made direct solar measurements. Past analysis has shown that comparisons between aircraft-derived AOD and those from sun photometer sites must be made with great care, accounting for horizontal variability in aerosol characteristics and loading, even over the remote Pacific Ocean (e.g., Shinozuka et al., 2004). The comparisons between AODs derived from the ATom slantwise profiles and the nearest available AERONET sites should be considered as simple "sanity checks", rather than as robust, quantitative evaluations. More detailed analyses comparing ATom-derived AOD and values from high-resolution satellite data and those calculated using global models are underway.

Figure 7 shows the calculated AOD for each profile with valid extinction data meeting the criteria in Sect. 2.8, amounting to 463 of the total 625 profiles made over the oceans. While there is great variability in AOD from these individual profiles, general patterns are evident. First, the Northern Hemisphere midlatitudes and polar regions have substantially higher AOD than the same latitudes in the Southern Hemisphere, often by a factor of 2 or more. This difference reflects the much higher continental emissions of aerosols and precursors in the Northern Hemisphere. Second, the tropical and subtropical Atlantic has the highest AOD values found during the ATom flights due to Saharan dust and strong emissions from African biomass burning. Finally, low values of AOD, of the order of 0.02, are frequently found over the Southern Ocean and near the Antarctic Peninsula. In the absence of high winds to produce abundant sea salt aerosol (Shinozuka et al., 2004), these regions of the troposphere generally have the least influence from anthropogenic and continental sources and thus the least aerosol extinction (although elevated concentrations of BB burning aerosol were detected in the UT of the Southern Ocean during ATom-2; Fig. 5a, c). The contributions of different aerosol types to extinction profiles in different regions of the atmosphere are examined in more detail in Sect. 3.3.1.

3.3 Aerosol characteristics in different air masses

To summarize and present the data, aerosol characteristics were averaged over the same spatial regions over which PALMS free-tropospheric compositions were averaged. These regions are schematically represented in Fig. 8, and include the tropics, the midlatitude, and polar regions for the Northern and Southern Hemisphere as well as for the Pacific and Atlantic ocean basins, and the northern and southern

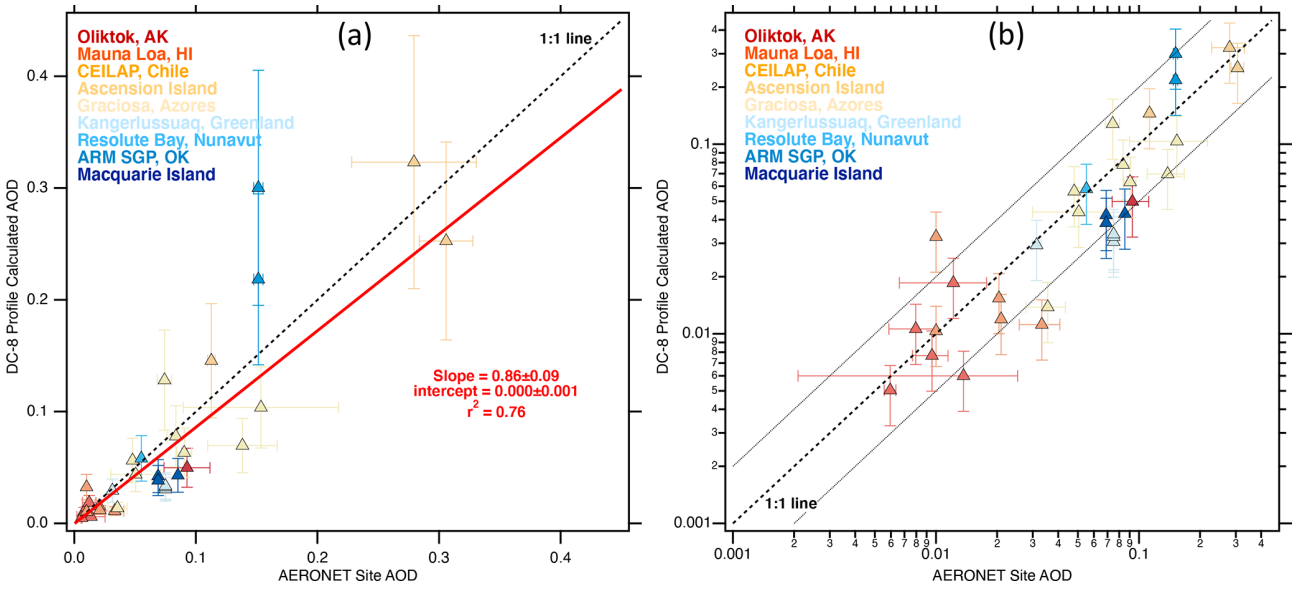

Figure 6. Aerosol optical depth (AOD) at 532 nm calculated from the in situ aerosol measurements on the DC-8 as a function of AOD measured by AERONET sites within 300 km and ±4 h of the profile. **(a)** Linear plot. Two-sided linear regression (red line) accounts for x and y uncertainties. **(b)** As in **(a)**, but a log–log plot. The dashed line is the 1 : 1 line, and dotted lines are a factor of 2 higher and lower. AERONET AOD at 532 nm is interpolated from measurements at 500 and 670 nm following Eq. (10). One outlier data point has been removed. Horizontal error bars indicate the variability in the AERONET AOD in ±4 h surrounding the measurement time. Vertical error bars indicate an approximate ±30 % uncertainty in the AOD derived from in situ measurements. Locations of the AERONET sites are given in Fig. 1.

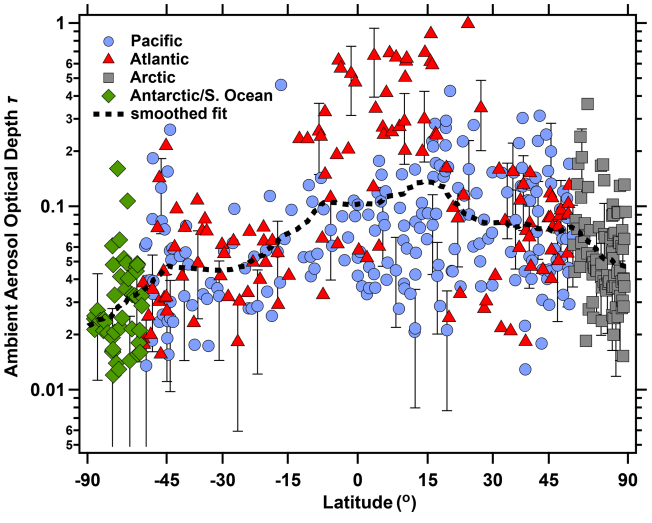

Figure 7. Ambient AOD calculated from in situ measurements as a function of latitude. Symbols indicate data taken over the Atlantic, Pacific, Southern Ocean and Antarctica, and the Arctic, with these regions described in Table S1. The smoothed dashed line is calculated using a locally weighted linear (LOWESS) regression to the logarithm of the AOD values.

high-latitude stratosphere. The precise latitudinal definitions of these regions were based on analysis of the air mass characteristics encountered, and varied with each ATom deployment as indicated in Table S1 in the Supplement. The top of the MBL in each profile was identified by manually inspecting the data for a sharp gradient in temperature, dew-point temperature, wind speed and direction, and gas-phase tracers such as O_3, NO_2, CO, and H_2O, as well as in particle number, with relatively homogeneous mixing ratios below this altitude. The top of the MBL was often quite ambiguous, particularly over colder waters where thorough atmospheric mixing may not take place. Different definitions of the MBL height are unlikely to substantively change most conclusions given the relatively coarse temporal resolution of the averaged data (∼ 60 s) and the associated vertical resolution (∼ 450 m). However, if aerosols with MBL characteristics (e.g., high concentrations of sea salt particles) are present above the identified top of the MBL, they may skew average compositions for the FT.

The stratosphere was defined as $O_3 > 100$ ppbv and CO < 100 ppbv in the Southern Hemisphere and $O_3 > 300$ ppbv and CO < 100 ppbv in the Northern Hemisphere. These definitions were chosen based on the occurrence of a mode of nearly pure sulfuric acid particles and particles with a meteoric core and sulfuric acid coating, indicating that the aircraft was sampling predominantly stratospheric particles (Murphy et al., 2021). The maximum GPS-derived altitude reached by the DC-8 was 13.2 km, and much of the stratospheric air was sampled when the tropopause heights were low in the winter hemisphere or in

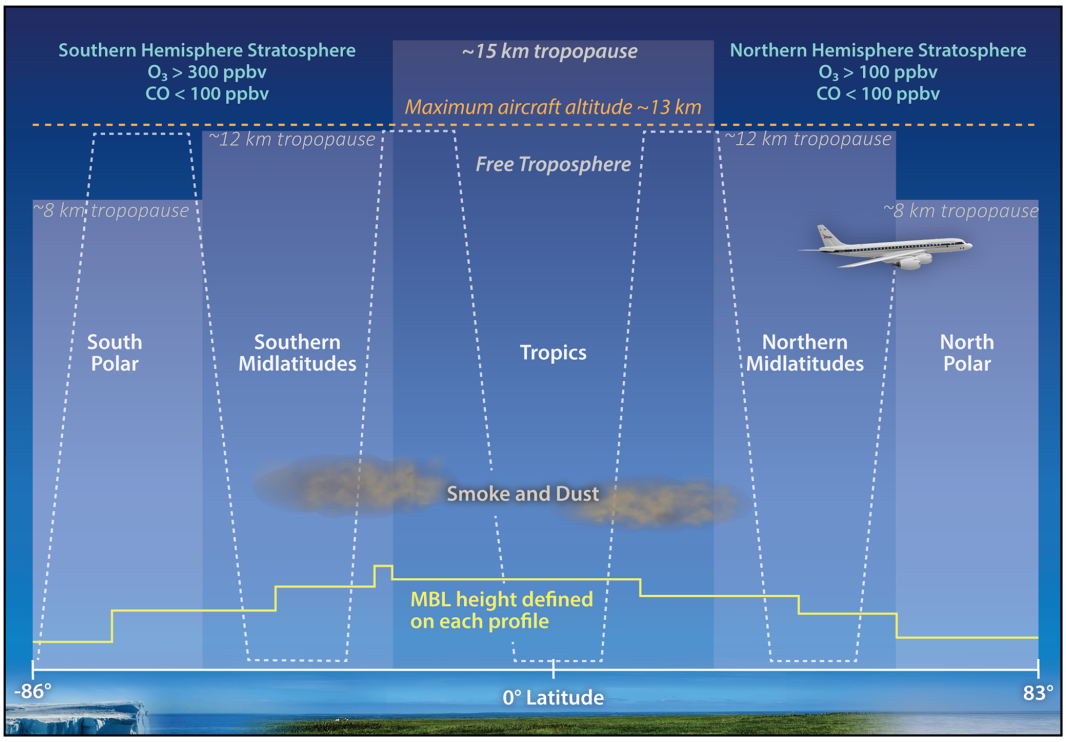

Figure 8. Schematic representation of the air mass classification scheme. The boundaries between the polar, midlatitude, and tropical air masses vary for each ATom deployment and ocean basin, and they are listed in Table S1 in the Supplement. Data taken in biomass burning smoke ("smoke") and mineral dust ("dust") plumes are combined when concentration criteria are met (Sect. 2.3) regardless of latitude, while stratospheric regions are separated into Northern or Southern Hemisphere because of different aerosol characteristics in each (Murphy et al., 2021).

tropopause folds. The maximum O_3 observed of 957 ppbv was measured at an altitude of 11.3 km at 68° N latitude when CO was 22.2 ppbv.

Regardless of altitude or region, samples were classified as being in a biomass burning plume when the number fraction of particles classified by PALMS as "biomass burning" by their potassium- and carbon-rich ion signatures (Hudson et al., 2004; Schill et al., 2020) was > 0.5 and AMS-measured OA mass concentrations were $> 1\,\mu g\,m^{-3}$. Similarly, dust cases were identified when the number fraction of PALMS "mineral dust" particles was > 0.3 and coarse-mode volume was $> 2\,\mu m^3\,cm^{-3}$.

3.3.1 Extinction profiles

The contribution of different aerosol components to extinction varies significantly with altitude and air mass type. In Fig. 9 we present vertical profiles, averaged in 1 km bins, of the average contribution to extinction for the different aerosol types for all of the ATom deployments. The fractional contributions of each aerosol type to extinction are shown in Fig. S5. These profiles include all non-cloudy data within the geographic region, including data taken in the MBL, in dust and BB plumes, and in the stratosphere. Sea salt in the MBL and associated water dominate the extinction in most of the regions. However, there are notable exceptions. Over the Arctic (Fig. 9a), there are significant contributions from biomass burning and sulfate–organic particles, as well as associated water, declining with increasing altitude. Two of the ATom deployments took place in winter and spring, when Northern Hemisphere pollution substantially affects the lower Arctic troposphere. The vertical profiles of extinction are consistent with the phenomenon of chronic background "Arctic haze" (Brock et al., 2011). In sharp contrast, the Antarctic–Southern Ocean profiles (Fig. 9b) shows the dominance of sea salt and water, with minor contributions to extinction from biomass burning layers encountered in the upper troposphere.

In the Pacific northern midlatitudes (Fig. 9c), biomass burning and sulfate–organic particles also contribute significantly to extinction and dominate above the MBL. These aerosol types are associated with plumes of pollution and biomass burning from Asia. Dust contributes as well, but to a lesser extent. Fewer such layers were encountered over the Atlantic at northern midlatitudes (Fig. 9d). Over the tropical and subtropical Atlantic (Fig. 9f), there is a significant contribution from Saharan dust in the lower troposphere along with biomass burning, sulfate–organic particles, sea salt, and absorption from rBC. In contrast, the Pacific tropical lower

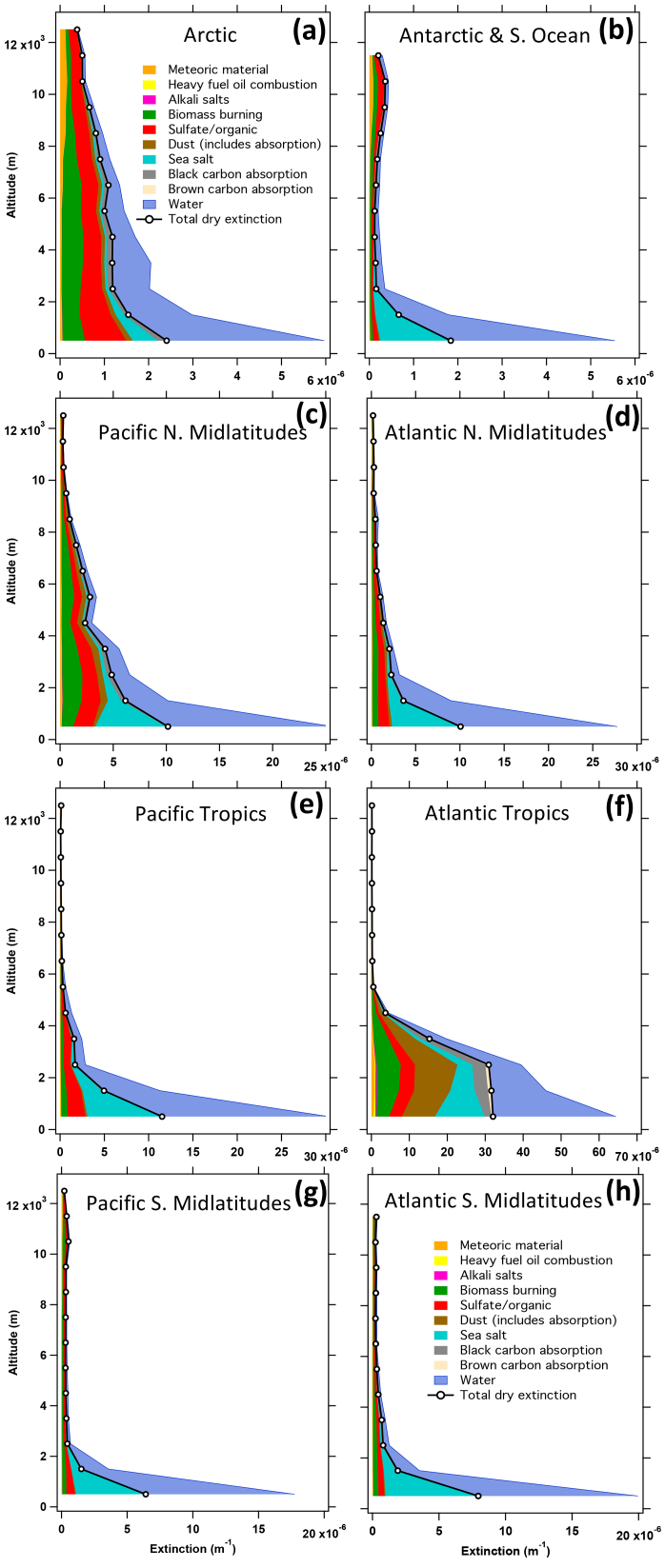

Figure 9. Mean vertical profiles of extinction from each of the aerosol types for different regions across all of the ATom deployments. Note that scales on the *x* axes vary. Descriptions of the regions are given in Fig. 8 and Table S1. The fractional contribution of the aerosol types to total extinction and the number of data points in each 1 km altitude bin are given in Fig. S5.

troposphere (Fig. 9e) shows the dominance of sea salt and lesser contributions from other components, similar to the Pacific and Atlantic southern midlatitudes (Fig. 9g, h).

Extinction in air classified as being in the MBL (Fig. 10a), in dust plumes (Fig. 10b), or in biomass burning plumes (Fig. 10c) may also be attributed to specific aerosol components using the ATom dataset. Unsurprisingly, sea salt and associated water dominate extinction in the MBL, followed by sulfate–organic mixtures, biomass burning aerosol, and dust. In dust plumes, mineral dust particles dominate, followed by water, sulfate–organic particles, and BB particles. In biomass burning plumes, particles containing biomass burning material dominate extinction, while sulfate–organic particles and water also contribute substantially to extinction. Absorption from rBC, which includes enhancement due to substantial non-absorbing coatings shown to be present by the SP2 measurements, is also a significant contributor to the extinction budget of these plumes.

3.3.2 Size-dependent composition

The PALMS single-particle mass spectrometer measures the composition and size of individual particles, which can then be mapped to high-resolution particle size distributions to provide a representation of the composition-based size distribution. Since many global models carry only the mass of different aerosol species and then prescribe their size distribution with modal or sectional representations (e.g., Chin et al., 2002; Liu et al., 2012; Mann et al., 2010), the high-resolution observations from ATom provide an important point of comparison. Aerosol–radiation and aerosol–cloud interactions flow directly from the size of the particles and their optical and hygroscopic properties; thus, it is essential that models predict the right aerosol properties for the right reasons. In this section we present the average composition-dependent size distribution of the aerosol in the different air mass types, which is useful for evaluating how different compositions influence optical properties.

Two distinct volume (mass) modes are present in all air mass types: an accumulation mode between 0.08 and $\sim 1\,\mu m$ and a coarse mode at larger sizes (Fig. 11). Small peaks between ~ 0.6 and $2\,\mu m$ (e.g., Fig. 11l) are likely due to ambiguous instrument response at particle sizes near the wavelength of the lasers and to overlaps between the underwing CAS instrument and the in-cabin LAS instrument. Most of the other fine structure in the shape of these modes is due to averaging together different size distributions. These average size distributions do not properly represent the aerosol's modal characteristics. For example, averaging size distributions with two peaks might produce a mean distribution with an excessively broad, flat mode that does not accurately describe the characteristics of either – or any – atmospheric size distribution. However, these average size distributions usefully describe the contributions of different particle types to the different modes. In Sect. 3.3.3, we use modal representations of the measured size distributions to more accurately describe the shape of the aerosol size distributions and their statistics in different air mass types.

The composition-based size distributions with regional labels (i.e., the left two columns) are from the 3–4 km layer of the FT only and exclude data from strong BB and dust plumes as well as stratospheric intrusions. Size distributions from the MBL, stratosphere, and strong BB and dust plumes (right column) are not regionally separated; e.g., Fig. 11c is an average of all MBL size distributions in all regions.

Water is an important component in all of the regionally averaged size distributions (left two columns). In the Pacific and Atlantic northern midlatitudes (Fig. 11d, e) as well as the Atlantic tropics (Fig. 11h), the dry volume (ignoring water) associated with the coarse mode is substantially larger than that of the accumulation mode, primarily due to the contribution of mineral dust to the coarse mode. In the Arctic (Fig. 11a), dust is a major fraction of the dry coarse mode, but the accumulation mode is larger due mostly to the sulfate–organic and BB particles characteristic of Arctic haze (e.g., Brock et al., 2011). These regional-scale contributions of dust to the coarse mode are largely a result of averaging discrete layers or plumes of dust over the region rather than the ubiquitous presence of dust throughout the FT (Froyd et al., 2021). In the southern midlatitude Pacific and the Antarctic–Southern oceans, which are more remote from continental sources (Fig. 11b, j), sea salt dominates the coarse mode of the FT when averaged over the region, while sulfate–organic particles contribute most to the accumulation mode. Biomass burning particles are substantial portions of the dry accumulation mode in all regions except the Antarctic–Southern Ocean (Fig. 11b) and to a lesser extent over the tropical and South Pacific (Fig. 11g, j) and the South Atlantic (Fig. 11k). The biomass burning particles are found mostly in the upper end of the accumulation-mode volume, consistent with the larger diameters typically found near wildfire sources (Radke et al., 1977; Moore et al., 2021) compared to secondary particles from natural and anthropogenic sulfur and organic sources.

Size distributions measured in the Southern Hemisphere stratosphere (Fig. 11l) are unique from the tropospheric size distributions, with an accumulation-mode composition dominated by nearly pure sulfuric acid, meteoric materials mixed with sulfuric acid, and mixed sulfate–organic particles and sea salt from FT air mixed with the stratospheric air. During ATom, particles from three specific events – a volcanic eruption, a pyro-cumulus injection, and lofting of dust – strongly influenced the stratospheric aerosol during ATom; these cases are discussed in Murphy et al. (2021).

3.3.3 Modal parameters

Many global models use modal representations of the particle size distribution because sectional models are computationally expensive. As described briefly in Sect. 2.4 and in

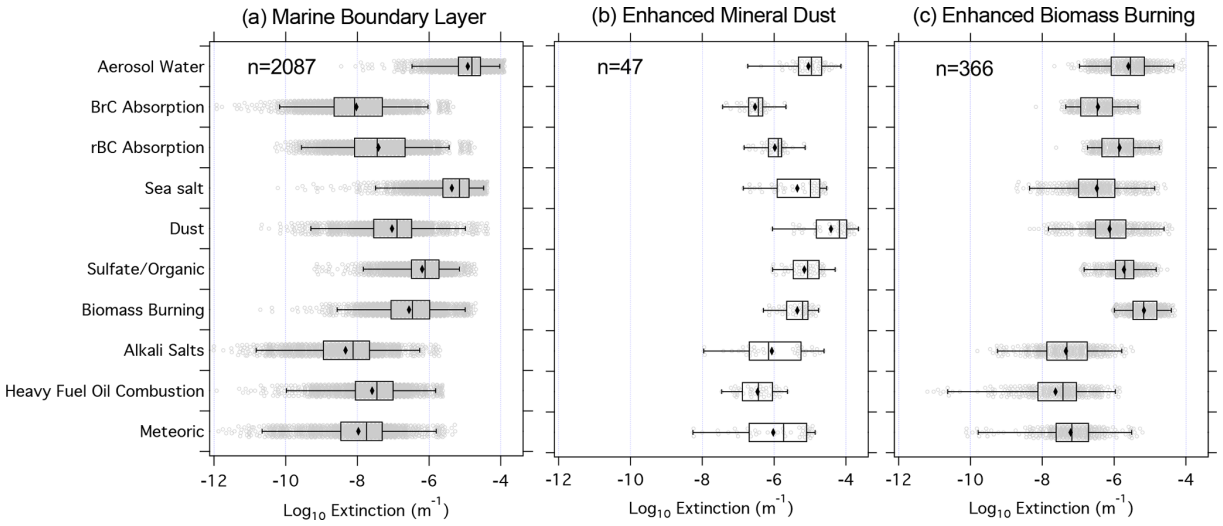

Figure 10. Contributions of different aerosol components to the logarithm of aerosol extinction **(a)** in the MBL, **(b)** in regions of enhanced mineral dust particle concentrations, and **(c)** in regions of enhanced biomass burning particle concentrations. Absorption only is shown for the BrC and rBC components. Each gray point is calculated from a single 60 s measurement. Boxes indicate the interquartile range, the central line represents the median, the diamond symbol represents the mean of the logarithm, and the whiskers are at the 2nd and 98th percentiles. The number of 60 s data points in each air mass type is indicated.

more detail in the Supplement, the measured size distributions were fitted using four lognormal functions representing the nucleation, Aitken, accumulation, and coarse modes. After fitting, the integrated number, surface, and volume were compared with those from the raw size distributions. The number, surface, and volume from the four modes of the fitted and measured distributions were similar and highly correlated, with regression slopes between 0.94 and 1.08 and r^2 values > 0.76 (Tables S2–S4). The four-mode lognormal fits efficiently describe the measured size distributions and provide measurement-based lognormal parameters for comparison with prescribed values used in many global models. Further, the modal fits provide a physically rational way to average size distributions together, since the average geometric mean diameter (D_g) and standard deviation (σ_g) for an air mass can be calculated directly. If one were to instead average all of the size distributions in an air mass together and then fit lognormal parameters, σ_g would be too large because the average size distribution is broader than the individual size distributions contributing to that average. AOD and direct radiative forcing are sensitive to the value of σ_g (Brock et al., 2016b).

As an example of the fitted lognormal parameters, vertical profiles for the tropics of the Pacific and Atlantic (Fig. 12) show several interesting features. It is important to note that there is considerable vertical and horizontal variability in aerosol properties in any given single profile due to the effects of quasi-horizontal transport from continental sources in thin layers, near-surface wind speed, outflow from deep convection, removal in clouds, and other processes (e.g., Clarke and Kapustin, 2002; Shinozuka et al., 2004). The average profiles presented in Fig. 12 are intended to highlight systematic features in the vertical distribution of aerosol properties that are robust when averaged across many profiles (Table S5) over four seasons. Low nucleation-mode concentrations ($< 30\,\mathrm{cm}^{-3}$) were present at altitudes < 5–$6\,\mathrm{km}$ (Fig. 12a, e), and lognormal fits could not be made (although raw nucleation-mode concentration data are still shown). Nucleation- and Aitken-mode concentrations decreased from values $> 10^4$ and $> 10^3\,\mathrm{cm}^{-3}$, respectively, at the top of the profile to values ~ 10 and $\sim 200\,\mathrm{cm}^{-3}$ at 2 km as a result of new particle formation in the UT and coagulational loss during slow descent (Fig. 12a; Clark and Kapustin, 2002; Williamson et al., 2019). Growth due to condensation during this descent is evident in the slightly increasing modal diameter of the Aitken and accumulation modes with decreasing altitude (Fig. 12b), although this growth is somewhat obscured by the shift in growing particles from the nucleation mode to the Aitken mode. Of course, other processes such as cloud processing, wet scavenging, and loss of OA by chemical processing can also affect the variation in modal diameter with altitude. However, we note that the σ_g values of the accumulation and Aitken modes tend to decrease toward the surface in the troposphere (Fig. 12c, f), which is consistent with condensational growth, leading to a narrowing of the size distribution (McMurry and Wilson, 1982). The new particle formation in the tropical UT is tightly coupled to the very low concentrations of accumulation-mode particles (Fig. 12a) due to scavenging during deep convection (Clarke and Kapustin, 2002; Williamson et al., 2019). Nucleation-mode concentrations are lower in the UT over the Atlantic (Fig. 12d) than over the Pacific (Fig. 12a), although the same

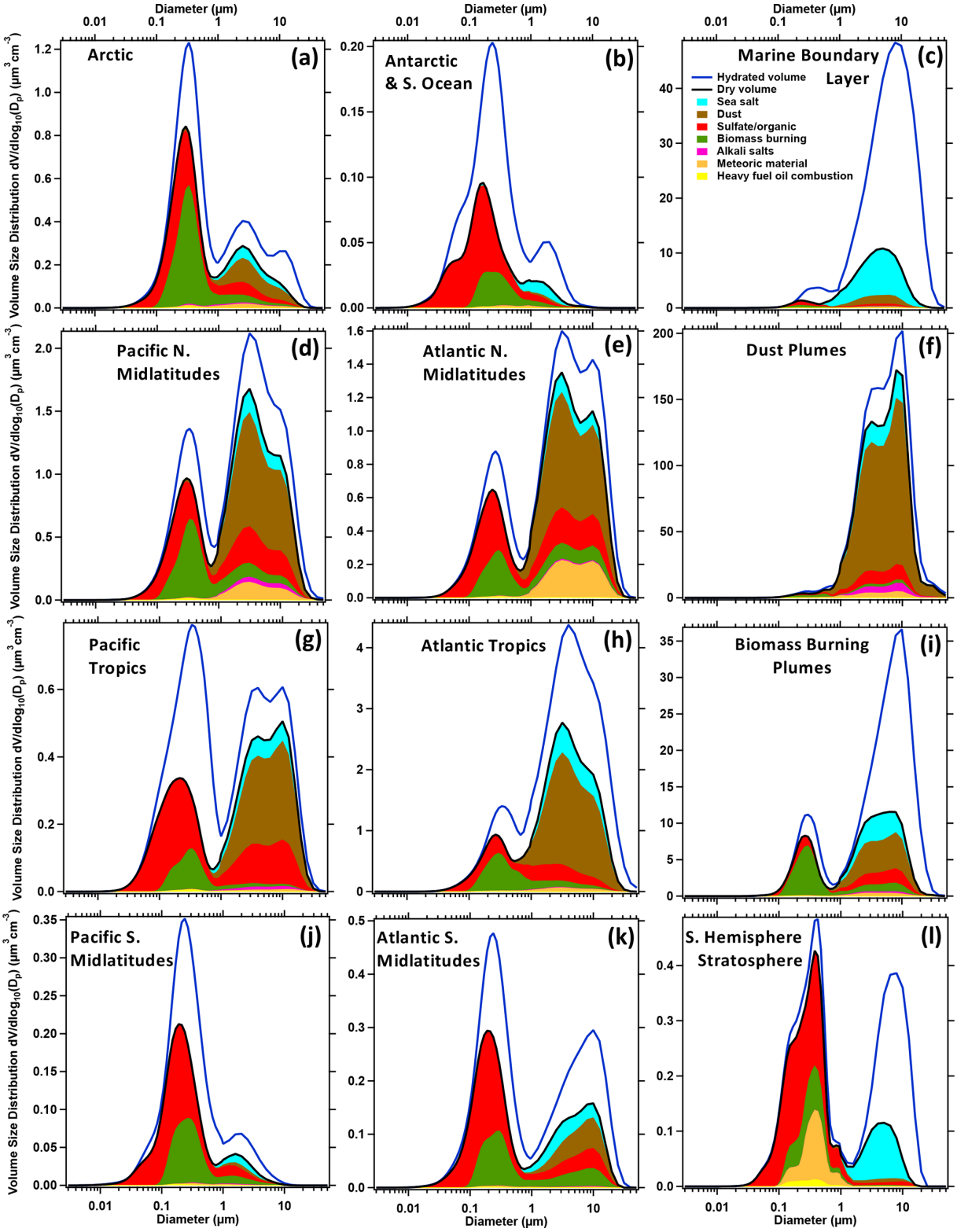

Figure 11. Volume of particles of different aerosol types as a function of diameter, averaged over all data in different regions and air mass types across all of the ATom deployments. Note that scales on the *y* axes vary. Descriptions of the regions are given in Fig. 7 and Table S1. Regional data (left two columns) are from the FT only and exclude data from BB and dust plumes as well as stratospheric intrusions. Size distributions from the MBL, stratosphere, and BB and dust plumes (right column) are not separated by ocean basin or latitude range. One pass of a binomial smoothing filter (Marchand and Marmet, 1983) has been applied to the data; PALMS particle types shown below 0.14 μm are extrapolated for smoothness.

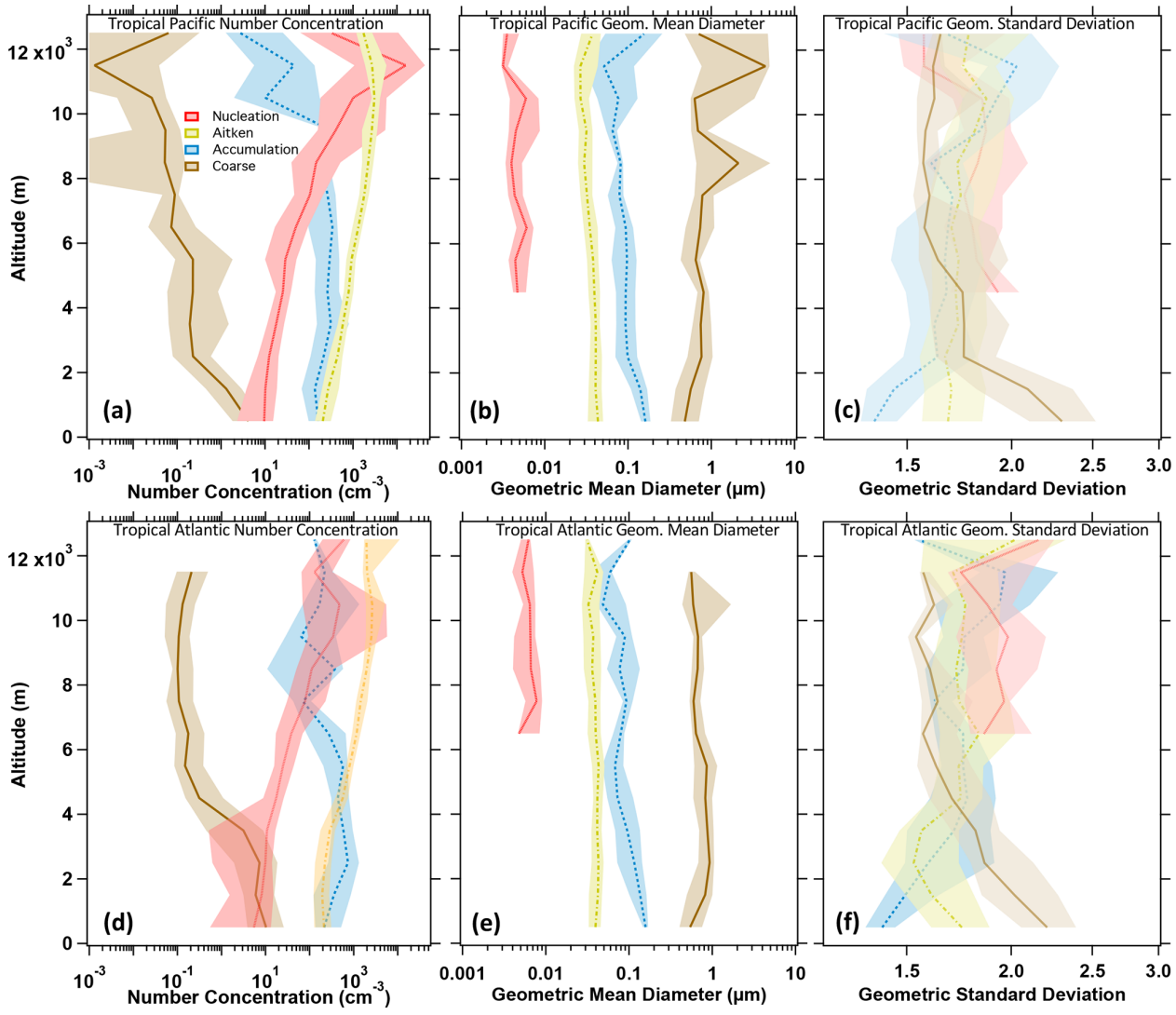

Figure 12. Vertical profiles of fitted lognormal parameters for the nucleation, Aitken, accumulation, and coarse modes for the Pacific tropics **(a, b, c)** and the Atlantic tropics **(d, e, f)** for the entire ATom project. Lines are median values, and shaded regions show the interquartile range. Number concentrations for the nucleation mode extend to lower altitudes than the geometric mean diameter and standard deviation because samples with very low or zero concentrations could not be fitted, yet they still provide valid concentration data that should be averaged. Similar vertical profiles for other regions sampled during ATom are in Figs. S1–S2. The number of 60 s samples contributing to the values in each altitude bin is provided in Fig. S7.

general trend of declining concentration towards the surface remains.

The number concentration of coarse-mode particles declines rapidly with increasing altitude above the MBL, while accumulation-mode concentrations do not fall consistently with increasing altitude (Fig. 12a, d). Coarse-mode particle concentrations in the lower troposphere are consistently higher over the Atlantic than over the Pacific due to smoke and Saharan dust. The σ_g of the lognormal distribution is >2 in the lowest 2 km of the profile, where sea salt dominates, but <2 in the middle and upper troposphere, where dust dominates the coarse mode. In general, the value of σ_g ranges from ~ 1.5 to ~ 2 for all modes throughout the profiles except for the coarse sea salt mode at altitudes < 2 km.

Similar plots for the other regions measured during ATom are presented in the Supplement (Figs. S1–S2). The modal parameters from the ATom data are compared with two previously published datasets in Sect. 4.1.1.

3.3.4 Single-scatter albedo and absorption

Single-scatter albedo ω_0 is the ratio of light scattering to the sum of scattering and absorption. This parameter is key in determining the direct radiative effect of aerosol (McComiskey et al., 2008). In most of the air masses encountered in ATom,

values of ω_0 at both dry and ambient RH conditions tend to decrease from values > 0.96 near the surface to a broad minimum in the lower or middle FT, before increasing again in the UT (Fig. 13). These profiles result because extinction falls more rapidly with increasing altitude from the boundary layer to the FT than absorption due to rBC and BrC (Figs. 9, 13). This decrease in ω_0 in most of the profiles (Fig. 13) may be associated with the general shift of accumulation-mode particles to smaller particle sizes with increasing altitude (Fig. 12), which would reduce their aerosol mass scattering efficiency, while the mass absorption efficiency of absorbing rBC particles does not change much with increasing altitude. In other words, shifts in aerosol size can change ω_0 even if the relative mass of scattering and absorbing components does not change substantially.

3.3.5 Cloud condensation nuclei

The concentrations of CCN at STP conditions, determined from the size distributions and calculated hygroscopicity at five values of supersaturation (Sect. 2.6), show substantial variations across the different regions sampled during ATom (Fig. 14). In the midlatitudes of the Northern Hemisphere (Fig. 14c, d), concentrations are substantially higher in the middle and lower FT than at similar latitudes in the Southern Hemisphere (Fig. 14g, h). For example, at supersaturations of 0.2 %, concentrations in the Southern Hemisphere FT are ~ 10–$50\,\mathrm{cm}^{-3}$ throughout the profile, while in the Northern Hemisphere the concentrations fall with increasing altitude from $> 100\,\mathrm{cm}^{-3}$ in the MBL to $\sim 50\,\mathrm{cm}^{-3}$ in the middle troposphere. In the tropics, concentrations fall steadily from $> 200\,\mathrm{cm}^{-3}$ near the surface to $\sim 10\,\mathrm{cm}^{-3}$ at 10 km of altitude. The spread in CCN concentrations for the different supersaturations increases with altitude in the tropics and northern midlatitudes due to the shift in modal diameter to smaller sizes (Fig. 12). In the Arctic, Antarctic–Southern Ocean, and southern midlatitude profiles the CCN concentrations do not spread with increasing altitude as much because the aerosol size distributions in these regions do not shift to smaller sizes with increasing altitude (Figs. S1, S2).

4 Discussion

4.1 Comparisons with previously published work

It is far beyond the scope of this work to provide a comprehensive comparison of the ATom observations with the extensive literature on global aerosol microphysical properties, which are derived from a panoply of in situ and remote sensing measurements and model simulations. However, it is useful to briefly compare the airborne data for a few parameters that are of special interest regarding the direct radiative effect. Here we compare modal fits to the ATom size distributions with model assumptions and a marine dataset, discuss the ATom observations in the context of an existing comprehensive airborne dataset, and evaluate the MAC values we calculate for the coated rBC relative to some recently published analyses.

4.1.1 Lognormal size distribution parameters

Two frequently used datasets, the OPAC database (Hess et al., 1998; Koepke et al., 2015), which is commonly used by global models, and the shipborne dataset reported by Quinn et al. (2017), provide useful comparisons. The measurements of Quinn et al. (2017; hereafter Q17) were made from 1993–2015 during multiple research cruises over the Arctic, Pacific, Southern, and Atlantic oceans using a suite of instruments to obtain the particle size distribution from 0.02–10 µm diameter at dry conditions. These observations are thus directly comparable to the dry Aitken-, accumulation-, and coarse-mode size distributions measured in the MBL during ATom. In addition, we can compare our observations with the modal aerosol model (MAM; Liu et al., 2012, 2020), which places various aerosol types into prescribed lognormal modes, usually using four or seven such modes.

Global models that use a modal description of aerosol size distributions often use the OPAC database to prescribe lognormal parameters. The OPAC database provides lognormal parameters for several particle types, including "insoluble", "water-soluble", "soot", and mineral particles in three different size classes: Aitken (referred to as "nucleation" in OPAC), accumulation, and coarse modes, with sea salt in the latter two modes only. The OPAC database is meant to represent "average" atmospheric conditions, presumably including polluted air masses, while the ATom dataset focuses on remote marine air with aged aerosol from a mix of continental and marine sources.

The most direct comparisons between the ATom dataset and the OPAC database are of the "water-soluble", "sea salt", and "mineral" OPAC components with the sulfate–organic, sea salt, and dust aerosols measured during ATom. The sulfate–organic particles are best described by modal fits to the Aitken and accumulation modes, while sea salt and dust particles are best described by the coarse-mode fits. The comparisons (Fig. 15; Table S7) show that, in general, σ_g is wider in the OPAC database than in the ATom observations, except for coarse-mode sea salt (in which case OPAC is lower than the observations) and accumulation-mode dust (in which case they are comparable). In contrast to OPAC, several versions of the modal aerosol model (MAM), used in various Earth system models (e.g., Liu et al., 2012, 2020), incorporate σ_g values that range from 1.6 to 2.0 for the Aitken, accumulation, and coarse modes, which are much more aligned with the ATom and Q17 measurements, except for coarse-mode sea salt. The larger σ_g in the OPAC database for all aerosol types except sea salt (Fig. 15b) would tend to increase the amount of extinction and scattering per unit aerosol mass (Brock et al., 2016b), potentially leading

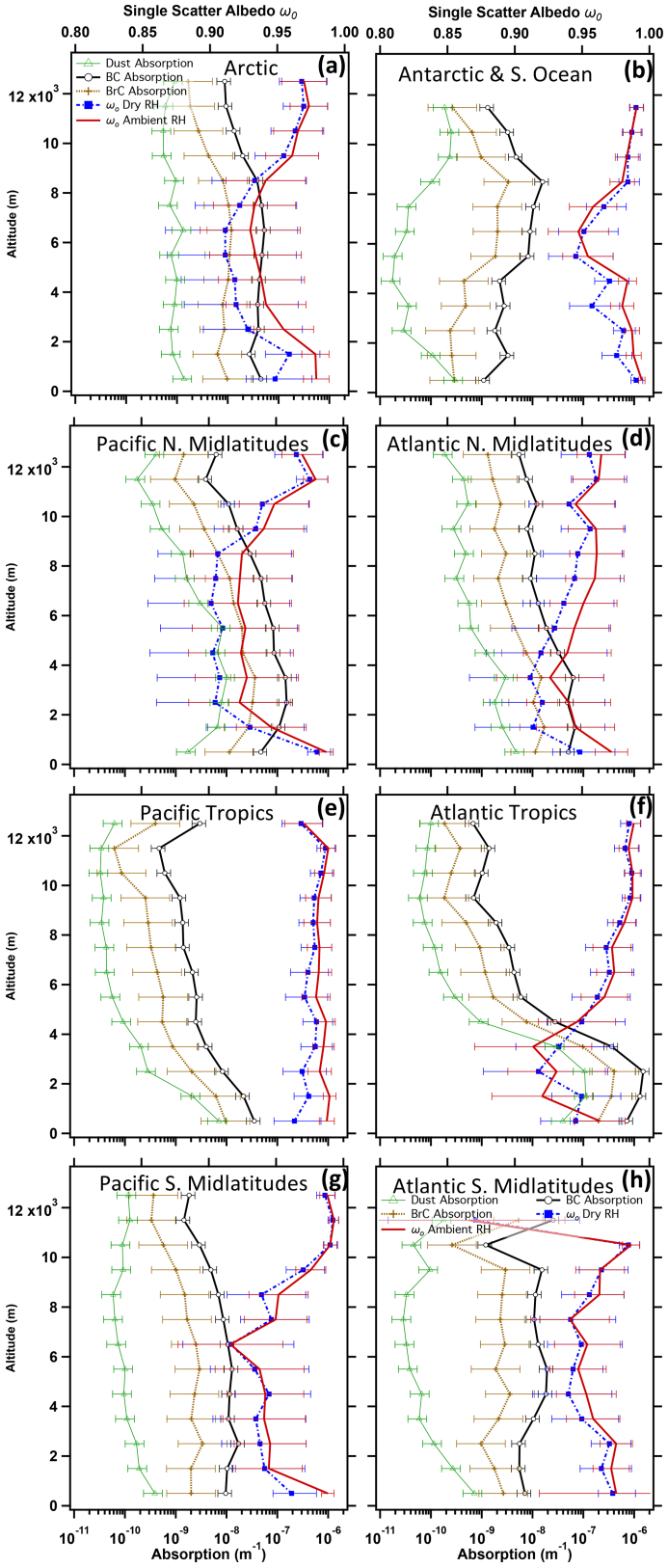

Figure 13. Median vertical profiles of absorption at the 532 nm wavelength from rBC, BrC, and dust (bottom axis) as well as single-scattering albedo ω_0 at 532 nm wavelength dry and ambient RH conditions (top axis) for different regions sampled during the entire ATom project. **(a)** Arctic. **(b)** Antarctic and Southern Ocean. **(c)** Pacific northern midlatitudes. **(d)** Atlantic northern midlatitudes. **(e)** Pacific tropics. **(f)** Atlantic tropics. **(g)** Pacific southern midlatitudes. **(h)** Atlantic southern midlatitudes.

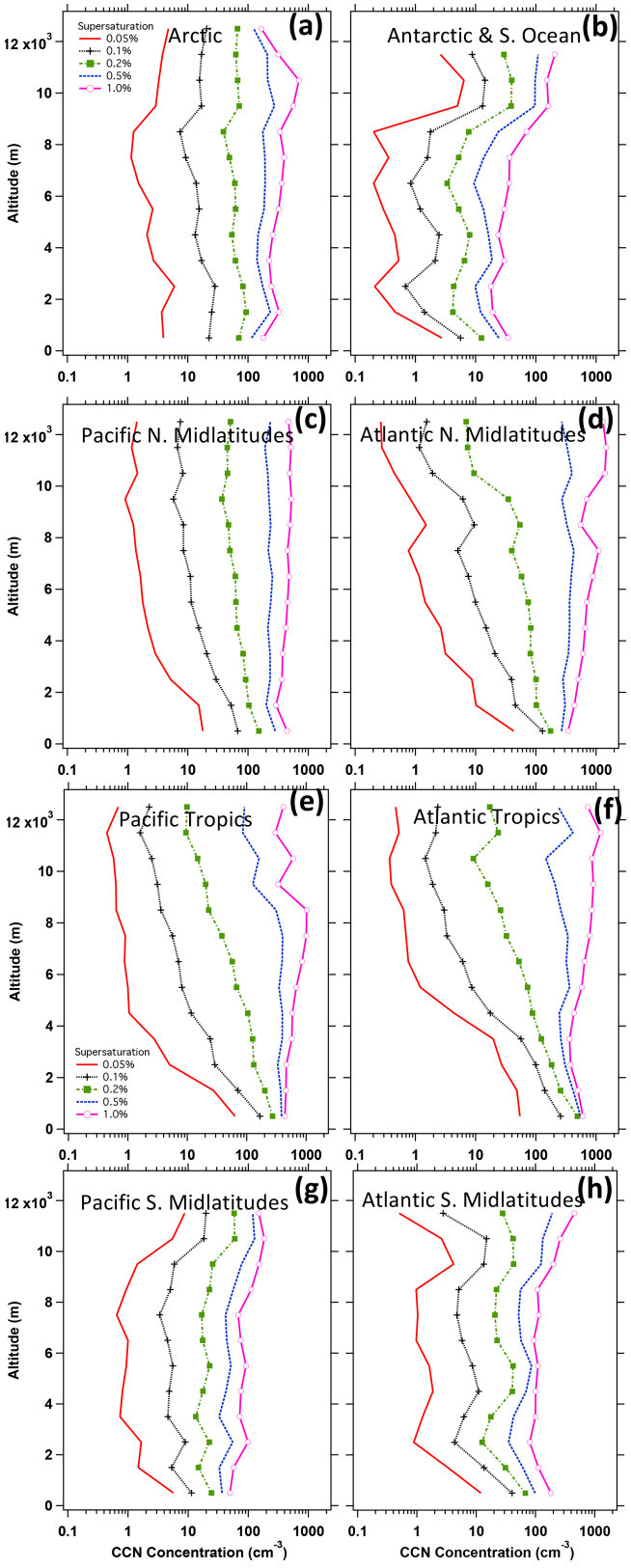

Figure 14. Median vertical profiles of calculated CCN concentration at STP for supersaturations of 0.05 %, 0.1 %, 0.2 %, 0.5 %, and 1 % for different regions sampled during the entire ATom project. **(a)** Arctic. **(b)** Antarctic and Southern Ocean. **(c)** Pacific northern midlatitudes. **(d)** Atlantic northern midlatitudes. **(e)** Pacific tropics. **(f)** Atlantic tropics. **(g)** Pacific southern midlatitudes. **(h)** Atlantic southern midlatitudes.

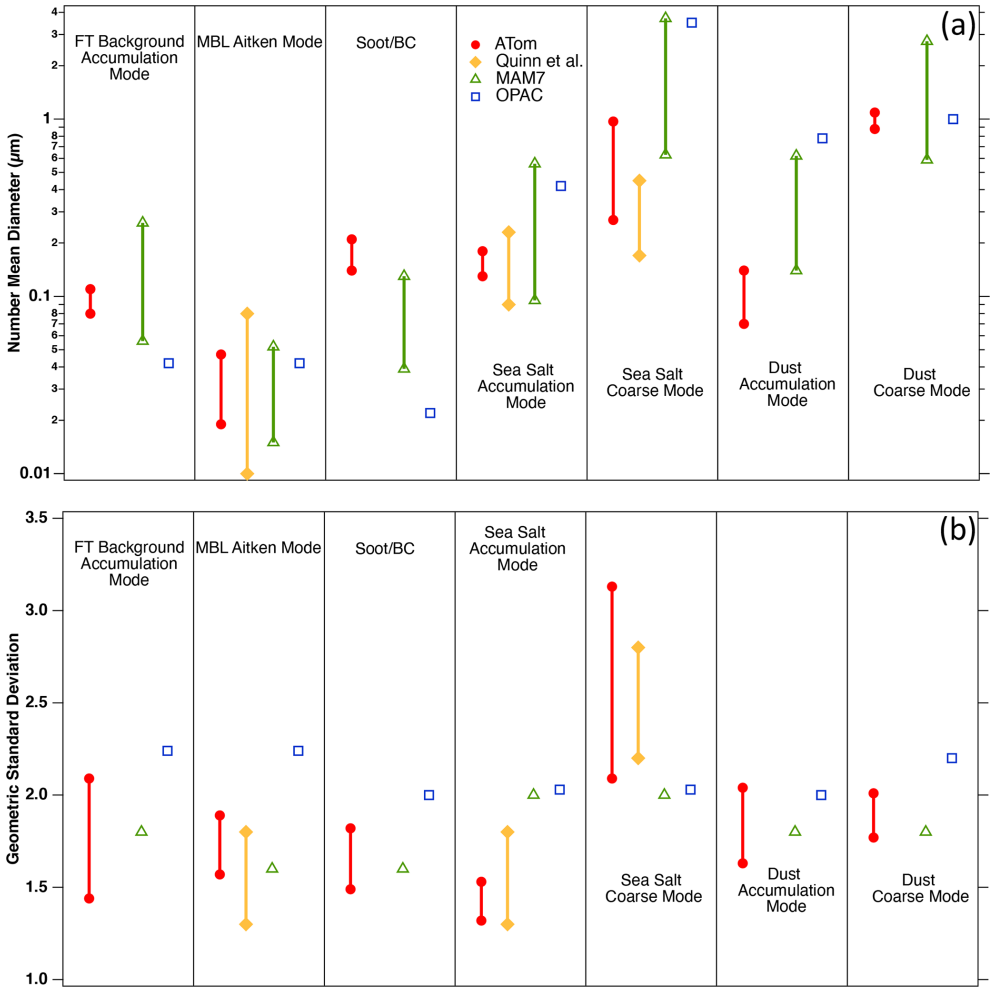

Figure 15. Lognormal parameters for different aerosol types from fits to the ATom dataset (showing interquartile range), from fits to shipboard size distribution measurements on the remote oceans (Quinn et al., 2017, showing full range), from the MAM7 modal aerosol model (Liu et al., 2012, 2016, showing interdecile range), and from the OPAC parameterization (Hess et al., 1998). **(a)** Number geometric mean diameter; **(b)** geometric standard deviation. The MAM7 parameterization provides a single fixed value of geometric standard deviation but a range of diameters for each aerosol type.

to an overprediction in AOD and direct radiative effect when the OPAC parameters are applied to the remote FT in global models. Additionally, the geometric mean diameters for both number and volume differ considerably between the OPAC database and the ATom observations (Fig. 15a). For example, the accumulation-mode number geometric mean diameter $D_{g,n}$ in the observations is approximately twice that of the OPAC water-soluble fraction. This may in part be caused by the OPAC database including Aitken-mode particles in the water-soluble category.

The comparisons between the shipborne measurements in Q17 and the ATom measurements are more direct, as both use similar modal fitting procedures and definitions for the modes and are made primarily over the remote Pacific and Atlantic oceans. The modal fits from ATom and from Q17 are generally quite consistent. The Aitken- and accumulation-mode parameters are similar between ATom and the shipborne measurements, with the range of ATom parameters generally narrower than the Q17 parameters, which span a longer time period and larger range of meteorological conditions than the airborne measurements. Both the Q17 and ATom data suggest values of $\sigma_g < 1.9$ in the MBL for both the accumulation and coarse modes, while the OPAC database has a significantly larger value of σ_g for these modes and all aerosol types. For the coarse mode in the MBL, referred to as the "sea spray" mode in Q17 and the "sea salt" coarse mode in the OPAC database, both the Q17 and ATom datasets report a value $D_{g,n}$ that is considerably smaller than that in OPAC and MAM7, as well as a significantly larger σ_g. These differences are important, as sea salt is the single largest contributor to AOD over the oceans (e.g., Haywood

et al., 1999), and AOD (hence the direct radiative effect) is sensitive to these parameters (Brock et al., 2016b).

4.1.2 Previous airborne campaigns

There have been a number of field programs that have made airborne aerosol measurements over many of the same regions that ATom systematically sampled. One of most relevant analyses is that of Clarke and Kapustin (2010), who summarized 11 separate NASA airborne campaigns that included consistent aerosol measurements made by the same research group at the University of Hawaii. These measurements include size distributions, σ_s, refractory and non-refractory particle number concentrations, and proxies for CCN, as well as additional measurements specific to different campaigns. From these measurements they have interpreted the abundances of sea salt, dust, BC, and non-refractory (usually sulfate–organic) particles. Most of their measurements were focused on the Pacific Ocean, but their analysis includes data measured over the Southern, Arctic, and western Atlantic oceans. The analysis of Clarke and Kapustin (2010) emphasizes the relationship between refractory and non-refractory particle number concentration, CCN, light scattering, AOD, and carbon monoxide, which is used as an indicator of combustion over the relevant timescales. Similar to Clarke and Kapustin (2010), the ATom dataset shows very low values of scattering ($< 1\,\mathrm{Mm}^{-1}$) in the FT of the remote Southern Hemisphere and the clear influence of combustion sources on aerosol abundance and properties throughout the troposphere in the northern midlatitudes. While there are many opportunities to compare detailed aerosol properties, especially intensive values, between the ATom dataset and that described by Clarke and Kapustin (2010), such detailed analysis is beyond the scope of this paper. In Sect. 4.2 we discuss some differences between the two datasets.

Another particularly relevant airborne field program, the HIPPO project, involved systematic profiling flights over the Pacific Ocean using an instrumented G-V business jet aircraft over all four seasons (Wofsy, 2011). The HIPPO project focused on gas-phase measurements and contained only an SP2 instrument to measure rBC particles (Schwarz et al., 2013). An analysis using rBC data from both ATom-1 and HIPPO shows very similar profiles over the Pacific Ocean (Katich et al., 2018). The additional data from ATom's Atlantic leg provide a marked contrast between the continentally influenced Atlantic and the more remote Pacific, with much higher rBC concentrations found over the Atlantic. Both datasets have proven useful in constraining global models that represent BC emissions and processes.

4.1.3 Mass absorption cross sections for rBC

Because light absorption by BC is a key uncertainty in global estimates of the direct radiative effect, it is useful to evaluate the assumptions we make in its calculation from the SP2 observations. We have calculated absorption assuming that the measured rBC particles are well-aged and compact with a density of $1.8 \times 10^3\,\mathrm{kg\,m}^{-3}$ and that core–shell Mie theory using the measured coating thickness, assumed to be a non-absorbing organic–sulfate mixture, provides a realistic approximation to their optical properties. Detailed consideration of different modeling approaches (Romshoo et al., 2021) suggests that core–shell Mie theory overestimates MAC values of coated BC by a factor of 1.1–1.5, with values increasing with increasing organic fraction (corresponding to coating thickness), for a fractal dimension for the BC core of 1.7, but with smaller discrepancies as fractal dimension increases toward 3 (a spherical core). Fierce et al. (2020) further report that core–shell Mie theory substantially overpredicts the absorption by BC in measurements in urban outflow but that this discrepancy can be reduced by accounting for heterogeneity in particle composition and coating thickness. In contrast, Wu et al. (2021) found that core–shell Mie theory provided MAC values in agreement with, or even underestimating, directly measured MACs in aging biomass burning plumes downwind of West Africa. Zanatta et al. (2018) reported that core–shell Mie theory slightly underpredicted the measured MAC for aged, coated soot in the Arctic. China et al. (2015) found that aged soot particles measured at a mountaintop site in the Azores had a compact morphology with thin coatings and that radiative forcing calculated using core–shell Mie theory was within 12 % of that calculated using the discrete dipole approach.

Almost 30 % by number of FT particles measured by PALMS during ATom were of BB origin (Schill et al., 2020). Thus, we expect both compact core morphologies and substantial non-absorbing coatings in the rBC particles associated with the BB particles; these characteristics are supported by the coating thicknesses measured by the SP2 instrument (Table S6) and by the small values of water-soluble BrC absorption measured in filter extracts (Zeng et al., 2020). The MAC values for rBC we calculate from the ATom dataset using core–shell Mie theory were $14.4 \pm 1.4\,\mathrm{m}^2\,\mathrm{g}^{-1}$ at a wavelength of 532 nm averaged over the free troposphere for all four ATom deployments (Table S6). Values in identifiable BB plumes were $13.3 \pm 0.4\,\mathrm{m}^2\,\mathrm{g}^{-1}$. These values are generally consistent with those measured at 514 nm in West African biomass burning plumes ranging from ~ 11.3 to $\sim 14.2\,\mathrm{m}^2\,\mathrm{g}^{-1}$ for plume ages of ~ 1 to > 9 h, respectively (Wu et al., 2021). Thus, the MAC values we calculate using core–shell Mie theory appear to be reasonable given the likely BB source of most of the rBC. Further, since no observations of soot morphology were made during ATom, we lack a basis for any additional refinement in our estimate of MAC values for coated rBC.

4.2 Considerations for using the ATom combined aerosol dataset

The ATom combined aerosol dataset presented here is unique in several ways. First, the aerosol composition measurements are not directly used; instead the relative abundances of the various species and aerosol types as a function of diameter are mapped onto the size distribution. The integration of these composition-resolved size distributions provides the concentrations of the different aerosol components. Second, the optical properties and CCN concentrations were calculated from these size distributions rather than directly measured. The exceptions to this process are the rBC and BrC concentrations as well as the light absorption associated with them. Third, ATom's strategy to make pre-planned survey flight patterns (Thompson et al., 2021) means that the sampling was unbiased, with the exception of deviations to avoid hazardous flight conditions (e.g., deep convection and low clouds) and to follow air traffic control instructions (e.g., sometimes staying below air traffic corridors over the North Atlantic Ocean). These features have resulted in an aerosol dataset that is internally self-consistent (e.g., total scattering can be calculated by summing the scattering from the different composition-resolved size distributions) and absolutely unique in its representativeness and spatial coverage, ranging from 84 ° N to 86 ° S and from ∼ 160 m to ∼ 12 km over both the Pacific and Atlantic Ocean in four seasons.

One of the existing datasets most similar to the ATom aerosol dataset is that compiled by Clarke and Kapustin (2002, 2010). As with the ATom data, Clarke and Kapustin (2010) packaged their airborne data from multiple instruments, including several gas-phase species, into a dataset in NetCDF format, and they have made it available through the Global Aerosol Synthesis and Science Project (GASSP) database (Reddington et al., 2017) and through the other data repositories indicated in Clarke and Kapustin (2010). However, there are several differences between the data analyzed by Clarke and Kapustin (2010) and the ATom data presented here. Among the most significant are the following: (1) the ATom flights do not include any direct measurements of aerosol scattering or hygroscopicity (although dry extinction and absorption were directly measured on ATom-4); (2) the ATom flights included online measurements of aerosol composition and type from 0.05 to ∼ 4 µm in diameter; (3) the ATom composition data are mapped to the size distributions rather than directly used; (4) many of the properties of the aerosol, including the optical properties, hygroscopicity, and CCN abundance, are calculated from these composition-resolved size distributions rather than directly measured; and (5) the ATom flights used systematic survey sampling, while many of the flights analyzed by Clarke and Kapustin were focused on specific regions, events, or processes. The differences in instrumentation, sampling strategy, and spatial and temporal coverage provide opportunities to use both datasets to examine processes affecting aerosol properties and abundance, as well as temporal and regional differences, and to constrain the global model simulations of aerosols. Additional data compiled in the GASSP archive, including extensive measurements made at various locations around the world on the British Facility for Airborne Atmospheric Measurements BAE-146 aircraft, provide further information on detailed aerosol optical, microphysical, and chemical properties.

Although the combined ATom aerosol dataset offers a comprehensive and detailed picture of global-scale aerosol properties, it is limited in important ways. Most significantly, the ATom measurements do not represent a climatology, although they are representative of seasonally typical values for a subset of measured parameters that have been compared to climatologies (Strode et al., 2018; Bourgeois et al., 2020). The four circuits around the globe, once in each season, provide a snapshot of aerosol conditions at those particular times without targeting specific phenomena, unlike most airborne projects. Comparisons between models and the ATom data will be most effective if meteorology and emissions are prescribed or nudged to match the times of the ATom flights and if the model domain is sampled along the aircraft flight track. Similarly, comparisons with remote sensing measurements should overlap in space and time to the extent possible.

There are limitations to specific aspects of the data presented here, as well. The compositional data we consider in this combined dataset represent only a fraction of the richness of the data from the HR-ToF-AMS and PALMS spectrometers and of the filter-based bulk measurements. Data from these instruments include detailed information on molecular markers of specific sources and processes (e.g., $f57$, $f44$), elemental composition of OA (H / C and O / C ratios; Hodzic et al., 2020), ionic balance and acidity (Nault et al., 2021), speciation of inorganic ions, and the presence of rare particle types (e.g., Murphy et al., 2018). Potential users of the data are encouraged to communicate with the instrument teams to make full use of the available information in their analyses.

The particle size distributions are measured using a condensation technique (the NMASS battery of CPCs) which reports a Kelvin (condensation) diameter. These data are combined with an optical particle spectrometer (the UHSAS) which measures an optical size. Thus, discontinuities can occur at the boundary between the instruments at about 60 nm (Brock et al., 2019). Unfortunately, this is near the critical diameter for CCN activation at typical water supersaturations for stratocumulus and cumulus clouds. Smoothing is used to minimize potential discontinuities. At diameters from 0.6–2 µm, the laser optical particle spectrometers are in a regime of Mie oscillations, wherein particle sizing is relatively insensitive or even ambiguous. This can cause spurious high-frequency features in the size distribution in this size range, as noted in Sect. 3.3.2. These features do not substantially affect the optical properties or modal parameters but could be misinterpreted as physical attributes.

The modal parameters fitted to the size distributions rely upon a priori assumptions regarding the number of modes and their characteristics (see the Supplement). There are cases in the remote FT when the Aitken and accumulation modes are subjectively indistinguishable, yet the fitting procedure attempts to fit two modes. The user of the combined dataset is cautioned that there are times when the accumulation mode might actually be an extension of a single Aitken mode. In addition, when there are very few coarse-mode particles, the fitting algorithm may still attempt to describe the few counts present with lognormal parameters, leading to excessive noise in the modal parameters.

The composition of the coarse mode is measured using the PALMS instrument sampling behind an inlet that removes particles with $D_p > 4.8\,\mu m$ in the lower troposphere and $> 3.2\,\mu m$ in the UT (McNaughton et al., 2007). The composition of larger particles measured by the underwing CAS instrument is assumed to be the same as those in the largest PALMS size class (1.13 to $\sim 4\,\mu m$). If the composition of particles with $D_p > 4\,\mu m$ measured by the CAS is different, this will produce a bias. This potential bias is likely to be small in the MBL since these larger particles are almost certainly sea spray aerosol. In calculating optical properties, these coarse-mode particles are assumed to be spherical; no attempt has been made to simulate dust or sea salt properties using non-spherical approaches.

We have not attempted to propagate uncertainties beyond the size distribution uncertainties described by Brock et al. (2019) based on comprehensive instrument evaluations by Kupc et al. (2018) and Williamson et al. (2018). The final average uncertainty in integrated particle volume is estimated to be $+13\,\%/-28\,\%$ for the accumulation mode when counting statistics are not a limiting factor. Integrated aerosol volumes determined independently from the size distributions and from the AMS instrument are highly consistent (Guo et al., 2021), which lends confidence to the measurements. Determining uncertainties associated with applying composition data to the size distributions, with calculating hygroscopic growth, or with determining the resulting optical properties and CCN concentrations would require Monte Carlo simulations over a large number of parameters for each of $> 2.4 \times 10^4$ measurements, which is impractical. Comparisons of calculated dry extinction and absorption with directly measured values during ATom-4 (Fig. 4) suggest errors in dry extinction and absorption of $< 20\,\%$, while comparisons of the derived AOD with directly measured values from nearby AERONET sites (Fig. 6) show no substantial biases. While the normalized mean bias was only $-7\,\%$, there was considerable scatter in the comparison, and it is not possible to disentangle atmospheric inhomogeneity from measurement uncertainty given the spatial mismatch between the slantwise aircraft profiles and the AERONET locations. We hope to gain a better understanding of errors in the ATom AOD product through ongoing comparisons with satellite observations.

Finally, we note that we anticipate continued evolution of this publicly available dataset. Despite our best efforts, there are undoubtedly errors or inconsistencies that will need to be corrected, as well as newly calculated parameters that could enhance its usefulness. We encourage users of the data to report any issues or suggestions for improvement to the lead author.

5 Conclusions

The ATom project made four surveys, once in each season, of the composition of the remote oceanic troposphere and portions of the lower stratosphere at high latitudes. The aircraft repeatedly profiled between $\sim 160\,m$ and $\sim 12\,km$, mapping out the vertical and horizontal variation in aerosol and gas-phase properties. We have combined dry aerosol composition and size distribution measurements made over the remote Pacific and Atlantic oceans, as well as over portions of the Arctic and Antarctic, to comprehensively describe the chemical, microphysical, and optical characteristics of the aerosol. Inorganic electrolyte composition was determined using an algebraic composition model, and aerosol water was then estimated using κ-Köhler theory. From the hydrated, composition-resolved size distributions, we have calculated a number of intensive and extensive parameters that are related to the climate effects of the aerosol. These parameters include various optical properties at 10 wavelengths, cloud condensation nuclei concentrations at five supersaturations, and lognormal fits to four modes of the particle size distribution. Mid-visible dry extinction and absorption coefficients calculated from the composition-resolved size distributions were in excellent agreement with directly measured dry extinction and absorption coefficients made with independent instruments during the ATom-4 deployment. Mid-visible AOD was calculated by vertically integrating ambient extinction values during profiles and showed little bias compared with values directly measured with AERONET sun photometers, despite substantial scatter due to the distances between the slantwise profiles and the AERONET sites.

Initial findings from the combined dataset show that the remote Northern Hemisphere lower and free troposphere has considerably more aerosol from continental sources than the Southern Hemisphere, consistent with understanding gained from past in situ studies (e.g., Clarke and Kapustin, 2010). Dust and sulfate–organic mixtures contribute substantially to AOD in the middle troposphere over the midlatitude northern Pacific Ocean and the lower and middle troposphere over the tropical Atlantic Ocean. Unsurprisingly, sea salt particles and associated water dominate AOD over most of the remote oceans, especially in the Southern Hemisphere, while BB particles contribute over the subtropical and tropical Atlantic Ocean and to a lesser extent over the North Pacific. Single-scatter albedo was found to vary substantially with altitude due to changes in both composition and size. The geometric

standard deviations of lognormal fits to the Aitken and accumulation modes generally lay between 1.5 and 2.0, which is narrower than values in some modal representations used in global models. Within the MBL, the lognormal parameters for these modes and for the coarse mode are generally consistent with values from extensive shipboard measurements in the remote oceans.

The ATom aerosol dataset presented here is unique in that online, size-resolved aerosol composition measurements have been mapped to aerosol size distributions, thus providing separate size distributions for several different aerosol constituents. These data products more closely match the way aerosol components are treated in global models than is typical for other airborne datasets and are, to our knowledge, unique. From these composition-resolved size distributions, hygroscopicity, CCN concentrations, and optical properties have been calculated, resulting in a single, self-consistent, global-scale dataset for use by the scientific community. The global-scale mapping of atmospheric composition provided by ATom's representative profiling survey flights, while not a climatology with statistical information on time-varying properties, provides unique information that can help constrain model representations of aerosol emissions, transport, removal, and processing, as well as a priori assumptions used in retrievals of aerosol properties from remote sensing measurements. The data are accessible for public scientific use as described in the "Data availability" statement below.

Data availability. The ATom data products described in this paper are publicly available at the Oak Ridge National Laboratory Distributed Active Archive Center (https://doi.org/10.3334/ORNLDAAC/1908, Brock et al., 2021). Additional ATom data are available at https://doi.org/10.3334/ORNLDAAC/1925 (Wofsy et al., 2021). AERONET data are available at https://aeronet.gsfc.nasa.gov (last access: 6 October 2020, Aeronet, 2020).

Supplement. The supplement related to this article is available online at: https://doi.org/10.5194/acp-21-15023-2021-supplement.

Author contributions. CAB, KDF, GS, MD, CJW, CS, AK, and BW performed the size distribution measurements. KDF, GS, DMM, JLJ, PCJ, BAN, JCS, DAD, and DJP made aerosol composition measurements. JPS and JMK made black carbon particle measurements; LZ, RW, JD, and ES made measurements of brown carbon. GSD and JPD made water vapor measurements. TPB and JMDD made measurements of temperature and pressure. CRT, JP, TBR, and IB made measurements of ozone. BCD, RC, and SCW made measurements of carbon monoxide. NJW made measurements of aerosol extinction and absorption. SW calculated stratospheric optical depth values. CAB wrote the paper with significant contributions from KDF, MD, CJW, GS, DMM, NLW, PCJ, JLJ, JMK, JD, and JP.

Competing interests. The authors declare that they have no conflict of interest.

Disclaimer. The contents do not necessarily represent the official views of NOAA or of the respective granting agencies. The use or mention of commercial products or services does not represent an endorsement by the authors or by any agency.

Publisher's note: Copernicus Publications remains neutral with regard to jurisdictional claims in published maps and institutional affiliations.

Acknowledgements. The authors thank the following investigators for their effort in establishing and maintaining the AERONET sites used in this analysis: Resolute Bay – Ihab Abboud and Vitali Fioletov; ARM-Oliktok, ARM-Graciosa, and ARM-Southern Great Plains – Rick Wagener and Lynn Ma; ARM Macquarie Island – Lynn Ma; Mauna Loa, Ascension Island, and Kangerlussuaq – Brent Holben; CEILAP RG – Brent Holben, Eduardo Quel, Lidia Otero, and Jacobo Salvador. We also thank the NASA Langley Research Center Atmospheric Science Data Center for providing the GLOSSAC stratospheric AOD data.

Financial support. This research has been supported by the National Aeronautics and Space Administration (award nos. NNH15AB12I, NNX15AJ23G, NNX15AH33A, NNH13ZDA001N, NNX15AT90G, 80NSSC19K0124, and 80NSSC18K0630), the Austrian Science Fund FWF's Erwin Schrodinger Fellowship (grant no. J-3613), and the European Research Council under the European Union's Horizon 2020 framework (grant no. 640458). Additional support was provided by the US National Oceanic and Atmospheric Administration's Atmospheric Chemistry, Carbon Cycle, and Climate Program, and by the University of Vienna.

Review statement. This paper was edited by Manabu Shiraiwa and reviewed by two anonymous referees.

References

Aeronet: Aerosol Robotic network [dataset], available at: https://aeronet.gsfc.nasa.gov/, last access: 6 October 2020.

Anderson, T. L., Wu, Y., Chu, D. A., Schmid, B., Redemann, J., and Dubovik, O.: Testing the MODIS satellite retrieval of aerosol fine-mode fraction, J. Geophys. Res., 110, D18204, https://doi.org/10.1029/2005JD005978, 2005.

Andrews, E., Sheridan, P. J., Fiebig, M., McComiskey, A., Ogren, J. A., Arnott, P. Covert, D., Elleman, R., Gasparini, R., Collins, D., Jonsson, H., Schmid, B., and Wang, J.: Comparison of methods for deriving aerosol asymmetry parameter, J. Geophys. Res., 111, D05S04, https://doi.org/10.1029/2004JD005734, 2006.

Andrews, E., Ogren, J. A., Kinne, S., and Samset, B.: Comparison of AOD, AAOD and column single scattering albedo from

AERONET retrievals and in situ profiling measurements, Atmos. Chem. Phys., 17, 6041–6072, https://doi.org/10.5194/acp-17-6041-2017, 2017.

Baumgardner, D., Jonsson, H., Dawson, W., O'Connor, D., and Newton, R.: The cloud, aerosol and precipitation spectrometer: a new instrument for cloud investigations, Atmos. Res., 59–60, 251–264, https://doi.org/10.1016/S0169-8095(01)00119-3, 2001.

Bohren, C. F. and Huffman, D. R.: Absorption and Scattering of Light by Small Particles, John Wiley & Sons, New York, NY, USA, ISBN 978-0-471-29340-8, 1998.

Bond, T. C., Doherty, S. J., Fahey, D. W., Forster, P. M., Berntsen, T., DeAngelo, B. J., Flanner, M. G., Ghan, S., Kärcher, B., Koch, D., Kinne, S., Kondo, Y., Quinn, P. K., Sarofim, M. C., Schultz, M. G., Schulz, M., Venkataraman, C., Zhang, H., Zhang, S., Bellouin, N., Guttikunda, S., K., Hopke, P. K., Jacobson, M. Z., Kaiser, J. W., Klimont, Z., Lohmann, U., Schwarz, J. P., Shindell, D., Storelvmo, T., Warren, S. G., and Zender, C. S.: Bounding the role of black carbon in the climate system: A scientific assessment, J. Geophys. Res.-Atmos., 118, 5380–5552, https://doi.org/10.1002/jgrd.50171, 2013.

Bourgeois, I., Peischl, J., Thompson, C. R., Aikin, K. C., Campos, T., Clark, H., Commane, R., Daube, B., Diskin, G. W., Elkins, J. W., Gao, R.-S., Gaudel, A., Hintsa, E. J., Johnson, B. J., Kivi, R., McKain, K., Moore, F. L., Parrish, D. D., Querel, R., Ray, E., Sánchez, R., Sweeney, C., Tarasick, D. W., Thompson, A. M., Thouret, V., Witte, J. C., Wofsy, S. C., and Ryerson, T. B.: Global-scale distribution of ozone in the remote troposphere from the ATom and HIPPO airborne field missions, Atmos. Chem. Phys., 20, 10611–10635, https://doi.org/10.5194/acp-20-10611-2020, 2020.

Brock, C. A., Cozic, J., Bahreini, R., Froyd, K. D., Middlebrook, A. M., McComiskey, A., Brioude, J., Cooper, O. R., Stohl, A., Aikin, K. C., de Gouw, J. A., Fahey, D. W., Ferrare, R. A., Gao, R.-S., Gore, W., Holloway, J. S., Hübler, G., Jefferson, A., Lack, D. A., Lance, S., Moore, R. H., Murphy, D. M., Nenes, A., Novelli, P. C., Nowak, J. B., Ogren, J. A., Peischl, J., Pierce, R. B., Pilewskie, P., Quinn, P. K., Ryerson, T. B., Schmidt, K. S., Schwarz, J. P., Sodemann, H., Spackman, J. R., Stark, H., Thomson, D. S., Thornberry, T., Veres, P., Watts, L. A., Warneke, C., and Wollny, A. G.: Characteristics, sources, and transport of aerosols measured in spring 2008 during the aerosol, radiation, and cloud processes affecting Arctic Climate (ARCPAC) Project, Atmos. Chem. Phys., 11, 2423–2453, https://doi.org/10.5194/acp-11-2423-2011, 2011.

Brock, C. A., Wagner, N. L., Anderson, B. E., Attwood, A. R., Beyersdorf, A., Campuzano-Jost, P., Carlton, A. G., Day, D. A., Diskin, G. S., Gordon, T. D., Jimenez, J. L., Lack, D. A., Liao, J., Markovic, M. Z., Middlebrook, A. M., Ng, N. L., Perring, A. E., Richardson, M. S., Schwarz, J. P., Washenfelder, R. A., Welti, A., Xu, L., Ziemba, L. D., and Murphy, D. M.: Aerosol optical properties in the southeastern United States in summer – Part 1: Hygroscopic growth, Atmos. Chem. Phys., 16, 4987–5007, https://doi.org/10.5194/acp-16-4987-2016, 2016a.

Brock, C. A., Wagner, N. L., Anderson, B. E., Beyersdorf, A., Campuzano-Jost, P., Day, D. A., Diskin, G. S., Gordon, T. D., Jimenez, J. L., Lack, D. A., Liao, J., Markovic, M. Z., Middlebrook, A. M., Perring, A. E., Richardson, M. S., Schwarz, J. P., Welti, A., Ziemba, L. D., and Murphy, D. M.: Aerosol optical properties in the southeastern United States in summer – Part 2: Sensitivity of aerosol optical depth to relative humidity and aerosol parameters, Atmos. Chem. Phys., 16, 5009–5019, https://doi.org/10.5194/acp-16-5009-2016, 2016b.

Brock, C. A., Williamson, C., Kupc, A., Froyd, K. D., Erdesz, F., Wagner, N., Richardson, M., Schwarz, J. P., Gao, R.-S., Katich, J. M., Campuzano-Jost, P., Nault, B. A., Schroder, J. C., Jimenez, J. L., Weinzierl, B., Dollner, M., Bui, T., and Murphy, D. M.: Aerosol size distributions during the Atmospheric Tomography Mission (ATom): methods, uncertainties, and data products, Atmos. Meas. Tech., 12, 3081–3099, https://doi.org/10.5194/amt-12-3081-2019, 2019.

Brock, C. A., Froyd, K. D., Dollner, M., Williamson, C. J., Schill, G. P., Murphy, D. M., Wagner, N. L., Kupc, A., Jimenez, J. L., Campuzano-Jost, P., Nault, B. A., Schroder, J. C., Day, D. A., Price, D. J., Weinzierl, B. B., Schwarz, J. P., Katich, J. M., Wang, S., Zeng, L. H., Weber, R., Dibb, J. E., Scheuer, E., Diskin, G. S., DiGangi, J. P., Bui, T. P., Dean-Day, J. M., Thompson, C. R., Peischl, J., Ryerson, T. B., Bourgeois, I., Daube, B. C., Commane, R., Wofsy, S. C., and Wang, S.: ATom: Comprehensive Aerosol Properties, 2016–2018, ORNL DAAC, Oak Ridge, Tennessee, USA [data set], https://doi.org/10.3334/ORNLDAAC/1908, 2021.

Burgos, M. A., Andrews, E., Titos, G., Benedetti, A., Bian, H., Buchard, V., Curci, G., Kipling, Z., Kirkevåg, A., Kokkola, H., Laakso, A., Letertre-Danczak, J., Lund, M. T., Matsui, H., Myhre, G., Randles, C., Schulz, M., van Noije, T., Zhang, K., Alados-Arboledas, L., Baltensperger, U., Jefferson, A., Sherman, J., Sun, J., Weingartner, E., and Zieger, P.: A global model–measurement evaluation of particle light scattering coefficients at elevated relative humidity, Atmos. Chem. Phys., 20, 10231–10258, https://doi.org/10.5194/acp-20-10231-2020, 2020.

Canagaratna, M., Jayne, J., Jimenez, J., Allan, J., Alfarra, M., Zhang, Q., Onasch, T. B., Drewnick, F., Coe, H., Middlebrook, A. M., Delia, A., Williams, L. R., Trimborn, A. M., Northway, M. J., DeCarlo, P. F., Kolb, C. E., Davidovits, P., and Worsnop, D. R.: Chemical and microphysical characterization of ambient aerosols with the Aerodyne aerosol mass spectrometer, Mass Spec. Rev., 26, 185–222, 2007.

Chin, M., Paul Ginoux, P., Kinne, S., Torres, O., Holben, B. N., Duncan, B. N., Martin, R. V., Logan, J. A., Higurashi, A., and Nakajima, T.: Tropospheric aerosol optical thickness from the GOCART model and comparisons with satellite and sun photometer measurements. J. Atmos. Sci., 59, 461–483, https://doi.org/10.1175/1520-0469(2002)059<0461:TAOTFT>2.0.CO;2, 2002.

China, S., Scarnato, B., Owen, R. C., Zhang, B., Ampadu, M. T., Kumar, S., Dzepina, K., Dziobak, M. P., Fialho, P., Perlinger, J. A., Hueber, J., Helmig, D., Mazzoleni, L. R., and Mazzoleni, C.: Morphology and mixing state of aged soot particles at a remote marine free troposphere site: Implications for optical properties, Geophys. Res. Lett., 42, 1243–1250, https://doi.org/10.1002/2014GL062404, 2015.

Clarke, A. D. and Kapustin, V. N.: A Pacific aerosol survey. Part I: A decade of data on particle production, transport, evolution, and mixing in the troposphere, J. Atmos. Sci., 59, 363–382, https://doi.org/10.1175/1520-0469(2002)059<0363:APASPI>2.0.CO;2, 2002.

Clarke, A. D. and Kapustin, V. N.: Hemispheric aerosol vertical profiles: Anthropogenic impacts on optical depth and cloud nuclei, Science, 329, 1488–1492, https://doi.org/10.1126/science.1188838, 2010.

Clarke, A. D., Shinozuka, Y., Kapustin, V. N., Howell, S., Huebert, B., Doherty, S., Anderson, T., Covert, D., Anderson, J., Hua, X., Moore II, K. G., McNaughton, C., Carmichael, G., and Weber, R.: Size distributions and mixtures of dust and black carbon aerosol in Asian outflow: Physiochemistry and optical properties, J. Geophys. Res., 109, D15S09, https://doi.org/10.1029/2003JD004378, 2004.

DeCarlo, P. F., Kimmel, J. R., Trimborn, A., Northway, M. J., Jayne, J. T., Aiken, A. C., Gonin, M., Fuhrer, K., Horvath, T., Docherty, K. S., Worsnop, D. R., and Jimenez, J. L.: Field-deployable, high-resolution, time-of-flight aerosol mass spectrometer, Anal. Chem., 78, 8281–8289, https://doi.org/10.1021/ac061249n, 2006.

Di Lorenzo, R. A. and Young, C. J.: Size separation method for absorption characterization in brown carbon: Application to an aged biomass burning sample, Geophys. Res. Letts., 43, 458–465, https://doi.org/10.1002/2015GL066954, 2016.

Dubovik, O., Smirnov, A., Holben, B. N., King, M. D., Kaufman, Y. J., Eck, T. F., and Slutsker, I.: Accuracy assessment of aerosol optical properties retrieval from AERONET sun and sky radiance measurements, J. Geophys. Res., 105, 9791–9806, https://doi.org/10.1029/2000JD900040, 2000.

Dubovik, O., Li, Z., Mishchenko, M. I., Tanré, D., Karol, Y., Bojkov, B., Cairns, B., Diner, D. J., Espinosa, W. R., Goloub, P., Gu, X., Hasekamp, O., Hong, J., Hou, W., Knobelspiesse, K. D., Landgraf, J., Li, L., Litvinov, P., Liu, Y., Lopatin, A., Marbach, T., Maring, H., Martins, V., Meijer, Y., Milinevsky, G., Mukai, S., Parol, F., Qiao, Y., Remer, L., Rietjens, J., Sano, I., Stammes, P., Stamnes, S., Sun, X., Tabary, P., Travis, L. D., Waquet, F., Xu, F., Yan, C., and Yin, D.: Polarimetric remote sensing of atmospheric aerosols: Instruments, methodologies, results, and perspectives, J. Quant. Spectrosc. Radiat. Transf., 224, 474–511, https://doi.org/10.1016/j.jqsrt.2018.11.024, 2019.

Fiebig, M. and Ogren, J. A.: Retrieval and climatology of the aerosol asymmetry parameter in the NOAA aerosol monitoring network, J. Geophys. Res., 111, D21204, https://doi.org/10.1029/2005JD006545, 2006.

Fierce, L., Onasch, T. B., Cappa, C. d., Mazzoleni, C., China, S.,Bhandari, J., Davidovits, P., Fischer, D. A., Helgestad, T., Lambe, A. T., Sedlacek, A. J., Smith, G. D., and Wolff, L.: Radiative absorption enhancements by black carbon controlled by particle-to-particle heterogeneity in composition, Proc. Nat. Acad. Sci., USA, 117, 5196–5203, https://doi.org/10.1073/pnas.1919723117, 2020.

Forrister, H., Liu, J., Scheuer, E., Dibb, J., Ziemba, L., Thornhill, K. L., Anderson, B., Diskin, G., Perring, A. E., Schwarz, J. P., Campuzano-Jost, P., Day, D. A., Palm, B. B., Jimenez, J. L., Nenes, A., and Weber, R. J.: Evolution of brown carbon in wildfire plumes, Geophys. Res. Lett., 42, 4623–4630, https://doi.org/10.1002/2015GL063897, 2015.

Froyd, K. D., Murphy, D. M., Brock, C. A., Campuzano-Jost, P., Dibb, J. E., Jimenez, J.-L., Kupc, A., Middlebrook, A. M., Schill, G. P., Thornhill, K. L., Williamson, C. J., Wilson, J. C., and Ziemba, L. D.: A new method to quantify mineral dust and other aerosol species from aircraft platforms using single-particle mass spectrometry, Atmos. Meas. Tech., 12, 6209–6239, https://doi.org/10.5194/amt-12-6209-2019, 2019.

Froyd, K. D., Yu, P., Schill, G. P., Brock, C. A., Kupc, A., Williamson, C. J., Jensen, E. J., Ray, E., Rosenlof, K. H., Bian, H., Darmenov, A. S., Colarco, P. R., Diskin, G. S., Bui, T. P., and Murphy, D. M.: Global-scale measurements reveal cirrus clouds are seeded by mineral dust, Nat. Geosci., submitted, 2021.

Gao, R., Schwarz, J., Kelly, K., Fahey, D., Watts, L, Thompson, T., Spackman, R., Slowik, J. G., Cross, E. S., Han, J.-H., Davidovits, P., Onasch, T. B., and Worsnop, D.: A novel method for estimating light-scattering properties of soot aerosols using a modified single-particle soot photometer, Aerosol Sci. Tech., 41, 125–135, https://doi.org/10.1080/02786820601118398, 2007.

Good, N., Topping, D. O., Allan, J. D., Flynn, M., Fuentes, E., Irwin, M., Williams, P. I., Coe, H., and McFiggans, G.: Consistency between parameterisations of aerosol hygroscopicity and CCN activity during the RHaMBLe discovery cruise, Atmos. Chem. Phys., 10, 3189–3203, https://doi.org/10.5194/acp-10-3189-2010, 2010.

Guo, H., Campuzano-Jost, P., Nault, B. A., Day, D. A., Schroder, J. C., Kim, D., Dibb, J. E., Dollner, M., Weinzierl, B., and Jimenez, J. L.: The importance of size ranges in aerosol instrument intercomparisons: a case study for the Atmospheric Tomography Mission, Atmos. Meas. Tech., 14, 3631–3655, https://doi.org/10.5194/amt-14-3631-2021, 2021.

Hale, G. M. and Querry, M. R.: Optical constants of water in the 200-nm to 200-µm wavelength region, Appl. Optics, 12, 555–563, 1973.

Hand, J. L. and Kreidenweis, S. M.: A new method for retrieving particle refractive index and effective density from aerosol size distribution data, Aerosol. Sci. Tech., 36, 1012–1026, https://doi.org/10.1080/02786820290092276, 2002.

Haynes, W. M., Lide, D. R., and Bruno, T. J.: CRC Handbook of Chemistry and Physics: A Ready-Reference Book of Chemical and Physical Data, CRC Press, Boca Raton, FL, USA, 2014.

Haywood, J. M., Ramaswamy, V., and Soden, B. J.: Tropospheric aerosol climate forcing in clear-sky satellite observations over the oceans, Science, 283, 1299–1303, https://doi.org/10.1126/science.283.5406.1299, 1999.

Hess, M., Koepke, P., and Schult, I.: Optical properties of aerosols and clouds: The software package OPAC. Bull. Amer. Meteor. Soc., 79, 831–844, https://doi.org/10.1175/1520-0477(1998)079<0831:OPOAAC>2.0.CO;2, 1998.

Hodzic, A., Campuzano-Jost, P., Bian, H., Chin, M., Colarco, P. R., Day, D. A., Froyd, K. D., Heinold, B., Jo, D. S., Katich, J. M., Kodros, J. K., Nault, B. A., Pierce, J. R., Ray, E., Schacht, J., Schill, G. P., Schroder, J. C., Schwarz, J. P., Sueper, D. T., Tegen, I., Tilmes, S., Tsigaridis, K., Yu, P., and Jimenez, J. L.: Characterization of organic aerosol across the global remote troposphere: a comparison of ATom measurements and global chemistry models, Atmos. Chem. Phys., 20, 4607–4635, https://doi.org/10.5194/acp-20-4607-2020, 2020.

Holben B. N., Eck, T. F., Slutsker, I., Tanre, D., Buis, J. P., Setzer, A., Vermote, E., Reagan, J. A., Kaufman, Y., Nakajima, T., Lavenu, F., Jankowiak, I., and Smirnov, A.: AERONET – A federated instrument network and data archive for aerosol characterization, Remote Sens. Environ., 66, 1–16, https://doi.org/10.1016/S0034-4257(98)00031-5, 1998.

Holben, B. N., Eck, T. F., Slutsker, I., Smirnov, A., Sinyuk, A., Schafer, J., Giles, D., and Dubovik O.: AERONET's Version 2.0 quality assurance criteria, available at: http://aeronet.gsfc.nasa.gov/new_web/Documents/AERONETcriteria_final1.pdf (last access: 6 October 2020), 2006.

Hudson, P. K., Murphy, D. M., Cziczo, D. J., Thomson, D. S., de Gouw, J. A., Warneke, C., Holloway, J., Jost, H. J., and Hübler, G.: Biomass-burning particle measurements: Characteristics composition and chemical processing, J. Geophys. Res.-Atmos., 109, D23S27, https://doi.org/10.1029/2003JD004398, 2004.

IPCC: Climate Change 2013: The Physical Science Basis. Contribution of Working Group I to the Fifth Assessment Report of the Intergovernmental Panel on Climate Change, edited by: Stocker, T. F., Qin, D., Plattner, G.-K., Tignor, M., Allen, S. K., Boschung, J., Nauels, A., Xia, Y., Bex, V., and Midgley, P. M., Cambridge University Press, Cambridge, UK and New York, NY, USA, 1535 pp., 2013.

Jimenez, J. L., Campuzano-Jost, P., Day, D. A., Nault, B. A., Guo, H., Schroder, J. C., and Cubison, M. J.: Frequently AMS Questions for AMS Data Users, available at: http://cires1.colorado.edu/jimenez-group/wiki/index.php/FAQ_for_AMS_Data_Users, last access: 20 January 2021.

Kahn, R. A., Berkoff, T. A., Brock, C., Chen, G., Ferrare, R. A., Ghan, S., Hanisco, T. F, Hegg, D. A., Martins, J. V., McNaughton, C. S., Murphy, D. M., Ogren, J. A., Penner, J. E., Pilewskie, P., Seinfeld, J. H., and Worsnop, D. R.: SAM-CAAM: A concept for acquiring systematic aircraft measurements to characterize aerosol air masses, Bull. Am. Meteor. Soc., 98, 2215–2228, https://doi.org/10.1175/BAMS-D-16-0003.1, 2017.

Katich, J. M., Samset, B. H., Bui, T. P., Dollner, M., Froyd, K., Campuzano-Jost, P., Nault, B., Schroder, J., Weinzierl, B., and Schwarz, J. P.: Strong contrast in remote black carbon aerosol loadings between the Atlantic and Pacific basins, J. Geophys. Res., 123, 13386–13395, https://doi.org/10.1029/2018JD029206, 2018.

Koepke, P., Gasteiger, J., and Hess, M.: Technical Note: Optical properties of desert aerosol with non-spherical mineral particles: data incorporated to OPAC, Atmos. Chem. Phys., 15, 5947–5956, https://doi.org/10.5194/acp-15-5947-2015, 2015.

Kovilakam, M., Thomason, L. W., Ernest, N., Rieger, L., Bourassa, A., and Millán, L.: The Global Space-based Stratospheric Aerosol Climatology (version 2.0): 1979–2018, Earth Syst. Sci. Data, 12, 2607–2634, https://doi.org/10.5194/essd-12-2607-2020, 2020.

Kuang, Y., Zhao, C., Tao, J., Bian, Y., Ma, N., and Zhao, G.: A novel method for deriving the aerosol hygroscopicity parameter based only on measurements from a humidified nephelometer system, Atmos. Chem. Phys., 17, 6651–6662, https://doi.org/10.5194/acp-17-6651-2017, 2017.

Kupc, A., Williamson, C., Wagner, N. L., Richardson, M., and Brock, C. A.: Modification, calibration, and performance of the Ultra-High Sensitivity Aerosol Spectrometer for particle size distribution and volatility measurements during the Atmospheric Tomography Mission (ATom) airborne campaign, Atmos. Meas. Tech., 11, 369–383, https://doi.org/10.5194/amt-11-369-2018, 2018.

Lack, D. A., Cappa, C. D., Langridge, J., Richardson, M., Law, D., McLaughlin, R., and Murphy, D. M.: Aircraft instrument for comprehensive characterisation of aerosol optical properties, Part 2: Black and brown carbon absorption and absorption enhancement measured with photo acoustic spectroscopy, Aerosol Sci. Technol. 45, 555–568, https://doi.org/10.1080/02786826.2011.645955, 2012.

Langridge, J., Richardson, M., Lack, D. A., Law, D., and Murphy, D. M. : Aircraft instrument for comprehensive characterisation of aerosol optical properties, Part I: Wavelength dependent optical extinction and its relative humidity dependence measured using cavity ringdown spectroscopy, Aerosol Sci. Technol. 45, 1305–1318, https://doi.org/10.1080/02786826.2011.592745, 2011

Liu, D., He, C., Schwarz, J. P., and Wang, X.: Lifecycle of light-absorbing carbonaceous aerosols in the atmosphere, npj Clim. Atmos. Sci., 3, 40, https://doi.org/10.1038/s41612-020-00145-8, 2020.

Liu, X., Easter, R. C., Ghan, S. J., Zaveri, R., Rasch, P., Shi, X., Lamarque, J.-F., Gettelman, A., Morrison, H., Vitt, F., Conley, A., Park, S., Neale, R., Hannay, C., Ekman, A. M. L., Hess, P., Mahowald, N., Collins, W., Iacono, M. J., Bretherton, C. S., Flanner, M. G., and Mitchell, D.: Toward a minimal representation of aerosols in climate models: description and evaluation in the Community Atmosphere Model CAM5, Geosci. Model Dev., 5, 709–739, https://doi.org/10.5194/gmd-5-709-2012, 2012.

Liu, X., Ma, P.-L., Wang, H., Tilmes, S., Singh, B., Easter, R. C., Ghan, S. J., and Rasch, P. J.: Description and evaluation of a new four-mode version of the Modal Aerosol Module (MAM4) within version 5.3 of the Community Atmosphere Model, Geosci. Model Dev., 9, 505–522, https://doi.org/10.5194/gmd-9-505-2016, 2016.

Mann, G. W., Carslaw, K. S., Spracklen, D. V., Ridley, D. A., Manktelow, P. T., Chipperfield, M. P., Pickering, S. J., and Johnson, C. E.: Description and evaluation of GLOMAP-mode: a modal global aerosol microphysics model for the UKCA composition-climate model, Geosci. Model Dev., 3, 519–551, https://doi.org/10.5194/gmd-3-519-2010, 2010.

Marchand, P. and Marmet, L.: Binomial smoothing filter: A way to avoid some pitfalls of least square polynomial smoothing, Rev. Sci. Instrum., 54, 1034–1041, https://doi.org/10.1063/1.1137498, 1983.

McComiskey, A., Schwartz, S. E., Schmid, B., Guan, H., Lewis, E. R., Ricchiazzi, P., and Ogren, J. A.: Direct aerosol forcing: Calculation from observables and sensitivities to inputs, J. Geophys. Res., 113, D09202, https://doi.org/10.1029/2007JD009170, 2008.

McManus, J. B., Nelson, D. D., Shorter, J. H., Jimenez, R., Herndon, S., Saleska, S. R., and Zahniser, M. S.: A high precision pulsed quantum cascade laser spectrometer for measurements of stable isotopes of carbon dioxide, J. Mod. Optic., 52, 2309–2321, 2005.

McMurry, P. H. and Wilson, J. C.: Growth laws for the formation of secondary ambient aerosols: Implications for chemical conversion mechanisms, Atmos. Environ., 16, 121–134, https://doi.org/10.1016/0004-6981(82)90319-5, 1982.

McNaughton, C. S., Clarke, A. D., Howell, S. G., Pinkerton, M., Anderson, B., Thornhill, L., Hudgins, C., Winstead, E., Dibb, J. E., Scheuer, E., and Maring, H.: Results from the DC-8 Inlet Characterization Experiment (DICE): Airborne versus surface sampling of mineral dust and sea salt aerosols, Aerosol Sci. Tech-

nol., 41, 136–159, https://doi.org/10.1080/02786820601118406, 2007.

Moore, R. H., Wiggins, E. B., Ahern, A. T., Zimmerman, S., Montgomery, L., Campuzano Jost, P., Robinson, C. E., Ziemba, L. D., Winstead, E. L., Anderson, B. E., Brock, C. A., Brown, M. D., Chen, G., Crosbie, E. C., Guo, H., Jimenez, J. L., Jordan, C. E., Lyu, M., Nault, B. A., Rothfuss, N. E., Sanchez, K. J., Schueneman, M., Shingler, T. J., Shook, M. A., Thornhill, K. L., Wagner, N. L., and Wang, J.: Sizing response of the Ultra-High Sensitivity Aerosol Spectrometer (UHSAS) and Laser Aerosol Spectrometer (LAS) to changes in submicron aerosol composition and refractive index, Atmos. Meas. Tech., 14, 4517–4542, https://doi.org/10.5194/amt-14-4517-2021, 2021.

Moosmüller, H. and Ogren, J. A.: Parameterization of the aerosol upscatter fraction as function of the backscatter fraction and their relationships to the asymmetry parameter for radiative transfer calculations, Atmosphere, 8, 133, https://doi.org/10.3390/atmos8080133, 2017.

Moteki, N., Kondo, Y., and Nakamura, S.: Method to measure refractive indices of small nonspherical particles: Application to black carbon particles, J. Aerosol Sci., 41, 513–521, https://doi.org/10.1016/j.jaerosci.2010.02.013, 2010.

Murphy, D. M., Cziczo, D. J., Hudson, P. K., Thomson, D. S., Wilson, J. C., Kojima, T., and Buseck, P. R.: Particle generation and resuspension in aircraft inlets when flying in clouds, Aerosol Sci. Tech., 38, 401–409, https://doi.org/10.1080/02786820490443094, 2004.

Murphy, D. M., Cziczo, D. J., Froyd, K. D., Hudson, P. K., Matthew, B. M., Middlebrook, A. M., Peltier, R. E., Sullivan, A., Thomson, D. S., and Weber, R. J.: Single-particle mass spectrometry of tropospheric aerosol particles, J. Geophys. Res., 111, D23S32, https://doi.org/10.1029/2006JD007340, 2006.

Murphy, D. M., Froyd, K. D., Apel, E., Blake, D., Blake, N., Evangeliou, N., Hornbrook, S., Peischl, J., Ray, E., Ryerson, T. B., Thompson, C., and Stohl, A.: An aerosol particle containing enriched uranium encountered in the remote upper troposphere, J. Environ. Radioactiv., 184–185, 95–100, https://doi.org/10.1016/j.jenvrad.2018.01.006, 2018.

Murphy, D. M., Froyd, K. D., Bourgeois, I., Brock, C. A., Kupc, A., Peischl, J., Schill, G. P., Thompson, C. R., Williamson, C. J., and Yu, P.: Radiative and chemical implications of the size and composition of aerosol particles in the existing or modified global stratosphere, Atmos. Chem. Phys., 21, 8915–8932, https://doi.org/10.5194/acp-21-8915-2021, 2021.

Nakao, S.: Why would apparent κ linearly change with O / C? Assessing the role of volatility, solubility, and surface activity of organic aerosols, Aerosol Sci. Technol., 51, 1377–1388, https://doi.org/10.1080/02786826.2017.1352082, 2017.

NASA: NASA Armstrong Fact Sheet: DC-8 Airborne Science Laboratory, available at: https://www.nasa.gov/centers/armstrong/news/FactSheets/FS-050-DFRC.html, (last access: 6 October 2020), 2015.

NASA/LARC/SD/ASDC: Global Space-based Stratospheric Aerosol Climatology Version 2.0, NASA Langley Atmospheric Science Data Center DAAC [data set], https://doi.org/10.5067/GLOSSAC-L3-V2.0, 2018.

Nault, B. A., Campuzano-Jost, P., Day, D. A., Jo, D. S., Schroder, J. C., Allen, H. M., Bahreini, R., Bian, H., Blake, D. R., Chin, M., Clegg, S. L., Colarco, P. R., Crounse, J. D., Cubison, M. J., DeCarlo, P. F., Dibb, J. E., Diskin, G. S., Hodzic, A., Hu, W., Katich, J. M., Kim, M. J., Kodros, J. K., Kupc, A., Lopez-Hilfiker, F. D., Marais, E. A., Middlebrook, A. M., Neuman, J. A., Nowak, J. B., Palm, B. B., Paulot, F., Pierce, J. R., Schill, G. P., Scheuer, E., Thornton, J. A., Tsigaridis, K., Wennberg, P. O., Williamson, C. J., and Jimenez, J. L.: Models underestimate the increase of acidity with remoteness biasing radiative impact calculations, Commun. Earth Environ. 2, 93, https://doi.org/10.1038/s43247-021-00164-0, 2021.

Ovadnevaite, J., Ceburnis, D., Canagaratna, M., Berresheim, H., Bialek, J., Martucci, G., Worsnop, D. R., and O'Dowd, C.: On the effect of wind speed on submicron sea salt mass concentrations and source fluxes, J. Geophys. Res., 117, D16201, https://doi.org/10.1029/2011JD017379, 2012.

Park, K., Kittelson, D. B., Zachariah, M. R., and McMurry, P. H.: Measurement of inherent material density of nanoparticle agglomerates, J. Nanopart. Res., 6, 267–272, 2004.

Petters, M. D. and Kreidenweis, S. M.: A single parameter representation of hygroscopic growth and cloud condensation nucleus activity, Atmos. Chem. Phys., 7, 1961–1971, https://doi.org/10.5194/acp-7-1961-2007, 2007.

Petzold, A., Ogren, J. A., Fiebig, M., Laj, P., Li, S.-M., Baltensperger, U., Holzer-Popp, T., Kinne, S., Pappalardo, G., Sugimoto, N., Wehrli, C., Wiedensohler, A., and Zhang, X.-Y.: Recommendations for reporting "black carbon" measurements, Atmos. Chem. Phys., 13, 8365–8379, https://doi.org/10.5194/acp-13-8365-2013, 2013.

Podolske, J. R., Sachse, G. W., and Diskin, G. S.: Calibration and data retrieval algorithms for the NASA Langley/Ames diode laser hygrometer for the NASA Transport and Chemical Evolution Over the Pacific (TRACE-P) mission, J. Geophys. Res., 108, 8792, https://doi.org/10.1029/2002JD003156, 2003.

Quinn, P. K., Coffman, D. J., Johnson, J. E., Upchurch, L. M., and Bates, T. S.: Small fraction of marine cloud condensation nuclei made up of sea spray aerosol, Nat. Geosci., 10, 674–679, https://doi.org/10.1038/ngeo3003, 2017.

Radke, L. F., Stith, J. L, Hegg, D. A., and Hobbs, P. V., Airborne studies of particles and gases from forest fires, J. Air Poll. Control Assoc., 28, 30–34, https://doi.org/10.1080/00022470.1978.10470566, 1977.

Reddington, C. L., Carslaw, K. S., Stier, P., Schutgens, N., Coe, H., Liu, D., Allan, J., Browse, J., Pringle, K. J., Lee, L. A., Yoshioka, M., Johnson, J. S., Regayre, L. A., Spracklen, D. V., Mann, G. W., Clarke, A., Hermann, M., Henning, S., Wex, H., Kristensen, T. B., Leaitch, W. R., Pöschl, U., Rose, D., Andreae, M. O., Schmale, J., Kondo, Y., Oshima, N., Schwarz, J. P., Nenes, A., Anderson, B., Roberts, G. C., Snider, J. R., Leck, C., Quinn, P. K., Chi, X., Ding, A., Jimenez, J. L., and Zhang, Q., The Global Aerosol Synthesis and Science Project (GASSP): Measurements and modeling to reduce uncertainty, Bull. Amer. Meteor. Soc., 98, 1857–1877, 2017.

Rickards, A. M. J., Miles, R. E. H., Davies, J. F., Marshall, F. H., and Reid, J. P.: Measurements of the sensitivity of aerosol hygroscopicity and the κ parameter to the O / C ratio, J. Phys. Chem. A, 117, 14120–14131, https://doi.org/10.1021/jp407991n, 2013.

Romshoo, B., Müller, T., Pfeifer, S., Saturno, J., Nowak, A., Ciupek, K., Quincey, P., and Wiedensohler, A.: Optical properties of coated black carbon aggregates: numerical simulations, radiative forcing estimates, and size-resolved param-

eterization scheme, Atmos. Chem. Phys., 21, 12989–13010, https://doi.org/10.5194/acp-21-12989-2021, 2021.

Ryerson, T. B., Buhr, M. P., Frost, G. J., Goldan, P. D., Holloway, J. S., Hübler, G., Jobson, B. T., Kuster, W. C., McKeen, S. A., Parrish, D. D., Roberts, J. M., Sueper, D. T., Trainer, M., Williams, J., and Fehsenfeld, F. C.: Emissions lifetimes and ozone formation in power plant plumes, J. Geophys. Res., 103, 22569–22583, https://doi.org/10.1029/98JD01620, 1998.

Schill, G. P., Froyd, K. D., Bian, H., Kupc, A., Williamson, C., Brock, C. A. Ray, E., Hornbrook, R. S., Hills, A. J., Apel, E. C., Chin, M., Colarco, P. R., and Murphy, D. M.: Widespread biomass burning smoke throughout the remote troposphere, Nat. Geosci. 13, 422–427, https://doi.org/10.1038/s41561-020-0586-1, 2020.

Schroder, J. C., Campuzano-Jost, P., Day, D. A., Shah, V., Larson, K., Sommers, J. M., Sullivan, A. P., Campos, T., Reeves, J. M., Hills, A., Hornbrook, R. S., Blake, N. J., Scheuer, E., Guo, H., Fibiger, D. L., McDuffie, E. E., Hayes, P. L., Weber, R. J., Dibb, J. E., Apel, E. C., Jaeglé, L., Brown, S. S., Thornton, J. A., and Jimenez, J. L.: Sources and secondary production of organic aerosols in the northeastern United States during WINTER. J. Geophys. Res.-Atmos., 123, 7771–7796, https://doi.org/10.1029/2018JD028475, 2018.

Schwarz, J. P., Spackman, J. R., Gao, R. S., Perring, A. E., Cross, E., and Onasch, T. B., et al.: The detection efficiency of the single particle soot photometer, Aerosol Sci. Technol., 44, 612–628, https://doi.org/10.1080/02786826.2010.481298, 2010.

Schwarz, J. P., Samset, B. H., Perring, A. E., Spackman, J. R., Gao, R. S., Stier, P., Schulz, M., Moore, F. L., Ray, E. A., and Fahey, D. W.: Global-scale seasonally resolved black carbon vertical profiles over the Pacific, Geophys. Res. Lett., 40, 5542–5547, https://doi.org/10.1002/2013GL057775, 2013.

Scott, T., Bui, R. Chan, and Bowen, S. W.: The Meteorological Measurement System on the NASA ER-2 aircraft, J. Atmos. Ocean. Technol., 7, 525–540, https://doi.org/10.1175/1520-0426(1990)007<0525:TMMSOT>2.0.CO;2, 1990.

Shinozuka, Y., Clarke, A. D., Howell, S. G., Kapustin, V. N., and Huebert, B. J.: Sea-salt vertical profiles over theSouthern and tropical Pacific oceans: Microphysics, optical properties, spatial variability, and variations with wind speed, J. Geophys.Res., 109, D24201, https://doi.org/10.1029/2004JD004975, 2004.

Smirnov, A., Holben, B. N., Slutsker, I., Giles, D. M., McClain, C. R., Eck, T. F., Sakerin, S. M., Macke, A., Croot, P., Zibordi, G., Quinn, P. K., Sciare, J., Kinne, S., Harvey, M., Smyth, T. J., Piketh, S., Zielinski, T., Proshutinsky, A., Goes, J. I., Nelson, N. B., Larouche, P., Radionov, V. F., Goloub, P., Moorthy, K. K., Matarrese, R., Robertson, E. J., and Jourdin, F.: Maritime Aerosol Network as a component of Aerosol Robotic Network, J. Geophys. Res., 114, D06204, https://doi.org/10.1029/2008JD011257, 2009.

Spanu, A., Dollner, M., Gasteiger, J., Bui, T. P., and Weinzierl, B.: Flow-induced errors in airborne in situ measurements of aerosols and clouds, Atmos. Meas. Tech., 13, 1963–1987, https://doi.org/10.5194/amt-13-1963-2020, 2020.

Stokes, R. H. and Robinson, R. A.: Interactions in aqueous nonelectrolyte solutions: I. Solute-solvent equilibria, J. Phys. Chem., 70, 2126–2130, https://doi.org/10.1021/j100879a010, 1966.

Strode, S. A., Liu, J., Lait, L., Commane, R., Daube, B., Wofsy, S., Conaty, A., Newman, P., and Prather, M.: Forecasting carbon monoxide on a global scale for the ATom-1 aircraft mission: insights from airborne and satellite observations and modeling, Atmos. Chem. Phys., 18, 10955–10971, https://doi.org/10.5194/acp-18-10955-2018, 2018.

Tang, I. N.: Chemical and size effects of hygroscopic aerosols on light scattering coefficients, J. Geophys. Res., 101, 19245–19250, https://doi.org/10.1029/96JD03003, 1996.

Thomson, D. S., Schein, M. E., and Murphy, D. M.: Particle analysis by laser mass spectrometry WB-57F instrument overview, Aerosol Sci. Tech., 33, 153–169, https://doi.org/10.1080/027868200410903, 2000.

Titos, G., Cazorla, A., Zieger, P., Andrews, E., Lyamani, H., Granados-Muñoz, M. J., Olmo, F. J., and Alados-Arboledas, L.: Effect of hygroscopic growth on the aerosol light-scattering coefficient: A review of measurements, techniques and error sources, Atmos. Environ., 141, 494–507, https://doi.org/10.1016/j.atmosenv.2016.07.021, 2016.

Varma, R. M., Ball, S. M., Brauers, T., Dorn, H.-P., Heitmann, U., Jones, R. L., Platt, U., Pöhler, D., Ruth, A. A., Shillings, A. J. L., Thieser, J., Wahner, A., and Venables, D. S.: Light extinction by secondary organic aerosol: an intercomparison of three broadband cavity spectrometers, Atmos. Meas. Tech., 6, 3115–3130, https://doi.org/10.5194/amt-6-3115-2013, 2013.

Walser, A., Sauer, D., Spanu, A., Gasteiger, J., and Weinzierl, B.: On the parametrization of optical particle counter response including instrument-induced broadening of size spectra and a self-consistent evaluation of calibration measurements, Atmos. Meas. Tech., 10, 4341–4361, https://doi.org/10.5194/amt-10-4341-2017, 2017.

Wang, X., Heald, C. L., Sedlacek, A. J., de Sá, S. S., Martin, S. T., Alexander, M. L., Watson, T. B., Aiken, A. C., Springston, S. R., and Artaxo, P.: Deriving brown carbon from multiwavelength absorption measurements: method and application to AERONET and Aethalometer observations, Atmos. Chem. Phys., 16, 12733–12752, https://doi.org/10.5194/acp-16-12733-2016, 2016.

Washenfelder, R. A., Attwood, A. R., Brock, C. A., Guo, H., Xu, L., Weber, R. J., Ng, N. L., Allen, H. M., Ayres, B. R., Baumann, K., Cohen, R. C., Draper, D. C., Duffey, K. C., Edgerton, E., Fry, J. L., Hu, W. W., Jimenez, J. L., Palm, B. B., Romer, P., Stone, E. A., Wooldridge, P. J., and Brown, S. S.: Biomass burning dominates brown carbon absorption in the rural southeastern United States, Geophys. Res. Lett., 42, 653–664, https://doi.org/10.1002/2014GL062444, 2015.

Weinzierl, B., Sauer, D., Esselborn, M., Petzold, A., Veira, A., Rose, M., Mund, S., Wirth, M., Ansmann, A., Tesche, M., Gross, S., and Freudenthaler, V., Microphysical and optical properties of dust and tropical biomass burning aerosol layers in the Cape Verde region – an overview of the airborne in situ and lidar measurements during SAMUM-2, Tellus B, 63, 589–618, https://doi.org/10.1111/j.1600-0889.2011.00566.x, 2011.

Williamson, C., Kupc, A., Wilson, J., Gesler, D. W., Reeves, J. M., Erdesz, F., McLaughlin, R., and Brock, C. A.: Fast time response measurements of particle size distributions in the 3–60 nm size range with the nucleation mode aerosol size spectrometer, Atmos. Meas. Tech., 11, 3491–3509, https://doi.org/10.5194/amt-11-3491-2018, 2018.

Williamson, C. J., Kupc, A., Axisa, A., Kelsey R., Bilsback, K. R, Bui, T. P., Campuzano-Jost, P., Dollner, M., Froyd, K. D., Hodshire, A. L., Jimenez, J. L., Kodros, J. K., Luo, G., Murphy, D.

M., Nault, B. A., Ray, E. A., Weinzierl, B., Wilson, J. C., Yu, F., Yu, P., Pierce, J. R., and Brock, C. A.: A large source of cloud condensation nuclei from new particle formation in the tropics, Nature 574, 399–403, https://doi.org/10.1038/s41586-019-1638-9, 2019.

Wofsy S. C.: HIAPER Pole-to-Pole Observations (HIPPO): Fine-grained, global-scale measurements of climatically important atmospheric gases and aerosols, Phil. Trans. R. Soc. A., 369, 2073–2086, https://doi.org/10.1098/rsta.2010.0313, 2011.

Wofsy, S. C., Afshar, S., Allen, H. M., Apel, E., Asher, E. C., Barletta, B., Bent, J., Bian, H., Biggs, B. C., Blake, D. R., Blake, N., Bourgeois, I., Brock, C. A., Brune, W. H., Budney, J. W., Bui, T. P., Butler, A., Campuzano-Jost, P., Chang, C. S., Chin, M., Commane, R., Correa, G., Crounse, J. D., Cullis, P. D., Daube, B. C., Day, D. A., Dean-Day, J. M., Dibb, J. E., Digangi, J. P., Diskin, G. S., Dollner, M., Elkins, J. W., Erdesz, F., Fiore, A. M., Flynn, C. M., Froyd, K., Gesler, D. W., Hall, S. R., Hanisco, T. F., Hannun, R. A., Hills, A. J., Hintsa, E. J., Hoffman, A., Hornbrook, R. S., Huey, L. G., Hughes, S., Jimenez, J. L., Johnson, B. J., Katich, J. M., Keeling, R., Kim, M. J., Kupc, A., Lait, L. R., Lamarque, J. F., Liu, J., McKain, K., McLaughlin, R. J., Meinardi, S., Miller, D. O., Montzka, S. A., Moore, F. L., Morgan, E. J., Murphy, D. M., Murray, L. T., Nault, B. A., Neuman, J. A., Newman, P. A., Nicely, J. M., Pan, X., Paplawsky, W., Peischl, J., Prather, M. J., Price, D. J., Ray, E., Reeves, J. M., Richardson, M., Rollins, A. W., Rosenlof, K. H., Ryerson, T. B., Scheuer, E., Schill, G. P., Schröder, J. C., Schwarz, J. P., St. Clair, J. M., Steenrod, S. D., Stephens, B. B., Strode, S. A., Sweeney, C., Tanner, D., Teng, A. P., Thames, A. B., Thompson, C. R., Ullmann, K., Veres, P. R., Vizenor, N., Wagner, N. L., Watt, A., Weber, R., Weinzierl, B., Wennberg, P., Williamson, C. J., Wilson, J. C., Wolfe, G. M., Woods, C. T., and Zeng, L. H.: ATom: Merged Atmospheric Chemistry, Trace Gases, and Aerosols, ORNL Distributed Active Archive Center [data set], https://doi.org/10.3334/ORNLDAAC/1581, 2018.

Wofsy, S. C., Afshar, S., Allen, H. M., Apel, E. C., Asher, E. C., Barletta, B., Bent, J., Bian, H., Biggs, B. C., Blake, D. R., Blake, N., Bourgeois, I., Brock, C. A., Brune, W. H., Budney, J. W., Bui, T. P., Butler, A., Campuzano-Jost, P., Chang, C. S., Chin, M., Commane, R., Correa, G., Crounse, J. D., Cullis, P. D., Daube, B. C., Day, D. A., Dean-Day, J. M., Dibb, J. E., DiGangi, J. P., Diskin, G. S., Dollner, M., Elkins, J. W., Erdesz, F., Fiore, A. M., Flynn, C. M., Froyd, K. D., Gesler, D. W., Hall, S. R., Hanisco, T. F., Hannun, R. A., Hills, A. J., Hintsa, E. J., Hoffman, A., Hornbrook, R. S., Huey, L. G., Hughes, S., Jimenez, J. L., Johnson, B. J., Katich, J. M., Keeling, R. F., Kim, M. J., Kupc, A., Lait, L. R., McKain, K., Mclaughlin, R. J., Meinardi, S., Miller, D. O., Montzka, S. A., Moore, F. L., Morgan, E. J., Murphy, D. M., Murray, L. T., Nault, B. A., Neuman, J. A., Newman, P. A., Nicely, J. M., Pan, X., Paplawsky, W., Peischl, J., Prather, M. J., Price, D. J., Ray, E. A., Reeves, J. M., Richardson, M., Rollins, A. W., Rosenlof, K. H., Ryerson, T. B., Scheuer, E., Schill, G. P., Schroder, J. C., Schwarz, J. P., St. Clair, J. M., Steenrod, S. D., Stephens, B. B., Strode, S. A., Sweeney, C., Tanner, D., Teng, A. P., Thames, A. B., Thompson, C. R., Ullmann, K., Veres, P. R., Wagner, N. L., Watt, A., Weber, R., Weinzierl, B. B., Wennberg, P. O., Williamson, C. J., Wilson, J. C., Wolfe, G. M., Woods, C. T., Zeng, L. H., and Vieznor, N.: ATom: Merged Atmospheric Chemistry, Trace Gases, and Aerosols, Version 2, ORNL DAAC, Oak Ridge, Tennessee, USA [data set], https://doi.org/10.3334/ORNLDAAC/1925, 2021.

Wong, J. P. S., Nenes, A., and Weber, R. J.: Changes in light absorptivity of molecular weight separated brown carbon due to photolytic aging, Environ. Sci. Technol., 51, 8414–8421, https://doi.org/10.1021/acs.est.7b01739, 2017.

Wong, J. P. S., Tsagkaraki, M., Tsiodra, I., Mihalopoulos, N., Violaki, K., Kanakidou, M., Sciare, J., Nenes, A., and Weber, R. J.: Atmospheric evolution of molecular-weight-separated brown carbon from biomass burning, Atmos. Chem. Phys., 19, 7319–7334, https://doi.org/10.5194/acp-19-7319-2019, 2019.

Wu, H., Taylor, J. W., Langridge, J. M., Yu, C., Allan, J. D., Szpek, K., Cotterell, M. I., Williams, P. I., Flynn, M., Barker, P., Fox, C., Allen, G., Lee, J., and Coe, H.: Rapid transformation of ambient absorbing aerosols from West African biomass burning, Atmos. Chem. Phys., 21, 9417–9440, https://doi.org/10.5194/acp-21-9417-2021, 2021.

Yang, J.-M.: Towards a combined SAGE II and SCIAMACHY aerosol dataset and implications for stratospheric aerosol trend analysis over East Asia, Atmos. Ocean. Sci. Lett., 10, 343–347, https://doi.org/10.1080/16742834.2017.1341812, 2017.

Zanatta, M., Laj, P., Gysel, M., Baltensperger, U., Vratolis, S., Eleftheriadis, K., Kondo, Y., Dubuisson, P., Winiarek, V., Kazadzis, S., Tunved, P., and Jacobi, H.-W.: Effects of mixing state on optical and radiative properties of black carbon in the European Arctic, Atmos. Chem. Phys., 18, 14037–14057, https://doi.org/10.5194/acp-18-14037-2018, 2018.

Zaveri, R. A., Easter, R.C., and Wexler, A. S.: A new method for multicomponent activity coefficients of electrolytes in aqueous atmospheric aerosols, J. Geophys. Res., 110, D02201, https://doi.org/10.1029/2004JD004681, 2005.

Zeng, L., Zhang, A., Wang, Y., Wagner, N. L., Katich, J. M., Schwarz, J. P., Schill, G. P., Brock, C., Froyd, K. D., Murphy, D. J., Williamson, C. J., Kupc, A., Scheuer, E., Dibb, J., and Weber, R. J.: Global measurements of brown carbon and estimated direct radiative effects, Geophys. Res. Lett., 47, e2020GL088747, https://doi.org/10.1029/2020GL088747, 2020.

Zieger, P., Väisänen, O., Corbin, J., Partridge, D. G., Bastelberger, S., Mousavi-Fard, M., Rosati, B., Gysel, M., Krieger, U. K., Leck, C., Nenes, A., Riipinen, I., Virtanen, A., and Salter, M. E.: Revising the hygroscopicity of inorganic sea salt particles, Nat. Commun. 8, 15883, https://doi.org/10.1038/ncomms15883, 2017.